universität wien

DISSERTATION | DOCTORAL THESIS

Titel | Title

Polymer based photonic materials for cold neutron optics

verfasst von | submitted by

Elhoucine Hadden

angestrebter akademischer Grad | in partial fulfilment of the requirements for the degree of

Doktor der Naturwissenschaften (Dr.rer.nat.)

Wien | Vienna, 2024

Studienkennzahl lt. Studienblatt | Degree programme code as it appears on the student record sheet:	UA 796 605 411
Dissertationsgebiet lt. Studienblatt | Field of study as it appears on the student record sheet:	Physik
Betreut von | Supervisor:	ao. Univ.-Prof. Dr. Martin Fally Dipl.-Ing. Dr. Jürgen Klepp

Contents

Abstract

This research advances the study of light and neutron diffraction in holographic gratings through model development, material optimization, and tailored experimental methodologies. The focus is on achieving high scattering length density (SLD) modulation and structural stability, and on providing the necessary tools for analyzing the intricate and variable nature of neutron diffraction data. Simplified first-order adaptations of the Rigorous Coupled-Wave Analysis (RCWA) theory were developed to enable accurate and computationally efficient analysis.

Material studies cover Bayfol® HX200 photopolymers, nanodiamond-based nanoparticle composites (NDPC), and hyperbranched polymer (HBP) dispersed nanocomposites, each evaluated for suitability in light and neutron diffraction. Commercial Bayfol foils, in particular, were optimized for neutron diffraction, with certain writing intensities and dosages enhancing their efficiency. Both light and neutron diffraction patterns aligned with the predictions of the non-local photopolymerization-driven diffusion (NPDD) model, offering insight into the underlying processes influencing optical performance.

NDPC gratings achieved record-breaking SLD modulation amplitudes with high diffraction efficiency, minimal angular and wavelength selectivity losses, and robustness that supports their application in advanced neutron optics, including a planned very cold neutron (VCN) interferometer for 2025. HBP gratings similarly exhibited high modulation amplitudes, positioning them as promising candidates.

Experimental setups were refined for noise reduction, and a rigorous data reduction and background treatment protocol was developed to accurately derive diffraction efficiency across varied setups. Bayesian inference methods, including Markov Chain Monte Carlo sampling and Bayesian Model Selection, were also introduced as supplementary tools for probabilistic model validation in cases with extensive parameter ranges or nonuniformities.

Through theoretical, material, and experimental advancements, this thesis establishes a framework for future interdisciplinary research in neutron optics and holography, contributing to the ongoing development of diffraction-based applications in materials science and fundamental physics.

Zusammenfassung

In dieser Arbeit werden Licht- und Neutronenbeugung in holographischen Gittern durch Modellentwicklung, Materialoptimierung und maßgeschneiderte experimentelle Methoden untersucht. Der Schwerpunkt liegt auf der Optimierung der Streulängendichtemodulation und struktureller Stabilität der Gitter, sowie auf Entwicklung der notwendigen Werkzeuge zur Analyse der komplexen und variablen Eigenschaften von Neutronenbeugungsdaten. Näherungen zur sogenannten Rigorous Coupled-Wave Analysis Theorie wurden entwickelt, um eine präzise und recheneffiziente Analyse zu ermöglichen.

Die Materialstudien umfassen Bayfol®-HX200-Photopolymer, nanodiamant-basierte Komposite und nanokomposite Materialien mit hochverzweigten Polymeren, die jeweils auf ihre Eignung für Licht- und Neutronenbeugung untersucht wurden. Insbesondere wurde die Herstellung von Gittern in kommerziellen Bayfol-Folien für die Neutronenbeugung optimiert, wobei bestimmte Schreibintensitäten und -dosen deren Effizienz steigerten. Die Beugungsmuster von Licht und Neutronen entsprachen den Vorhersagen des Modells der nicht-lokalen, photopolymerisationsgetriebenen Diffusion und lieferten Einblicke in die zugrunde liegenden Prozesse, die die optische Leistung beeinflussen.

Nanodiamant-basierte Gitter erzielten beispiellose Streulängendichten Modulationsamplituden mit hoher Beugungseffizienz, minimalen Intensitätsverlusten an die Winkel- und Wellenlängenselektivität sowie einer Robustheit, die ihre Anwendung in der fortschrittlichen Neutronenoptik erlaubt, einschließlich eines geplanten sehr kalten Neutroneninterferometers in naher Zukunft. Auch Gitter basierende auf hochverzweigten Polymeren zeigten hohe Modulationsamplituden, wodurch sie als vielversprechende Kandidaten gelten.

Die experimentellen Aufbauten wurden zur Reduzierung von Störsignalen verbessert, und ein rigoroses Protokoll zur Datenreduktion und Hintergrundbehandlung wurde entwickelt, um die Beugungseffizienz in verschiedenen Aufbauten genau zu bestimmen. Zudem wurden Bayessche Inferenzmethoden, einschließlich Markov-Chain-Monte-Carlo sampling und Bayesianische Modellwahl, als ergänzende Werkzeuge für die probabilistische Modellvalidierung bei umfangreichen Parameterbereichen oder Inhomogenitäten eingeführt.

Durch theoretische, materielle und experimentelle Fortschritte etabliert diese Dissertation ein Fundament für künftige interdisziplinäre Forschungen in der Neutronenoptik und Holographie und trägt zur Weiterentwicklung von beugungsbasierten Anwendungen in der Materialwissenschaft und der fundamentalen Physik bei.

Chapter 1

Introduction

Cold and very cold neutrons provide a unique gateway to revealing structures at atomic, subatomic, and mesoscopic levels. Neutron optics, dedicated to the precise control and manipulation of these neutrons, enables high-precision experiments that offer detailed insights into material properties and fundamental physics. The unique properties of cold and very cold neutron optics make them indispensable in neutron scattering, imaging, and interferometry, driving advancements in scientific research.

This introductory chapter outlines the impetus for advancing neutron optics, particularly in addressing the challenges associated with very cold neutron (VCN) wavelengths. Historical developments and material innovations that have shaped this field are briefly highlighted, setting the stage for a deeper exploration into the specific challenges and solutions presented in slow neutron optics. The forthcoming sections provide a detailed perspective on these advancements, framing the overall direction and scope of the thesis.

1.1 Motivation

The advancement of neutron optics is driven by significant scientific interest and the development of powerful neutron sources [1, 2]. This is particularly crucial for VCNs, which have wavelengths that are too long to be diffracted by perfect crystals yet not long enough to be totally reflected by surfaces at all angles [3]. It is common to refer to moderated neutrons, including thermal, as *slow* neutrons. In this research, the term *slow* is reserved only to CN and VCN, focusing mainly on the range of (5 Å $< \lambda < 521$ Å). The lower limit is set based on the Bragg cut-off of large lattice constant crystals e.g. 5 Å for lead. For the upper limit, the approximate 300 neV threshold for ultra-cold neutrons (UCNs) is used. An emerging example of the increasing interest about VCNs is the HighNESS project, aiming to install a second source of slow neutrons at the European Spallation Source (ESS) [4–6]. These efforts must be accompanied by innovative neutron-optical techniques to efficiently utilize the potential gains in VCN flux.

The broader context of neutron optics underscores a fundamental challenge: the inherently low neutron counts for VCNs due to the Maxwellian energy distribution of neutron spectra from reactors [7, 8]. This limitation heightens the need for highly efficient neutron-optical components that can maximize the usage of available neutron

flux, making the development of such components not just a scientific pursuit but a necessity for many practical applications in neutron experiments.

The main features of slow neutrons are twofold. Firstly, the real part of the complex refractive index deviates more significantly from unity when compared to thermal neutrons, paving the way for the use of refractive optics (at the cost of non-negligible losses from absorption). For example, the refractive index of an MgF_2 bulk material with a scattering length density (SLD) $5.13 \times 10^{-6}\,\text{Å}^{-2}$ is $1 - 2.04 \times 10^{-5}$ and $1 - 8.18 \times 10^{-3}$ for neutron wavelengths of 5 Å and 100 Å, respectively. Secondly, CN and VCN wavelengths are large enough to enable diffraction from micro-structured devices. Therefore, scientific knowledge about slow neutron diffraction evolved from traditional ruled or blazed mechanical gratings to more advanced materials and techniques. The detailed historical context is provided in the next section, with a focus here on the particularities of the devices and materials used so far.

Mechanically ruled (or blazed) gratings and photolithographed rectangular profile gratings were favored for use in neutron interferometers due to their stability, simplicity, and availability [9, 10]. However, these structures faced two primary limitations: 1) they permitted only small diffraction angles, limited by the grating periods of a few microns; 2) they functioned as optically thin gratings, leading to the simultaneous excitation of multiple diffraction orders and thus reduced efficiencies [11]. Addressing the first limitation, advancements in fabrication technologies, such as photolithography, chemical, and mechanical processing, enabled the creation of periodic structures with grating periods down to approximately 100 nm, like those obtained by stretching nanogratings using hybrid molds and nanoimprint lithography [12]. However, these optically thin structures are still not preferred for neutron application due to their propensity for multiple order excitation.

While thin gratings are generally preferred in the considered application to minimize wavelength and angular selectivity issues, it is important that they are of adequate thickness—and with suitably small grating periods—to prevent the overlap of multiple diffraction orders at a given angular position. Gratings should only enable enhanced diffraction for higher orders when they are intentionally designed for that purpose. This approach represents a potential path for future developments, aiming for optimal space management through higher diffraction angles of higher orders. Despite these limitations, mechanically modulated gratings continue to play a crucial role in creating wide-area absorption gratings, which are indispensable in both neutron and X-ray imaging [13].

This necessity has spurred research into materials like Holographic Polymer Dispersed Liquid Crystals (H-PDLC) and the less pertinent polymer-ionic liquid composites [14–17]. H-PDLC materials offer a unique advantage: they enable the creation of holographic optical elements (HOEs) with a highly modulated neutron optical potential, allowing for the achievement of high diffraction efficiencies. Nonetheless, they are challenged by mechanical instability, such as shrinkage, and excessive holographic scattering due to high anisotropy, which adversely impacts the grating recording process. This has led to a search for more stable and similarly efficient alternatives.

The advent of Nanoparticle-Polymer Composites (NPCs) has revolutionized the field of neutron optics, particularly in the creation of holographic optical elements. These composites have been instrumental in developing two- and three-port beam splitters, mirrors using free-standing NPC gratings with SiO_2 nanoparticles, and other

essential components in neutron interferometry and scattering experiments [18–20]. The offered versatility by the free choice of the nanoparticles depending on the desired application, allow for the creation of standard phase gratings, neutron absorption gratings typically incorporating Gd or gadolinium oxide (Gd_2O_3) nanoparticles and polarizing mirrors or beam-splitters via superparamagnetic nanoparticles [13, 21].

In this study, nanodiamond dispersed Polymer Composites (NDPC), a subclass of NPCs, have been specifically focused on due to their exceptional properties that align well with the desired requirements [22, 23]. Nanodiamond (ND) nanoparticles stand out for their high coherent scattering length and minimal losses from absorption and incoherent scattering, akin to those observed in bulk diamond. These properties, combined with their mechanical and thermal stability, make ND an ideal candidate for neutron holographic optical elements.

In addition to the focus on ND-dispersed photopolymers, this research also explored other materials to broaden the understanding of neutron optics. A significant part of the study involved the optimization of the recording process for Covestro HX200 Bayfol® foils [24]. These foils represent a class of commercial photosensitive materials known for their high light refractive index modulation. Their easy availability and low cost add to their attractiveness to be used in neutron experiments. The performed measurements included results from single photopolymer films, as well as multilayered structures.

The study also extended to Hyperbranched Polymers (HBPs), known for their ultra-high refractive index modulation amplitudes in visible light wavelengths [25]. These materials have shown great potential in optical applications due to refractive index modulation amplitudes that can reach up to 4×10^{-2}. This promising characteristic motivated the exploration of HBP-based nanocomposites for neutron optics applications. To evaluate their potential, light optical and neutron diffraction properties of a HBP-based holographic grating will be discussed.

This exploration of various materials, including the shift towards ND-dispersed photo-polymers, underscores the comprehensive approach. While ND-based composites set a new standard for efficiency and versatility, the insights gained from studying other materials like Bayfol® foils and HPBs have been instrumental in understanding the broader spectrum of neutron-optical components. This multifaceted research approach ensures a thorough investigation of potential solutions, paving the way for future advancements in the field.

1.2 Historical Context

The evolution of slow-neutron optics has significant implications for experiments e.g. in the study of analogous diffusion phenomena of light and neutrons, or in experimental tests of quantum mechanical models [26–28]. It has grown into other connected fields of application, particularly in VCN interferometry experiments. Since the advent of matter-wave duality, neutron interferometry emerged, aiming to harness the unique characteristics of neutrons. While H. Rauch and S. A. Werner's comprehensive catalog of neutron interferometry experiments from 1974–2014 [26] provides valuable insights, it appears to focus primarily on thermal neutrons. As a result, some experiments involving slow neutrons are missing. This section offers a brief, non-exhaustive summary

of significant milestones in slow neutron optics and interferometry, acknowledging that some developments may not be fully captured.

1932-1937: Foundational years

The discovery of the neutron by James Chadwick in 1932 [29] opened new frontiers in physics, leading to a myriad of experiments to understand neutron-matter interactions. Subsequent research by E. Amaldi and E. Fermi between 1935 and 1937 elucidated the scattering and absorption characteristics of slow neutrons [30, 31]. This period also witnessed the first demonstrations of neutron diffraction by V. Halban, P. Preiswerk in 1936 [32] and independently by D. P. Mitchell, P. N Powers [33], laying the groundwork for the future of neutron optics. Around the same time, O. Halpern and M. H. Johnson explored magnetic scattering of neutrons [34], paving the way for future studies on neutron spin and polarizing optics.

1944: First neutron reactor source

The operation of the X-10 Graphite reactor at Oak Ridge National Laboratory in 1944 [35, 36] was a major milestone. It's worth noting that earlier references to neutron scattering and Bragg reflection [32, 33] predate some claims in the latter references [1].

1947-1961: Early stage advances

Goldberger and Seitz carefully formulated a theoretical expression of the neutron refractive index in 1947 [37]. The formulation was subsequently re-evaluated and expanded upon by D. Kleinman and G. Snow in 1951 [38], O. Halpern in 1952 [39], and D. Hughes in his seminal work, "Neutron Optics" [40]. These contributions marked the emergence of neutron optics as a well-defined research field. During this period, the focus expanded beyond using perfect crystals as monochromators. Efforts were directed toward developing neutron guides and highly reflective mirrors to address the crowding around neutron sources and allow for the time-shared operation of multiple instruments ([41]).

1962: First neutron interferometer

In 1962, H. Maier-Leibnitz and T. Springer constructed the first neutron interferometer at the laboratory for technical physics at the Technical University of Munich, operating at wavelengths around 4 Å [42]. They explored various optical arrangements, initially employing slits, conventional prisms, and multi-layer mirrors [2]. Due to the small deflection angles caused by the neutron's refractive index (only differing from unity by 10^{-5}-10^{-4}), refractive optics were less preferred because of the small deflection angles. This lead to a shift towards amplitude division setups.

1969-1980: Emergence of new neutron optical components and instrumentation methods

The first observation of thermal neutron diffraction from ruled gratings [45] marked a significant development. These gratings later enabled studies of resonance phenomena and coherence length of slow neutron wave trains. Other non-conventional optics also emerged e.g. manipulation of the neutron's path and/or spin (by precession) through the application of magnetic fields [46]. A pivotal advancement in neutron interferometry came in 1974 with Rauch, Treimer, and Bonse's use of a monolithic slab of perfect

[1] The claim that scattering of slow neutrons by perfect crystals was first predicted in 1937 by G. C. Wick in Ref. [36], and the claim that neutron Bragg reflection was demonstrated experimentally for the first time by E. Wollan in Ref. [35], are inaccurate. The latter is probably a valid claim but only for neutrons produced in a research reactor source

[2] Notably, this same optical setup was later transferred to the ILL's H18 VCN beamline, finding success in various applications [43, 44].

crystals to manipulate neutron beams [47]. Both triple (LLL) and double (LL) Laue case interferometers were successfully demonstrated. The stability, optimal spatial separation, and high diffraction efficiency of the monolithic slab proved instrumental in these experiments. This has motivated, and continues to motivate, numerous interferometry experiments (many of which are listed in Ref. [26]). The latter aim at exploring and testing the quantum mechanical properties of neutrons and matter. In 1976, A. G. Klein and G. I. Opat first demonstrated neutron Fresnel diffraction [48], paving the way for the application of holographic methods in creating holographic zone plates [49, 50]. In 1981, a Billet-type split lens interferometer based on Fresnel diffraction was built [51]. Despite the limitations posed by the inherent chromatic aberrations of zone plates, this attempt highlighted the significant potential of VCNs, especially possibilities offered by their large wavelengths for exploring refraction. A couple of years before, in 1979, Graf, Rauch, and Stern reported on cold neutron diffraction from ruled gratings, contributing further to the understanding of the particle's behavior [9].

1980-1989: Consolidation and refinement Phase
After successfully developing a neutron turbine in Munich, A. Steyerl's work laid the groundwork for a VCN and UCN instrument proposal submitted by P. Ageron at the ILL's high-flux reactor (HFR). The turbine's successful operation at the ILL was reported by Steyerl in 1986 [7]. The establishment of the PF2/VCN platform marked significant progress in slow neutron optics and interferometry. Concurrently, advancements in holography and the formulation of comprehensive models for wave propagation in such periodic media enabled the adoption of holographic optical elements in neutron experiments [52–56]. The introduction of the first Mach-Zehnder type interferometer using reflection-mode diffraction gratings by A.I. Ioffe et al. in 1985 for thermal neutrons [10] represented a notable innovation. The decade saw crucial developments in neutron optics, thoroughly documented in A. G. Klein and S. A. Werner's article [57] and in Sears's book [58], which became key references in the field. Additionally, two major workshop proceedings in 1986 [59] and 1987 [60] highlighted several advances in cold neutron experiments.

1989 to present: Theoretical maturity and ongoing experimental challenges
M. Gruber et al. showcased the first VCN interferometer using phase gratings at the PF2/VCN instrument in 1989 [61]. This paved the way for a new generation of VCN experiments utilizing the diverse grating types discussed in the previous section. For example, we refer to the publications listed on the PF2 instrument webpage page at the ILL website [62] and others [11, 63–74]. In fact, despite the attained theoretical maturity, experimental efforts have been hindered by persistent challenges that are primarily related to low neutron flux and the scarcity of efficient optical materials. The latter, addressed by the here-presented research, continue to shape the trajectory of VCN experimentation. Finally, it is important to note that while this summary highlights critical milestones, it is not exhaustive.

The subsequent section will outline the primary challenges addressed in each section of the thesis, leveraging the historical achievements and the contemporary landscape of neutron interferometry and optics.

1.3 Thesis Outline

This thesis is organized into six main chapters, focusing on the study of neutron optics, specifically examining the diffraction properties of various gratings. A brief overview of each chapter is as follows:

- **Chapter 2: Literature Review** Theoretical approaches for wave propagation analysis in phase gratings are reviewed. First, key estimations used in experimental procedures are demonstrated based on Kogelnik's two-wave coupling theory [75]. Next, a practical and time-efficient variant from the Rigorous Coupled-Wave Analysis (RCWA) model is derived [52, 56]. The terminology of diffraction regimes is highlighted. Moreover, the transmission matrix method for modelling diffraction from multilayer volume holographic gratings is presented.
- **Chapter 3: Materials and Methods** describes the studied materials and the experimental procedures including the holographic recording, the light optical measurements and the neutron setup configurations at the PF2/VCN platform and SANS-I at PSI, SINQ, respectively.
- **Chapter 4: Data Reduction and Background Treatment** Various methods for background estimation were developed and compared. From data extraction to the derivation of diffraction efficiency curves, background analysis challenges associated with low statistics in slow neutron counting were addressed, particularly the ambiguity in defining the zero-th order background.
- **Chapter 5: Results and Discussion** presents and analyzes the research findings within the theoretical and experimental context established in previous chapters.
- **Chapter ??: Conclusions and Perspectives** summarizes the key research findings, discusses the contributions to the field of neutron optics, and outlines future research directions.

The **Appendices** provide supplementary material, including methods for raw data extraction, uncertainty calculations, statistical analyses etc... supporting the thesis's main findings.

Chapter 2

Literature review

A comprehensive review of the existing literature, including theoretical models and relevant studies, will be presented to shape the foundation and direction of this research. A practical numerical model based on the Rigorous Coupled Wave Analysis (RCWA) theory will be presented. This model will be applied to scenarios with non-uniform gratings, aiming to maintain accuracy in parameter determination and to explore structure reconstruction capabilities through phase retrieval. At first, single layer gratings will be considered. Next, a proper formulation for multilayer gratings which involves a refractive index changes across layers will be provided.

2.1 Wave propagation in a planar, lossless and non-magnetic phase grating

A proper description of wave propagation in a media, is derived from Maxwell's equations according to its intrinsic properties. This research is restricted to non magnetic (magnetic permeability $\mu_r = 1$), isotropic (ϵ_r is scalar) and lossless dielectric media (conductivity $\sigma_e = 0$) in the absence of free charge (free charge density $\rho_f = 0$). The derivation of the corresponding propagation equation is presented in Appendix A based on the following first assumption.

Assumption 1: The incident plane wave polarization is orthogonal to the plane of incidence (H mode) i.e., a linear polarization in the y-direction is considered for an incidence at an angle θ with respect to the sample surface (see Figure 2.1). The surface normal $\vec{n}$ is chosen to be parallel to the z-direction and the x-axis orthogonal to $\vec{n}$ within the plane of incidence. Consequently, it is possible to use a scalar wave equation.

As a result, Equation A.3 is reduced to the Helmholtz equation:

$$\left[\nabla^2 + k^2\epsilon_r\right]\ \tilde{\mathrm{E}}(x,z) = 0 \tag{2.1}$$

In order to solve this equation, few additional assumptions are typically used in simplified models.

Assumption 2: The average refractive index n_0 is assumed to be the same inside the grating and outside its boundaries. If not, external angles should be changed by the internal angles using Snell's law.

Assumption 3: A sinusoidal spatial modulation of the relative dielectric constant (refractive index) is considered. For unslanted gratings–slant angle $\phi = \pi/2$ between the grating vector and the z-axis)–the modulation is along the x-axis (see Figure 2.1).

Assumption 4: It is considered that the relative dielectric constant (refractive index) remains the same along the z-direction i.e., there is no decay along the grating thickness. Later in this work, the effect of a modulation profile will be introduced in a more general numerical approach.

As a result, for *phase* gratings, the *relative* dielectric constant of a uniform grating takes this form:

$$\epsilon_r(x,z) \underset{\text{No decay}}{\equiv} \epsilon_0 + \sum_{j\neq 0} \tilde{\epsilon_j} \exp\left(\imath j \vec{K}\cdot\vec{r}\right) \underset{\text{pure phase}}{\equiv} \epsilon_0 + 2\sum_{j>0} \epsilon_j \cos\left(j\vec{K}\cdot\vec{r} + \varphi_j\right) \tag{2.2}$$

The space coordinates are $\vec{r} = (x, y, z)$, the grating vector is $\vec{K} = \frac{2\pi}{\Lambda}(\sin\phi, 0, \cos\phi)$ is the grating vector, Λ is the grating period. $|\tilde{\epsilon_j}| = \epsilon_j$ refers to the amplitude of the j-th Fourier component (FC) of the relative dielectric constant with $\tilde{\epsilon}_{-j} = \tilde{\epsilon}_j^*$ for a phase grating, and $\varphi_j = \arg(\tilde{\epsilon_j})$ is the corresponding relative phase of the j-th order. Therefore, replacing the complex amplitudes with ($\tilde{\epsilon}_j = \epsilon_j \exp(\imath\varphi_j)$ and $\tilde{\epsilon}_{-j} = \epsilon_j \exp(-\imath\varphi_j)$) the simplified form is obtained with the cosine function. In the context of holographic gratings, the cosine form is commonly used, while in acousto-optics, a sinusoidal form is preferred by convention. The existence of multiple FCs arises from the non-linearity of the photo-polymerization process during the development of the structure. Moreover, by measuring the intensities of the diffracted waves one can only retrieve the modulation amplitudes but not the phases of the FCs, which is known as the phase problem of crystallography (or diffraction). Several techniques have been developed to tackle this issue [76], as will be discussed later in this chapter.

In the field of optics, the refractive index is often used interchangeably with the dielectric constant, given the relationship $\epsilon_r = n^2$. Let us consider this equivalent expression:

$$n(x,z) = n_0 + \sum_{j>0} n_j \cos\left(j\vec{K}\cdot\vec{r} + \varphi_j\right) \tag{2.3}$$

Considering the following fifth assumption, the identification of terms from the dielectric constant and the squared refractive index expressions yield: $\epsilon_j = 2n_0 n_j$.

Assumption 5: It is assumed that $n_0 \gg n_j,\ \forall\ j > 0$, which is true almost for every practical case.

The above identification result elucidates the intricacies of light interaction within the holographic grating, where the refractive index modulation is intrinsically linked to the material's polarizability, as reflected in the dielectric constant. This linkage is explicitly demonstrated through the Clausius-Mossotti relation (or equivalently, the

Lorentz–Lorenz equation), which connects the dielectric constant ϵ_r to the microscopic polarizability of the material [77, 78]:

$$\frac{\epsilon_r - 1}{\epsilon_r + 2} = \sum_i \frac{N_i P_i}{3\epsilon_0} \tag{2.4}$$

Here, N_i and P_i represent the atomic number density and the atomic polarizability of the i-th component of the material, respectively. While this is the general form of the relation illustrating the direct link, it is important to note that it may not be the precise expression for the specific case of a holographic grating. It shows how molecular polarizability changes, induced by the photopolymerization process, directly influence the dielectric constant of the material. In contrast, neutron interaction within the same holographic context exhibits a distinctly different behavior. When magnetic interactions are neglected, neutrons are insensitive to the electronic structure alterations which may influence the dielectric constant. This difference could lead to differences in variations of the refractive index modulation amplitudes between light and neutrons for a given structure, especially when varying specific recording parameters.

The modulation amplitude of light is directly influenced by changes in polarizability, whereas the neutron's modulation amplitude is largely unaffected by these changes, being more dependent on the induced SLD contrast. This will be further discussed in the next subsections. The fundamental disparity in interaction principles is pivotal for understanding the differential responses of light and neutrons in holographic grating structures, offering a nuanced perspective in the study of diffractive optics.

Focus will be next shifted towards establishing and solving the coupled differential equations system using Kogelnik's two-wave coupling theory.

2.2 Analytical solution using Kogelnik two-wave coupling theory

The choice of Kogelnik's theory as the foundational framework for the discussion and subsequent comparative analysis in later subsections is primarily due to its straightforward approach in introducing key concepts and its extensive application [75, 79]. This theory is preferred because it offers a clear analytical solution for two coupled waves and is versatile for various case studies: phase, absorption, mixed or magnetic gratings etc. Therefore, a review of Kogelnik's model is essential, particularly to facilitate extending analogous principles to cold neutron optics.

It is proposed that Equation 2.1 be analytically solved according to Kogelnik's two coupled waves theory. Figure 2.1 shows the corresponding geometrical configuration for the considered case of unslanted gratings. The proposed model incorporates the following set of approximations to simplify the coupled wave system.

Kogelnik 1-st approximation: A monochromatic incident wave on the grating at the Bragg angle is considered, with small deviations arising from slight variations in the latter and/or the mean wavelength.

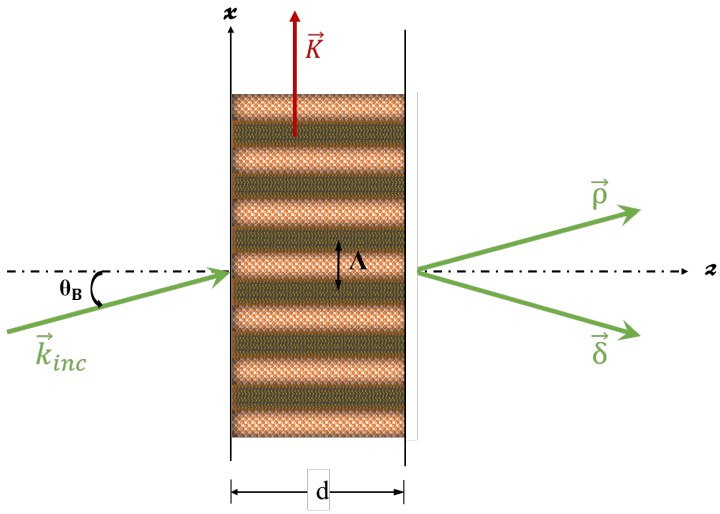

Figure 2.1: Propagation geometry for an unslanted transmission volume hologram grating according to Kogelnik's two-wave coupling theory.

Kogelnik 2nd approximation: Only two waves: a reference wave R and a signal wave S, are significantly propagating inside the grating. The other diffraction orders are considered to strongly violate the Bragg condition and their influence on the energy interchange between the latter waves is neglected. The validity of this consideration is restricted to Bragg's diffraction regime, which will be presented in more details in subsection 2.6.1.

In most practical cases that fall within Kogelnik's assumptions for volume gratings, only the first order FC of the refractive index is kept for a sinusoidal, isotropic, and of *pure-phase* type grating. When the grating is also unslanted, the refractive index expression is reduced to this form.

$$n(x) = n_0 + n_1 \cdot \cos(Kx)$$

By inserting this expression in the right hand side of Equation 2.1, one can can calculate the following:

$$k^2 n^2(x) = k^2 \left[n_0 + n_1 \cos\left(Kx\right)\right]^2$$

The following parameters are defined:

$$\beta = \frac{2\pi}{\lambda} n_0 = k n_0 \qquad ; \qquad \kappa = \frac{\pi n_1}{\lambda} \tag{2.5}$$

Consequently, considering that $n_1^2 \simeq 0$ by assuming $n_0 \gg n_1$, the following expression is obtained:

$$k^2 n^2(x) = \beta^2 + 4\beta \cdot \kappa \cos\left(Kx\right) \tag{2.6}$$

The central parameter of this theory is the coupling constant κ, as it intuitively couples the energy interchange between the reference and the signal waves via the modulation amplitude n_1. The total electric field inside the grating may be described as the superposition of two waves with complex amplitudes $\tilde{R}(z)$ and $\tilde{S}(z)$ varying along the grating's depth direction as a result of the energy interchange.

$$\tilde{E}(x,z) = \tilde{R}(z) \exp\left(-\imath\vec{\rho}\cdot\vec{r}\right) + \tilde{S}(z) \exp\left(-\imath\vec{\delta}\cdot\vec{r}\right) \tag{2.7}$$

The stated approximations allow for considering that the propagation vector of the reference wave is the same as in free space (as if there was no coupling), and hence, $|\,\vec{\rho}\,| = \rho = \beta$. On the other hand, $\vec{\delta}$ is defined by the following condition, know as the K-Vector Closure method (KVCM).

$$\vec{\rho} = \beta \cdot \begin{pmatrix} \sin\theta \\ 0 \\ \cos\theta \end{pmatrix} \quad ; \quad \vec{K} = \begin{pmatrix} K \\ 0 \\ 0 \end{pmatrix} \quad ; \quad \vec{\delta} := \vec{\rho} - \vec{K} = \beta \cdot \begin{pmatrix} \sin\theta - \frac{K}{\beta} \\ 0 \\ \cos\theta \end{pmatrix} \tag{2.8}$$

The general form of KVCM is: $\vec{\delta}_m = \vec{\rho} + m \cdot K$, with $m \in \mathbb{Z}$. Hence, the existence (or cut-off) of a diffraction order depends on the magnitude of $\vec{\delta}_m$ projection on the x-axis–which should not exceed $|\beta|$–provided that Maxwell equations impose the conservation of the tangential component [79]. For two coupled waves, the Bragg condition is fulfilled by the condition $|\,\vec{\delta}\,| = \beta$ as depicted in Figure 2.2b, which translates to its well-known form:

$$\sin\theta = \frac{K}{2\beta} \Longleftrightarrow 2\Lambda \sin\theta = \frac{\lambda}{n_0}. \tag{2.9}$$

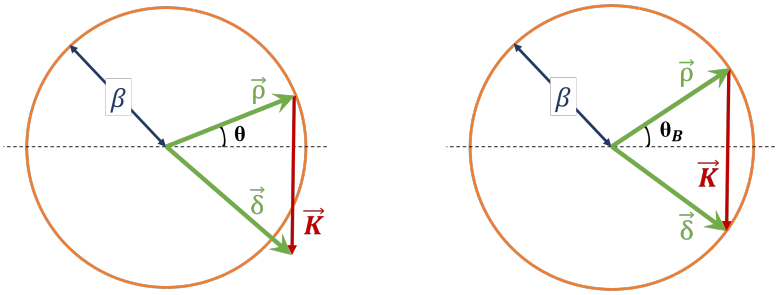

(a) $\theta \neq \theta_B$ (b) $\theta = \theta_B$

Figure 2.2: Illustration of the momentum conservation in KVCM geometry for the (a) near Bragg and (b) in-Bragg diffraction of two coupled waves by a planar hologram grating according.

As stated above, the violation of this condition (*cf.* Fig.2.2a) may arise from an angular deviation $\Delta\theta$ or from the corresponding wavelength by a variation denoted as $\Delta\lambda$. As long as these variations are small enough to write $\theta = \theta_B + \Delta\theta$ and $\lambda = \lambda_B + \Delta\lambda$, it is straightforward to examine the similarity of their effects by differentiating Equation 2.9:

$$\frac{d}{d\lambda}\Big(\sin\big(\theta(\lambda)\big)\Big)\Big|_{\theta=\theta_B} = \frac{d}{d\theta_B}\frac{d\theta_B}{d\lambda_B}\sin\theta_B = \frac{d\theta_B}{d\lambda_B}\cos\theta_B$$

$$\frac{d}{d\lambda}\Big(\frac{K}{2\beta}\Big)\Big|_{\lambda=\lambda_B} = \frac{K}{2\beta\lambda_B} = \frac{K}{4\pi n_0}$$

As a result:

$$\frac{d}{d\lambda}\theta(\lambda)\Big|_{\theta=\theta_B} = \frac{K}{4\pi n_0 \cos\theta_B}$$

The dephasing measure ϑ, defined here below, explicitly shows the θ-λ connection.

$$\vartheta := \frac{\beta^2 - \delta^2}{2\beta} = \frac{1}{2\beta}\left(\beta^2 - (\vec{\rho} \pm \vec{K})^2\right) = K\left(\sin\theta \pm \frac{K}{2\beta}\right)$$

An additional limitation in the number of generated diffracted orders is set by this parameter. In fact, it has been demonstrated that power exchange between the input wave and diffracted orders is favored for smaller ϑ values [79]. The dephasing parameter can also be put in this more explicit form: $\vartheta = K(\sin\theta - \sin\theta_B)$. However, in most practical cases the former expression is used to derive the *linearized* form:

$$\vartheta = K\sin\theta - \frac{K^2}{4\pi n_0}\lambda \simeq \Delta\theta K\cos\theta_B - \Delta\lambda\frac{K^2}{4\pi n_0} \tag{2.10}$$

Moving back attention to the first part of Helmholtz equation (see Equation 2.1), it is possible to calculate these terms:

$$\begin{aligned}
\frac{\partial^2}{\partial x^2}\tilde{\mathrm{E}}(x,z) &= -\rho_x^2\tilde{R}(z)\exp\left[-\imath(\rho_x x+\rho_z z)\right] - \delta_x^2\tilde{S}(z)\exp\left[-\imath(\delta_x x+\delta_z z)\right]\\
\frac{\partial^2}{\partial y^2}\tilde{\mathrm{E}}(x,z) &= 0\\
\frac{\partial^2}{\partial z^2}\tilde{\mathrm{E}}(x,z) &= \tilde{R}''(z)\exp\left[-\imath(\rho_x x+\rho_z z)\right] + \tilde{S}''(z)\exp\left[-\imath(\delta_x x+\delta_z z)\right]\\
&\quad - 2\imath\rho_z\left[\tilde{R}'(z)\exp\left[-\imath(\rho_x x+\rho_z z)\right] + \tilde{S}'(z)\exp\left[-\imath(\delta_x x+\delta_z z)\right]\right]\\
&\quad - \rho_z^2\left[\tilde{R}(z)\exp\left[-\imath(\rho_x x+\rho_z z)\right] + \tilde{S}(z)\exp\left[-\imath(\delta_x x+\delta_z z)\right]\right]
\end{aligned}$$

with $\tilde{R}'(z)$ and $\tilde{R}''(z)$ referring to the first and the second derivatives $\frac{\partial\tilde{R}(z)}{\partial z}$ and $\frac{\partial^2\tilde{R}(z)}{\partial z^2}$ respectively (same for $\tilde{S}'(z)$ and $\tilde{S}''(z)$). The above system was simplified by the fact that $\rho_z = \delta_z$ for an *unslanted* grating. The above equations corresponding to a second order two-wave coupling can be further simplified into a first order differential equations system, when the following approximation is valid.

Kogelnik 3rd approximation: The energy interchange between the reference and the signal waves is considered to be slow. This allows neglecting the second derivatives of the wave amplitudes. Consequently, the complexity is reduced and the problem can easily be solved analytically. In fact, looking at the above equations, this corresponds to considering that $\tilde{R}'' \ll \rho_z\tilde{R}'$ and $\tilde{S}'' \ll \delta_z\ \tilde{S}'$. This is the exact form of the slowly varying envelope approximation (SVEA). All considered samples in this study are volume holograms that are thick enough to relax the energy transfer between the reference and signal light waves, making field variations more gradual i.e. this does not apply to most surface relief gratings for example, because of the abrupt change in the refractive index and surface profile.

As a result, the 1-st order system is obtained. The derivation of the corresponding solutions is presented in Appendix B. It is customary to write the diffraction formulas in terms of ξ and ν, defined in Equation 2.11 and Equation 2.12 respectively, for the case of unslanted lossless transmission grating (but have to be redefined for each different case).

$$\xi = \frac{\vartheta d}{2c_z} = \frac{Kd\cos\theta_B}{2c_z}\Delta\theta - \frac{K^2 d}{8\pi n c_z}\Delta\lambda \tag{2.11}$$

$$\nu = \frac{\kappa d}{c_z} = \frac{\pi n_1 d}{\lambda\cos\theta} \tag{2.12}$$

Hence, the reference and signal amplitudes can be reformulated:

$$\tilde{S}(d) = -\imath\nu\,\mathrm{sinc}\left(\sqrt{\nu^2+\xi^2}\right)\exp\left(-\imath\xi\right) \tag{2.13}$$

$$\tilde{R}(d) = \left[\cos\left(\sqrt{\nu^2+\xi^2}\right) + \imath\xi\,\mathrm{sinc}\left(\sqrt{\nu^2+\xi^2}\right)\right]\exp\left(-\imath\xi\right) \tag{2.14}$$

And the diffraction efficiency writes:

$$\eta = \nu^2\,\mathrm{sinc}^2\left(\sqrt{\nu^2+\xi^2}\right) \tag{2.15}$$

At this stage, with the theoretical foundation for understanding wave propagation in volume holographic gratings now established, a set of practical approximations can be derived.

2.3 Deriving theoretical and experimental estimations from Kogelnik's approximate model

The simplified case of two-wave coupling, allows us to derive several practical calculations. Starting with the expression for diffraction efficiency at Bragg ($\xi = 0$), denoted as η_0:

$$\eta_0 = \sin^2(\nu) \tag{2.16}$$

This expression is essential for predicting the output signal in holographic grating applications for light (neutron) beam manipulation. It was also employed by Tomita et al. in developing an empirical model that accounts for an Uchida-type decay in the refractive index profile [80, 81] [1]. The formula has been rearranged as follows for better clarity and more ease of implementation without having to deal with different quadrants of the grating strength ν (between 0 and 2π as described in Ref. [81]):

$$\eta(\Delta\theta) = \frac{\{\sinh^2(B) + \sin^2(\nu\sqrt{1+A^2})\}(1+B^2)\sin^2(\nu)}{(1+A^2+B^2)(\sinh^2(B)+\sin^2(\nu))} \tag{2.17}$$

Here, $\Delta\theta = \theta_B - \theta$ represents the detuning angle. The parameters A and B are defined as $A = \frac{\pi d \sin\Delta\theta}{\Lambda\nu}$ and $B = \frac{\alpha_g d}{2}$, where d is the physical thickness of the grating. The parameter α_g denotes a decay constant of the refractive index modulation profile across the depth of the hologram in an Uchida-type attenuation [80]. Although this model lacks a rigorous theoretical foundation, it provides acceptable accuracy in determining grating parameters [81]. It will be used for finding good starting parameters before fitting procedures which employ more rigorous models.

Using Kogelnik's theory simulations, we note that when moving far-off-Bragg and looking at the normalized diffraction efficiency η/η_0 against ξ for various ν values (see Figure 2.3), half power values emerge for $\xi \approx \dfrac{\pi}{2}$.

[1] An Uchida type decay corresponds to an exponential decay profile of the refractive index modulation along the sample thickness.

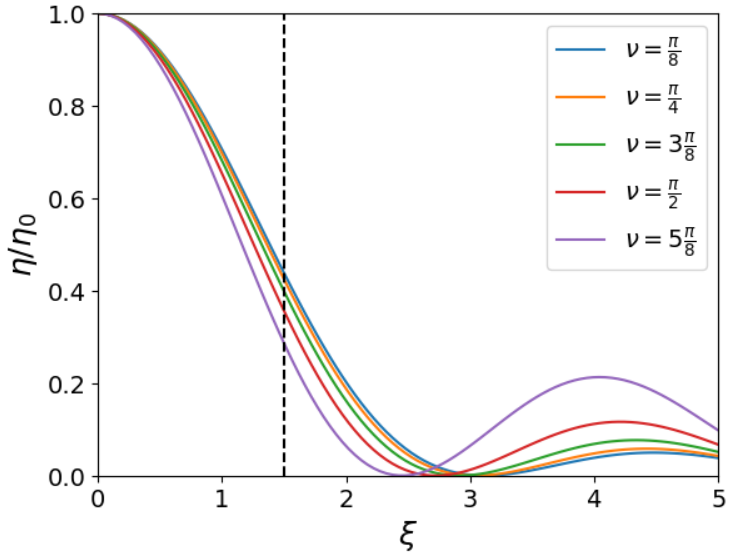

Figure 2.3: Normalized diffraction efficiency as a function of ξ for different ν values according to Kogelnik's theory simulations.

This allows for estimating the peak width. It is approximately twice the full width at half maximum (FWHM), which in turn is roughly twice $\Delta\theta_{1/2}$ as can be seen in the Figure.

$$\xi_{1/2} \approx \frac{\pi}{2} \;\Leftrightarrow\; \frac{Kd\cos(\theta_{1/2})\Delta\theta_{1/2}}{2\cos(\theta_{1/2})} \approx \frac{\pi}{2} \;\;;\;\; \Delta\theta_{1/2} \approx \frac{\Lambda}{2d}$$
$$\Longrightarrow \text{Peak width} \approx \frac{2\Lambda}{d} \tag{2.18}$$

Additionally, when considering wavelength dependence, the following estimation is obtained provided that $\Delta\lambda \approx 2 \times \Delta\lambda_{1/2}$:

$$\xi_{1/2} \approx \frac{\pi}{2} \;\Leftrightarrow\; \frac{K^2 d}{8\pi n\cos\theta}\Delta\lambda_{1/2} \approx \frac{\pi}{2}$$
$$\Longrightarrow \frac{\Delta\lambda}{\lambda} \approx \frac{\Lambda}{4d}\cot(\theta) \tag{2.19}$$

This relation defines the bandwidth of the hologram grating. These are practical approximations routinely used in experimental arrangements. Specifically, Equation 2.18 enables informed decisions regarding beam divergence in neutron experiments with gratings of known period and thickness (more details in the next subsection).

An initial estimation of the thickness parameter can be gleaned from the minima positions in the Bragg detuning curve. At these minima, the first derivative of the diffraction efficiency with respect to the angle, $\frac{\partial\eta(\theta)}{\partial\theta}$, equals zero. Mathematically, this condition is expressed as $\text{sinc}^2(\sqrt{\nu^2+\xi^2}) = 0$. It is satisfied when $\sqrt{\nu^2+\xi_{0,m}^2} = m.\pi$, where m is an integer, leading to the equation $\xi_{0,m}^2 = (m.\pi)^2 - \nu^2$. Consequently, it is possible to arrive to the following formula which allows for estimating the grating's thickness [82].

$$\lim_{m\to\infty}(\theta_{0,m} - \theta_{0,m+1}) = \frac{\Lambda}{d} \tag{2.20}$$

This equation provides us with an approximate value of the thickness, serving as a reliable starting parameter for fitting. Moreover, it offers insight into how the diffraction intensity oscillates at varying thickness values (to be discussed more in detail in the terminology section). This will be explored further in the later sections of the study, particularly when discussing terminology.

At this point, it is essential to discuss how Kogelnik's two wave-coupling theory applies to neutrons, and the considerations necessary for this application.

2.4 Application of Kogelnik's two-wave coupling theory in neutron diffraction studies and its correspondence with Dynamical Diffraction Theory

In the case of neutrons, a Helmholtz-type wave equation analogous to Equation 2.1 is derived. This derivation stems from the time-independent one-particle Schrödinger Equation, as delineated in [83]:

$$\left[-\frac{\hbar^2}{2m_{\mathrm{N}}}\nabla^2 + V_N(\vec{\mathrm{r}})\right]\psi(\vec{\mathrm{r}}) = E_{\mathrm{N}}\psi(\vec{\mathrm{r}}) \tag{2.21}$$

In this context, $\hbar$ signifies the reduced Planck constant, and m_{N} denotes the mass of the neutron. The term V_N, representing the neutron optical potential, is formulated as follows for the considered one-dimensional case:

$$V_N(x) = \frac{2\pi\hbar^2}{m_N}\Big(ß + \Delta ß\cos\left(Kx\right)\Big) \tag{2.22}$$

In this study, the parameters of main interest are the FCs of the coherent scattering length density (SLD) modulation amplitudes $\Delta ß_j = \Delta(b_c\rho)_j$, where b_c and ρ are the coherent scattering length and the atomic density of the material, respectively. Consequently, the optical potential is expressed in terms of the materials coherent SLD denoted as ß and its spatial modulation amplitude $\Delta ß$ [58, 83, 84]. From this expression, the first order neutron refractive index can be deduced as:

$$n(x) = \sqrt{1 - \frac{V_N}{E_{\mathrm{N}}}} \simeq 1 - \frac{\lambda_N^2}{2\pi}\Big(ß + \Delta ß\cos\left(Kx\right)\Big) \tag{2.23}$$

In the two-wave coupling case, the equivalence between the Dynamical Diffraction Theory (DDT) and Kogelnik's theory assures that Equation 2.15 is applicable to neutron diffraction. To align this equation with neutron-specific phenomena, a redefinition of parameters is necessary, as outlined in [18, 85]:

$$\nu = \frac{\lambda d\Delta ß}{2\cos(\theta)} \quad ; \quad \xi = \frac{\pi d(\theta_B - \theta)}{\Lambda} \tag{2.24}$$

These expressions, ν and ξ, are tailored to the characteristics of neutron diffraction, elucidating the nuances of neutron interactions within a holographic grating. Another

consequence of the demonstrated equivalence to the DDT, by considering $\nu = \frac{\pi d}{\Delta_K}$, is the possibility to define a Pendellösung period–also called the extinction length in some references–as:

$$\Delta_K = \frac{2\pi \cos(\theta_B)}{\lambda \Delta ß} \tag{2.25}$$

Pendellösung oscillations, which modulate the diffraction efficiency amplitude along the depth of the sample parallel to the grating surface, arise due to the coupling and energy interchange between the direct beam and diffracted orders within the grating. The first experimental demonstration of this phenomenon with neutrons was reported by Schull in 1968, who observed Pendellösung interference fringes by varying the wavelength [86]. For highlighting similarities between neutron and X-ray diffraction for example in the Laue case in periodic media, some of the parameters presented in this study, including the extinction length, were defined by Punegov in terms of FCs of the X-ray polarizability [87].

The significance of this effect is underscored by the relationship between the Pendellösung period and the first-order diffraction efficiency at the Bragg angle, as shown when inserting the Δ_K expression into Equation 2.16:

$$\eta_{\pm 1}(\theta_B) = \sin^2(\nu) \simeq \sin^2\left(\frac{\lambda \Delta ß}{2} d\right) \tag{2.26}$$

The cosine of theta is omitted from this simplified expression, based on the assumption that it approximates unity. Nevertheless, the observed diffraction efficiency variations in a rocking curve are also manifestations of Pendellösung oscillations, which depend on the angle of incidence. This relationship is crucial in designing neutron optical components, illustrating how diffraction efficiency can be modulated by adjusting the sample thickness [88] or by fine-tuning the materials and conditions used in the recording process to maximize the modulation amplitudes $\Delta ß_j$. Although increasing thickness is a straightforward method, it can lead to angular or wavelength selectivity issues, which should be avoided. For thick gratings, the majority of neutrons transmit without fulfilling the diffraction conditions, exacerbating the already low count of slow neutrons. Furthermore, the necessity to maintain the angular divergence of the incident beam smaller than the peak width(estimated by Equation 2.18), compounds the issue, resulting in diminished neutron counts—a non-ideal scenario.

It is crucial to ensure that the beam divergence remains less than the expected peak width due to the inherent limitation in diffraction efficiency—capped at 50% for crystals, gratings, and all types of thermal and cold neutron optical devices—stemming from Pendellösung effects. Averaging over the Pendellösung fringes, which occurs when this condition is not met, precludes surpassing the 50% efficiency threshold [58, 89]. In response, this research focuses on relatively thin gratings (10 µm-100 µm) characterized by high SLD modulation amplitudes, enabling us to achieve substantial diffraction efficiencies. These efficiencies can be finely adjusted for the development of optical elements by varying the effective thickness through sample tilting at an angle ζ. Such strategies have paved the way for creating two-port and three-port beam splitters, mirrors, and other devices, as indicated in the introduction section [19, 20, 89].

2.5 Exploring the RCWA theory: Derivation of a simplified model

While Kogelnik's theory provides a satisfactory explanation for light diffraction from planar gratings and for neutrons under certain conditions and approximations, it falls short when more than two diffracted waves are involved. The Rigorous Coupled Wave Analysis (RCWA) theory presents a robust framework for addressing the complexities of wave diffraction, particularly in situations involving multiple waves. In this Chapter, the Multi-Coupled Wave Analysis (MCWA) theory will be introduced as a practical adaptation of the RCWA theory.

2.5.1 Beta-value Method (BVM)

The RCWA model, as described by Moharam and Gaylord [52, 56], is an exact formulation of wave propagation in holographic gratings that does not involve any approximations. However, certain fundamental approximations can be introduced for many practical cases in order to facilitate numerical computation of the scattered waves analysis. In this section, a simplified MCWA model will be derived based on a few assumptions, the validity of which will be discussed in Chapter 5.

For this purpose, the Beta-value method (BVM) will be employed. The main difference between the previously discussed KVCM method and the BVM method is the choice of the boundary conditions [90, 91]. Specifically, $|\vec{k}_j| = \beta = kn_0 \ \forall -s \leq j \leq +s$ is set for $(2s+1)$ diffracted orders, where $k = (2\pi/\lambda)$. This choice ensures energy conservation. The corresponding geometry is depicted in Figure 2.4, where three regions are considered: the incoming beam media region ($z < 0$), the grating region ($0 \leq z \leq d$), and the scattered waves region ($z > d$). In the first region, it is generally necessary to consider both the incoming beam and the backward-diffracted beam, particularly for reflection gratings. However, in the considered case of transmission grating, reflection from the sample surface is disregarded, particularly for neutrons where the condition $n_{ext} = n_0$ is satisfied.
The incident beam is elastically scattered into multiple diffraction orders that obey the following relations:

$$k_{j,x} = k_{0,x} + jK_x = \beta \sin\theta \pm jK_x \tag{2.27}$$

$$k_{j,y} = 0 \tag{2.28}$$

$$k_{j,z} = \sqrt{\beta^2 - k_{j,x}^2} = \beta\sqrt{1 - \left[\sin\theta \pm j(\frac{K_x}{\beta})\right]^2} \tag{2.29}$$

The Bragg mismatch parameter δq is defined as follows:

$$\delta q_j = k_{0,z} - k_{j,z} = \beta\left(\cos\theta - \sqrt{1 - \left[\sin\theta \pm j(\frac{K_x}{\beta})\right]^2}\right) \tag{2.30}$$

The right-hand side expression of $k_{j,x}$ explicitly indicates its dependence on the ratio of the wavelength to the grating periodicity constant. When this ratio is greater than unity, which is often the case in laser diffraction experiments, it leads to the creation of

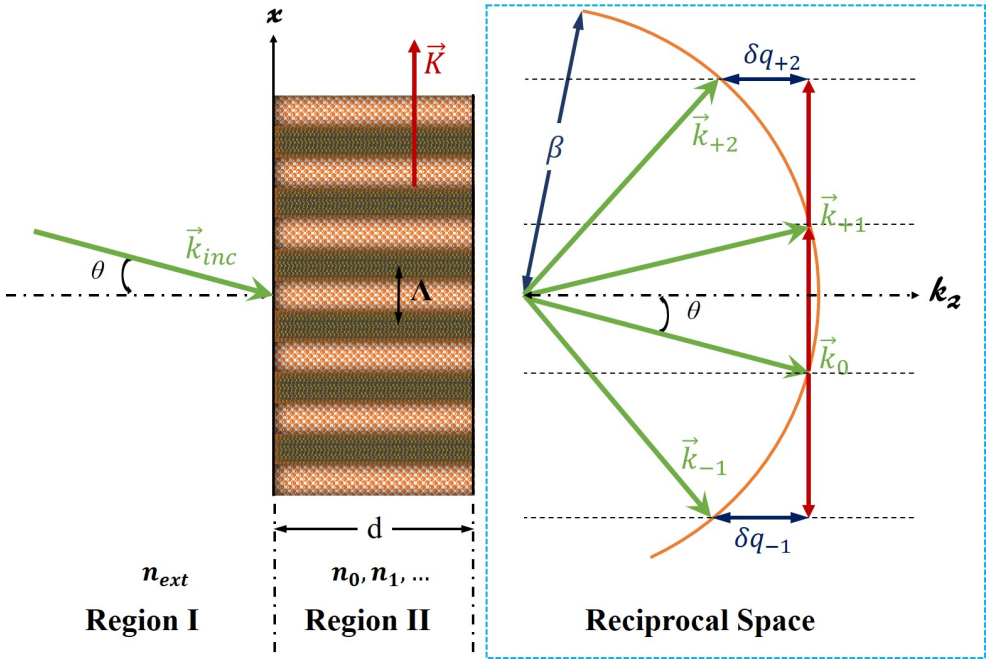

Figure 2.4: Beta-value method (BVM) Geometry for an unslanted planar grating diffraction in the MCWA theory

evanescent waves that must be accounted for to ensure the stability and convergence of the method [56]. In that case, the z-component of the wave vectors, $k_{j,z}$, must be redefined in the grating and output regions as follows:

$$k^s_{j,z,} = \begin{cases} k\sqrt{n_s^2 - (\frac{k_{j,x}}{k})^2} & \text{if } kn_s > k_{j,x} \quad , \quad k_{j,z} \in \mathbb{R} \\ -\imath k\sqrt{(\frac{k_{j,x}}{k})^2 - n_s^2} & \text{if } k_{j,x} > kn_s \quad , \quad k_{j,z} \in \imath\mathbb{R} \end{cases} \qquad s = 0,\ ext \tag{2.31}$$

2.5.2 Setting the simplified RCWA system: the multi-wave coupling analysis theory

For simplicity, only seven-waves coupling theory will be established, and the following truncated form of Equation 2.3 will be considered:

$$n(x,z) = n_0 + n_1(z)\cos(Kx) + n_2(z)\cos(2Kx) + n_3(z)\cos(3Kx) \tag{2.32}$$

The refractive index modulation amplitudes in Equation 2.32 are expressed as a sum of FCs. The following expressions employs the general form of the modulation amplitudes $n_j(z)$ (for $j > 0$), which includes the relative phases between the components and the attenuation of the grating strength profile:

$$n_j(z) = n_j^0 \exp\Big(-(\frac{z}{L} + \imath\varphi_j)\Big) \tag{2.33}$$

$L = (1/\alpha)$ denotes the decay length with α being the linear absorption coefficient. It represents the sample thickness at which the grating-strength has decreased to $1/e$

of its initial value n_j^0 (at $z = 0$). Mean modulation amplitudes $< n_j >$ are commonly defined by averaging over the sample thickness d (cf. Ref. [18]):

$$< n_j >= \frac{n_j^0}{d} \exp(-\imath\varphi_j) \int_0^{z=d} \exp(-\frac{z}{L}) dz = \frac{\ell_{eff}}{d} n_j^0 \exp(-\imath\varphi_j) \tag{2.34}$$

Here, $\ell_{eff} = L\left[1 - \exp(-\frac{d}{L})\right]$ is the effective length of an attenuated grating structure (not to be confused with the effective *physical* thickness d_{eff} of a tilted grating). When L approaches infinity (for a non-attenuated sample case), $\lim_{L\to\infty} \ell_{\text{eff}} = d$. Equation 2.34 can also be written in terms of the SLD modulation amplitudes via the following relation: $\Delta ß_j = (2\pi/\lambda_N^2) n_j$. While SLD modulation amplitudes will eventually need to be used in the neutron diffraction data analysis, refractive index modulation amplitudes will continue to be used in the general formulation, which applies to both light and neutrons. The results will later be reformulated to use SLD modulation amplitudes in the specific case for neutrons.

The RCWA general approach consists of finding a solution of the coupled-wave equation in each region and then matching the solutions using the boundary conditions at the interfaces. This is the same for light and neutrons, as the problem involves solving the following time-independent Schrodinger equation (Helmholtz-type wave equation):

$$\left[\nabla^2 + k^2 n^2(x,z)\right] \psi(x,z) = 0 \tag{2.35}$$

Here, $\psi(x,z)$ is the wave function, which can be expanded in terms of the space harmonics of the fields within the periodic structure using the coupled-wave ansatz:

$$\psi(x,z) = \sum_j S_j(z) \exp(-\imath \vec{k_j} \cdot \vec{r}) \tag{2.36}$$

Here, $S_j(z)$ are the diffracted amplitudes to be determined. Starting with the first part of the wave equation, one gets:

$$\frac{\partial^2}{\partial x^2}\psi(x,z) = \sum_j -k_{j,x}^2 S_j(z) \exp(-\imath \vec{k_j} \cdot \vec{r})$$

$$\frac{\partial^2}{\partial y^2}\psi(x,z) = 0$$

$$\frac{\partial^2}{\partial z^2}\psi(x,z) = \sum_j S_j''(z) \exp(-\imath \vec{k_j} \cdot \vec{r}) - 2\imath k_{j,z} S_j'(z) \exp(-\imath \vec{k_j} \cdot \vec{r}) - k_{j,z}^2 S_j(z) \exp(-\imath \vec{k_j} \cdot \vec{r})$$

Gathering three parts, the following expression is obtained:

$$\nabla^2\psi(x,z) = \sum_j S_j''(z) \exp(-\imath \vec{k_j} \cdot \vec{r}) - 2\imath k_{j,z} S_j'(z) \exp(-\imath \vec{k_j} \cdot \vec{r}) - \beta^2 S_j(z) \exp(-\imath \vec{k_j} \cdot \vec{r}) \tag{2.37}$$

An analytical solution is only possible for two waves according to Kong's second-order coupled-mode method [90, 92]. The term containing the second derivative $S_j''(z)$ could be kept, which requires more numerical efforts solving the system. However, it has been demonstrated in other studies that it is more important to include higher order waves rather than keeping the second derivatives [56]. Therefore, this second derivative

term will not be considered in the rest of this work. The validity of this argument will be reconsidered Chapter 5.

The calculation of the second part of the wave equation is presented in Appendix C. Gathering both parts from Equation C.6 and Equation 2.37 (after disregarding the second derivative term), the wave equation takes this form:

$$\begin{aligned} 2\imath k_{j,z} S'_j(z) = \beta^2 \Bigg\{ & \frac{n_1(z)}{n_0} \Big[S_{j-1}(z) \exp\left(\imath(\delta q_{j-1} - \delta q_j) z\right) \\ & + S_{j+1}(z) \exp\left(\imath(\delta q_{j+1} - \delta q_j) z\right) \Big] + \frac{n_2(z)}{n_0} \Big[S_{j-2}(z) \exp\left(\imath(\delta q_{j-2} - \delta q_j) z\right) \\ & + S_{j+2}(z) \exp\left(\imath(\delta q_{j+2} - \delta q_j) z\right) \Big] + \frac{n_3(z)}{n_0} \Big[S_{j-3}(z) \exp\left(\imath(\delta q_{j-3} - \delta q_j) z\right) \\ & + S_{j+3}(z) \exp\left(\imath(\delta q_{j+3} - \delta q_j) z\right) \Big] + \ldots \Bigg\} \end{aligned} \tag{2.38}$$

Once the system is solved and the wave amplitudes are determined, the corresponding efficiencies η_j can be computed, using the equation below [93]:

$$\eta_j = Re\{\frac{k_{j,z}}{k_{0,z}}\} |S_j(z = d)|^2 \tag{2.39}$$

2.5.3 Reconstruction of the grating structure and phase effects

Aiming to obtain information about the materials and structures used, the above equations can be reformulated using the scattering length density modulation amplitudes instead of the refractive index modulation. The former option provides an equivalent representation, while allowing for some simplifications. These simplifications eventually lower the computational cost.

For this purpose, $n_j(z)$ is substituted with $(\Delta ß_j(z)\lambda^2/2\pi)$ in the coupled wave equation above. It is also possible to simplify with $n_0 \simeq 1$ when it is applicable. In order to reconstruct the structure, the modulation amplitudes expressions are expanded to include the relative phases between the FCs. Consequently, The coupled waves system takes the following compact form:

$$\left(\frac{\imath}{\pi n_0}\right) k_{j,z} S'_j(z) = \sum_{m=-u}^{m=+u} \Delta ß_m(z) S_{j+m}(z) \exp\left(\imath(\delta q_{j+m} - \delta q_j) z\right) , \qquad u \in \mathbb{N} \tag{2.40}$$

$$\Delta ß_{\pm s}(z) = \Delta ß_s^0 \exp\left(-\frac{z}{L}\right) \exp\left(\pm \imath \varphi_s\right) , \qquad s \in \mathbb{N} \tag{2.41}$$

The bounds of the summation index m are set by the highest order of the FCs being included e.g. for three harmonics $u = 3$, the index m iterates from m=-3 to m=3. The plots in Figure 2.5 illustrate the influence of phase variations.
The relative phases influence the energy interchange between diffraction orders. Indeed, the influence depends on the comparability of the first and higher order modulation amplitudes (here, we have $n_1 \approx 3 \times n_2$ in the simulation). In most cases of a symmetric grating, they take values close to zero or values close to π (a negative modulation amplitude) [76]. These values determine whether the contribution of higher orders efficiency to lower orders signal is constructive or destructive, and vice versa. A phase

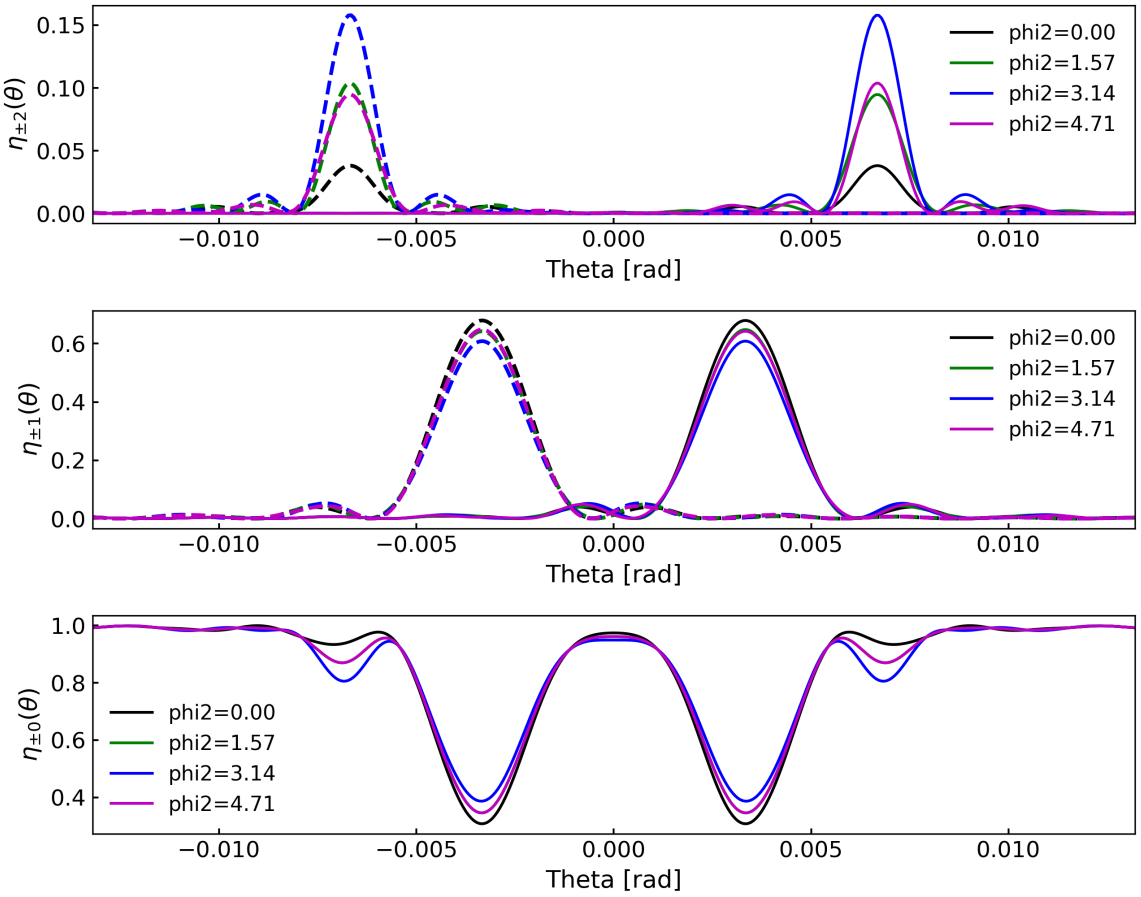

Figure 2.5: Illustration of the effects of varying a relative phase between first and second FCs of the neutron refractive index pattern.

shift of $(\pi/2)$ is an important feature in the study of electro-optics and photopolymers in the existence of external fields, which is known as dynamical holography [16, 94]. However, such features are not expected in the frame of this study.

2.6 Terminology of diffraction regimes and numerical resolution of the coupled waves system

2.6.1 Diffraction regimes terminology

In this section, planar gratings are classified following the terminology clarified in Ref. [53], along with other related references [54, 55, 95]. Gratings can be classified as thin or thick holograms based on two distinct criteria. The first criterion relies on the angular and wavelength selectivity of the hologram, using the ratio of grating thickness d to grating period Λ. A hologram is considered thin when $(d/\Lambda) < 10$ due to its broad angular and wavelength selectivity, and thick when $(d/\Lambda) > 10$ because of its high selectivity.

Additionally, a completely different classification (not to be confused with the previous) can be based on the Klein-Cook parameter Q and the grating strength ν, some-

times referred to as the modulation parameter. For light, the dimensionless Klein-Cook parameter is $Q = (2\pi\lambda d)/(n_0\Lambda^2)$ and the grating strength ν has already been defined in Equation 2.12. For neutrons, the parameters take this form:

$$Q_{\mathrm{N}} = \frac{2\pi\lambda_N d}{\Lambda^2} \quad ; \quad \nu_{\mathrm{N}} = \frac{\pi d n_1}{\lambda_N \cos\theta} = \frac{\lambda_N d}{2}\Delta\ß_1. \tag{2.42}$$

Here, it is assumed that $n_0 = 1$ and $\cos\theta \simeq 1$. In some related fields like acousto-optics, *thin* refers to the Raman-Nath regime, characterized by multiwave coupling neglecting dephasing. In this case, diffraction efficiency is described by an integer-order Bessel function:

$$\eta_i \ = J_i^2(2\nu)$$

There is some ambiguity in literature stemming from the multiple conditions present about the occurrence boundaries for this regime. This depends on the field of application. It is necessary to combine the following two conditions in order to describe how well the above condition is obtained for diffraction from a *thin* grating in the Raman-Nath regime: $(Q\nu/\cos\theta_B) < 1$ and $\Big(Q/\big(2\nu\cos\theta_B\big)\Big) < 10$ [53].

For visible light diffraction from transmission planar gratings with small grating periods, diffraction generally occurs in the Bragg regime due to the widely separated diffracted orders. Bragg regime diffraction occurs when $(Q\nu/\cos\theta_B) > 1$ and $(Q/2\nu\cos\theta_B) > 10$, with only one wave (and only two around the Bragg angle) propagating in the grating.

When one of the two conditions is violated, diffraction occurs in the intermediate regime. The latter involves multiple coupled waves with clear angular dependence, requiring rigorous coupled wave analysis (RCWA). In this research focused on neutron diffraction from highly modulated gratings, the intermediate regime is prevalent.

It is important to note that the combination of the above classification of diffraction regimes with the diffraction efficiency expression shown in Equation 2.26, provides a framework for designing neutron mirrors and beam-splitters. This has been illustrated in Figure 1 of Ref. [89] through the exploration of Pendellösung oscillations, or by tuning the grating parameters. However, it should be noted that the existing literature considers pure sinusoidal gratings only, which is not exactly the case for the considered ones.

2.6.2 Numerical resolution of the multi-wave coupling system

Unlike the case of two-wave coupling, where analytical solutions can be simply obtained as demonstrated in section 2.2, the task of solving for a higher number of orders (equations), especially when higher order harmonics of the refractive index are involved, is not straightforward. In such cases, the system has to be solved numerically.

For this purpose, and based on identical system formulations up to Equation 2.38, it is possible to employ one of the following approaches: 1) using a numerical integration module for solving the system via Runge-Kutta type (or other) integration methods. The integrator with the best numerical stability has been employed after a comparative analysis of different integrators (explicit and implicit Runge-Kutta methods with different orders, multi-step variable-order method based on a backward differentiation formula, etc...). This, though, comes at the cost of relatively longer durations for the

codes to run. 2) by transforming the coupled-wave equations problem into an eigenvalue/eigenvector problem. This transformation of the system to $\vec{S}(z) = [M] \cdot \vec{S}(z)$ is possible by posing $S_j(z) = \tilde{S}_j(z) \exp(-i\delta q_j z)$ in Equation 2.38. This approach is only applicable to non-attenuated gratings, or smoothly attenuated gratings by considering an arbitrary number of assembled non-decayed holograms (see Ref. [96]), as it includes a z-dependence in the matrix coefficients. The applicability of this photopolymer division approach will be reviewed later in this section and in Chapter 5, particularly, in the discussion of available approaches for modelling multilayer volume gratings.

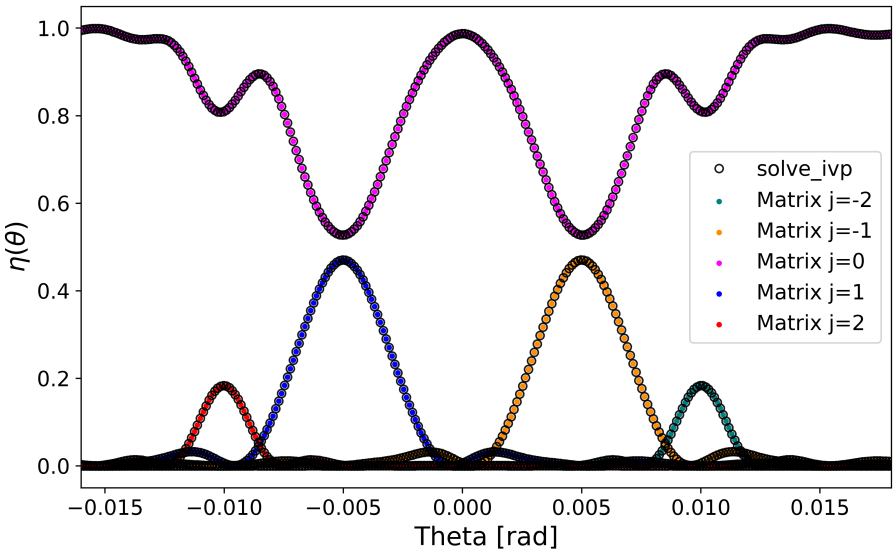

Figure 2.6: Superposed diffraction efficiency estimates obtained using two numerical methods for solving a system of five coupled wave differential equations: numerical integration solver results with empty black-edge circles and matrix transformation with edge-free colored markers. Identical sample parameters, chosen arbitrarily, were used for comparison: $\Lambda = 300\,\text{nm}$, $\lambda_N = 3\,\text{nm}$, $\Delta ß_1 = 9\,\mu\text{m}^{-2}$, $\Delta ß_2 = 4\,\mu\text{m}^{-2}$, $\varphi_2 = \pi$, and thickness $d = 60\,\mu\text{m}$. The used simulations corresponding to the matrix solver were provided by I. Masiello [97].

Figure 2.6 displays curves superimposed from simulations of diffraction efficiency using both approaches. The visual inspection shows a perfect congruence of the simulation outputs. When plotted on a logarithmic scale, the same perfectly superposed curves were also observed. The calculation of the residuals demonstrates that their magnitude can be minimized to the limits allowed by numerical methods, dependent on the settings of the numerical integrator. For the settings used, the residuals are smaller than 10^{-14} in magnitude.

It is critical to note that while matrix transformations offer significant time efficiency and immediate simulation outputs (unlike the numerical integration, which requires compile time dependent on precision settings), they cannot be conveniently applied to samples presenting a refractive index profile due to the z-dependence of the matrix coefficients. Consequently, for the considered samples, which typically feature attenuated profiles, only integration solvers have been employed for fitting procedures.

2.7 Modelling of multilayered gratings

Multilayered volume holographic gratings (MVHGs), also known as stratified volume holographic optical elements (SVHOEs), comprise a series of modulated and non-modulated (buffer) layers. This category of holographic optical elements exhibits distinctive angular, wavelength, and temporal response characteristics. Consequently, MVHGs have been employed in various light optical applications, such as generating modulated (or split) femtosecond sub-pulses [98–100], waveguide-grating filters and couplers [101–103], holographic multiplexing [104, 105] etc. Only recently, they have been considered for neutron optical applications [106]. In this section, a straightforward and reliable theoretical framework will be developed for simulating and modeling data obtained from MVHGs. This will be achieved based on existing models in the literature and tailored to the specific requirements of this research, ensuring generality for use in both light and neutrons when conditions of Bragg diffraction are met. In particular, an equal averaged refractive index of the photopolymer and the buffer layers will not be assumed in this study. For the case of multi-wave coupling, with more than two waves involved, the elaborated model will be presented in Chapter 5.

The most pertinent theoretical models are the one proposed by E.F Pen and M. Yu Rodionov [107] as well as Au's formulation [108]. Both models address hologram non-uniformities by treating each photopolymer layer as an arbitrary number of superimposed uniform layers defined by their transfer matrices (see also Ref. [96]). This approach is often referred to as the Transfer Matrix Method (TMM). Despite both being inspired from Kogelnik's two coupled waves theory, the key distinction between the two models is that Pen and Rodionov's formulation is based on KVCM method, while Au employs the BVM. In Chapter 5, a comparative analysis will be performed to demonstrate the supremacy of Au's formulation.

Let S denote each substrate (buffer) layer and P each modulated photopolymer layer, with D being the thickness of the full stack of layers. A sketch is provided in Figure 2.7 for the considered case of two-wave coupling with a refractive index pattern similar to Equation 2.2 according to the notations in section 2.5.
The amplitudes of the readout waves $S_0(z = D)$ and $S_{\pm1}(z = D)$ from a stack of n alternated SP layers take the following form:

$$\begin{pmatrix} S_0(z=D) \\ S_{\pm1}(z=D) \end{pmatrix} = \prod_{j=1}^{n} T_j \begin{pmatrix} 1 \\ 0 \end{pmatrix} = T_n T_{n-1} \cdots T_1 \begin{pmatrix} 1 \\ 0 \end{pmatrix} \tag{2.43}$$

The transfer matrix T_j of the j-th layer is given by [108]:

$$T_j = \begin{pmatrix} \cos(\omega_j) + \imath \frac{\xi_j \sin(\omega_j)}{\omega_j} & -\imath \sqrt{\frac{c_{\pm1,j}}{c_{0,j}}} \frac{\nu_j \sin(\omega_j)}{\omega_j} \\ -\imath \sqrt{\frac{c_{0,j}}{c_{\pm1,j}}} \frac{\nu_j \sin(\omega_j)}{\omega_j} & \cos(\omega_j) - \imath \frac{\xi_j \sin(\omega_j)}{\omega_j} \end{pmatrix} e^{-\imath \xi_j} \tag{2.44}$$

where $c_{0,j} = k_{0,z}/\beta_j$ and $c_{\pm1,j} = k_{\pm1,z}/\beta_j$ are the obliquity factors (z-axis projection of the coupled waves) in the BVM method, based on the off-Bragg parameter δq (see Equation 2.30). For the expressions of the z-components of the wave vectors see Equations 2.31. The angle θ refers to the *internal* angle within the material. In the case of differing refractive indices between the photopolymer and buffer layers—an aspect not

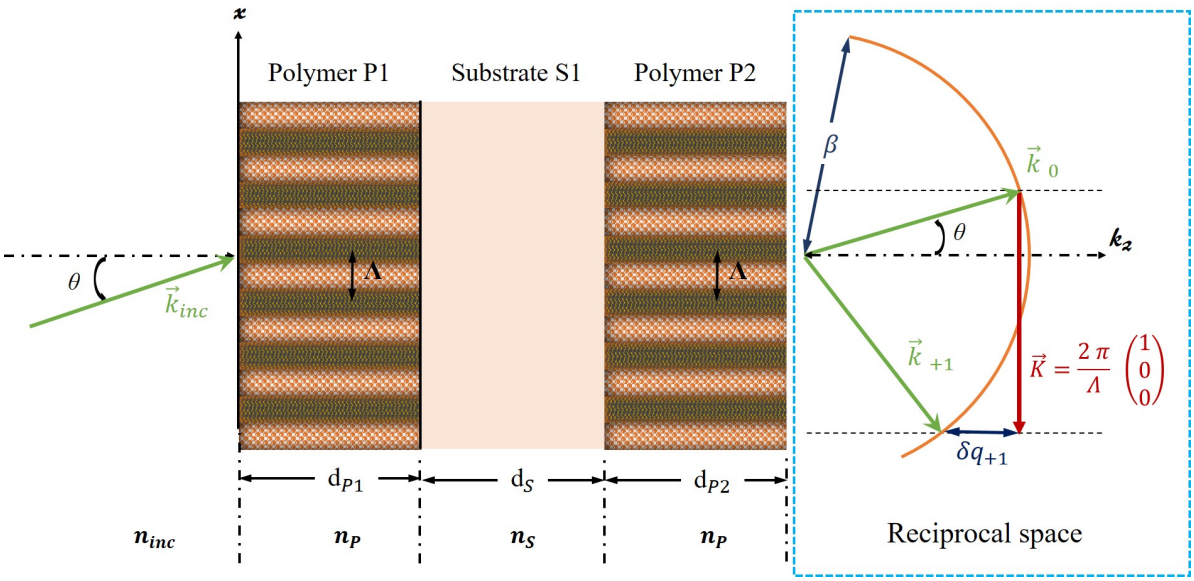

Figure 2.7: Beta-value method reconstruction geometry for a Polymer-Substrate-Polymer multilayer holographic grating.

considered in the above references but included in the considered model—the parameters take the following form:

$$\omega_j = \sqrt{\nu_j^2 + \xi_j^2} \tag{2.45}$$

$$\xi_j = \frac{d_j}{2}\delta q_{\pm 1,j} = \frac{d_j \beta_j (c_{0,j} - c_{\pm 1,j})}{2} \tag{2.46}$$

$$\nu_j = \frac{\beta_j^2}{2n_0}\frac{n_1 d_j}{\sqrt{k_{0,z}k_{\pm 1,z}}} = \frac{\beta_j n_1 d_j}{2n_0\sqrt{c_{0,j}c_{\pm 1,j}}} \tag{2.47}$$

$$c_{\pm 1,j} = c_{0,j} - \left(\frac{\delta q_{\pm 1,j}}{\beta_j}\right) = \sqrt{1 - \left[\sin(\theta_j) \pm \frac{K_x}{\beta_j}\right]^2} \quad ; \quad c_{0,j} = \cos(\theta_j) \tag{2.48}$$

For the non-modulated layers, ν is equal to zero. The refractive index of the photopolymers is denoted n_0 to continue with the same previous notations. It is important to use internal angles within each layer, which are simply obtained by the application of Snell's law. It is straightforward that there is no need for division into multiple layers for non-modulated media, nor in the case of uniform modulation. Otherwise, non-uniformities can be easily implemented (see [107, 108]). In this study, only an Uchida-type profile of the modulation was accounted for [80]. For each slice layer $P_{a\to b}$, an averaged modulation amplitude is calculated as follows:

$$n_1(P_{a\to b}) = \frac{n_1(z=a)L}{b-a}\left[\exp(-a/L) - \exp(-b/L)\right]$$

A moderate number of five slice layers have been used for each photopolymer, offering compromise between a gradual attenuation and reduced numerical complexity. Though, in case of strong attenuation, this number has to be increased.

Once the output amplitudes $S_0(z = D)$ and $S_{\pm1}(z = D)$ have been calculated, the diffraction efficiency curves η_0 and $\eta_{\pm1}$ of the multilayer structure can be derived as follows (cf. Equation 2.39):

$$\eta_0 = |S_0(z = D)|^2 \quad \text{and} \quad \eta_{\pm1} = \frac{c_{\pm1,n}}{c_{0,n}} |S_{\pm1}(z = D)|^2$$

In summary, this formulation provides a practical framework for analyzing the optical behavior of MVHGs and modeling of experimental data (limitations will be discussed in Chapter 5). However, when more than two waves are involved, which is often the case in slow neutron diffraction experiments, it is clearly not valid. In that case, this model must be abandoned and replaced with a more general formulation. For this purpose, a tailored model will be presented in Chapter 5.

Chapter 3

Materials and methods

This chapter provides a comprehensive description of the materials and methodologies employed in this research, laying the foundation for understanding the experimental processes and the underlying principles. Focusing on photosensitive materials used in holographic recording, the intricate interplay of light and neutron optical components is thoroughly explored. Dissecting the fabrication processes and the unique properties of the materials used, a clear path from conceptualization to practical implementation is established.

3.1 Photosensitive materials for holographic recording of light and neutron optical components

In this section, the various photosensitive materials under study are presented, with their suitability for creating effective neutron optical components discussed. While ND-NPC gratings stand out for their optimal performance in neutron optics, the accessibility and cost-effectiveness of Bayfol foils are invaluable for proof-of-concept experiments. Additionally, another class of materials, Hyperbranched Polymers (HBPs), is presented. This material class is recognized for the high refractive index modulation in light-based studies.

3.1.1 Selection criteria for materials in holographic neutron optical components

The aim is to select the optimal blend of materials composing the NPC (or Photopolymer) films used in the holographic recording of effective and flux-economic neutron optical components. Essential to this optimization is understanding the relationship between diffraction efficiency and the material properties, as captured by Equation 2.26 from the Chapter 2. This equation establishes that the maximum first-order (Bragg-matched) diffraction efficiency, $\eta_{\pm1}(\theta_B)$, is influenced by the sample thickness (d), the probe wavelength (λ), and the coherent SLD modulation amplitude Δß. As previously discussed, increasing the thickness is not desired. Consequently, for a given wavelength, enhancing the Δß becomes essential, thereby achieving higher refractive index modulation Δn.

As derived in Appendix A of Ref. [22], the first-order (Bragg-matched) refractive index modulation amplitude n_1 can be written as follows:

$$n_1 = a_1 \Delta f |n_{\mathrm{NP}} - n_{\mathrm{P}}| \tag{3.1}$$

where a_1 relates to the first-order Fourier component of periodically modulated pattern (could be sinusoidal, rectangular etc...). Here, n_{NP} and n_{P} are the refractive indices of the nanoparticles (or polymerized monomers in photopolymers) and the host polymer, respectively, which are proportionate to their neutron scattering lengths $b_{c,\mathrm{NP}}$ and $b_{c,\mathrm{P}}$. The term Δf denotes the amplitude of volume fraction modulation under the Maxwell-Garnett approximation for multicomponent photopolymer systems, consisting of homogeneously distributed and non-interacting spherical particles [109].

To maximize the refractive index modulation, selecting materials that provide a high coherent contrast $|b_{c,\mathrm{NP}} - b_{c,\mathrm{P}}|$ is paramount, particularly as $b_{c,\mathrm{P}} \simeq 1 \times 10^{-6}\,\text{Å}^{-2}$ typically remains much lower than b_{NP} in standard photopolymers i.e. the exact value for PMMA is $1.06 \times 10^{-6}\,\text{Å}^{-2}$ [110]). For large grating period values, achieving a nearly sinusoidal modulation pattern is preferable, setting a_1 close to unity and minimizing higher-order contributions, although the inherent non-linearity in the photopolymerization process often introduces these contributions. For small grating periods, depending on the experimental arrangement and the wavelength distribution, higher orders are not always considered detrimental (sometimes intentionally simulated). Furthermore, optimizing Δf involves enhancing the spatial variation in material composition through an enhanced mutual diffusion of particles (high photosensitivity, low viscosity etc...). Adjusting holographic recording parameters (to be detailed later in this section), such as laser power and exposure time, is also essential for optimizing the holographic assembly dynamics, thereby, ensuring the stability and inhibiting any further photosensitivity of the recorded structure post-processing. This comprehensive approach ensures the production of high-performance neutron optical components via holographic techniques.

Following the outlined material selection criteria, the subsequent subsections present the chosen samples. Initial focus is on Nanodiamond based Nanoparticle Polymer Composite (ND-NPC or NDPC) gratings, with further materials discussed thereafter.

3.1.2 Nanodiamond based NPC gratings: properties, synthesis and preparation

This research primarily concentrates on the strategic application of Nanodiamond based Nanoparticle Polymer Composite (ND-NPC or NDPC) gratings. This section delineates the fundamental properties, synthesis methodologies, and preparation protocols of ND-NPC gratings. Emphasizing their significance, a detailed exploration of their compositional structure and the techniques employed in their development is presented. This discussion sets the stage for a deeper understanding of how these materials contribute to enhancing the functionality and efficiency of neutron optical components.

Composition of the Studied ND-NPC Films

The following table outlines the varied compositions of the studied ND-NPC films, highlighting the specific constituents and their respective proportions in the composite.

Sample	Substrate	Composition (vol.%)			Constituents of A-DPH (wt.%)		
		ND	THFA	A-DPH-12E	RB	NPG	TCT
ND061716 (1)	thick glass	19.6	55.0	25.4	2.5	5.6	No
ND012706 (2)	thin glass	20.5	52.9	26.6	2.4	5.3	No
ND012707 (3)	thick glass	20.5	52.9	26.6	2.4	5.3	No
ND012206 (4)	thick glass	20.2	54.8	25.0	2.9	6.3	2.1
ND012213 (5)	thick glass	20.2	54.8	25.0	2.9	6.3	2.1
ND012212 (6)	thin glass	20.2	54.8	25.0	2.9	6.3	2.1
ND012214 (7)	thin glass	20.2	54.8	25.0	2.9	6.3	2.1

Table 3.1: Composition of ND-NPC films [111]

Acronym Key:

- thin glass: glass substrate (∼1 mm)
- thick glass: glass substrate (∼0.2 mm)
- ND: Nanodiamond nanoparticles.
- THFA: Single functional acrylic acid tetrahydrofurfuryl ester (THFA, Tokyo Chemical Industry Co. Ltd., purity > 98.0%).
- A-DPH-12E: Multifunctional monomer, ethoxylated dipentaerythritol hexaacrylate (A-DPH, Shin-Nakamura Chem. Co. Ltd., purity ≥ 99.0%).
- RB: Rose Bengal ester (Tokyo Chemical Industry Co. Ltd., RB).
- NPG: N-phenyl glycine (Tokyo Chemical Industry Co. Ltd., NPG, purity > 97.0%).
- TCT: 2,4,6-Tris(trichloromethyl)-1,3,5-triazine (Wako Pure Chemical Co., purity > 95.0%).

For clarity in subsequent discussions, the films will be referred to by their indices (e.g., ND grating-1 for ND061716) instead of their full names.

The refractive index of various acrylate monomers in the visible light spectrum is typically around 1.50. Assuming that compositional variations are negligible, it is considered that n_P=1.4980 is a valid value for all the gratings [22].

The ND-NPC films were composed to enable comparative analysis of their properties. All these samples were recorded using the same setup, and using the same recording parameters. The initial three samples were prepared without the additional Photo-initiator (TCT), with varying substrate thicknesses in ND grating-2 and ND grating-3. For reproducibility tests, ND grating-4 to ND grating-7 were created with

identical compositions and substrates, differing only in substrate thickness between the sets. Moreover, variations in the volume percentage of Nanodiamond (ND) nanoparticles and the constituents of A-DPH-12E were carefully controlled to assess their impact on the overall performance. This comparative approach allows for a deeper understanding of how each component influences the properties of these gratings.

Next, the synthesis process of ND-NPC films will be summarized. The next focus will be on detailing the characteristics of the chosen materials and highlighting variations between the samples studied in this key reference [22]. This discussion aims to provide a comprehensive understanding of methodological choices, setting the stage for the results and analysis presented in later chapters.

Characteristics of Nanodiamond Nanoparticles

Nanodiamond (ND) nanoparticles are produced by detonation in an ultra-extreme environment of high temperature and pressure [113]. General information about the synthesis of ND nanoparticles provided by Daicel Corp. is available on their website [112]. For a detailed account of the specifics of the ND nanoparticles' synthesis and their full physico-chemical characterizations, the study by Tomita et al. [22] is referred to. It outlines the exact synthesis method for surface-modified ND nanoparticles. Here, a concise summary of their synthesis and properties is provided.

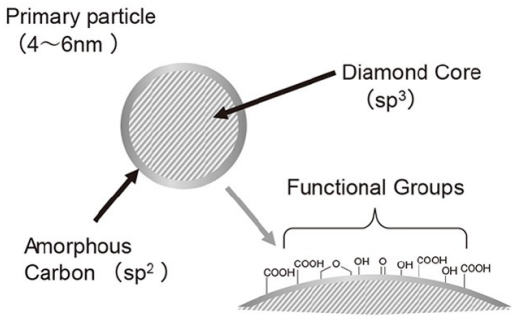

Figure 3.1: Surface modified ND nanoparticles [112]. Credit: Daicel Corp.

As depicted in Figure 3.1, each ND consists of a nanoscale sp^3 diamond core, typically 4-6 nm in diameter. This core is surrounded by a shell of sp^2 and amorphous carbon, and further enveloped by hundreds of functional groups on the external surface. Post-synthesis, the NDs undergo a purification process involving both chemical and mechanical treatments to remove detonation byproducts. In aqueous solutions, they carry a ζ-potential allowing them to be homogeneously dispersed [112]. For the considered samples, an ND sol is prepared by dispersing these particles in MIBK (Methyl Isobutyl Ketone), a chosen organic solvent for its volatility.

These ND nanoparticles inherit the remarkable properties of bulk diamonds, such as extreme hardness, high thermal conductivity, and chemical neutrality. They have a high refractive index for bulk Diamond (n_{bulk}=2.42) and a high number density ($\rho_{\text{Diamond}} = \frac{N_A \rho_{\text{mass}}}{M} \simeq 1.76 \times 10^{23}\,\text{cm}^{-3}$). Light scattering measurements, as detailed in Ref. [22], indicate that the average size of the surface-modified ND nanoparticles is approximately 9.6 nm. Additionally, the refractive index of the nanoparticles n_{ND} = 1.9420, was measured using a prism coupler on an NDPC grating, as reported in the same study. ND nanoparticles are particularly suitable due to their high optical neutron potential V_N in the order of micro electron volt, substantial coherent scattering length b_c, and significant SLD ($\approx 11.7 \times 10^{-6}$ Å^{-2}). The presence of sp^2 (graphene and graphite), amorphous Carbon, and the functional groups on the surface may slightly impact (reduce) the SLD value. On the other hand, the very low loss cross section

(almost zero) make them ideal for neutron diffraction applications.

The synthesis process of the ND sol has been outlined. Next, the fabrication process of the ND-NPC films will be detailed.

Synthesis Process and Comparative Analysis

The prepared ND sol is mixed with two acrylate monomers, THFA and A-DPH-12E, distinct from the acrylate monomers used in previous studies [22, 114]. The single functional monomer THFA, is selected for its low viscosity, adhesion and mechanical properties [115]. The same applies for A-DPH-12E, known for its high photochemical reactivity. It lowers the viscosity of the monomer blend, facilitates crosslinking, and hence, enhances the photopolymerization-driven mutual diffusion [116] of the nanoparticles and the monomers. The latter incorporates a different photoinitiator system from the reference study: a radical electron-donor/acceptor photoinitiator system composed of the RB photosensitizing dye [117] along with the NPG photoinitiator alone for the first three ND gratings in Table 3.1 to provide photosensitivity in green spectrum [118]. For the other samples, TCT was incorporated as an additional photoinitiator in an attempt to further enhance the photosensitivity [119].

The ND sol and monomer mixture is degassed by heating in a vacuum chamber at 60°C for three hours to evaporate MIBK. Next, the relative concentrations of ND, THFA, and A-DPH are measured. The resulting syrup is subsequently cast onto a glass substrate and covered with another one, priming the material for hologram recording. The image in Figure 3.2, shows how the good mechanical and thermal properties of the NPC films, allow for the creation of large area holograms ($>1\,\mathrm{cm}$).

Figure 3.2: NDPC holographic grating recorded in ND-NPC Film

Attention is directed towards the comprehensive studies that extensively discuss the morphology, distribution, and diffusion mechanisms of ND dispersed NPC and other materials [22, 76]. These studies include TEM (Transmission Electron Microscopy, SEM (Scanning Electron Microscopy), AFM (Atomic Force Microscopy), and EPMA (Electron Probe Microanalyzer) profile testing, providing a broad overview of the material properties. Therefore, no such extensive analysis is necessary for these gratings since the holographic assembly is confirmed. The post-recording particle distribution can be evaluated using the spatial modulation amplitude of the ND's volume fraction, Δf, inferred from the light optical properties of the sample. This approach provides a reliable evaluation of particle distribution within the grating. Moreover, the use of RCWA for studying neutron optical properties includes phase retrieval capabilities [76]. This allows for the reconstruction of grating structure.

In brief, this meticulous selection of the blend materials and their properties underpins the comparative analysis of results from NDPC gratings, ensuring enhanced performance for holographic optical elements tailored for neutron diffractive elements.

3.1.3 Bayfol® HX200 foils prepared for neutron diffraction applications

The Bayfol foils were all recorded using a standard two-wave interference setup at a laser wavelength λ_{rec}= 514 nm. All the employed setups satisfied the condition $P_{\text{tot}} = 2P_{\text{rec}}$, with $P_{\text{rec}} = P_{\text{R}} = P_{\text{T}}$. Here, P_{T} and P_{R} refer to the power of the incident waves at the sample surface from the transmission path and the reflection path, respectively (see subsection 3.2.1).

Single-layer Bayfol holographic gratings recorded at varying dosages

In this study, a set of Bayfol® HX200 foils were used to record single 50 µm photopolymer (SP structure) holographic gratings. For the structure, SP refers to a single foil which consists of a substrate (S layer) having a thickness of 50 µm (fixed for all samples) and a photopolymer (P layer) of varying thicknesses. The structure column in the tables indicates the order in which the layers were stacked. These samples were meticulously prepared by Elias Düker for his Master thesis, and his contribution is gratefully acknowledged here [120]. The gratings were formed with a period of approximately 495 nm, achieved by setting the recording angle to around 30°. The exposure time for all samples was fixed at 1.5 seconds, while the recording dosage was varied by adjusting the output power of the laser. A calibration measurement for the employed setup indicated that the total power on the sample, P_{tot}, was related to the output power, P_{out}, by the relation $P_{\text{tot}} = (P_{\text{out}}/2.63)$. The hologram diameter is approximately 0.9 cm and the recording dosage was calculated using this formula:

$$\text{Dosage } [\text{mJ/cm}^2] = \frac{P_{\text{tot}}[\text{mW}] \times \text{time } [\text{s}] \times 0.94}{\text{surface } [\text{cm}^2]} \tag{3.2}$$

where 0.94 corresponds to the Fresnel correction at a recording angle of 30°. Applying this formula for the considered setup yields: Dosage $[\text{mJ/cm}^2] = P_{\text{out}}[\text{mW}] \times 0.8423$. Table 3.2 lists the output laser power values used and the corresponding recording dosages.

Label	Intensity [mW]	Dosage [mJ/cm^2]
ED 5	5.1	4.3
ED 8	8.2	6.9
ED 21	21.1	17.8
ED 34	34.1	28.7

Table 3.2: Reading of the output laser power and the corresponding recording dosages for the samples prepared by Elias Düker [120].

In order to extend the range of the study to higher dosage values, another set of Bayfol foils was prepared by Dr. Jürgen Klepp. Similar 50 µm thick (SP structure) photopolymers were used. The same setup was kept for the recording and the same Fresnel correction is applied for the dosage calculation. The same approach was employed for varying the dosage, with a fixed exposure time at 1.5 seconds. Table 3.3 lists the output laser power values and the corresponding recording dosages for this set of samples. Two additional samples having a thickness of 70 µm and different grating periods were prepared. The slightly lower dosage was intentionally chosen to compensate for the small difference in the Fresnel correction, in order to obtain the same dosage.

Label	Nominal Thick. [µm]	Intensity [mW]	Dosage [mJ/cm^2]
JK_pp50_38	50	38	32.0
JK_pp50_61	50	61	51.4
JK_pp50_98	50	98	82.5
JK_pp50_158	50	158	133.1
JK_pp50_254	50	254	213.9

Table 3.3: Output laser power and corresponding recording dosages for the samples prepared to extend the dosage range of the study. The two last samples were prepared at similar conditions with different periods.

Single-layer Bayfol holographic gratings with varying photopolymer thicknesses recorded at different laser power values

A set of Bayfol® HX200 foils were used to record single photopolymer (SP) holographic gratings with varying photopolymer thicknesses, including both commercialized and non-commercialized variants. These samples were meticulously prepared by Simon Moser for his Master thesis [121], and his contribution is gratefully acknowledged. The photopolymer thicknesses used were 16 µm, 32 µm, and 50 µm, each recorded at a fixed dosage of 100 mJ/cm^2. The exposure time was adjusted to achieve this fixed dosage, based on the following output laser power values: 10 mW, 30 mW, and 50 mW. The holographic recording process was conducted using a two-wave interference setup, same as above and as described in subsection 3.2.1, with minor differences. In particular, the recording angle was set to record gratings with a period of approximately 350 nm. This list of samples is provided in Table 3.4

Label	Nominal Thick. [µm]	Intensity [mW]
SM_16µm_10mW	16	10
SM_16µm_30mW	16	30
SM_16µm_50mW	16	50
SM_32µm_10mW	32	10
SM_32µm_30mW	32	30
SM_32µm_50mW	32	50
SM_50µm_10mW	50	10
SM_50µm_30mW	50	30
SM_50µm_50mW	50	50

Table 3.4: Samples prepared at varying photopolymer thickness and writing intensity [121].

Other single- and multi-layer Bayfol holographic gratings

Additional Bayfol samples were prepared at the Laser Lab (University of Vienna). However, only the ones with best characteristics were selected for neutron diffraction measurements. Among these, the following two samples prepared by Dr. Jürgen Klepp, described in Table 3.5. These samples have a similar grating period of approximately 495 nm. They were recorded using equal object and reference writing intensities $P_T = P_R = 0.8$ mW and a duration of 10 s, resulting in a total dosage of approximately 23.5 mJ/cm^2 for each. The "pp70_SP" sample consists of a grating recorded on a 70 µm-thick single layer photopolymer. On the other hand, the sample "pp50_SPSP"

corresponds to a multilayer grating recorded on two stacked SP foils, both having the same photopolymer thickness of 50 µm.

Label	Structure	Nominal Thick. [μm]
pp70_SP	SP	70
pp50_SPSP	SPSP	50

Table 3.5: Samples prepared at a recording dosage of 23.5 mJ/cm^2, a laser power of 0.8 mW and a recording duration $t_{\text{rec}} = 10$ s.

3.1.4 Synthesis and preparation of NPC materials with hyperbranched polymers (HBPs) as organic nanoparticles

The considered HBP-dispersed NPC sample shares the same composition and preparation method as the 25 vol.% sample described in Ref. [111, 116]. This percentage is optimal for maximizing the saturated refractive index modulation amplitude, as exceeding this value results in an exponential increase in viscosity. While the detailed material synthesis and sample preparation are documented in Refs. [116, 122], a concise description of the NPC film composition and the main properties of the compounds will be provided.

Polymers with highly branched main chains formed by condensation reactions assimilate hard nanospheres and are considered tunable organic nanoparticles in terms of size and refractive index [123]. Same as inorganic nanoparticles, they are thermally and mechanically stable. The Hyperbranched polymers are obtained from a polycondensation reaction of m-phenylenediamine (m-PDA, Sigma-Aldrich), a triazine compound TCT: 2,4,6-Tris(trichloromethyl)-1,3,5-triazine (Evonik Degussa Japan Co., Ltd.) and N, N-dimethylacetamide (DMAc, Junsei Chemical Co., Ltd.). The full description of the synthesis was reported in Refs. [122, 124]. The molecular structure is shown in Figure 1 of Ref. [124], highlighting the aromatic ring units that result in a thermally stable and mechanically robust structure. Additionally, the combination of triazine and aromatic ring units (cf. Ref. [125]) results in an ultrahigh refractive index: $n_{\mathbf{NP}}$=1.82 (1.80) compared to $n_{\mathbf{P}}$= 1.50 (1.49) at a light wavelength λ=532 (633) nm. These values surpasse typical values for polymers and other types of hyperbranched organic nanoparticles.

The prepared nanoparticles (in a powder form) were added to a single functional 4-hydroxybutyl acrylate (4-HBA, purity $>$ 97%) as a host monomer (known for its low viscosity) and multifunctional monomer A-DPH-12E as crosslinking monomer. Their refractive indices are 1.452 and 1.478, respectively, at a light wavelength of 589 nm, resulting in an averaged refractive index of 1.5733 (1.562) for the NPC film at a light wavelength of 532 (640) nm. The volume ratios of the film components are 25 vol.% for the HBP, 72 vol.% of 4-HBA and 3 vol.% of A-DPH-12E. A three-component photosensitizer-initiator system was employed. It consists of: 1) A red photosensitizing cyanine dye: 3, 3'-Dipropylthiadicarbocyanine Iodide ($DiSC_3(5)$, purity $>$ 98%), since the recording was performed at λ_{rec}= 640 nm. 2) A triazine compound acting as an electron acceptor: TCT: 2,4,6-Tris(trichloromethyl)-1,3,5-triazine (Evonik Degussa Japan Co., Ltd.). 3) Borate salt compound acting as an electron donor, tetrabutylammonium butyltriphenylborate (N3B) The employed relative molar

concentration 1:10:8 of $DiSC_3(5)$:TCT:N3B was reported to be optimal in Ref. [116] for increasing the saturated refractive index modulation.

Having outlined the selected materials, the experimental arrangements used for the holographic recording of the considered gratings and the evaluation of their optical and neutron optical performance are now presented in the next section.

3.2 Methods

In this section, the technical approaches are detailed. It encompasses the process of holographic recording and the subsequent light optical diffraction measurements. Moreover, the specific configurations of neutron diffraction setups are discussed, both at the PF2/VCN platform of the ILL and at the SANS-I instrument in Paul Scherrer Institute (PSI). Two experimental campaigns were conducted at PF2 in 2021, followed by a third campaign after the instrument's modernization in 2023. Additionally, two more campaigns were performed using the same setup configuration at the SANS-I instrument in 2021 and 2022, respectively. The procedural rigor and scientific methodology underlying the experimental results are outlined, thereby facilitating the understanding of the empirical aspects.

3.2.1 Holographic recording of volume gratings and light optical diffraction measurements

This subsection concisely describes the experimental arrangements used for holographic recording and optical diffraction measurements. Different configurations were employed depending on the sample type. For the commercial Bayfol foils, separate setups were used for recording and readout measurements at the Laser Lab of the University of Vienna. In contrast, a single experimental arrangement was used for both recording and readout of the NPC samples prepared by the Japanese collaborators [111]. Despite these variations, the fundamental principles of the process remained consistent across all setups.

Principle of a two-wave interference setup

A conventional two-wave interference setup requires a laser source that emits a coherent beam at a wavelength matching the photosensitivity of the blend materials. The studied HBP-dispersed NPC film was red-sensitive, and hence, a recording wavelength λ_{rec}=640 nm was used (see Figure 2 in Ref. [116]). On the other hand, for recording NDPC gratings and Bayfol photopolymers, which are sensitive to green light, wavelengths of 532 nm and 514 nm were employed, respectively.

The laser beam, as emitted, may not have the desired diameter or polarization for recording. Therefore, a beam expansion system is utilized to achieve a typical beam diameter of approximately 1 cm. Additionally, a combination of a half-wave plate and polarizers is employed to precisely control the polarization of the beam. Except for the setup used in recording a light reflection grating, where a p-polarization was set, all setups were configured for s-polarization. The expanded and polarized beam is then split into two waves: a reference wave and an object wave, with an intensity ratio

close to 1:1. Matching the polarization and ensuring equal intensities of the object and reference beams maximizes the visibility V of the interference fringes [79], defined as:

$$V = \frac{2E_O E_R}{E_O^2 + E_R^2}$$

where E_O and E_R are the amplitudes of the object and reference waves, respectively. While minor deviations from a 1:1 ratio have negligible impact, significant deviations rapidly decrease visibility, leading to a loss of interference quality. The two waves are then recombined at the position of the sample, as depicted in Figure 3.3, using two mirrors.

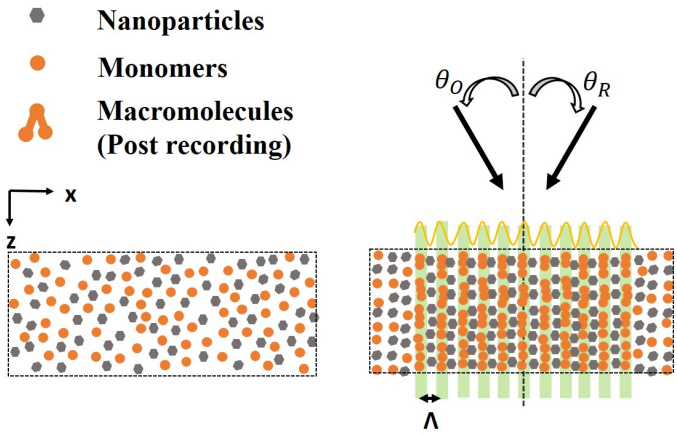

Figure 3.3: Sketch of the recording process and the holographic assembly of the unslanted NPC transmission gratings.

This sketch illustrates the holographic assembly for NPC materials, but the process is analogous for photopolymers where monomers are dispersed in a host polymer. Here, $\theta_O = \theta_R = \theta_{r,\text{ext}}$, where $\theta_{r,\text{ext}}$ denotes the external recording angle in free space. The corresponding angle in the material, $\theta_{r,P}$, is determined by Snell's law. The grating periodicity Λ based on the used recording wavelength λ_{rec} and the average refractive index of the material n_0 is: $\Lambda = \dfrac{\lambda_{\text{rec}}}{2n_0 \sin(\theta_{r,P})}$.

Additionally, the recording angle determines the Fresnel correction factor $T = 1 - R$, which must be applied to the total laser power at the interface. The reflectivity R_s is given by the following expression for an s-polarized beam:

$$R_s = \left(\frac{n_{\text{ext}} \cos(\theta_{r,\text{ext}}) - |n_0| \sqrt{1 - \left(\frac{n_{\text{ext}} \sin(\theta_{r,\text{ext}})}{|n_0|} \right)^2}}{n_{\text{ext}} \cos(\theta_{r,\text{ext}}) + |n_0| \sqrt{1 - \left(\frac{n_{\text{ext}} \sin(\theta_{r,\text{ext}})}{|n_0|} \right)^2}} \right)^2 \tag{3.3}$$

Now considering that in addition to the symmetric recording angles, a 1:1 intensity ratio is set, the total intensity at the sample can be written as $I_{tot} \propto (\mathrm{E_R} + \mathrm{E_O})^2$, with:

$$\mathrm{E_R} = \frac{\bar{\mathrm{E}}}{2} \exp\left[\imath(\frac{2\pi}{\lambda_{\mathrm{rec}}})\Big(z\cos(\theta_{r,\mathrm{ext}}) + x\sin(\theta_{r,\mathrm{ext}})\Big)\right]$$
$$\mathrm{E_O} = \frac{\bar{\mathrm{E}}}{2} \exp\left[\imath(\frac{2\pi}{\lambda_{\mathrm{rec}}})\Big(z\cos(\theta_{r,\mathrm{ext}}) - x\sin(\theta_{r,\mathrm{ext}})\Big)\right]$$

Consequently, one gets: $I_{\mathrm{tot}} \propto \bar{\mathrm{E}}^2 \cos^2\left[\left(\frac{2\pi}{\lambda_{\mathrm{rec}}}\right) x\sin(\theta_{r,\mathrm{ext}})\right]$.
Provided that $\cos^2(a) = \big(1+\cos(2a)\big)/2$, and replacing $\big(\lambda_{\mathrm{rec}}/(2\sin\theta_{r,\mathrm{ext}})\big)$ by Λ, this expression simplifies to: $I(x) \propto \frac{\bar{\mathrm{E}}^2}{2}[1+\cos(Kx)]$. This expression explicitly reveals the cosinusoidal modulation of the interference pattern along the x-axis with a period Λ, as depicted in Figure 3.3. However, it corresponds to an ideal case. A more rigorous expression takes this form [126]:

$$I(x,t) = I'_a\left[1 + \mathrm{V}\cos(Kx)\right], \tag{3.4}$$
$$I'_a = C_{fs} I_a \frac{B_a \lambda_{\mathrm{rec}}}{dN_a hc}. \tag{3.5}$$

Here, I'_a is the activation intensity which is proportional to $(\bar{\mathrm{E}}^2/2)$, d denotes the thickness of the layer, C_{fs} is a correction factor based on losses from light scattering and Fresnel reflection (around 0.9 for Bayfol HX200 photopolymers [24]). $B_a = 1 - \exp(-\epsilon_d A_d d)$ accounts for absorption which is mainly related to the initial molar concentration of the dye $A_d\,[\mathrm{mol/cm^3}]$ and its molar attenuation coefficient ϵ_d. The rest of parameters are the Avogadro number, Planck's constant and the speed of light. In fact, the exposure activates the sensitizer dye molecules and drives them to an excited state at a rate $k_a = Q_r \epsilon_d d I'_a$, with Q_r being the quantum efficiency of the reaction [24, 126]. These expressions are used in the frame of the Non-local Photopolymerization Driven Diffusion (NPDD) model, the most pertinent model to date [126–128]. The NPDD model is the successor of the Photopolymerization Driven Diffusion (PDD) model suggested by Zhao and Mouroulis, and By Noiret et al. in 1994 [129, 130]. The included non-locality of physical and photochemical processes involved during hologram formation allowed for explaining few aspects which could not be explained by the latter e.g. the large spatial frequency cut-off in spatial frequency response of holographic gratings. Though, in most general cases, predictions of both models fairly align [126].

Having presented the recording process of holographic gratings and the underlying physics, attention is now directed toward the key concepts that must be considered during light and neutron diffraction measurements.

3.2.2 Experimental considerations: Coherence length

In optics, constructive or destructive interference occur based on the phase difference between waves. The longitudinal coherence length ($\ell_{//,c}$) of a neutron beam, essential for evaluating its interference capabilities and accessing varying length scales, can be derived from basic principles [26]. Considering two components of the beam with slightly different wavelengths, λ_1 and λ_2, the phase difference ($\Delta\phi$) after traversing a

distance D is given by $\Delta\phi = |k_1 - k_2|\, D$, where $k = \frac{2\pi}{\lambda}$ is the wavenumber. Setting the phase difference equal to π for the onset of incoherence, the coherence condition is obtained: $2\left|\frac{1}{\lambda_1} - \frac{1}{\lambda_2}\right| \ell_{//,c} = 1$. Consequently, the longitudinal coherence length can be approximated using the average wavelength λ_{mean} and its spread $\Delta\lambda$, yielding:

$$\ell_{//,c} \approx \frac{\lambda_{mean}^2}{\Delta\lambda} \tag{3.6}$$

This expression provides a practical approximation for estimating the coherence length of particle beams. For example, in the 2023 experimental campaign (see paragraph 3.2.3), the beam has an average wavelength of 6 nm and a wavelength spread of about 1 nm. Hence, the resultant longitudinal coherence length is approximately 36 nm [131]. On the other hand, when using a light source such as a He-Ne laser in the performed experiments, this is not an issue as the coherence length is typically in the range of several meters.

To derive the transverse coherence length $\ell_{\perp,c}$ of a neutron beam, the beam's divergence is considered. It determines the beam's spatial spread perpendicular to its propagation direction. The transverse coherence length, characterizing the extent of spatial coherence across the beam's cross-section, is inversely proportional to the beam divergence and given by [26]:

$$\ell_{\perp,c} = \frac{\lambda_{mean}}{\text{beam divergence}} \tag{3.7}$$

This formula indicates that a greater spread of the beam results in a shorter transverse coherence length. Keeping with the same example as above with a beam divergence of 2 milliradians, the transverse coherence length of approximately 3 µm. This corresponds to seeing up to 6 periods of a grating with a 500 nm period in a coherent portion of the beam.

As depicted in Figure 3.4, from a geometric perspective, consider a neutron located at the boundary of the transversal coherence length (point A). If this neutron emerges at the sample surface at an angle θ (where $\theta_B \approx 0.33°$ for $\Lambda = 500$ nm), it traverses a path $\ell'_{//,c} = \ell_{\perp,c} \cos\theta / \tan\theta \approx \ell_{\perp,c} / \sin\theta$ along the thickness of the sample (along the z-axis) before it completely moves out of the coherent beam area. In a specific case where the transverse coherence length is 3 µm, the neutron would travel approximately half a millimeter inside the material before coherence is lost. Notably, this distance is an order of magnitude larger than the typical thickness of the relatively thin NPC samples.

In evaluating the implications of the findings, it's noteworthy that the Born approximation, known for assuming single scattering and minimal wave function disturbance, might still be valid from a corpuscular perspective. This is particularly true for thin samples with large grating periodicity where most of neutrons are assumed to simply transmit or experience a single scattering event. Nonetheless, even in the case of very thin holograms, multiple diffraction orders are excited simultaneously inside the grating, regardless of the angle of incidence, fulfilling the conditions of the Raman-Nath regime (see subsection 2.6.1). Consequently, irrespective of the sample's thickness, caution is warranted when applying this approximation to accurately interpret neutron diffraction results. The complex grating structures, potentially involving multiple

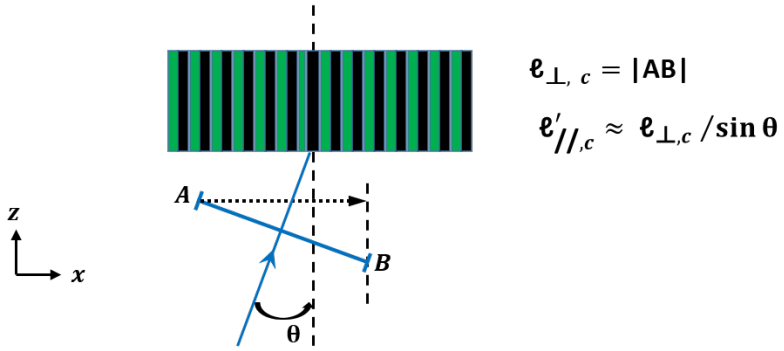

Figure 3.4: Geometric consideration sketch (not to scale)

scattering events, significantly affect the wave patterns. Under the Born approximation, diffraction is predominantly attributed to an average of the refractive index profile along the sample's depth, with single scattering events prevailing within the longitudinal coherence length, $\ell_{//,c}$.

Beyond the Born approximation, the beam divergence may lead to a Borrmann fan-like effect in neutron scattering [132–135], effectively illuminating the entire depth of the hologram through a coherent path, represented by $\ell'_{//,c}$. This effect suggests that as the coherent transverse segments composing the neutron beam–initially akin to plane waves–traverse the sample, they undergo splitting and multiple scattering (see Figure 3.4). In such scenarios, Born approximation is not considered valid anymore [85]. The interference among scattered waves from these segments causes the intensities in diffraction spots to be a superposition of contributions from all coherent beam portions. This intricate pattern of interaction emphasizes the necessity for advanced analysis techniques such as the RCWA theory, thereby, allowing for accurate interpretation of scattering data from holographic grating experiments [52, 79, 85, 91, 93]. As a consequence of the Borrmann fan effect, when the beam divergence is well-controlled, the neutrons are able to effectively probe the refractive index profile throughout the depth of the sample even in the case of a broad wavelength distribution.

3.2.3 Setup and experimental considerations at PF2/VCN

The first communication about successful operation of PF2 (Physique Fondamentale 2) instrument, which was initially named as "special instrument" before 1994, was published by A. Steyerl in 1986 [7]. Two previous communications of the status were also published [136, 137]. The instrument allows for the operation of up to five time-shared platforms sitting at the roof of the reactor building (level D): VCN, UCN, EDM, MAM and finally PF2/TEST which runs at a lower flux. Full description and technical details are available at the ILL website [62].

In the performed neutron diffraction measurements, the holographic grating is placed on a rotational stage. The latter allows for positioning the grating vector perpendicular to its rotation axis, which is normal to the optical table (orthogonal to the (x, z) plane in Figure 3.4). The corresponding angular position is denoted as θ. A θ-scan at small angles around normal incidence allows for producing the diffraction curves, often referred to as a rocking curve. Additionally, the sample can be tilted at a fixed angle ζ around an axis parallel to the grating vector.

In this subsection, the setup used in each of the experimental campaigns and some important experimental considerations will be described.

Significant gravitational fall

The neutron has a rest mass $m_N = 1.67492749804(95)\times10^{-27}$ kg and is subject to the gravitational force. The gravitational fall is proportional to the flight duration t via the relation $\Delta y[\text{mm}] = (gt^2/2)\times1000$ (for the reference, see Figure 3.4 with y-axis perpendicular to the optical table). The slower the neutron, the earlier it falls. The vertical displacement for a neutron speed $\vec{v} = (0, 0, v_N)$ and a wavelength λ_N, initially placed at origin and traveling along the z direction, is:

$$\Delta y[\text{mm}] \simeq \frac{g\ z^2\ \lambda_N^2}{2\times 3956^2} \times 1000 \tag{3.8}$$

Given that $t = (z/v_N)$ and $v_N[\text{m/s}] \simeq (3956/\lambda_N[\text{Å}])$. The gravitational fall for a neutron wavelength range between 2 nm and 10 nm is up to 50 mm for a total flight path of 4 meters. This implies that a change in the vertical position of an aperture does not only affect the captured flux, but also the wavelength distribution.

Wavelength distribution at PF2/VCN

The alignment and wavelength selection of a slow neutron beam is not straightforward (cf. Ref. [138]). A simple change of an aperture position and/or width may impact the selected wavelength distribution.

The VCN beam, produced from a liquid D_2 cold source held at a temperature of 25K, is filtered as it climbs a Curved Guide Tube (TGC) (see instrument layout at the ILL website [62]). It bypasses a turbine to directly feed the PF2/VCN platform. For some reasons that are currently under study by the ILL staff, the wavelength distribution and the flux have changed since the first communication by Steyerl. There is a noted absence of wavelengths longer than 10 nm, which was previously reported as a nominal (peak) wavelength in Ref. [61]. In an attempt to recover the losses, the full instrument was dismantled and the accessible guides were cleaned during the long shutdown [139]. Moreover, the vacuum duct collimator (see Figure 1 in Ref. [140]), which was still in place during the first experimental campaign in 2021 (see paragraph 3.2.3), has been replaced with a Nickel guide.

The characterization of the wavelength distribution at the beam entry has been recently performed by the ILL staff. Post-collimation and after reflection from the super-mirror, time-of-flight measurements are hard to perform because of the very low count rates. Therefore, in general, the final wavelength distribution is deduced by fitting the diffraction data (in general from a reference holographic grating sample). The convolution of the very broad wavelength distribution of the primary beam and the used collimation approximately results in an exponentially modified Gaussian (EMG) distribution (cf. Figure 2 in Ref. [141]). In the next paragraphs, the specifics of each of the used experimental setups will be presented.

Experimental Setup during the 2021 experimental campaign

A depiction of the setup under discussion is illustrated in Figure 3.5, which includes the neutron trajectory projection on (x, z)-plane and a detailed detector image showcasing

various diffraction spots.

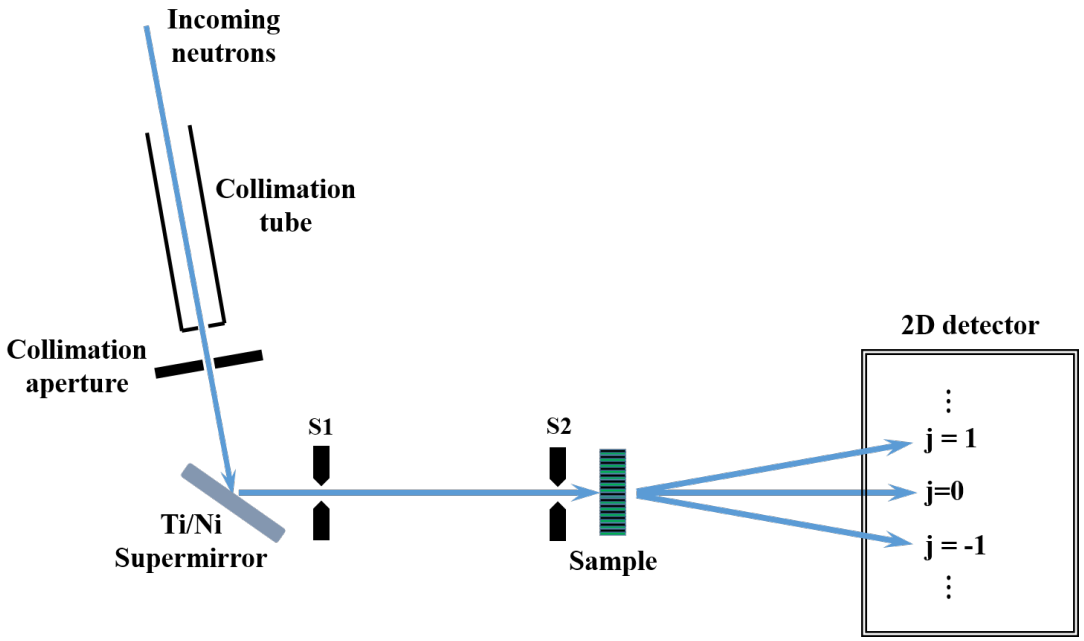

Figure 3.5: Sketch (not to scale) of the PF2/VCN instrument setup in the 2021 experimental campaign (top view).

The setup commences with a slow neutron beam sourced from the cold neutron source. The beam, characterized by a broad wavelength spectrum and significant divergence as outlined in Ref. [140], undergoes selection for a segment exhibiting a higher neutron flux yet shorter wavelengths for this campaign, adhering to an exponentially modified Gaussian wavelength profile as detailed in Ref. [141]. A collimation tube, coupled with a wide $12 \times 2\,\mathrm{cm}^2$ aperture, is utilized to refine the beam dimensions. Subsequently, the beam is redirected by a Ti/Ni super-mirror towards a the collimation system comprised of two cadmium apertures, $s_1 = 3\,\mathrm{mm}$ and $s_2 = 1\,\mathrm{mm}$, facilitating an initial beam divergence estimation of $(s_1 + s_2)/L_P \simeq 2.2\,\mathrm{mrad}$, with L_P denoting the 185 cm collimation distance. The sample to detector distance $L_D \simeq 140\,\mathrm{cm}$ ensures diffraction spots are distinctly discernible, though precise selection of regions of interest (ROIs) is imperative for effective background subtraction.

It is noteworthy that the choice of the necessary divergence depends on the peak width ($\approx \Lambda/d$), with broader peaks allowing for relaxed constraints. In fact, when it is too large, some of the rocking curve features may be washed out. Additionally, the collimation apertures are set to minimal sizes in order to avoid the convolution required in fitting procedures that consider beam divergence. Its incorporation into the model (model + wavelength distribution + convolution) significantly extends computation time and increases the number of fitting parameters, compromising parameter determination accuracy. Therefore, opting for longer measurement duration through finer collimation is preferred to eliminate the need for such convolution.

For neutron detection a two-dimensional Helium-3 detector with a 128×128 pixels of $2 \times 2\,\mathrm{mm}^2$ resolution is used [142]. To counteract any undesirable scattering from air, custom plastic tubes, filled with a flowing Helium-4 gas, are aligned along the neutron path. Unlike Helium-3, Helium-4 is almost transparent for neutrons.

At each angular position, a 2D-image is formed by the accumulation of neutron counts at the detector pixels. The data reduction procedure for deriving the diffraction efficiency curves from these images will be described in the next Chapter.

This experimental arrangement was used for diffraction measurements from all the samples described in Subsection 3.1.2 and some of the samples described in Subsection 3.1.3. The corresponding wavelength distribution was determined by fitting, and will be presented in Chapter 5.

Experimental Setup at PF2 during the 2023 campaign

This campaign was launched after the PF2 modernization program. This shutdown allowed for testing the thermal and vibrational stability at the VCN cabin. This was performed by C. Desalme for his BSc thesis [139], and will be concisely discussed in the next paragraph. The program included the dismantlement and cleaning of the accessible neutron guides. Additionally, at the beam entry, the vacuum duct placed next to the ZS6 shutter has been replaced with a Nickel coated neutron guide (m=1) made of glass. An improved shielding was established to reduce the radiation dosage and the background (see Appendix.D). The influence of this change on the background will be discussed in Chapter 4. Moreover, four motorized apertures were made available, allowing for a better control and repeatability of the measurements via the new user interface NOMAD [1]. The new apertures are composed of two horizontal (vertical) blades, allowing for setting the horizontal (vertical) position and width of each aperture. Two of them were used before the super-mirror instead of the wide collimation aperture shown in Figure 3.5, and the two others were used in a configuration similarly to s_1 and s_2. The first one has an opening $(\mathrm{H} \times \mathrm{W}) = (2 \times 2\,\mathrm{mm}^2)$ and was positioned to select a mean wavelength of $\approx 6\,\mathrm{nm}$ as indicated in Figure 3.6 [143].

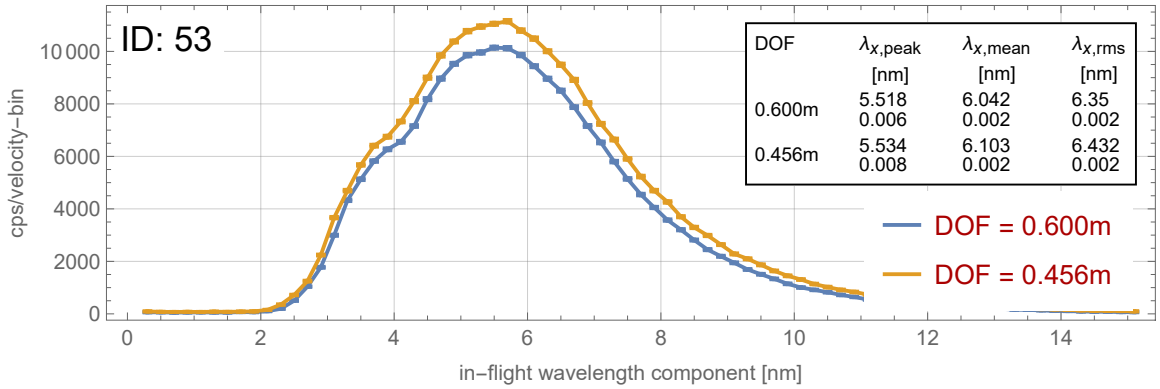

Figure 3.6: Time-of-flight (TOF) measurements corresponding to the chosen aperture setting at the beam entry of the 2023 experimental campaign setup, taken at two distinct positions [143].

The measurements were conducted at two different distances (DOF) between the first aperture and the chopper (0.456 m and 0.600 m). Variations in the results illustrate the effects of absorption and incoherent scattering over a flight path of approximately 15 cm in air. These results allow for a better understanding of the selected components.

[1] Before the upgrade, apertures width and position used to be adjusted manually, while the sample stage and the detection were controlled using an internally developed user interface.

Though, they barely allow to restrict the bounds of the WLD parameters in the fitting procedure. It is straightforward that the distribution will be narrower following a complete flight path of 240.5 cm to the sample, including three additional collimation apertures and a wavelength-dependent reflection from the super-mirror. A time-of-flight measurement after the mirror was not feasible due to the low counting rates and restricted time constraints.

The second aperture having a size of ($6 \times 6\,\mathrm{mm}^2$) was placed 24.5 cm away from the first one in order to reduce the beam cross section and divergence before the super-mirror. This would suppress background originating from neutrons shot by the mirror on the top of the setup towards the detector (or elsewhere). The opening of s_1 and s_2 (in analogy with Figure 3.5) is $6 \times 3\,\mathrm{mm}^2$ and $6 \times 2\,\mathrm{mm}^2$, respectively. A distance $L_P \simeq 149\,\mathrm{cm}$ was allowed to have a divergence of approximately 3.4 mrad. Samples were placed behind a Cadmium plate having a circular opening (Ø =10 mm) in order to make sure the neutron beam hits exactly at the hologram position during the alignment procedure. The same sample to detector distance $L_D \simeq 140\,\mathrm{cm}$ was feasible thanks to the rails system on which the detector has been placed. This was part of the modernization and allows for easy placement of the detector position along the x and z directions.

This experimental arrangement was used for diffraction measurements of grating-5 from the samples described in Subsection 3.1.2 and the rest of the samples described in Subsection 3.1.3 that were not studied in the previous reactor cycles. The WLD after collimation was also determined by fitting, and will be presented in Chapter 5.

Stability criteria for VCN neutron interferometry

The additional phase shift (ϕ_{add}) in VCN interferometry, resulting from an additional path length difference ($\delta_{//}$), is given by ($\phi_{add} = \frac{2\pi}{\lambda}\delta_{//}$). To achieve a 1-degree resolution, δ should be less than ($\lambda/2\pi$). For VCNs with wavelengths between 20 Å and 100 Å, the allowable additional path differences range from approximately 0.056 Å to 0.278 Å, a clear contrast to the sub-picometer requirements for thermal neutrons. While these requirements are less stringent, they are still challenging, especially for a platform situated atop a reactor building and exposed to significant noise.

The large hologram area further relaxes the negligible effects from vibrations along the y-axis, where displacements minimally affect the outcome. For an interferometer path length of less than 6 meters, the passage time t_0 for neutrons with a wavelength of 2 nm and 10 nm is approximately 30 ms and 150 ms, respectively, at corresponding speed of 200 m/s and 40 m/s. These periods are considerably longer than the roughly 100 µs required for stability in thermal neutron experiments, implying that control over vibrational displacements from noise frequencies above 5 Hz is necessary. This is consistent with stability criteria provided in Ref. [144] for an interferometer operating at $\lambda = 10\,\mathrm{nm}$, which coincides with the slowest neutrons considered, based on the primary beam characterization in Ref. [140]. According to Ref. [144], the condition $\delta x \ll \Lambda$ imposes the following limit to the maximum amplitude x_0 of a given vibrational mode $x = \delta_\perp \cos(\omega t)$ (with $\omega = 2\pi f$):

$$\delta_\perp \ll \frac{2\Lambda}{(t_0\omega)^2} \tag{3.9}$$

For a period Λ=500 nm and $t_0 \approx 0.15\,\mathrm{s}$, this translates to $\delta_\perp[\mu\mathrm{m}] \ll (1/f^2[\mathrm{Hz}])$. There-

fore, the optimization of space management with smaller grating periods require more severe control over the vibrational amplitudes.

The results from measurements performed by C. Desalme during the long shutdown indicate satisfactory values of the mean vibrational displacement amplitudes $\delta_x = 4.80 \times 10^{-11}$ m, $\delta_y = 2.91 \times 10^{-11}$ m and $\delta_z = 8.69 \times 10^{-11}$ m in the previously defined coordinates [139]. However, during the reactor operation the noise intensifies and this should be kept in consideration. Moreover, temperature variations over 24 hours is approximately 30 mK [139]. Hence, thermal expansion effects are negligible.

These points highlight that, despite the greater tolerances in path length differences afforded by larger grating periods in VCN interferometry, careful control over vibrational displacements remains critical. Furthermore, the slower velocities of VCNs require maintaining this stability for extended periods, typically in the order of tens to few hundreds of milliseconds, depending on the selected wavelength.

3.2.4 Experimental setup at SANS-I instrument, SINQ, Paul Scherrer Institute

Two experimental campaigns were carried out at the Swiss Spallation Neutron Source SINQ, in Paul Scherrer Institute (PSI). The first one in June 2021 and the second in June 2022. Both experiments were performed at the SANS-I instrument, and the same setup was used with minor changes.

A lead target ejects high-energy neutrons after being hit by accelerated protons at a velocity of 80% the speed of light (see SINQ webpage [145]). A tank filled with heavy water is used for the moderation of their energy, and for producing the cold neutrons used in SANS-I, a second tank filled with cold heavy hydrogen at approximately 23 K is employed to further reduce their energy. The wavelength spectrum ranges from 0.45 nm to 3 nm, and a helical slot velocity selector is used to select the desired wavelength with $(\Delta\lambda/\lambda) = 10\%$. For both campaigns, a neutron wavelength of $\lambda = 2$ nm was used, and a collimation length of 18 m between two apertures s_1 and s_2 was allowed to control the divergence. The same distance between the sample and the detector was maintained. A two-dimensional Helium-3 detector with a 128×128 pixels of 7.5×7.5 mm^2 resolution was in place. Further technical details are available on the instrument webpage (see Ref. [146]).

While $s_2 = 4$ mm was always kept for the aperture just before the sample, the opening of the first collimation aperture s_1 at the beam entry was changed. The 2021 campaign consisted of a single measurement of the NDPC grating-1, performed remotely with the assistance of the instrument manager, Dr. Joachim Kohlbrecher. For this experiment, an aperture opening $s_1 = 6$ mm was used. This sets the beam divergence to approximately 0.6 mrad compared to an expected peak width of 21 mrad. On the other hand, in the slightly longer campaign in June 2022, two samples were measured. For the NDPC grating-5, $s_1 = 10$ mm results in a beam divergence of 0.8 mrad for an expected peak width of 17 mrad. For the much thinner HBP-NPC sample, the expected peak width is wide (≈ 80 mrad). Hence, an even larger aperture $s_1 = 30$ mm was employed, resulting in a beam divergence of approximately 1.9 mrad. For both experimental campaigns, all the samples measured at SANS-I were tilted to $\zeta = 45°$. The reduction of the data collected at SANS-I has been performed using GRASP software [147].

In the following chapter, the data reduction procedures and background analysis will be discussed, focusing on their application to each of the performed measurements. This discussion aims to outline the methodologies necessary for the accurate interpretation of experimental data.

Chapter 4

Data reduction and background treatment

4.1 Experimental constraints and important considerations

Distinguishing signal from background in slow neutron diffraction experiments involving holographic optical components is often challenging. In particular, in the case of low diffraction efficiency or when the diffraction spots are either overlapping or adjacent on the detector. The difficulties are related to several factors: low neutron counts, broad wavelength distributions leading to overlapping patterns, limited space for moving the detector, as well as a variety of inherent and environmental background sources.

Most of the experiments were conducted at PF2/VCN, and others were performed at SANS-I instrument. The same sample geometry (and reference) shown in Figure 2 of Ref. [148] have been used throughout all experiments. It is necessary to establish a background subtraction procedure tailored to each case, taking into consideration: 1) The instrument or facility where measurements were performed. 2) The specifics of the experimental campaign, which can vary due to changes in setup, shielding, or the surrounding environment. 3) The properties of the studied samples.

At PF2/VCN platform, minimizing the detector's background begins with shielding the experimental room. Implementing a combination of Cadmium apertures and/or Boron glass apertures, with B4C (Boron carbide) shielding in the experimental setup further reduces it (see Appendix D). Additionally, the use of ^{4}He-filled tubes in the neutron flight path, as an alternative to vacuum tubes, significantly reduces undesired 4-π scattering on the detector. A system allowing for Helium flow through the tubes has been established for this purpose. This 4-π scattering refers to the isotropic scattering of neutrons in all directions, which can degrade the signal quality by contributing unwanted background noise to the measurements. It is not fully prevented though as the beam travels through the air before the first tube (placed between the collimation slits), between the tubes and after the second one (placed between the sample and the detector). In some measurements, a circular section with a diminished background, corresponding to the detector-side Helium tube surface, is evident on the detector. While these precautions are essential to substantially mitigate background from the source and neighboring instruments, post-measurement background treatment remains

a must for data reduction. On the other hand, at SANS-I instrument, the relatively smaller wavelength results in reduced diffraction angles. This necessitates a longer flight path between the sample and the detector. However, this is not problematic because the neutrons are traveling in ultra-high vacuum (see subsection 3.2.4).

Given these complexities and variances, the analysis will first focus on the treatment of data collected at the ILL. First, a strategy will be developed for raw counts extraction. Then, a statistical analysis of the background spread over the detector area will be conducted. The applicability of different background estimation methods will be discussed across different measurements, including various samples, experimental campaigns, and facilities.

4.2 Data reduction: methods and challenges

Data extraction and background treatment are closely interconnected processes. The depicted background is determined by the selected regions of interest (ROIs), used for the extracting the raw counts. This will be demonstrated in this section.

4.2.1 Raw counts extraction

Figure 4.1 shows the sum of all detector images from two distinct measurements: one formed by summing 40 detector images (angular steps) from an NDPC sample measured in 2021 campaign [149], displaying seven diffraction spots with high diffraction efficiencies; and the other formed by the sum of 18 detector images from a Bayfol foil sample measured in the 2023 campaign [131], showing three diffraction spots including low-efficiency first orders. Both measurements involved good statistics (approximately 82000 and 44000 counts per scan step, respectively, for the same duration of 4000 s per step). The labeling of the y-axis pixels from the top to the bottom in one image and vice versa in the other is because the images were formed by processing different types of data [1].

Rectangular ROIs are typically used, primarily because they effectively capture the shape of the forward-diffracted beam. This is less suitable for other diffraction orders. The shape of the forward-diffracted beam is actually defined by the convolution of the incident beam from the source with the rectangular shaped collimation apertures that were used. However, the distinct shapes of the other diffracted spots result from the broad WLD of the slow-neutron beam. Neutrons with longer wavelengths tend to appear lower—due to a more significant gravitational fall—and further from the direct beam because of larger Bragg angles. Due to the broad WLD and the limited space at PF2 instrument, achieving optimal separation of diffraction spots on the detector is sometimes problematic. The ROIs can also be configured in non-conventional shapes in a way that fully encompasses the diffraction spots without any overlaps. This results in smaller ROIs, and thereby, reduced background estimates. However, some unavoidable background is always captured. While the ROIs are designed to capture the entire spot, particularly at Bragg angle, the measured intensities of diffracted orders are

[1] Before the beamline modernization, data used to be collected using an in-house developed Labview interface that generates a data file for each scan position. One of the major upgrades of the instrument was the implementation of the NOMAD interface, which generates data files in Nexus format [150]

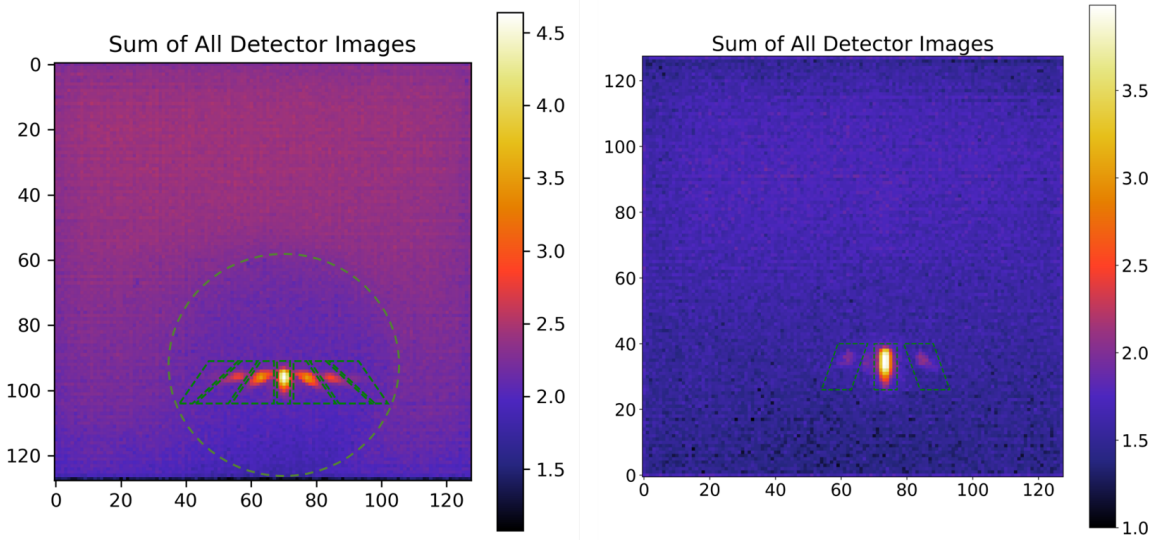

Figure 4.1: Summed detector images from two different measurements, showing multiple diffraction orders from an NDPC grating and a Bayfol foil [131, 149]. The ROIs, marked by dashed green lines, were used for data extraction. The color-bar indicates the number of counts in a logarithmic scale.

increasingly dominated by the background as one deviates further. A comprehensive explanation regarding the algorithm used for handling the edge pixels within the defined ROIs can be found in Appendix G. The most important considerations for the adopted process in this work, are consistency and symmetry. Consistency requires using the same ROIs across all angular positions, and symmetry implies that the ROIs for $j = \pm m$ orders have the same size and being mirror symmetric with respect to the forward-diffracted beam. The symmetry is the result of a perfectly placed grating with its vector and the normal of its surface being both in the (x, z)-plane.

The used experimental arrangements described in the previous Chapter, ensured the absence of any overlap during the performed measurements. However, when it is not the case, neutrons from different diffracted orders get counted on identical detector pixels. In such scenarios, a possible procedure has been highlighted in Ref. [97]. The suggested procedure consists in extracting counts from detector pixels solely based on an S/N threshold criterion, and assuming that these counts are devoid of background (pure net counts). Next, overlapping patterns are disentangled through fits of the beam profile using estimated shapes (fits with multiple Gaussians). While the usefulness of such an approach is proven, in this work, methods involving fixed ROI shapes are opted for. This guarantees a more consistent background level across the scan. The same argument holds for disregarding the extraction of detector counts line by line, yielding arbitrary shapes of the ROIs across angular positions.

Once the raw counts are extracted, the background analysis will be carried out. A comparison of different background estimation methods will be presented in the next subsection.

4.2.2 Challenges and potential assumptions for background spread

The motivation for this discussion, primarily rooted in the ambiguity of the forward diffracted beam background determination, is presented in Appendix E. In this subsection, some possible assumptions for describing the background spread are introduced, and their validity will be examined in the following sections.

Background Analysis: Potential Assumptions to be evaluated: The following paragraph lists possible approximations that will be subject to a validity check, i.e. to verfiy whether to hold or to reject a given assumption, in the next sections.

1. At each angular (rotation stage) position, the background distribution is uniform across all detector pixels within the area delineated by the He tube's surface (characterized by the diameter of the employed He tube, e.g., Ø = 20 cm during the 2023 experimental campaign) [131] [2]. This specific detector area is henceforth referred to as the low-background region. This assumption posits that the background exhibits vertical and horizontal homogeneity within this specified area.

2. The background is vertically homogeneous, but varies horizontally within the low-background region.

3. Contrarily, the background is horizontally homogeneous, but varies vertically within the low-background region.

4. Within a narrow slice-shaped region, defined by the vertical width of the ROIs used for count extraction (approximately 12 pixels in the 2023 experimental campaign), the background is uniform.

5. Throughout the θ-scan, irrespective of the angular position, the background distribution remains unchanged as long as the rocking curve width spans only a few degrees (negligible change in the sample section seen by the incident beam) [3].

The imperative for distinct evaluations of these materials arises from their unique compositions, structures, and inherent attributes. The periodic nature of gratings might lead to distinct backgrounds for different diffraction orders due to unique scattering patterns at varying length scales. Any disorder or imperfection at a specific scale could intensify the diffuse scattering for the corresponding diffracted order, as highlighted by Pynn [151] in a study that involved holographic gratings. Differences in characteristics, such as absorption, incoherent scattering and coherent scattering cross-sections, are also anticipated. The incoherent scattering, notably from hydrogen in polymers [152–154], contributes to the overall background level. In this study, the collective behaviour of the considered multi-component structures was evaluated based on averaged loss (absorption + incoherent scattering) cross sections. In all cases, these losses do not impact the computation of the diffraction efficiency itself thanks to the

[2] In all performed experiments, the centering of the direct beam spot was ensured, or nearly so, on the He tube to avoid losses in the flight path. Pixels outside this boundary–that is clearly observable for example in Figure 4.1–were excluded due to a substantially higher background. The focus is directed toward this area, which contains the diffraction signal with minimized background noise.

[3] Variations may stem from the flux fluctuations and from the surrounding experiments

normalization (to be discussed later in this Chapter). This is particularly true in the context of phase gratings. Though, it may cause difficulties in the data extraction, especially in the case of low S/N ratios.

The immediate goal is to verify the validity (or the non-validity) of the stated-above approximations for a couple of representative samples from each class. Next, the background subtraction procedure can be refined. Using the background as an adjustable parameter in efficiency calculations could be a methodologically sound approach, as evidenced in some previous studies [23, 76]. However, alternatives that minimize the computational complexity given the already intricate nature of the fits would be an asset.

4.2.3 Derivation of the diffraction efficiency and its uncertainty

Given the following expression for the diffraction efficiency of the j-th order at a given angular position θ:

$$\eta_j(\theta) = \frac{c_j - Bkg_j}{\sum_{i=-m}^{+m}(c_i - Bkg_i)} \tag{4.1}$$

where c_j denotes the signal raw counts and Bkg_j denotes the background counts for the j-th order. The variable i iterates over all the diffracted orders, including the j-th order. The associated uncertainty $\Delta\eta_j$ is derived through Gaussian error propagation:

$$\Delta\eta_j = \sqrt{\left(\frac{\partial\eta_j}{\partial c_j}\Delta c_j\right)^2 + \left(\frac{\partial\eta_j}{\partial Bkg_j}\Delta Bkg_j\right)^2 + \sum_{i\neq j}\left[\left(\frac{\partial\eta_j}{\partial c_i}\Delta c_i\right)^2 + \left(\frac{\partial\eta_j}{\partial Bkg_i}\Delta Bkg_i\right)^2\right]}$$

Here, Δc_j and ΔBkg_j are the uncertainties for the j-th order, while Δc_i and ΔBkg_i are for all other orders $i \neq j$. The partial derivatives are computed as follows:

$$\frac{\partial\eta_j}{\partial c_j} = \frac{1}{\sum_k(c_k - Bkg_k)} - \frac{c_j - Bkg_j}{\left(\sum_k(c_k - Bkg_k)\right)^2}$$

$$\frac{\partial\eta_j}{\partial Bkg_j} = -\frac{\partial\eta_j}{\partial c_j}$$

For $i \neq j$, the derivatives are:

$$\frac{\partial\eta_j}{\partial c_i} = -\frac{c_j - Bkg_j}{\left(\sum_k(c_k - Bkg_k)\right)^2}$$

$$\frac{\partial\eta_j}{\partial Bkg_i} = -\frac{\partial\eta_j}{\partial c_i}$$

The raw counts c_j for different diffracted orders are obtained from non-overlapping regions of interest (ROIs). Moreover, the background Bkg_j of each order is computed independently from the others. Hence, the covariance between the diffraction efficiencies η_j and η_i for $j \neq i$ is zero (except for *Method 1* in Appendix E). This assumption is based on the statistical independence between the raw counts c_j and also between their corresponding background estimates Bkg_j. This ensures that no covariance terms

need to be included in the uncertainty calculation. Consequently, if the common denominator is denoted as $D = \sum_k (c_k - Bkg_k)$, the propagated uncertainty for the j-th order diffraction efficiency is concisely expressed as:

$$\Delta\eta_j = \sqrt{\begin{aligned}&\left(\frac{\Delta c_j}{D} - \frac{(c_j - Bkg_j)\Delta c_j}{D^2}\right)^2 + \\ &\left(-\frac{\Delta Bkg_j}{D} + \frac{(c_j - Bkg_j)\Delta Bkg_j}{D^2}\right)^2 + \\ &\sum_{i\neq j}\left[\left(-\frac{(c_j - Bkg_j)\Delta c_i}{D^2}\right)^2 + \left(\frac{(c_j - Bkg_j)\Delta Bkg_i}{D^2}\right)^2\right]\end{aligned}}$$

Expanding this and combining like terms, the uncertainty expression simplifies to:

$$\Delta\eta_j = \frac{1}{D^2}\sqrt{\begin{aligned}&\left(\Delta c_j^2 + \Delta Bkg_j^2\right)\left(D - (c_j - Bkg_j)\right)^2 + \\ &(c_j - Bkg_j)^2 \sum_{i\neq j}\left(\Delta c_i^2 + \Delta Bkg_i^2\right)\end{aligned}} = \frac{1-\eta_j}{D}\sqrt{\sum_k \left(c_k + Bkg_k\right)} \quad (4.2)$$

This formula succinctly represents the propagated uncertainty for the j-th order diffraction efficiency, accounting for the contributions of uncertainties from all orders. Some methods, like Masiello's [97], and another method to be discussed later, calculate diffraction efficiency and its uncertainties using only net counts as the background treatment is included within the data extraction procedure. The demonstration in Appendix H explains how to derive the uncertainty from the diffraction efficiency expression that only employs the net counts. Such approaches are proven valid when background is relatively minor compared to the net counts, but may lead to inaccuracies in the uncertainty estimation when background noise is relatively high compared to the raw counts. Therefore, it is more recommended to use the main equation (see Equation 4.2) which considers both the raw counts and the uncertainties in the background, providing a more thorough analysis of uncertainty.

The detailed exploration in the next subsections is directed towards addressing this issue, ensuring broad applicability across various sample classes. An in-depth investigation is undertaken into the veracity of the assumptions outlined above, with a focus on data acquired at PF2. Initially, attention will be directed towards the Bayfol foils data gathered during the 2023 experimental campaign [131]. Afterwards, a comparative study will be conducted to assess the applicability of the findings to another class of materials—the NDPC grating. It was also measured during the same experimental campaign under identical setup conditions. The study will determine whether the findings for these foils can be generalized to NDPC gratings or if significant variations exist. Such a comparative analysis would offer insights into potential limitations of the initial conclusions drawn from the Bayfol foils data.

4.3 Data reduction and background analysis of post-upgrade data collected at PF2/VCN

4.3.1 Study of the background distribution for a Bayfol sample measured in the 2023 experimental campaign

Statistical analysis of the background counting

The following study focuses on crafting a methodical strategy for background subtraction for the sample labeled SM_32µm_10mW (see Section 3.1). The same study was performed for all the measured samples. However, this one was deliberately chosen because it is the only sample from the 2023 campaign that showcases non-negligible diffraction for second orders [131]. While higher diffraction efficiencies for second orders (compared to first orders) have already been reported for light in different works [155–157], this has not been observed for neutrons and has not been involved in this study. Though, this does not include the interest in future studies with neutrons, especially when higher diffraction angles are preferred.

Before proceeding with the analysis, the experimental constraints and data collection procedure are outlined. Data acquisition takes place at large-scale facilities where beamtime allocation is fiercely competitive and time slots are finite. As a result, it is unfeasible to conduct rocking curves with minute step increments and optimal statistics (count time). In fact, the minimum number of steps required to construct a full rocking curve is estimated based on prior knowledge about the sample. Next, a suitable duration is set for each step in order to allow for enough statistics ensuring discernible differences between low signal diffraction and background. It is typical to count around an hour per step. The 19 angular positions (see Figure 4.2) correspond to an incomplete rocking curve. Though, it may be adequate to detect certain systematic traits. The detailed figures that support the analyses can be found in Appendix I, Appendix J and Appendix K.

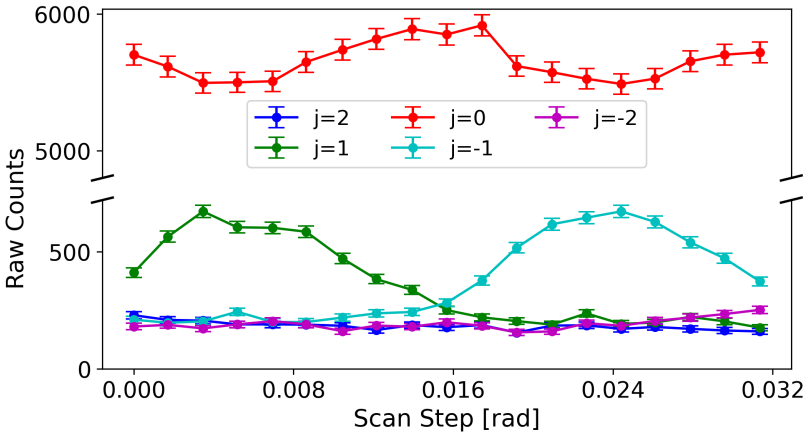

Figure 4.2: Raw counts extracted from selected ROIs for each of the diffracted orders vs. angular steps (arbitrary offset) for the Bayfol SM_32µm_10mW sample measurement.

For the initial study in Appendix I, a vertical ROI profile depicted in green on the left plots of the first figure set (which represent a logarithmic view of the detector

counts) was constructed e.g. see Figure 4.3.

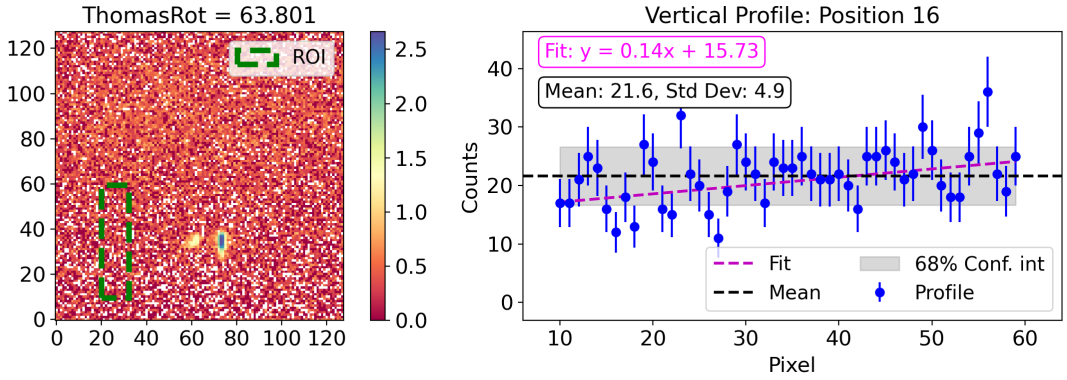

Figure 4.3: Vertical variations of the background an arbitrary angular position (here, the 15-th) for the Bayfol SM_32µm_10mW sample measurement.

The vertical profile starts at pixel 20 and extends to pixel 32 included in the horizontal x-direction of the detector. This range, distanced from the direct beam and the diffraction spots (also from the edges of the detector) was deliberately chosen, to ensure that diffraction signal did not influence the investigation. However, changing the position of the profile does not alter the observations. The analysis presented in the right side plots, is confined to ± 25 pixels around the central beam's vertical position (approximately at pixel 35) and within the low-background area, stretching from the 10-th to the 60-th pixel in y(vertical)-direction. The reason for this constraint is to prevent straying outside the low-background region, given the vertical profile's relative distance from the central beam position (which aligns roughly with the center of the He tube).

The right-side plots showcase the variations in background counts, represented in blue. The mean value of these counts is delineated by a black dashed line. A 1D linear regression fit, marked by a magenta dashed line, was performed to check for systematic variations of the profile counts. For the considered example, the slope is 0.142 ± 0.045. The fits consistently indicate a rise in the background (a positive slope, throughout all angular positions) from the detector's bottom to its top. As a result, it is essential to discard the first and the second assumptions described earlier in subsection 4.2.2. Specifically, the presumption of homogeneity across the entire low-background area fails, as vertical uniformity is already proven invalid. The next step involves assessing the horizontal uniformity and potential discrepancies across different angular position scans.

The second figure set in Appendix J divides each figure into four distinct plots e.g. see Figure 4.4. The top-left plot presents a logarithmic view of the entire detector pixel array, highlighting three slice-shaped regions of the same width (13 pixels for this measurement). The central strip, colored in green, is designed to cover the signal spots, maintaining the vertical width of the ROIs intended for count extraction. The two adjacent slices, matching in width, start a pixel above (in blue) and a pixel below (in red) the central slice, respectively. The purpose from their construction is to analyze the background distribution in various parts of the detector's low-background region. The top-right plot depicts the horizontal profiles of these three ROIs. Meanwhile, the bottom-left plot juxtaposes the signals from the central and upper profiles. In the

latter, the dashed black line represents the upper profile's mean and the surrounding grey shade representing the confidence interval from its standard deviation. Similarly, the bottom-right plot provides a comparative view for the lower strip profile. To evaluate horizontal homogeneity on the detector, 1D linear regression fits, marked by magenta dashed lines were performed for each of the top and the bottom ROIs' horizontal profiles.

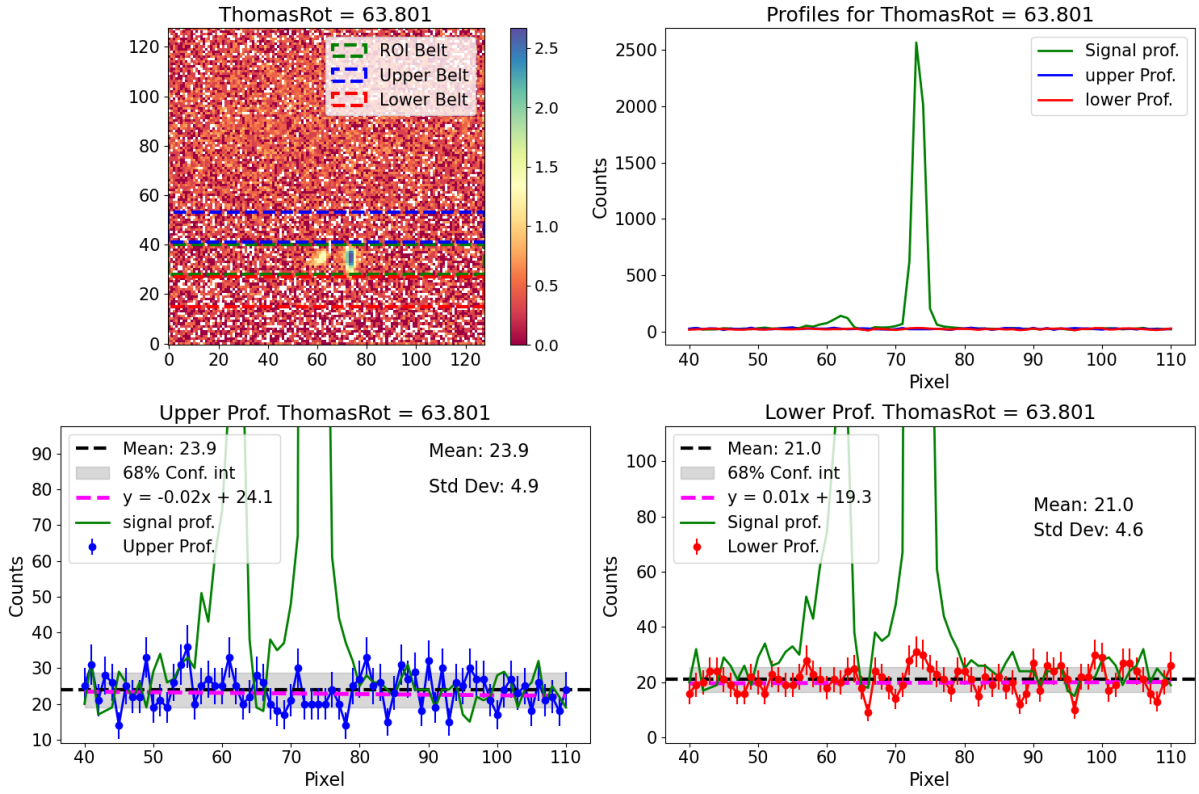

Figure 4.4: Horizontal background analysis at an arbitrary angular position (here the 15-th) for the Bayfol SM_32µm_10mW sample measurement.

Analyzing the components depicted in the figures, several insights emerge. Looking at the top-right plots, a prominent and consistent peak around 2500 counts is noted. It corresponds to the forward-diffracted beam. This translates to approximately 0.7 counts/s at this peak position, considering a duration of 3600 s per step. Some fluctuations in these counts are due to instabilities in the He flux. A detailed inspection of the bottom plots, where the middle profile is contrasted with the upper and lower profiles, indicates fluctuations ranging from 10 to 35 counts. Notably, most of these fluctuations represent values that are less than 1% of the direct beam's peak. These fluctuations do not appear to follow a systematic trend, instead seeming to be dispersed randomly. The linear fits of the profiles also suggest randomness, as no systematic variations are observed. While residuals were computed and examined for every angular position (details of which are not presented in this report), they appeared featureless and randomly distributed around zero (which indicates a good match between the linear regression fits and the data). Additionally, the sign of the slopes derived from the fits alternates between positive and negative, without any evident correlation between the slope signs of the upper and lower profiles, as illustrated in Figure 4.5.

The magnitude of the slopes is relatively small, but it is not always negligible. It seems to oscillate around a mean value that is close to zero. This indicates that the background appears to be distributed fairly uniformly, though in a stochastic manner, across the horizontal axis and consequently suggesting that the third assumption (see subsection 4.2.2) is rather a tenable approximation, but with a certain caution.

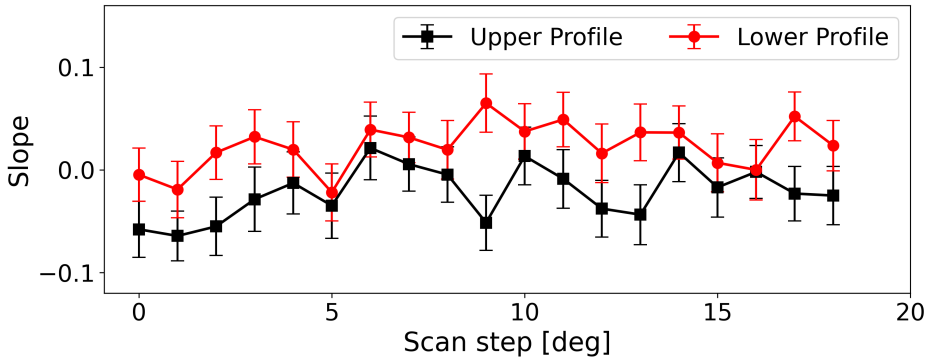

Figure 4.5: Slope values derived from the fits of the upper (blade) and lower (red) horizontal profiles.

The computed standard deviation values are almost equal to the square root of their corresponding mean values. This pattern is consistent with a generalized Poisson distribution for neutron counting, as noted in previous studies [158, 159]. This validates the use of the square root values as the error bars for a given number of detector counts.

Before proceeding to the statistical evaluation of the individual mean values of the upper and lower ROIs' profiles, the stability of the neutron flux during this measurement will first be examined.

Variation of the total neutron counts during the measurement

In order to comprehensively analyze the stability of the neutron flux during the measurement, the investigation started by checking the variations in total neutron counts at the detector over the range of angular positions, as depicted in Figure 4.6.
The data trend depicted in the graph indicates an increase until a peak in total counts near zero incidence, followed by a decrease. The disparity between the maximum and the minimum peak counts is roughly 1000 counts. This represents 2.4% of the maximum when excluding error bars and 3.4% when including them, indicating that this is not negligible. These variations are attributed to a combination of factors. Firstly, losses due to absorption and incoherent scattering cross-section, as described by the Beer-Lambert law, are affected by changes in effective depth d_{eff} as the angle of incidence varies. However, the change in the sample thickness, and the resulting change in the measured intensity in a Beer-Lambert fashion, are minor at the small angles considered here (± 15 mrad). Secondly, any horizontal displacement of the beam, possibly resulting from misalignment between the rotation axis and the circular aperture's center, can influence the counts. Finally, shifts in the aperture's position could alter the spectrum and flux, though such effects are generally minimal for slight (sub-millimeter) displacements. This is particularly true since an x-axis (see Figure 4.7) scan is routinely performed before each measurement to ensure the aperture's center aligns with the intensity plateau's center. The Figure shows an illustration of the effect of the

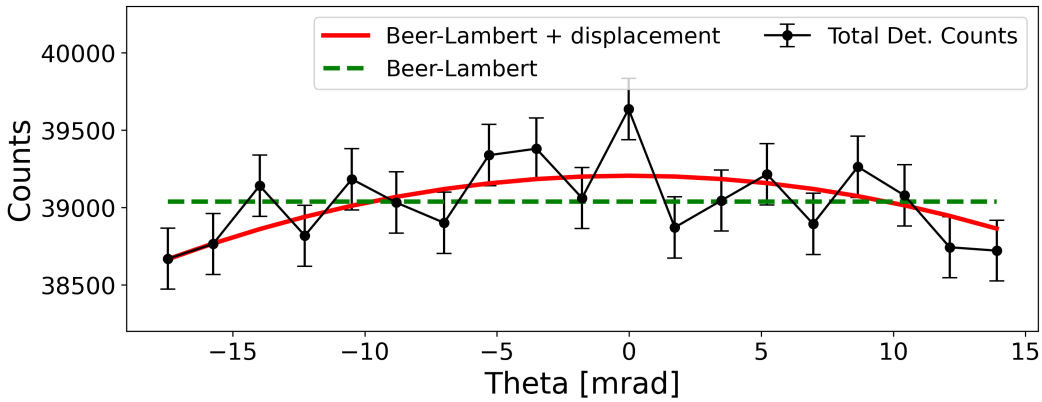

Figure 4.6: Variations of the total counts at the detector. The fit using Beer-Lambert attenuation function is represented by the dashed green line, while the fit considering both the attenuation and a potential horizontal beam displacement upon rotation is indicated by the red line.

offset on the intersection area, and hence the flux, between the incident neutron beam and the aperture.

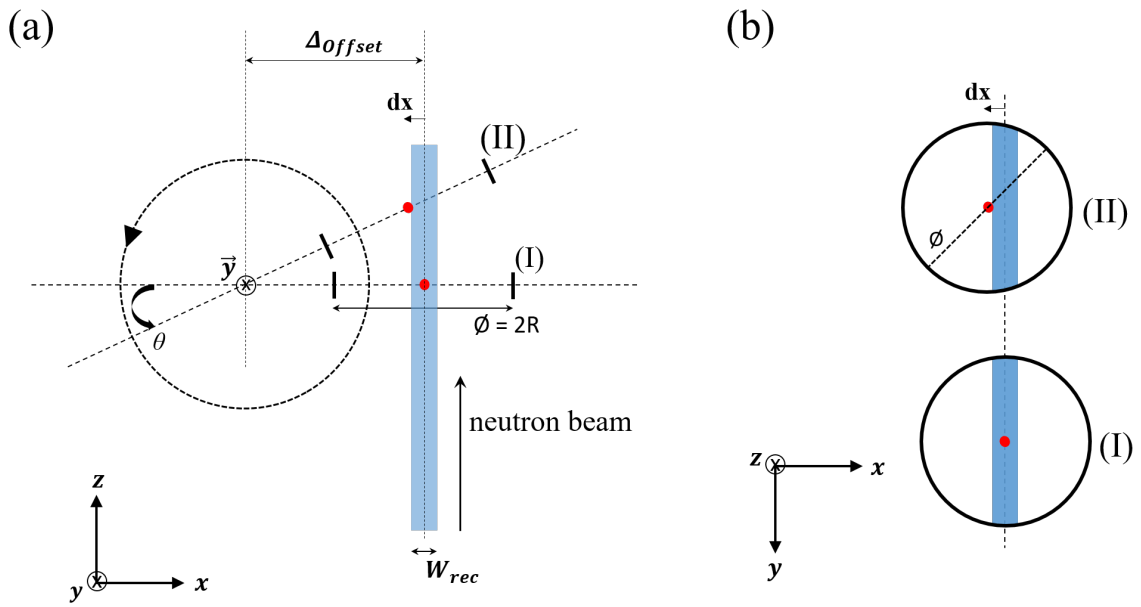

Figure 4.7: Exaggerated sketch illustrating the change in the intersection area between a circular aperture ($Ø = 10\,\text{mm}$) and a rectangular beam ($W_{\text{rec}} = 2$ mm) after a rotation to an angle θ from normal incidence. The exaggeration is used for clarity, emphasizing the displacement dx induced by an offset Δ_{offset} between the rotation axis of the sample holder and the center of the aperture (red dot). (a) Top view showing the initial and displaced positions of the aperture. (b) Front view depicting the change in the intersection area between the initial and displaced positions.

A comprehensive discussion on the influence of the offset-induced displacement is available in Appendix L. Additionally, Figure 4.8 demonstrates the variations in the intensity ratio (the intensity of the beam after a displacement dx from the center of

the aperture divided by the intensity at zero displacement) as a function of the beam's horizontal shift. It is important to note that before all the measurements, an x-axis scan is performed with a 1 mm step to make sure that the beam is hitting exactly at the center of the aperture [131].

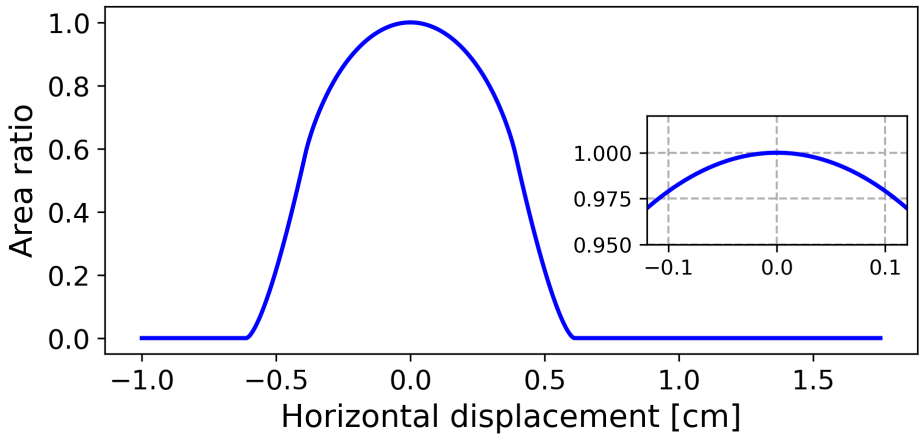

Figure 4.8: Simulation of the area ratio as a function of the beam's horizontal displacement for a circular aperture (R=0.5cm) and an infinite-height rectangular beam with a width W_{rec}=0.2cm. The inset focuses on the vicinity of zero displacement.

The initial fitting, which only accounted for losses from absorption and incoherent scattering, deduced a macroscopic neutron loss cross-section of $< \sigma_{\text{abs+inc}} >= (4.75 \pm 0.36)\,\text{cm}^{-1}$. Given the confined angular range ($\pm 1°$ about zero incidence), the effective thickness exhibits negligible deviation from the actual physical thickness d_0, leading to an almost linear fit characterized by χ_{red}=1.79 and a p-value of 2%.

In the subsequent fitting approach, and given the small angles involved, the assumption of a linear dependence of the horizontal displacement, dx, on θ was considered. It is described by: $dx = K\theta$. With K as a fit parameter, it offers insights into the potential displacement resulting from an angular step. The fitting outcomes are:

- Neutron loss cross-section estimate: $< \sigma_{\text{abs+inc}} >= (3.41 \pm 0.53)\,\text{cm}^{-1}$.
- Factor estimate: $K = (4.66 \pm 0.67)\,\text{cm.rad}^{-1}$ (approximately 0.7 mm displacement per 1° rotation)

Tools available on the NIST website were used [160] to evaluate the accuracy of the results. Simulations assessing neutron transmission and scattering cross sections for standard Poly(methyl methacrylate), PMMA photopolymers–a type of photopolymer typically used for such applications with known compositions–were executed. At a constant wavelength of 6 nm, the simulation revealed a neutron transmission rate of 98.24%. The coherent, absorption, and incoherent macroscopic scattering cross sections were evaluated at 0.013cm^{-1}, 0.634cm^{-1}, and 4.901cm^{-1} respectively. The primary source of neutron loss in this context is ascribed to incoherent scattering. Therefore, the deduced loss cross section of $\sigma_{abs+inc} = 3.4\text{cm}^{-1}$ seems reasonable. On the other hand, the implications of this horizontal displacement on the flux, in the absence of any sample and solely due to the rectangular beam's lateral shift within the circular aperture, are represented in Figure 4.9.

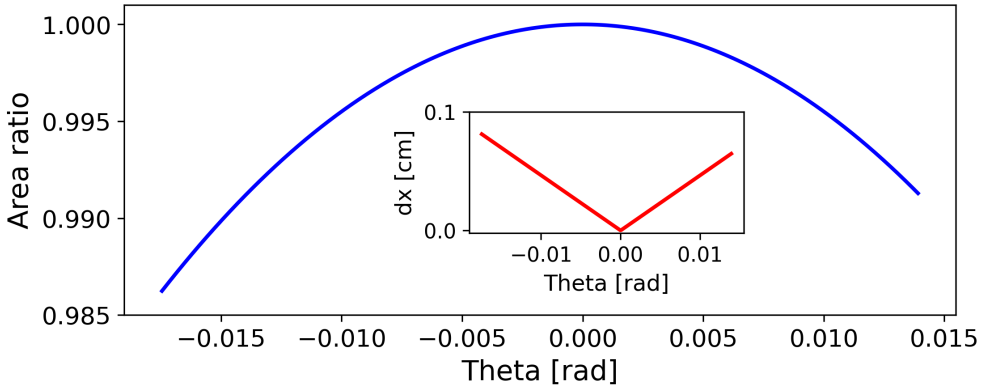

Figure 4.9: Estimated intensity ratio derived from the fit as a function of the beam's horizontal displacement. The inset delineates the displacement induced by rotation.

The inset in this figure illustrates the horizontal displacement as a function of θ, utilizing the determined K parameter from the fit. By factoring in this horizontal displacement, the fit quality noticeably improved, as indicated by χ_{red}=1.17 and a p-value of 29%. As a result, a better estimation of the loss cross-section has been achieved.

Comparative analysis of elaborated background estimation methods

For background estimation, the bottom plots in Appendix J are now considered. The study involves examining how the mean values morph with the changing angular position. At the outset, one significant observation is that the values derived from the upper profile consistently surpass those of the lower profile. Additionally, the middle profile in green tends to be always lower than the blue profile and higher than the red one. Such insights reaffirm earlier observations, suggesting a steady increase in the background as one progresses from the detector's base towards the top.

Building upon the preliminary analysis, the distribution of the individual mean values was examined. Several methodologies were tested to estimate the background per pixel in order to deduce an estimate for each order.

1. *Approach 1* (referred to as "Dynamic" in Figures): The background within the central ROI profile is interpolated using the *individual* mean values from both the upper and lower profiles at every angular position. This results in dynamic background levels which are then divided by the width of the profile to have an estimate of the background per pixel. The latter is then multiplied by the number of pixels contained in the ROI used for raw counts extraction for each of the diffracted orders to obtain the corresponding background.

2. *Approach 2*: An average mean value is computed from the individual mean values of the upper profile, then similarly for the lower profile. Following this, interpolation is performed using these values to establish a consistent "averaged" background level within the central profile. The latter is then used to estimate the background per pixel and to deduce the background of each diffracted order.

3. *Approach 3*: Analogous to the *Approach 2*. However, to account for possible neutron flux variations, it assigns a weight to each individual mean value. The

averaged mean $M_{\text{upp/low}}$ is derived from the weighted individual mean values as follows:

$$M_{\text{upp/low}} = \frac{\sum_{i=1}^{N} m_{upp/low,i} \times \text{Tot}_i}{\sum_{i=1}^{N} \text{Tot}_i} \tag{4.3}$$

Where N represents the cumulative number of angular positions. The numerator is the counts summation across all angular positions, multiplying each individual mean value $m_{upp/low,i}$ by the total counts Tot_i at that specific position. The denominator is the sum of all total counts, ensuring normalization.

4. *Approach 4* (referred to as "Prof. Fit" in Figures): Detailed description and supporting visualizations are in Appendix K. This method, similar to Masiello's [97], identifies the diffraction peaks' positions based on predefined threshold conditions (it is also possible, but not preferable, to manually add peaks that are not allowed by the filter function). Then, the full profile of the central region of interest (ROI) – shown as the green ROI in Appendix J – is fitted using a combination of Gaussian and Lorentzian functions centered on the identified peak positions. This approach is based on two ideas: first, that the convolution of the incoming beam profile with the collimation creates a Gaussian-shaped beam [97], and second, that diffuse scattering can be represented by a Lorentzian distribution [161]. For each order, the net counts are directly calculated from the area under the Gaussian component. The corresponding total background is obtained by integrating the sum of a global background estimate (found by the profile's minimum at each position) and the Lorentzian component in the ROI used for extracting net counts. This ROI is smaller than the full span of the Lorentzian component, so the integration is limited to the area around the peak.

In this analysis, *Approach 1* and *Approach 4* yield variable background values at different angular positions, whereas the second and third approaches assume a consistent, constant background. Except, *Approach 4*, the three others assume a uniform background across a 13-pixel-wide ROI. Notably, the constant background approaches produce very similar per-pixel values: 1.741 ± 0.366 for the second and 1.742 ± 0.366 for the third. This alignment suggests that minor variances in the total detector counts at diverse positions do not notably impact their computation. Consequently, *Approach 2* and *Approach 3* are practically equivalent for this measurement.

In contrast,*Approach 1* leads to fluctuating background values per pixel, ranging from 1.645 ± 0.356 to 1.794 ± 0.371. For a typical diffraction spot ROI of about 100 pixels, this results in background values between 164.5 ± 35.6 and 179.4 ± 37.1, compared to a stable background level of 174.1 ± 36.6 in the second and third methods. While having a specific background estimate for each scan position is ideal, the variation in background values in the first method remains within the error margins of the averaged background. Therefore, these three methods, based on interpolating background estimates from "diffraction-free" regions (the upper and the lower ROIs), are considered to yield statistically equivalent results and can be used interchangeably. Therefore, any of these methods can be employed to compare with the outcomes of the fourth technique.

On the other hand, the zero-th order, the distribution of higher orders across the detector pixels is modulated by the sample's differential response to assorted wavelengths. Consequently, the background for the zero-th order, which covers fewer pixels,

appears lowest. These three approaches fail from this regard. Though, they allow for estimating the blank background contribution, when the classification of different background contributions is required. This is clear when looking at the horizontal profile of the middle ROI. A higher background is observed for the forward diffracted beam. The presence of what resembles Yoneda fringes around the forward diffracted beam at several positions (see Appendix J and Appendix K), supports the hypothesis that background differences among the orders are due to off-specular scattering from the structure at various scales [151, 161]. Furthermore, since the ROIs for the diffraction spots are small and not representative of the entire horizontal profile, this can lead to negative net counts (including errors), which is not physically plausible and therefore cannot be considered reliable.

Approach 4 introduces a nuanced method for background estimation based on the signal ROI. For the forward diffracted order, the background ranges from 218.8 to 285.6 counts within a 91-pixel ROI. Extrapolating to a 100-pixel ROI, the background is estimated to be between 240.4 and 313.9 counts. While excellent at assessing the zero-th order background, it is less adept at discerning signal from noise in low-intensity situations.

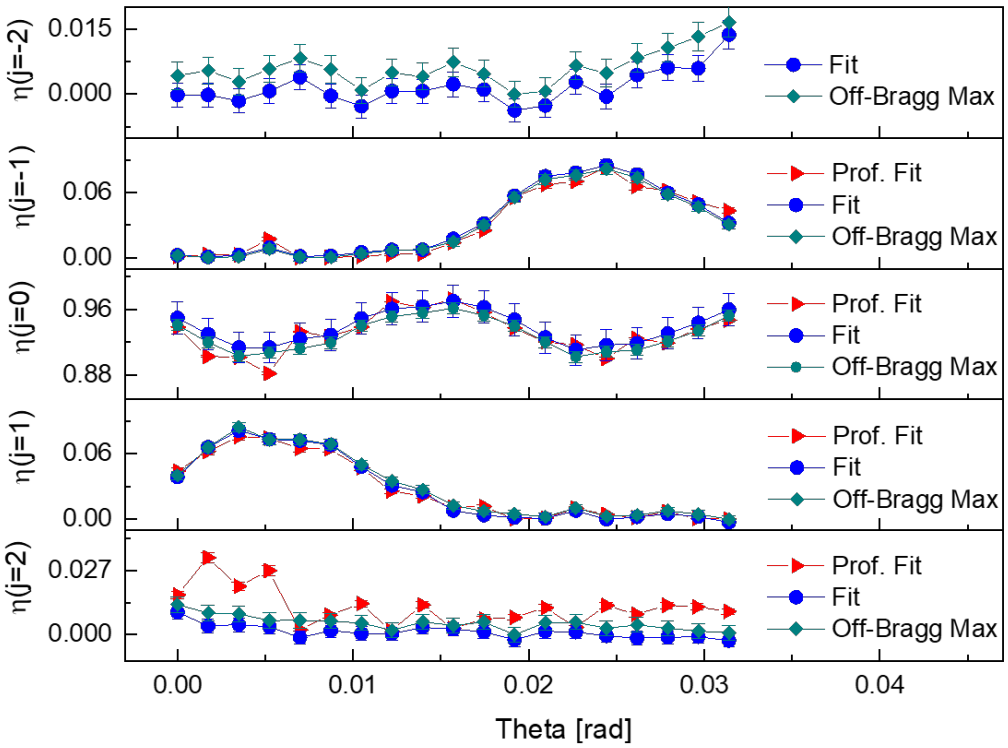

Figure 4.10: Comparison of diffraction efficiency curves for the Bayfol SM_32µm_10mW sample measurement derived using different background estimation methods: *Method 2* (diamond markers in teal), *Approach 4* (triangular red markers), and background for first and second orders as fit parameters with fixed (mean) zero-th order background estimated using Gaussian fits at different angular positions (blue circles).

Figure 4.10 reveals agreement between the methods for the zero-th and first orders,

where diffraction efficiencies are significant. However, for the second orders, *Approach 4* deviates, especially in the initial measurement positions, due to overestimation of net counts for j=2, indicating its reduced accuracy in low signal-to-noise areas. The j=-2 order's absence is due to the threshold criteria failing to detect a significant peak, and adjusting this threshold or peak detection conditions often mistakenly identifies background oscillations as peaks. This highlights the issues that arise from threshold-based methods for data extraction. Moreover, the smaller error estimates in this method result from the exclusion of background errors in calculations (the expression from Appendix H was intentionally used instead of Equation 4.2 only for this approach to highlight the differences), leading to an underestimation of total errors. Considering these factors, methods that incorporate both raw counts and background in error estimations are preferred.

The analysis indicates that *Approach 4* is optimal for high-intensity peaks like the zero-th order, but less suitable for higher orders with lower intensities. In contrast, *Approach 3* (similar to the first and second with a fixed background) can result in non-physical outcomes like negative net counts. Therefore, for higher orders, *Method 2* is preferred for its reliability and consistency with the results from the fit. This reduces the computational cost of taking additional fit parameters. With background levels consistently below 1% of the forward diffracted beam intensity and normalization in diffraction efficiency computation based on the total intensities of all diffracted orders, flux fluctuations—even when significantly higher than in this measurement—have minimal impact on the efficiency and error calculations.

To tackle the identified challenges, a fifth approach referred to as *Approach 5* (referred to as "Combined Bckg" in the Figures), has been elaborated. It combines background estimates from horizontal profile fits for the zero-th order, while using off-Bragg estimates for the other orders. The diffraction efficiency curves calculated using this method are compared with the *Method 2* and the background as fit parameter methods in Figure 4.11.

The comparative analysis shows a high level of agreement between the methods across all orders and angular positions. Notably, the second-orders' efficiencies from the fitting procedure exhibit some deviations that are due to allowing for negative counts, provided the error bars exceed zero. This also impacts the results for the zero-th order. Despite these deviations, first-order efficiencies display remarkable consistency across methods. *Method 2* and *Approach 5* approaches maintain this consistency despite having significantly different zero-th order background values (differing by about 90 counts at some positions). This suggests that extreme accuracy may not be critical. As long as the background estimates are within a reasonable range, the inherently high intensities of the zero-th order relax precision requirements. In order to substantiate this observation, further consideration of another sample from the same category, and which involves higher diffraction efficiencies, is required.

In the following subsection, the background estimation method (fifth approach) will be revisited using a similar sample from the same category.

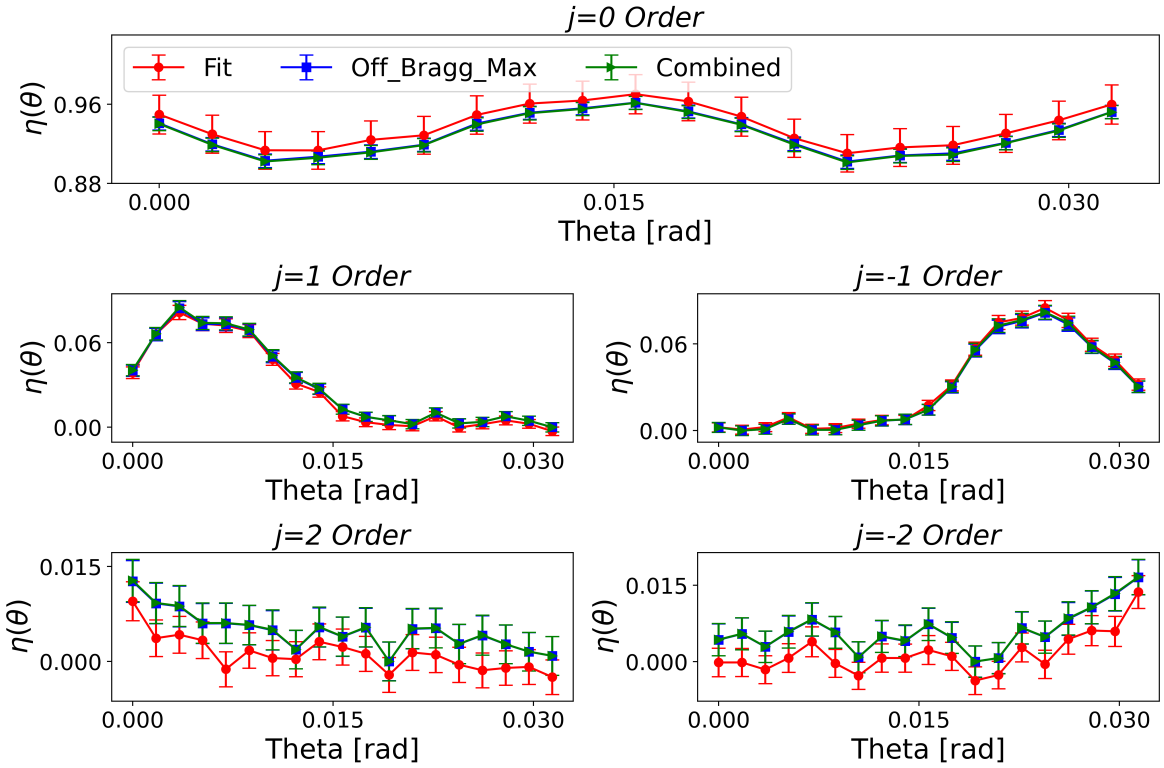

Figure 4.11: Comparison of diffraction efficiency curves for the Bayfol SM_32µm_10mW sample measurement derived using different background estimation methods: *Method 2* (blue squares),*Approach 5* (triangular markers in green), and background for first and second orders as fit parameters with fixed zero-th order background at 228 counts estimated using Gaussian fits at different angular positions (red circles).

4.3.2 Study of the background distribution for a similarly prepared sample measured in the 2023 experimental campaign

This section succinctly presents key findings from analyzing data from another Bayfol sample (SM_32µm_30mW) and contrasting them with previous results. Starting with the neutron counting, Figure 4.12 shows an unexpected increase in the flux at certain positions at the end of the measurement. These fluctuations are too large to be simply explained by Helium flux instabilities, and the origin is not yet well-understood.

Compared to the preceding sample, the average neutron count for this scan was marginally lower, influenced by a 400-second reduction in count time per step. A key focus now is to assess how these neutron flux variations affect the background estimates. The neutron counts fitting, which is based on the assumption of a stable neutron flux, is challenged by the significant flux variations observed in Figure 4.12a. Consequently, the fits were restricted to a relatively stable range of the scan, as depicted in Figure 4.12b. The fitting results are summarized as follows: the estimated neutron loss cross-section is $< \sigma_{\text{abs+inc}} >= (3.33 \pm 0.45)\,\text{cm}^{-1}$ for the Beer-Lambert fit, and $< \sigma_{\text{abs+inc}} >= (3.06 \pm 0.63)\,\text{cm}^{-1}$ for the "Beer-Lambert & displacement" fit. The displacement factor is $K = (2.3 \pm 1.8)\,\text{cm.rad}^{-1}$, indicating about 0.4 mm

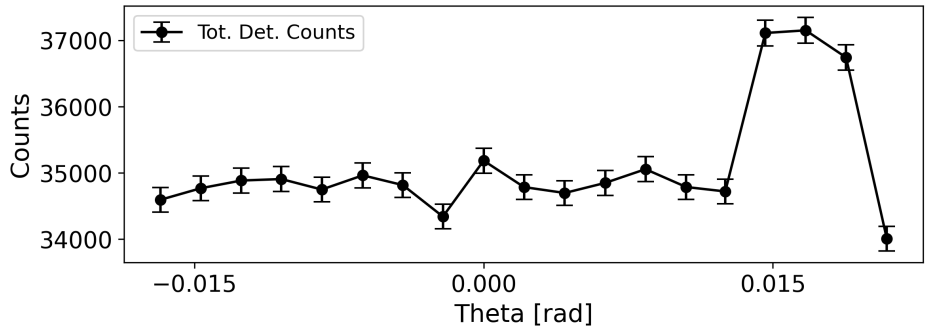

(a) Full Scan range.

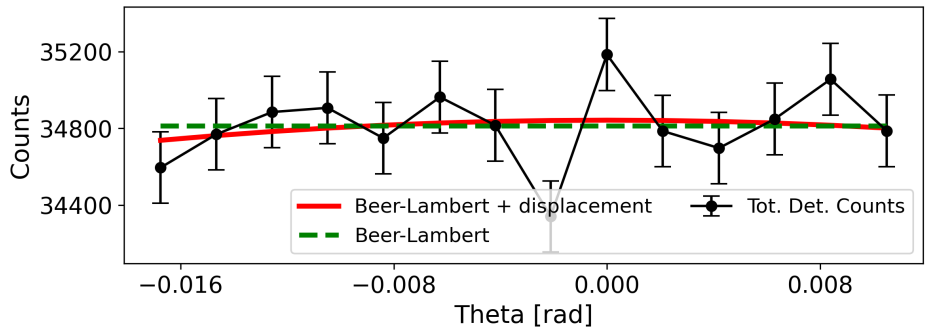

(b) Restricted Scan range with fits

Figure 4.12: Variations of the total detector counts (a) full experimental angular range (b) restricted with relatively stable flux for fitting [131].

displacement per 1° rotation. The fitting of total counts variations only offers an approximation, as even minor displacements in the sample position can affect the captured wavelength distribution and corresponding neutron counts. The displacement factor, approximately half of the previous estimate at ($K = 4.7 \pm 0.7\,\mathrm{cm.rad^{-1}}$), aligns with expectations, reflecting minor alignment variations from sample change and repositioning. The estimated neutron loss cross-section, consistent with the earlier result ($< \sigma_{\mathrm{abs+inc}} >= 3.41 \pm 0.53\,\mathrm{cm^{-1}}$), confirms the stability of the hologram's structural properties under different experimental recording conditions.

Utilizing three stacked horizontal ROIs and analyzing their profiles (as detailed in Appendix J) revealed higher background estimates at positions with increased neutron flux. The results align with previous observations regarding background variations both vertically and horizontally across the detector. Vertically, a background increase is noted when moving from the detector's bottom to the top. Horizontally, the background appears homogeneous, albeit with caution advised for this assumption. On the other hand, both background estimates derived from interpolated values or fits to signal ROI profiles seem to follow these flux variations. The assumption of a constant zero-th order background is hence less tenable, as a change of around 60 counts results in a non-negligible change net counts ($\simeq 1\%$). Moreover, the diffraction efficiency is low and the background is dominated by blank background rather than diffuse scattering. The corresponding variations did not exceed 20 counts (a change of less than 0.4% in diffraction efficiency). The Figure 4.13 compares the results from three distinct approaches: *Method 2*, applying a constant background of 160 counts for all

orders (coincidentally matching the minimum of both first orders); *Approach 5*, *Approach 4*; *Approach 1* with a mean zero-th order background of 206 counts after adding a correction term based on the assumption that background scales with the number of counts. Applying a *rough* empirical correction factor of approximately 1.2% of the raw counts (a deliberately chosen value), lead to a relatively higher estimate for the zero-th order, given its substantial count rate, despite the interpolated values originally suggesting lower background estimates due to its smaller ROI. The comparison exhibits high congruence among methods, with only minor deviations in *Approach 1*, again, due to occasional non-physical negative net counts at low S/N regions. Negative counts are obtained irrespective of the application of this "rough" empirical correction factor, which predominantly affects the background in the forward diffracted beam and high-efficiency diffraction orders around Bragg. These occurrences are attributed to neutron count fluctuations combined with the limited scope of the small ROIs encompassing the diffraction spots, inadequately representing the overall background.

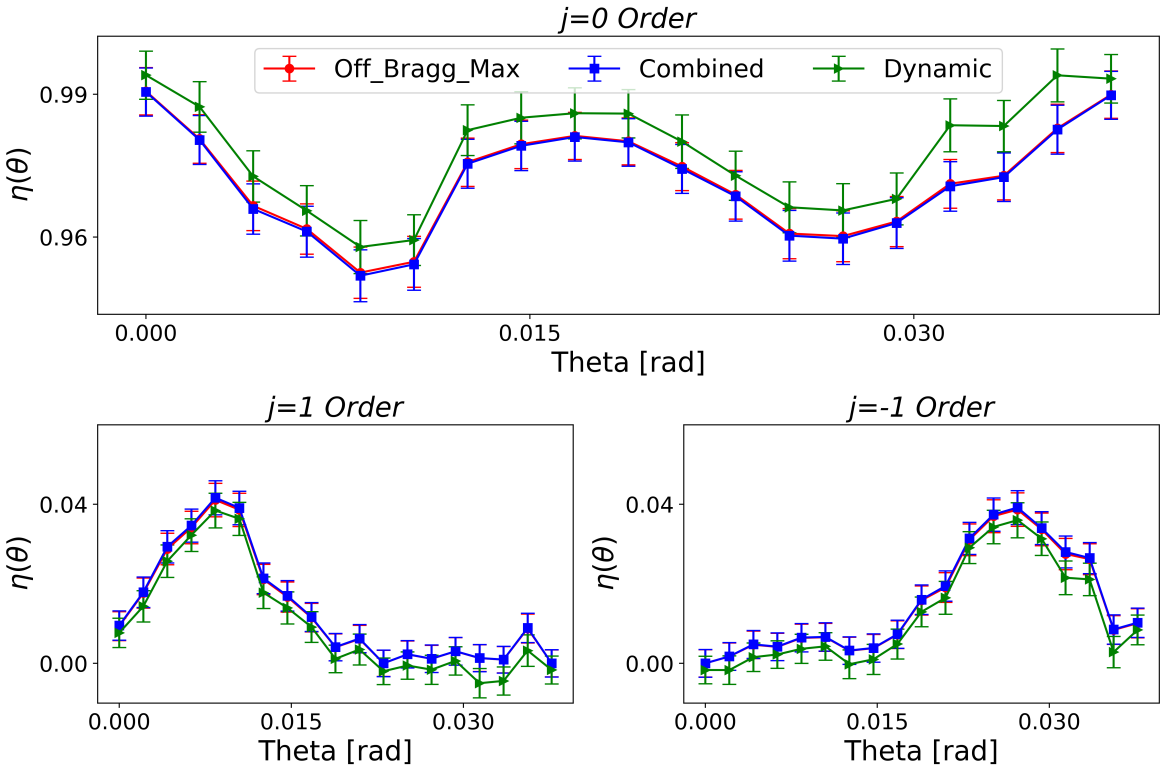

Figure 4.13: Comparison of diffraction efficiencies obtained by *Approach 1* (in green), *Method 2* (in red) and *Approach 5* (in blue) methods for the sample SM_32µm_30mW [131].

The analysis of the considered sample, with its relatively low diffraction efficiency of approximately 4%, revealed that the effects of unstable neutron flux were modest. This is largely attributed to the normalization in the efficiency calculations, which mitigates flux variation effects provided the background levels remain relatively stable for all diffracted orders. However, this observation underscores the necessity of examining samples with higher diffraction efficiencies, where changes in neutron flux could significantly impact the background and, consequently, the efficiency calculations.

Shifting focus to a different class of materials, a comparative analysis is now con-

ducted on a Nanodiamond-Polymer Composite (NDPC) grating, which exhibits the highest measured diffraction efficiency at zero tilt among all samples. This analysis aims to assess the applicability of the established technique in a high diffraction efficiency context.

4.3.3 Data Reduction and Background Analysis for the 2023 measurement of the NDPC grating-5 sample

In this analysis, the NDPC sample labelled as grating-5 (see subsection 3.1.2) is considered. Unlike commercial Bayfol foils, the NDPC gratings were custom made with unique properties, allowing to reach the highest possible diffraction efficiency. This applicability of methods will be evaluated for a higher S/N ratio scenario.

Before data reduction and fitting, it is only possible to have a rough estimation of the average wavelength. A first-order Bragg peak were obtained at a rotation motor position of (64.42±0.02) degrees, with the zero incidence position at (64.75±0.02) degrees. This yields a Bragg angle of (0.34±0.04) degrees. An average wavelength λ_{mean} between 5.3 nm and 6.7 nm, approximately equal to 5.9 nm is deduced. The examination of the total neutron counts during the "Nd012213" sample measurement, reveals higher instability with two major peaks in neutron flux, compared to the single peak observed in the previous sample analysis in sub-subsection 4.3.2. This experimental campaign [131] was primarily dedicated for exploring the parameter space of Bayfol samples, and not for NDPC gratings. A quick measurement with a short time step of only 2500 seconds was used. Notable flux fluctuations are observed, preventing the estimation of the loss cross section from this measurement. The loss cross section for nanodiamonds is known to be minimal. Any losses would likely stem from incoherent scattering from hydrogen in the Photopolymer or from other constituents of the NDPC grating.

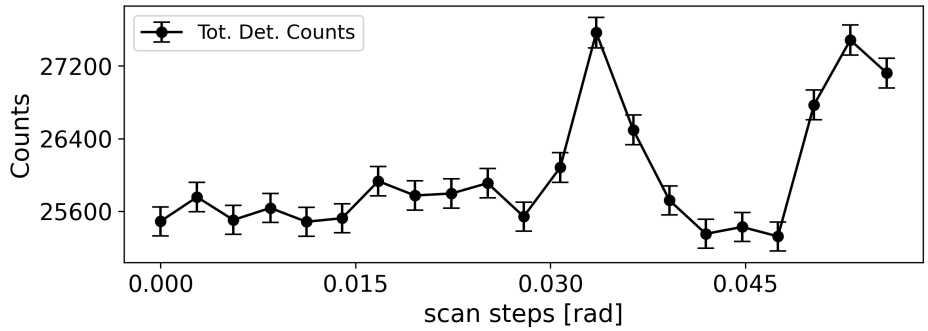

Figure 4.14: Total neutron counts variation during the measurement of ND012213 sample [131].

The Calculation of the diffraction efficiency demonstrates consistent alignment among the background estimation methods shown in Figure 4.15. This is particularly notable for first orders near and around Bragg peaks. *Approach 1* occasionally registers non-physical negative efficiencies, which undermines its reliability, though it generally conforms with other methods at most data points. Intriguingly, the zero-th order background, calculated either through weighted individual mean values or an unweighted average of the *Approach 1* estimates, yields comparable results of (111.2 ± 10.5) counts and 111.0 counts, respectively. This consistency, maintained despite a non-negligible

neutron flux oscillation of around 2000 counts (equivalent to 7% of the maximum total detector counts value), underscores the minimal influence of such variations on the analysis. For the *Method 2* and *Approach 4* methods, the zero-th order background estimates are (145 ± 12) counts and oscillating estimates around a mean value of (134.3 ± 11.6) counts, respectively. Further consistency extends to second-order calculations, though the 'Profile Fitting' method shows slight deviations. These deviations become even more pronounced at third orders, echoing the previously noted limitations of methods that directly extract net counts based on fits or predefined thresholds at low S/N ratios.

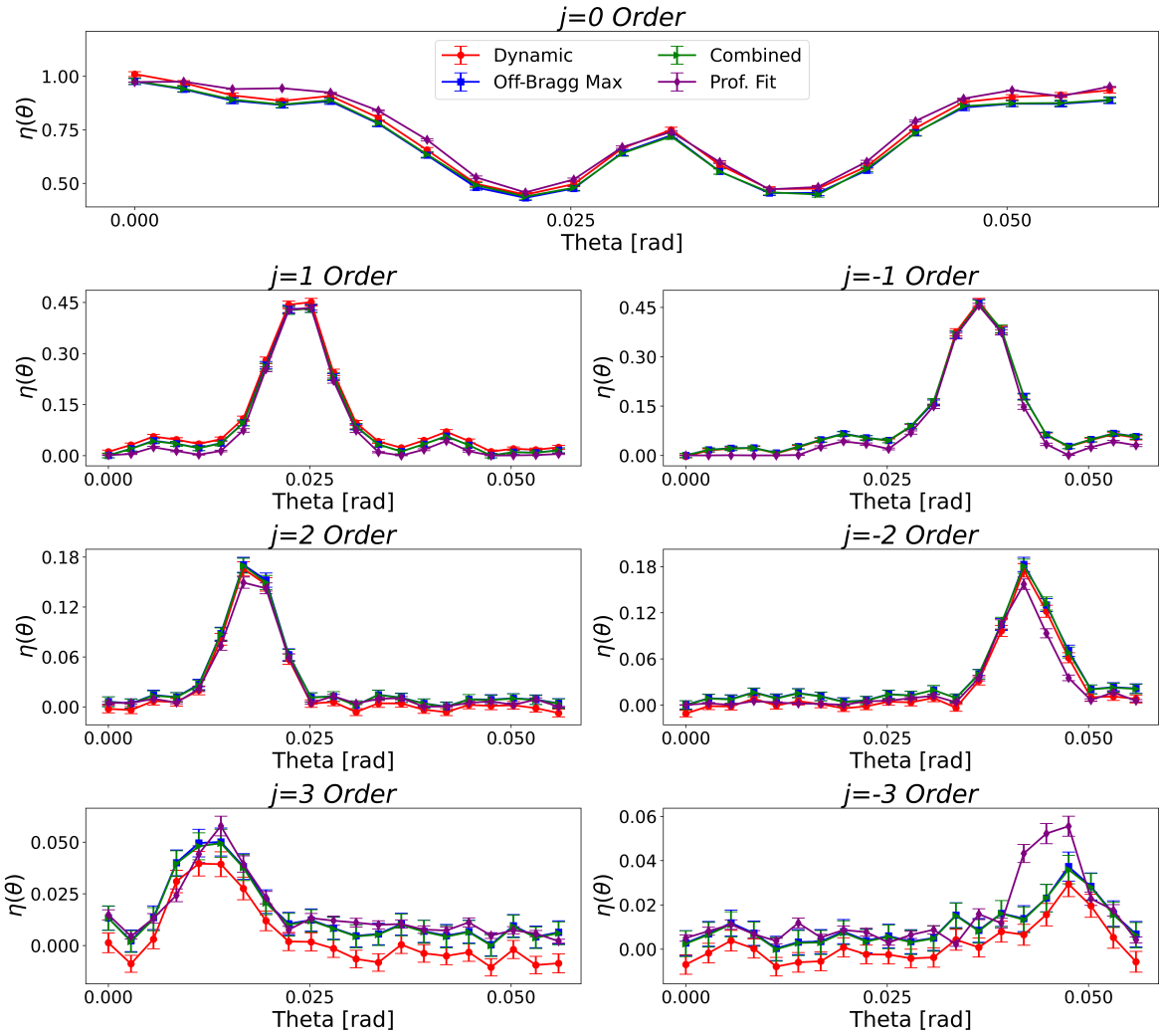

Figure 4.15: Comparison of diffraction efficiencies using *Approach 1* (red circles), *Method 2* (blue squares), *Approach 4* (diamond markers in purple), and *Approach 5* (green triangles) for the 2023 measurement of the NDPC grating-5 sample [131].

In order to further evaluate *Approach 5*, Figure 4.16 compares efficiency curves derived from this method against those obtained from an RCWA fit (Exact formulation without any approximations). The fit employs raw count data extracted line by line from detector pixels at each angular position, a fixed zero-th order background at 134 counts based on horizontal profile fits, with other background values as fitting parameters. In this figure, blue symbols indicate efficiency after the fit, red lines

show the RCWA fit, and green symbols denote data obtained using fixed ROIs for raw counts extraction and *Approach 5* method for background estimation. For clarity, triangular symbols were used to represent negative index orders. Clearly, comparing the background estimates is impractical due to differing ROIs. Comparing the derived efficiency curves presents a significant measure of congruence. Despite the different methods used for raw counts extraction and for background estimation, the congruence is impressive. This is consistent when considering a similar comparison that has been made for the NDPC grating-1 sample measurement performed before the instrument modernization. Therefore, the robustness of the method is validated to be used for the rest of samples data.

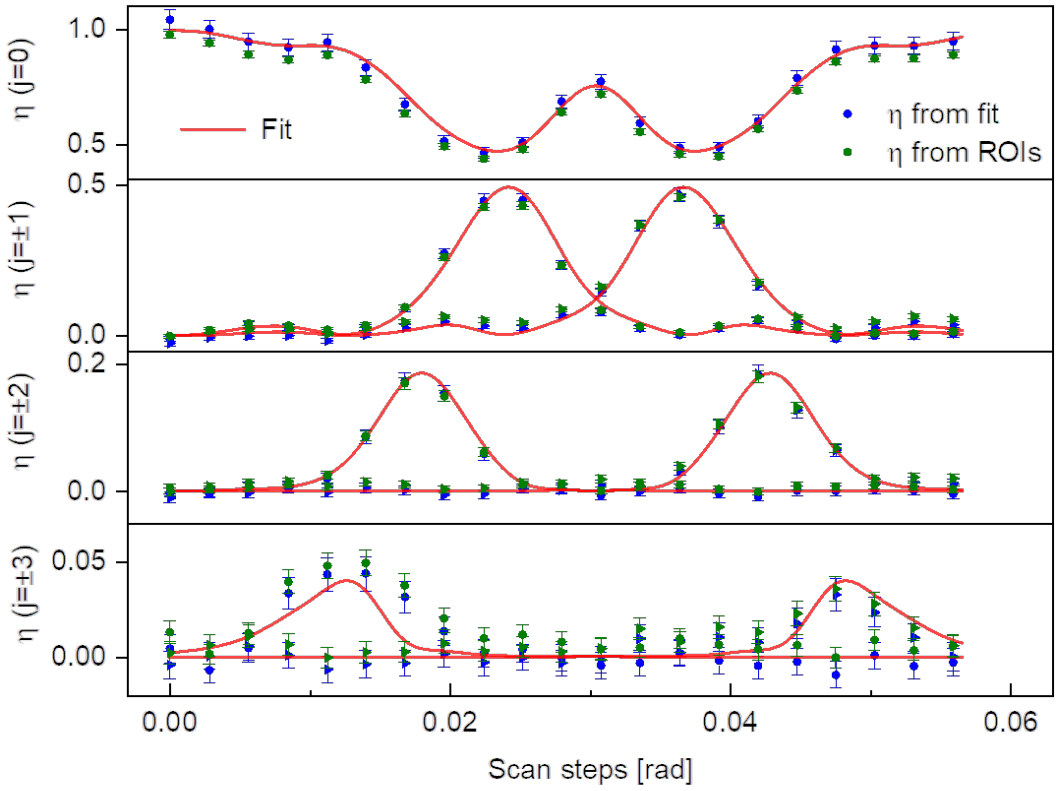

Figure 4.16: Comparison of NDPC grating-5 diffraction efficiency curves from an RCWA fit (raw data line by line extraction with variable backgrounds, zero-th order fixed) versus efficiencies using fixed shape ROIs and *Approach 5* for background estimation (green markers)[131].

In summary, the study demonstrates that minor inaccuracies in zero-th order background estimation minimally impact the integrity of subsequent diffraction efficiency evaluations. The comparative review confirms the efficacy of employing the elaborated *Approach 5* method paired with fixed shape ROIs for the data extraction. This approach, refined for the upgraded experimental setup, will now be assessed for its applicability to earlier collected data in the next chapter.

4.4 Pre-upgrade data reduction and background analysis at PF2/VCN

Following the validation of the background estimation method, the investigation is extended to include data collected before the PF2 instrument modernization. This analysis examines the approach's consistency. The exploration of the modernization effects on the background estimates is presented in Appendix F. The examination of background distribution across the detector from the 2021 measurements showed consistent results with prior observations, which validated the continued use of the existing data reduction approach.

Before modernization, Data was collected using a custom LabVIEW interface. Individual data files are generated for each scan position. These files included measurement details and pixel-wise detector counts. The analysis began with reviewing these files to examine flux variations, culminating in the creation of a comprehensive data file for the entire measurement set. Analysis of total detector counts revealed random fluctuations ranging between 1-5% (error bars included) around a mean value. Due to the variability and pattern of these fluctuations, determining the loss cross section by fitting was feasible for few samples only.

The developed data extraction and background analysis procedures (codes) handle the data in a similar fashion to the Nexus files generated by NOMAD. Utilizing the aggregated detector images and their corresponding horizontal profiles, diffraction peaks were pinpointed using the `find_peaks` function from the `scipy.signal` library, as illustrated in Figure 4.17.

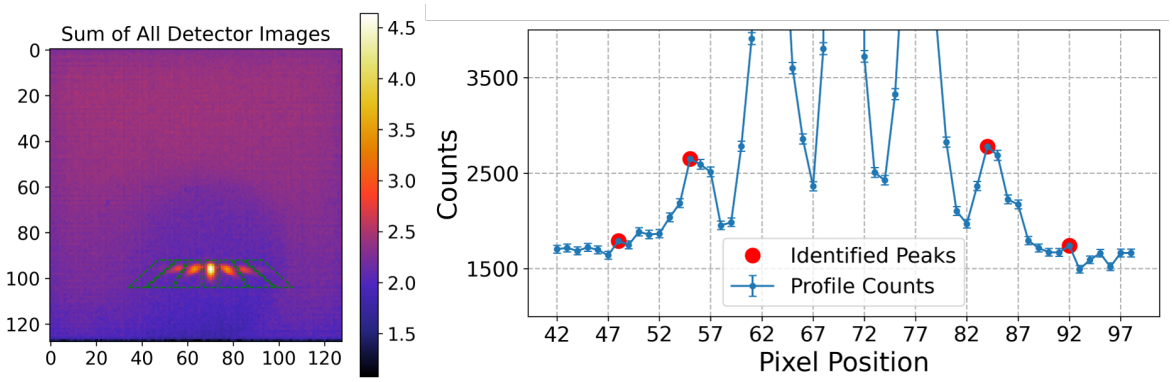

Figure 4.17: Identification of diffraction peaks and ROI selection using the summed detector images, shown for grating-5 at $\zeta = 0°$ measurement.

Subsequently, these positions are used in fitting the individual horizontal profiles as depicted in Figure 4.18.

The net counts obtained from the Gaussian components were compared with those derived using *Approach 5*. The two methods consistently validate each other, showing strong agreement, particularly for high-efficiency orders. Therefore, *Approach 5* has been consistently applied to all samples measured during this experimental campaign.

The robustness of this method permits the evaluation of its transferability to data from different instruments, such as SANS-I instrument at the Paul Scherrer Institute in the subsequent section.

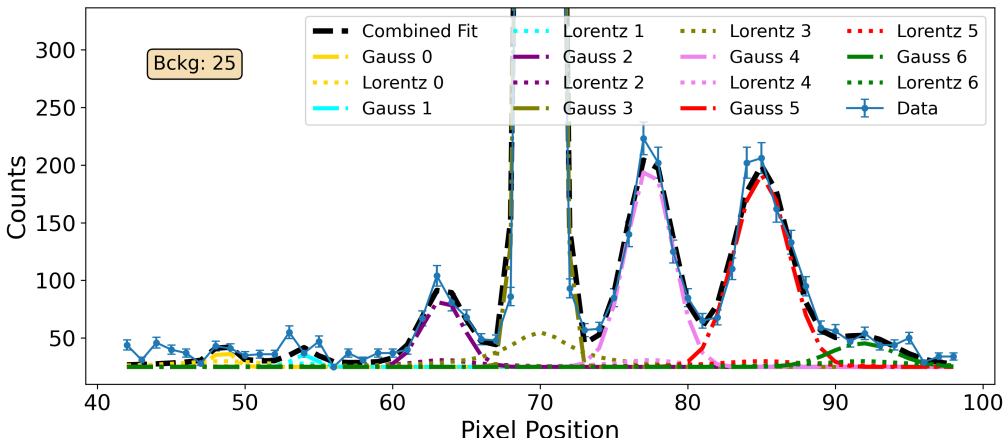

(a) Example of horizontal profile fitting.

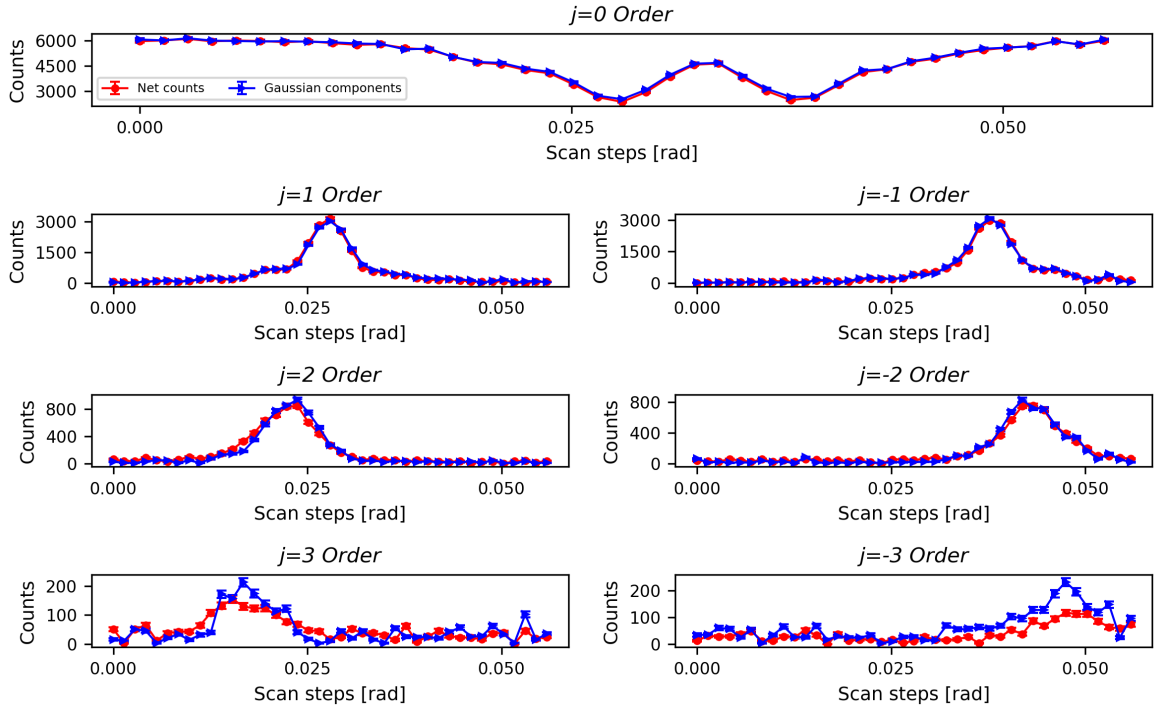

(b) Comparison of estimated net counts.

Figure 4.18: (a) Fitting the horizontal profile using a sum of Gaussian and Lorentzian functions for multiple peaks atop a constant background, here shown for the 15-th angular position of NDPC grating-5 at $\zeta = 0°$. (b) Comparison of net counts determined using *Approach 4* (in blue) and background subtraction using *Approach 5* (in red).

4.5 Data Reduction and background analysis at the SANS-I instrument, SINQ, PSI

This section details the data reduction process for samples measured the SANS-I instrument, using the experimental arrangements outlined in subsection 3.2.4. The back-

ground analysis is conducted in order to accurately derive the diffraction efficiencies and their associated errors. Initially, the case of a low-efficiency measurement from the HBP dispersed holographic grating (see subsection 3.1.4) is considered. The elaborated data reduction procedure will be next applied to the high-efficiency NDPC samples for refinement and comparison.

4.5.1 Data reduction procedure for the HBP based NPC sample measured at SANS-I

The SANS-I instrument and its experimental parameters, are defined and included within Grasp software [147]. The collected data files encapsulate all requisite information for retrieval upon import. This allows for streamlining the process of data extraction and enabling preliminary analysis with GRASP's comprehensive suite of analytical tools.

In contrast to the continuous flux from continuous reactors, spallation sources frequently undergo cycles of deactivation and reactivation during measurements. As a result, rather than employing a single and extended neutron counting interval at each angular position, a series of brief measurement runs are conducted in rounds at each position. Each round covers the entire angular range of the rocking curve. This methodology mitigates the risk associated with beam interruptions. If the beam is off, it only affects a single or a couple of runs rather than compromising an entire measurement. However, this practice renders *direct* background analyses akin to those performed for PF2 instrument data, which rely on detector images at various angular positions, unfeasible. This is primarily due to the reduced counts in each generated data file (run), which from a statistical standpoint, are insufficient for a robust analysis. Therefore, detector images from runs taken at identical angular positions are aggregated, thereby creating a singular composite image for each position. This approach allows for the accumulation of individual runs, enhancing the statistical robustness of the data. Such a methodology enables us to conduct background analyses analogous to those performed on PF2 data, where direct comparisons and inferences can be made with a higher degree of confidence.

To address the challenges presented by the sporadic flux from spallation sources, the reduction process is initiated by examining each run to assess flux stability. The calculation of the diffraction efficiency is inherently unaffected by flux variations as long as enough statistics are allowed, though, understanding these variations is still essential for estimating the macroscopic loss cross-section. The methodology, applied in the analysis of the HBP-based NPC sample, begins with an assessment of the flux stability across eight measurement rounds. Minor variations are observed in the duration of runs, resulting in an accumulated duration per angular position ranging from 2506 s to 2546 s. The total flux variations depicted in Figure 4.19 show fluctuations of $\pm 3.1\%$ around a mean value of 20,460 counts per angular position. By comparing the total flux variations with the counts per second, it is inferred that these variations are not due to differences in accumulated time per position but rather stem from the source itself.

The experimental configuration, with a $9 \times 18\text{mm}^2$ aperture at the collimation tube's end and a 4 mm circular aperture directly atop the fully exposed sample, guarantees that flux stability is unaffected by aspects such as the beam-sample intersection area.

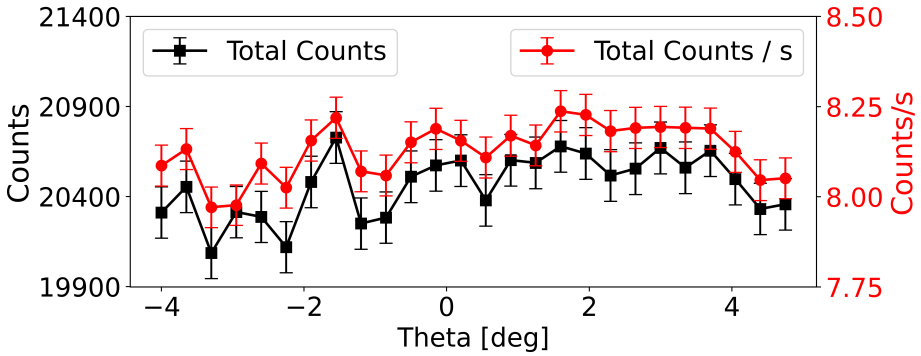

Figure 4.19: Variation of the accumulated detector counts per position and the total counts per second for the HBP based NPC sample measurement.

Consequently, observed flux variations are ascribed to source variability and statistical limitations rather than to the experimental setup. These variations, along with the sample's minimal thickness variation (approximately 12.5 µm), which scarcely affects transmission upon rotation, hinder the application of a Beer-Lambert fit for determining the loss cross-section.

Following a procedure analogous to the analysis of PF2 data, three vertical and two horizontal ROIs, each measuring 14×128 pixels, were delineated. Figure 4.20 displays the aggregated counts for each ROI per angular position, revealing that the signal ROI accounts for approximately 77% of the total detector counts (transmitted beam), while a significant fraction ($\approx$ 23% of neutrons) is dispersed randomly across the detector surface.

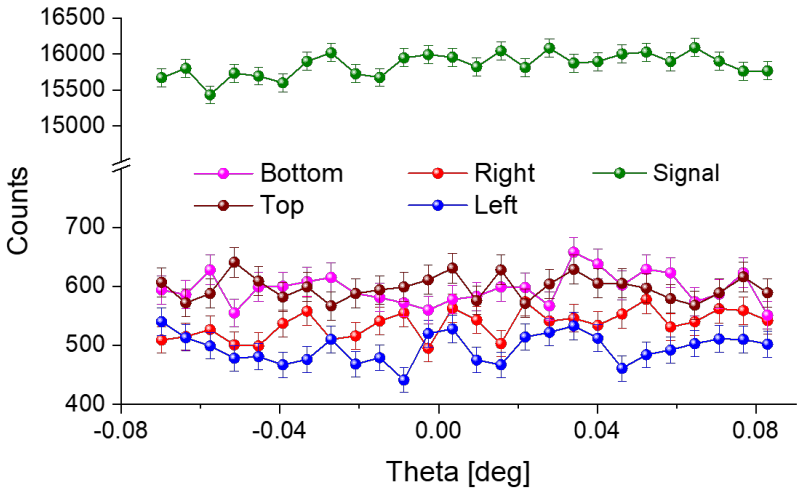

Figure 4.20: Counts variation extracted from vertical and horizontal ROIs for blank background estimation.

The analysis reveals that both the top and bottom ROIs capture nearly identical flux shares, about 2.9% each, demonstrating a vertical homogeneity in background distribution. In a similar vein, the left and right ROIs present closely matched flux contributions, around 2.4% and 2.6% respectively. This pattern is expected and is linked to

the relatively increased vertical divergence of the beam from the $9 \times 18\text{mm}^2$ aperture at the collimation tube's exit. Such a pattern lends support to the adoption of *Method 2*, enabling a background estimation directly from counts within a specified ROI. Notably, the blank background ranges between 0.25 and 0.37 counts per pixel, a markedly low figure compared to the estimates above 1.6 counts observed at PF2 for an equivalent counting duration. The upper limit of 0.37 counts per pixel will be used as a threshold for distinguishing signal from background noise.

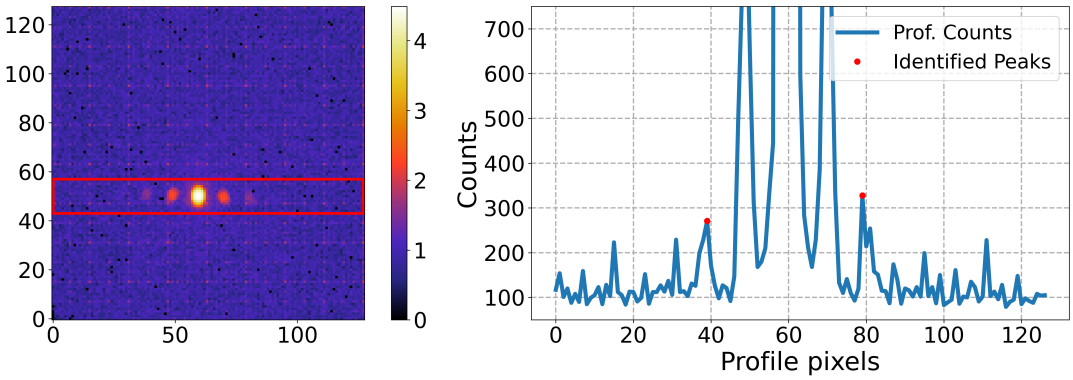

Figure 4.21: Diffraction peak identification for the HBP organic nanoparticles NPC sample, based on the aggregate sum of images across 26 angular positions and the horizontal profile for a ROI width of 14 pixels. Red markers indicate detected peaks.

For the identification of diffraction orders, a methodology akin to that outlined in the previous section (see Figure 4.21) was employed. Considering a 14 pixels width horizontal profile from the summed image of all 26 angular positions and utilizing the `find_peaks` function from the `scipy.signal` package, peaks were filtered and only those meeting the following criteria were left: 1) minimum peak separation of 5 pixels to make sure the code does not consider side lobe maxima as separate peaks 2) peak height exceeding a first threshold of 145 counts for at least one pixel or surpassing a secondary threshold of $0.37 \times 14 \times 26 = 136$ counts for two consecutive pixels 3) peak width of at least three pixels. The analysis identified 5 diffraction orders. While other intensity oscillations assimilating peaks are observed, they do not meet the criteria of having a width larger than two pixels, and are considered as artifacts. Only five orders are visibly distinct, and only these peaks meet the prescribed criteria. The identified peaks, positioned at [39, 49, 60, 70, 79] have corresponding heights of [271, 1027, 120780, 948, 328]. The near-mirror symmetry of the $j = \pm m$ diffraction peaks relative to the forward diffracted order's position support the accuracy of the identification process. However, the noted asymmetry in peak heights is not very significant and could be attributed to differences in the accumulated background at the corresponding ROIs. It arises from a small rotation of the grating vector around the beam axis during the alignment of the sample. Subsequent analysis involved fitting the horizontal profiles using the identified peak positions and heights, as depicted in Figure 4.22.

In the following subsection, the focus is pivoted from examining a low-efficiency sample to analyzing the high-efficiency NDPC samples measured using almost the same setup.

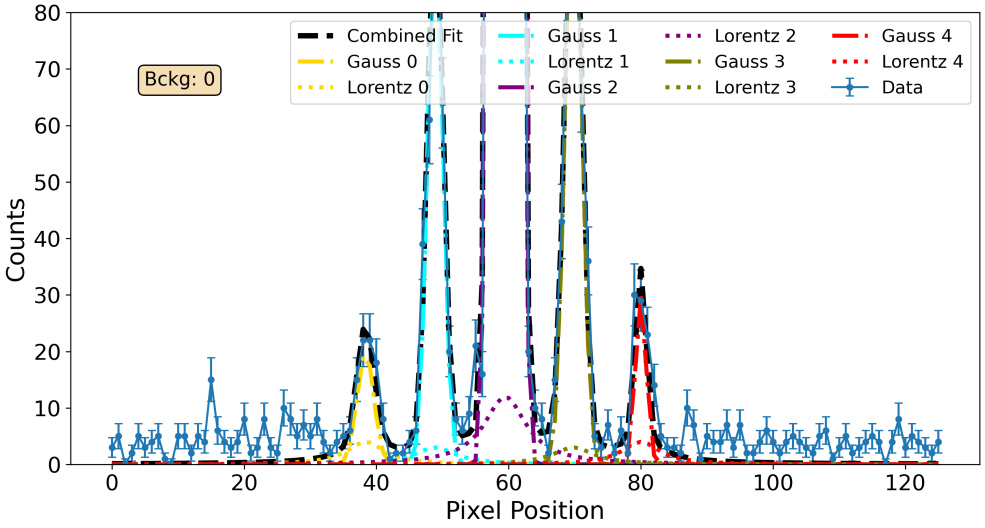

Figure 4.22: Example fit of the horizontal profile using a sum of Gaussian and Lorentzian functions for multiple peaks atop a constant background. This fit corresponds to the 11-th angular position of the HBP sample measurement.

4.5.2 Data reduction and background analysis of the NDPC measurements carried out at SANS-I

For this segment of the study, the focus is initially on the NDPC grating-5 sample, measured during the same experimental campaign but with a single difference in the setup: the size of the first aperture s_1 was adjusted to 10 mm, in contrast to the 30 mm used for the HBP-based NPC sample. An initial review of the data revealed that seven full measurement rounds were executed, resulting in a total duration per angular position ranging from 2595 to 2232 seconds. Analysis of the total flux and counts per second, illustrated in Figure 4.23, indicates that variations in both metrics are closely aligned, supporting the assumption that flux variations are predominantly due to the source, rather than slight discrepancies in accumulated count times. The total flux variations for the NDPC sample were maintained below ±3% around an average value per angular position of 9556 counts. This mean value is notably less than half that observed in the HBP sample, attributed to: 1) a beam divergence of 0.4 mrad for this measurement, compared to 0.9 mrad for the previous sample 2) this measurement counts 1 round less. Similarly, the statistics and the observed pattern that is mainly modulated by fluctuations from the source rather than from variations in the effective sample thickness preclude the possibility to infer an estimate of the sample's loss cross-section.

Subsequently, vertical and horizontal ROIs were defined to determine the maximum background noise level, thereby setting a threshold for diffraction order identification. The background was determined to be below 0.32 counts per pixel. Adapting the criteria from the prior analysis, the thresholds were adjusted to 120 counts for the primary and 114 counts for the secondary. Peaks identified at positions [39, 49, 59, 70, 81, 87, 95] with respective heights [200, 297, 2586, 62058, 2517, 316, 142] indicate the stimulation of 7 diffracted orders. These positions mirror those found in the HBP

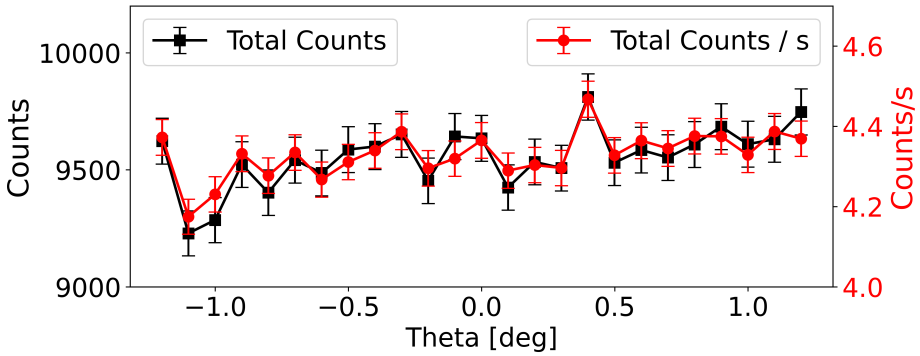

Figure 4.23: Variation of the accumulated detector counts per position and the total counts per second for the NDPC grating-5 measurement.

sample, aligning with expectations due to the identical grating period of 500 nm for both samples. The positions were utilized to fit horizontal profiles.

For NDPC grating-1, a series of 14 rounds of measurements were carried out across all angular positions, except the final position, which was subjected to one round less. A notable variation in total duration per position (ranging from 2922 s to 4316 s) was observed. However, this was offset by a corresponding variability in total counts per second, resulting in a less significant impact on the accumulated total counts, as illustrated in Figure 4.24. Estimating the loss cross-section remains infeasible. Nevertheless, the statistics remain robust, even at the last position, which recorded over 28,000 counts—nearly triple the average total counts of the grating-5 sample for context. Yet, a 4000-count disparity between the maximum and minimum undermines the utility of *Method 2*. The examination of aggregated detector images from the two final positions did not reveal any significant diffraction signal. Consequently, to proceed with data reduction, the angular range was narrowed by excluding these two positions from further consideration. The background was determined to be below 0.41 counts per pixel. Following the established methodology, the thresholds were updated to 190 counts for the primary criterion and 171 counts for the secondary, applied across the aggregation of 32 detector images (each representing an angular position before the exclusion of two last ones) with a ROI width of 13 pixels. This adjustment allowed the identification of 7 diffraction orders.

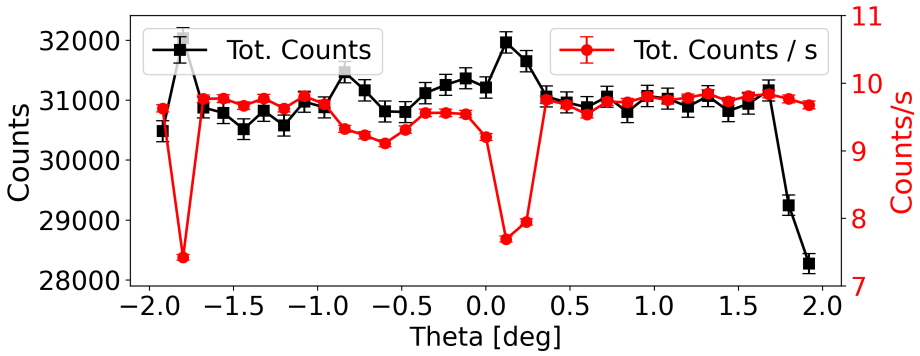

Figure 4.24: Fluctuations in accumulated detector counts per position and total counts per second for the NDPC grating-1 sample at SANS-I.

In conclusion, this chapter systematically presented the methodology for data reduction and background analysis, leading to the identification of diffraction orders and the derivation of their efficiencies and corresponding errors. Key experimental observations were highlighted, including variations in total detector counts to approximate the loss cross-section and the analysis of background levels for an accurate signal-noise separation. On the other hand, the initial comparison of background estimation techniques underscored the need for a meticulous approach to derive diffraction efficiency and for error estimation. By applying tailored methodologies and adjusting thresholds according to the specifics of each measurement, the challenges posed by statistical limitations were addressed. The observed differences in off-Bragg background estimates among different orders have been linked to off-specular scattering differences at varying length scales. *Approach 5* has also enabled an accurate estimation of the zero-th order background. This strategy significantly relaxes the computational load in subsequent analyses by empirically determining background parameters, reducing both ambiguity and the duration of the fits. It underscores the critical importance of a thorough analysis tailored to each instrument, setup, and sample measurement. Such preparatory work lays the ground for the insights to be discussed in subsequent chapters.

Chapter 5

Results and discussion

In this chapter, the main findings of this research are discussed, with an in-depth analysis of both the theoretical models and the experimental data obtained throughout the studies.

5.1 Comparative analysis of theoretical models for light and neutron diffraction from holographic gratings

In this section, a comparative analysis of key theoretical models used to describe light and neutron diffraction from phase holographic gratings is undertaken. This involves both single and multilayer gratings. First, a comparison between approximate variants grounded in the K-vector closure method (KVCM) and the Beta value method (BVM) will be performed. While these models have already been explored in previous works, a different statistical framework for their comparison is introduced, leveraging Bayesian inference techniques. To the best of our knowledge, the application of Markov Chain Monte Carlo (MCMC) and Bayesian Model Selection (BMS) techniques to diffraction data from holographic gratings has not been previously reported. Additionally, their potential limitations will be discussed. Next, a multi-wave coupling model for multilayer volume holographic gratings (MVHGs) tailored for neutrons will be presented.

5.1.1 Bayesian inference techniques for statistical comparison of theoretical models: KVCM vs. BVM

For simplicity, only the case of two coupled waves is considered. Kogelnik's model, based on the KVCM boundary conditions [75], is compared with the BVM-based two-coupled waves (2-CW) model [52, 56, 93]. For this purpose, a comprehensive MCMC sampling procedure has been employed, along with BMS for statistical evaluation. These methods not only allow for a broader understanding of the estimated parameters but also provide a robust statistical framework for assessing the performance of each theoretical model.

Standard fitting procedures

Standard fitting procedures in Python typically rely on optimization algorithms found in modules such as `scipy.optimize`, `lmfit`, or `easyscience`. These include methods like least squares minimization, the Levenberg–Marquardt algorithm (LMA), the Nelder–Mead minimization method, and the Trust Region Reflective (TRF) approach, among others. While the influence of different modules or minimization methods was explored for both neutron and light diffraction data, it was not included in this study. The differences in the retrieved fitting parameters across these methods were found to be negligible.

In the most common case, least squares minimization, the objective is to minimize the sum of squared residuals, defined as:

$$\mathrm{SSR}(\mathbf{p}) = \sum_{i=1}^{N} \left(\frac{\eta_i - f(\theta_i; \mathbf{p})}{\Delta\eta_i} \right)^2$$

where η_i represents the observed diffraction efficiency data points, $f(\theta_i; \mathbf{p})$ is the model prediction at diffraction angle θ_i given the parameter vector $\mathbf{p}$, and $\Delta\eta_i$ is the associated error. The goal is to find the parameter set $\mathbf{p}$ that minimizes $\mathrm{SSR}(\mathbf{p})$, which represents the sum of the squared, weighted residuals between the model and the data. This method assumes a unique "best" solution for the parameters. It lacks the ability to explore the range of parameter values and in quantifying confidence (or credible) intervals. This may be particularly interesting when dealing with noisy data or large measurement uncertainties, which applies to neutron scattering data. However, for light data, errors are very small and often considered negligible. In this study, only a proof-of-concept application of Bayesian inference methods to the studied diffraction data from holographic gratings is provided. Therefore, for simplicity and to remain focused on comparing the studied KVCM and BVM theoretical models, only light diffraction data will be considered.

Standard fitting procedures were applied to light diffraction data collected from a commercial Bayfol foil holographic grating (sample JK_pp50_61) at a readout wavelength $\lambda_l = 543.5\,\mathrm{nm}$. This sample was deliberately chosen as it involves a very high refractive index modulation amplitude, four times larger than what has been considered as a high value in Ref. [162], and a comparable thickness. As depicted in Figure 5.1, the following three models were used for fitting: 1) Kogelnik's model (see Section 2.2) 2) BVM-based 2-CW analysis (see Section 2.5) with the thickness d_l and the first-order refractive index modulation amplitude Δn_1 as free parameters 3) Same as 2) + a refractive index modulation profile with an attenuation length L as a free parameter.

The observations are in good agreement with what has been reported in Ref. [90] for small modulation, and in Ref. [162] for high modulation. This extends the validity of their findings to even higher amplitudes. In particular, a good congruence is observed between the fits using the KVCM based and BVM models (excluding side lobe minima) at and around Bragg's angle, while off-Bragg, the superiority of the BVM model is evident. This is also supported by simulations. Predicted oscillation periods (distance between successive side lobe minima) were calculated from by simulating each model's predictions over a wide angular range (about $\pm 0.5\,\mathrm{radians}$ around Bragg's angle), as depicted in Figure 5.2. The x-axis represents the internal θ position, the y-axis is set at

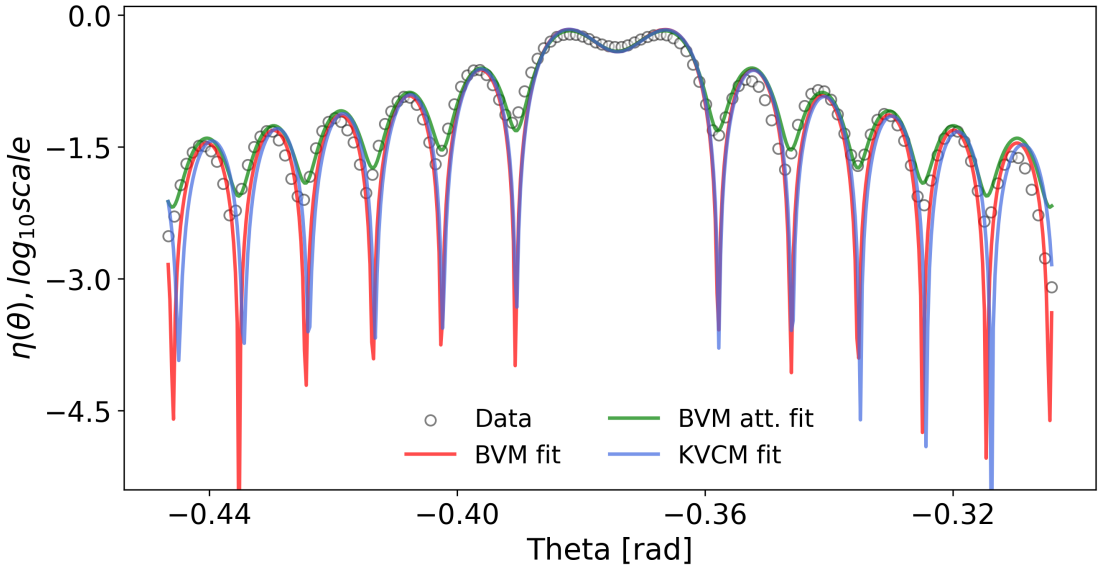

Figure 5.1: Light diffraction data and corresponding best match using least squares standard fits with three models: 1) KVCM-based Kogelnik model with two free parameters (in blue) 2) BVM-based 2-CW model with two free parameters (in red) 3) BVM-based 2-CW model with three free parameters (in green).

zero at Bragg's peak and represents the number of periods (positive or negative steps) from that position, while the z-axis represents the oscillation period. It can be seen that Kogelnik's symmetric predictions diverge further and further as one moves away from Bragg angle, despite the perfect match at its position. The oscillation period at Bragg angle corresponds to two merged oscillation periods in one broad peak. Despite the failure of the Kogelnik's theory far-off-Bragg, the Figure is a visual demonstration of the reliability of Equation 2.20 in grating thickness determination, as the oscillation period converges to $(\Lambda/d) = 0.016$.

Looking back at the fits to the diffraction data, a single set of optimal parameters has been retrieved for each model. The results are presented in Table 5.1.

Model	**Thickness [µm]**	$\Delta n_1(z=0) \times 10^{-3}$	**att. length L [µm]**	$\langle \Delta n_1 \rangle \times 10^{-3}$
Kogelnik	48.1 ± 0.2	12.8 ± 0.1	N.A	12.8 ± 0.1
BVM no att.	48.1 ± 0.2	12.8 ± 0.1	N.A	12.8 ± 0.1
BVM with att.	48.0 ± 0.1	19.5 ± 0.5	52.3 ± 3.2	12.8 ± 1.3

Table 5.1: Fitting parameters obtained from standard fits for different models.

Using the refractive index modulation at $z = 0$ and the attenuation length from the third model, it is possible to calculate the thickness averaged modulation $< \Delta n_1 > \times 10^{-3} = 12.8 \pm 1.3$. These results indicate full equivalence between the three models in terms of amplitude predictions, which has already been demonstrated in other studies and highlighted in Ref. [91]. The aim of this comparison using standard fits, is re-evaluated previously reported findings in literature for the case of the studied samples which are highly modulated. In addition, it is important to find good initial values for the subsequent application of Bayesian Statistical methods, particularly for MCMC sampling where the accuracy of the prior knowledge is essential [163, 164].

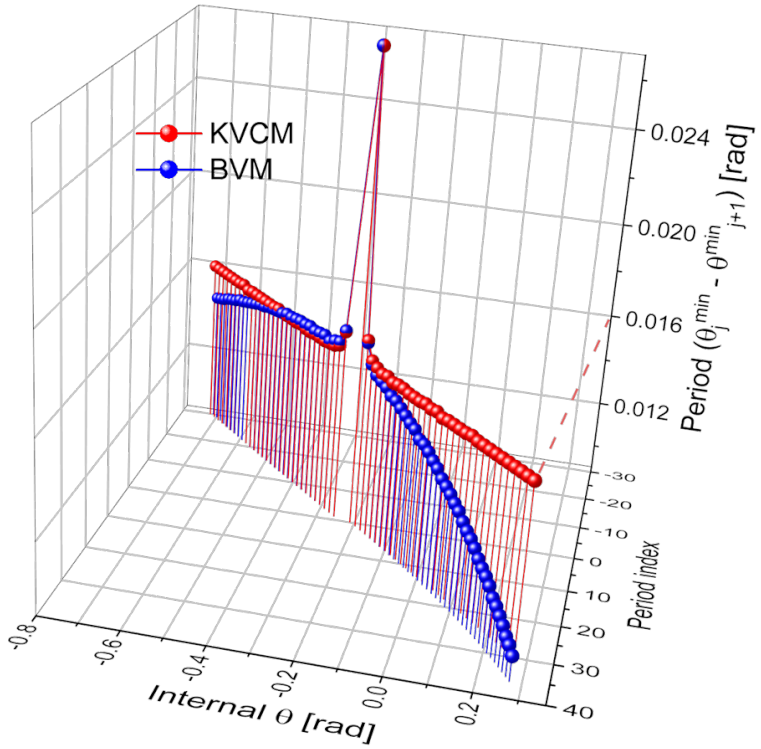

Figure 5.2: KVCM method vs. BVM oscillation periods taken at ±0.5 radians around Bragg's angle (internal angles) from theoretical predictions of two-coupled waves light diffraction. The parameters used for the simulation are the following: $\lambda_l = 543.5\,\text{nm}$, $d_l = 50\,\mu\text{m}$, $\Delta n_1 = 0.005$, $\Lambda = 800\,\text{nm}$.

Markov Chain Monte Carlo (MCMC) Overview

In contrast to standard fitting methods, MCMC sampling techniques allow for thorough exploration of the full posterior probability distribution of model parameters [163–165]. This posterior distribution is defined as the product of the likelihood and the prior probabilities, divided by the evidence term. Before defining and exploring each of these distributions in the subsequent paragraphs, it is important to highlight that for MCMC sampling, the evidence term is always ignored.

The likelihood function describes the probability of observing the data for a given the set of parameters. A multivariate normal (MVN) distribution is used to model the likelihood, with the mean vector corresponding to the observed diffraction efficiency data η, and the diagonal covariance matrix representing the squared errors $\Delta\eta$. The log-likelihood function is:

$$\log \mathcal{L}(\mathbf{p}) = \log \mathcal{N}\Big(\eta \mid f(\theta;\mathbf{p}), \text{diag}(\Delta\eta^2)\Big), \tag{5.1}$$

where $\mathcal{L}$ denotes the likelihood function, and $\mathcal{N}$ represents the normal (Gaussian) distribution, $\mathbf{p}$ represents the free parameters, $f(\theta;\mathbf{p})$ is the model prediction, and $\Delta\eta$ is the error vector associated with the measured efficiency data. Despite errors being always negligible for light diffraction data, systematic errors of 0.1% related to variations in the diffraction efficiency depending on experimental changes have been assumed i.e. the diameter of the laser beam, the position in the hologram from which

the data was collected. The impact of changing this value was investigated and will be discussed later.

The prior distribution encodes prior knowledge or constraints on the free parameters. Uniform priors are used for d_l and Δn_1 and L, ensuring that the parameters fall within defined bounds. The log-posterior function is given by:

$$\log \mathbb{P}(\mathbf{p}|\eta, \Delta\eta) = \log \mathbb{P}(\mathbf{p}) + \log \mathcal{L}(\mathbf{p}), \tag{5.2}$$

where $\log \mathbb{P}(\mathbf{p})$ is the log-prior and $\log \mathcal{L}(\mathbf{p})$ is the log-likelihood. This posterior function $\mathbb{P}$ provides the most probable parameter values given both the prior and the data.

The MCMC algorithm is initiated with parameter estimates, which are the fitting results presented in Table 5.1 after applying a certain perturbation to each parameter. In fact, small perturbations of 10^{-3}, 10^{-5} and 10^{-3} were applied to d_l, Δn_1 and L, respectively. Each perturbation is scaled according to the variability of each parameter. It is applied by adding a random value, drawn from a normal distribution using (`np.random.randn`), scaled by the corresponding perturbation and added to the initial value from the fit. This ensures that each walker starts in a slightly different place to explore a wider area of the parameter space and avoid getting stuck in local minima. Next, for each parameter, the algorithm starts to explore the posterior distribution by generating chains, referred to as walkers. These independent chains propose new states (parameter sets), and samples represent the collected parameter sets over iterations. The new states are evaluated through an acceptance probability calculated based on the prior distribution and likelihood probability. Each sample represents a potential state. More samples improve the accuracy of the posterior distribution estimation.

Discussion of the MCMC sampling results: KVCM vs. BVM

Several key decisions were made in setting up MCMC sampling. The number of walkers was set to 32. This satisfies the common rule of thumb of at least twice the number of free parameters for an adequate exploration. The same number was used for both considered cases of 2 and 3 free parameters. 1000 samples (or steps) per walker were drawn, similarly for the three models.

The trace plots for all three models—KVCM (Figure 5.3), BVM without decay (Figure 5.4), and BVM with attenuation (Figure 5.5)—show that the MCMC chains stabilize (reach equilibrium) early with no visible trends or drifts.
It consists of a display of the chains evolution for each of the considered parameters: Thickness, Δn_1 and L (when applicable). In the first 50 samples for Δn_1 in the KVCM and BVM without decay models, the chains exhibit more fluctuation before stabilizing, likely reflecting a burn-in period where walkers adjust to the parameter space. Beyond this, the chains oscillate around a stable mean, indicating convergence and thorough exploration of the posterior distribution. Additionally, the chains appear to be well-mixed, covering the parameter space comprehensively without getting trapped. This visual evidence supports the reliability of the choices taken during the process, ensuring robust parameter estimates. However, the effect of changes in the initial parameters or the perturbation values was investigated. Small changes had minor effects on convergence, while significant changes led to slower convergence or biased results. Smaller perturbation narrowed the exploration. On the other hand, larger ones initially improve exploration but cause instability and poor convergence in some walkers This results in some inconsistent chains failing to stabilize.

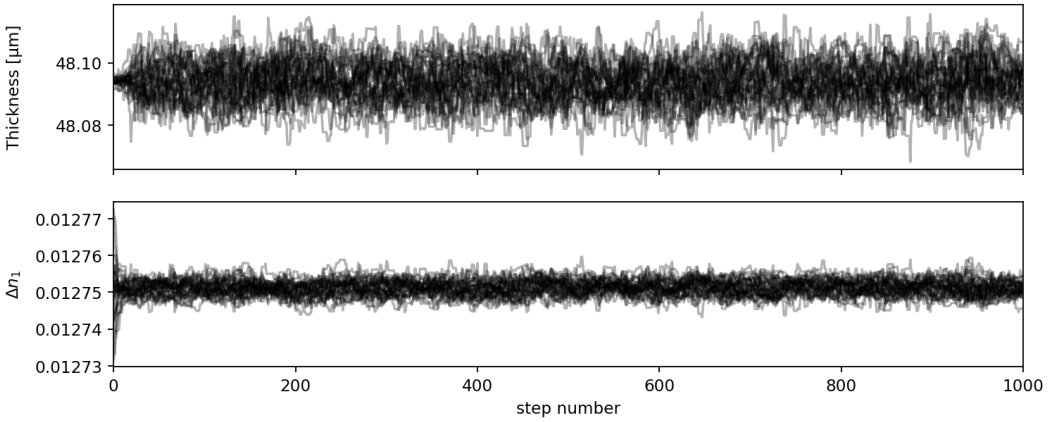

Figure 5.3: Trace plots from the MCMC sampling of the KVCM-based Kogelnik model.

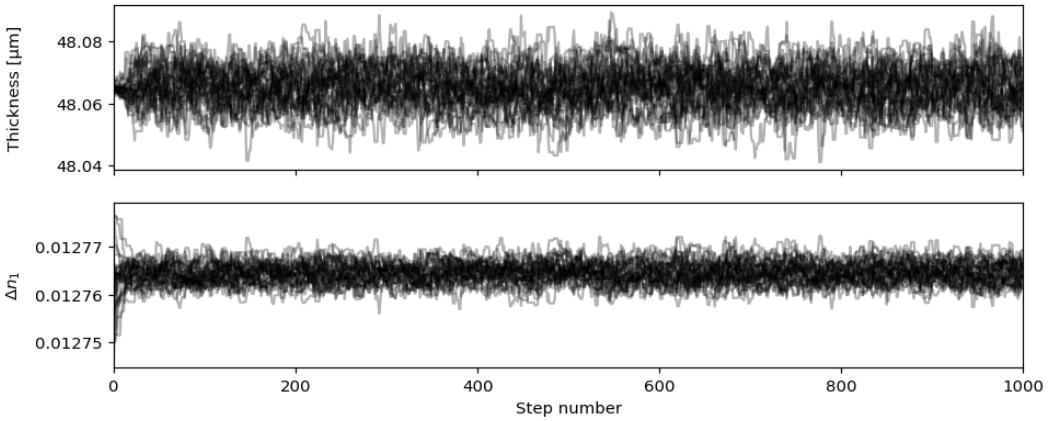

Figure 5.4: Trace plots from the MCMC sampling of the BVM-based 2-CW model.

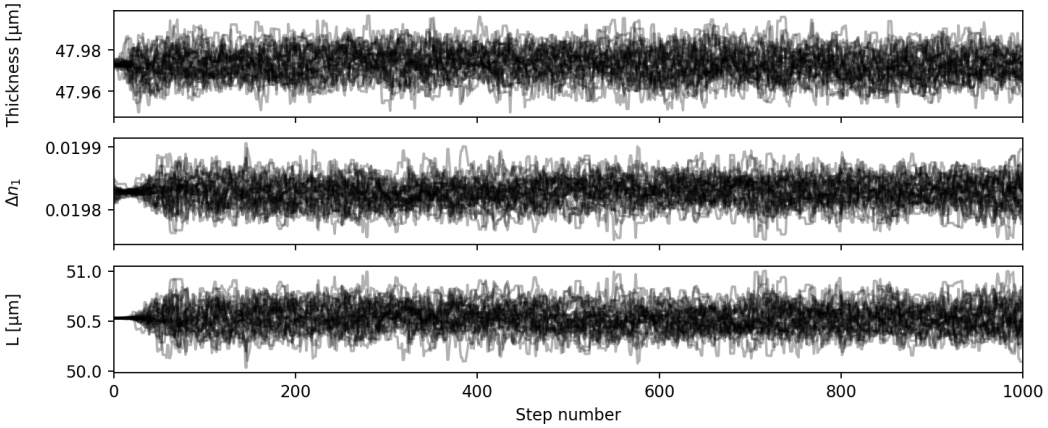

Figure 5.5: Trace plots from the MCMC sampling of the BVM-based 2-CW model with an attenuated refractive index profile.

While the visual inspection of the trace plots is encouraging, formal diagnostics are necessary to quantitatively verify convergence. The Gelman-Rubin statistic (R-

hat) was employed to assess the convergence of the chains [166]. The R-hat statistic compares the variance within each chain to the variance between chains. Values close to unity indicate that the chains have converged to the posterior distribution. For this analysis, the R-hat values were calculated using the `ArviZ` module [167], which implements the rank-normalized split-R-hat method as recommended in Ref. [166]. This method enhances robustness by rank-normalizing samples and splitting chains to detect non-stationary behavior. The calculated R-hat values are presented in Table 5.2.

Model	**Parameter**	**R-hat**
KVCM	Thickness [µm]	1.041
	Δn_1	1.038
BVM	Thickness [µm]	1.041
	Δn_1	1.038
BVM with Attenuation	Thickness [µm]	1.036
	Δn_1	1.055
	L [µm]	1.055

Table 5.2: R-hat values for each model and parameter.

An R-hat value of exactly 1 implies perfect convergence, while values slightly above 1 (up to 1.2) are typically acceptable and indicate sufficient convergence. The obtained values are very close to unity, confirming that the chains have also passed a formal statistical test for convergence.

The corner (or pair) plots for the three models—KVCM, BVM without attenuation, and BVM with attenuation—are shown in Figures 5.6, 5.7, and 5.8, respectively. These corner plots provide the joint and marginal posterior distributions of the parameters for each model. The histograms along the diagonal of the plot represent the marginal posterior distributions, while off-diagonal contour plots highlight the pairwise correlations between the parameters. Tilted or elongated contours indicate positive or negative correlations based on their orientation. However, nearly circular contours indicate minimal or no correlations at all. In the considered plots for the three models, the marginal distributions exhibit Gaussian-like behavior. This indicates good parameter estimates. Notably, for the KVCM and BVM without attenuation models, the joint distributions show some correlation between parameters, especially between thickness and refractive index modulation (Δn_1). This is more pronounced in the BVM model with attenuation, where the added parameter L (attenuation) correlates strongly with Δn_1. Despite these correlations, the parameters appear to be well constrained, as shown by the clear peaks in the marginal distributions.

The combination of the trace plots, corner plot, and R-hat diagnostic strongly supports the conclusion that the MCMC sampling procedure produced reliable posterior estimates for the parameters under the three considered models. The visual inspection, supported by formal convergence diagnostics, confirms that the sampling process was effective and appropriate for the data, providing a robust basis for parameter estimation in this context. For the three models, the posterior estimates and corresponding uncertainties (1σ confidence intervals) are presented in Table 5.3, and they are nearly identical to the standard fitting (see Table 5.1). However, it yields much smaller uncertainties.

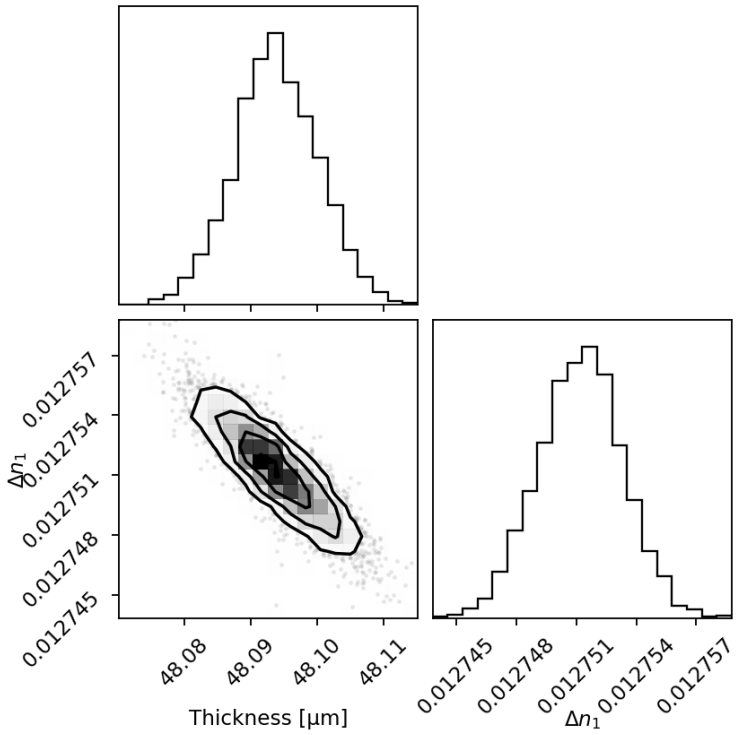

Figure 5.6: Corner plot from the MCMC sampling for the KVCM model.

Model	**Thickness [µm]**	$\Delta n_1(z=0) \times 10^{-3}$	L **[µm]**	$\langle \Delta n_1 \rangle \times 10^{-3}$
Kogelnik	48.1 ± 0.0	12.8 ± 0.0	N.A	12.8 ± 0.0
BVM no att.	48.1 ± 0.0	12.8 ± 0.0	N.A	12.8 ± 0.0
BVM with att.	48.0 ± 0.0	19.8 ± 0.0	50.5 ± 0.1	12.8 ± 0.0

Table 5.3: Posterior median values and uncertainties (1σ) for the non-fixed parameters in the three models using MCMC sampling.

The plots in Figure 5.9 show the posterior distributions within 68%, 95% and 99.7% credible intervals. Figure 5.9d was obtained using the same procedure, while considering much higher uncertainty in the data.

The posterior distribution shows a good fit to the data, with the parameter uncertainties reflected in the shaded regions. The exaggerated error case (Figure 5.9d) shows that higher errors result in larger credible intervals, reducing confidence in the parameter estimates. In all cases, the match between the latter and the data is no different from the standard fitting results shown in Figure 5.1. Therefore, the same previously drawn conclusions apply. The three models captures the main features of the considered data, but the BVM model with attenuation (Figure 5.9c) provides a slightly better fit, with even narrower credible intervals (zooming is required for their visualization).

Next, Bayesian model selection (BMS) technique will be introduced to gain further insights. This approach allows a more comprehensive comparison of how well the KVCM and BVM models capture the underlying phenomena, extending beyond the parameter estimates provided by MCMC sampling.

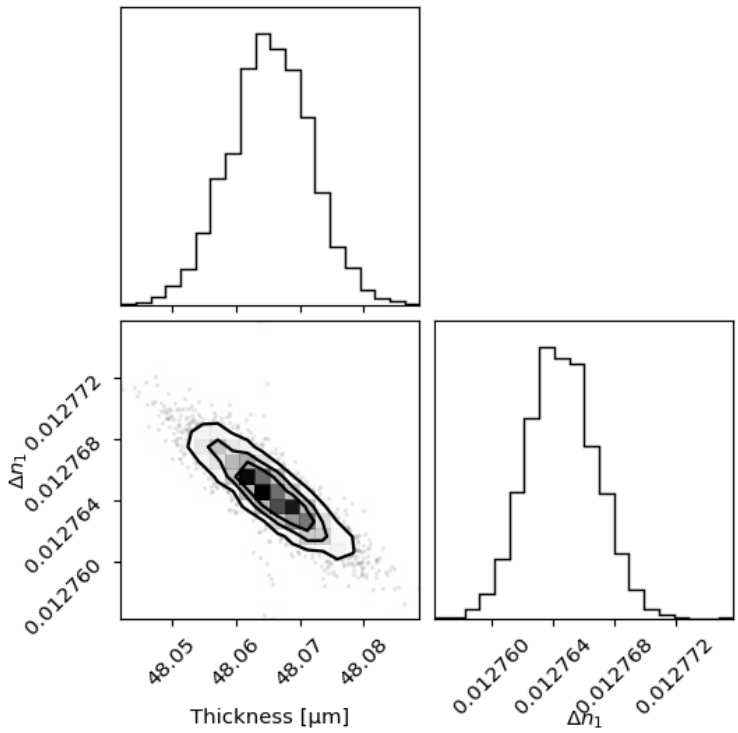

Figure 5.7: Corner plot from the MCMC sampling for the BVM model without attenuation.

Bayesian model selection for a comparative analysis

A Bayesian model selection was employed following a similar procedure to the MCMC sampling. The initial parameter guesses were obtained similarly through the standard fits, and the likelihood was computed using an MVN distribution as detailed in Equation 5.1. However, unlike MCMC, which focuses on sampling the posterior while neglecting the evidence term, the goal of BMS is to calculate the marginal likelihood (the **evidence**) to compare models.

Nested sampling was used for this purpose, offering an efficient method to compute the evidence by systematically exploring the parameters space [168]. As in the MCMC procedure, uniform priors were defined for each parameter. Nested sampling differs from the latter in that it does not require good initial guesses for convergence. Instead, it progressively contracts the sampling space, focusing on higher likelihood regions. Lower-likelihood areas are discarded. While MCMC is useful for estimating posterior distributions, nested sampling is better suited for computing the evidence. It allows for model comparison by evaluating the likelihood across the entire parameter space. The process yields posterior distributions (results were nearly identical to MCMC), but the primary goal here is the calculation of the evidence.

The marginal likelihood for the KVCM and BVM-based models was calculated and is presented in Table 5.4.
In $\mathbb{P}(D|M)$, D represents the data, and M denotes the model. It is important to note that including more parameters increases the model's flexibility but introduces

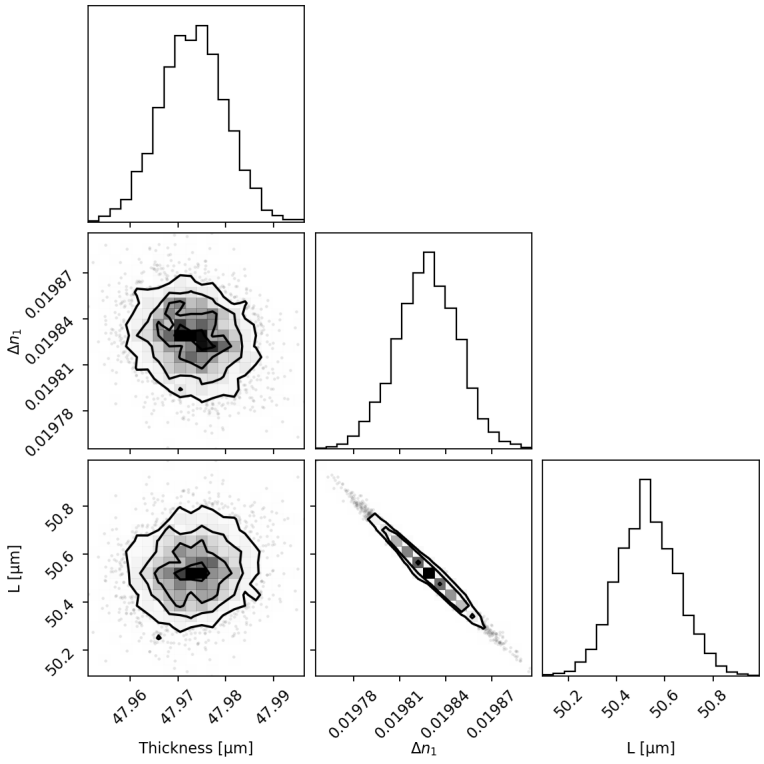

Figure 5.8: Corner plot from the MCMC sampling for the BVM model with attenuation.

Model	**Log Evidence** $\mathbb{P}(D\|M)$
KVCM	-87740
BVM	-74767
BVM with Attenuation	-54123

Table 5.4: Calculated Log Evidence for the KVCM and BVM based models.

additional complexity. Bayesian model selection inherently penalizes overly complex models, which helps avoid overfitting. The BVM model with attenuation yields the highest log evidence, implying it strikes the best balance between fitting the data and avoiding unnecessary complexity. This method quantitatively supports that the BVM with attenuation is the most suitable model for explaining the light diffraction behavior in the holographic grating.

In summary, while standard fitting procedures have been demonstrated to provide reliable estimates, MCMC and Bayesian methods offer a more comprehensive understanding of the uncertainties and the overall validity of the models. Through the application of these statistical techniques, informed decisions can be made about which theoretical framework best explains the observed diffraction behavior in holographic gratings. This could be of particular interest when multiple non-uniformities may emerge, to take informed decisions on which ones should be retained.

Transitioning from this statistical framework, it is also essential to address the limitations inherent in these techniques, particularly the increased computational demands

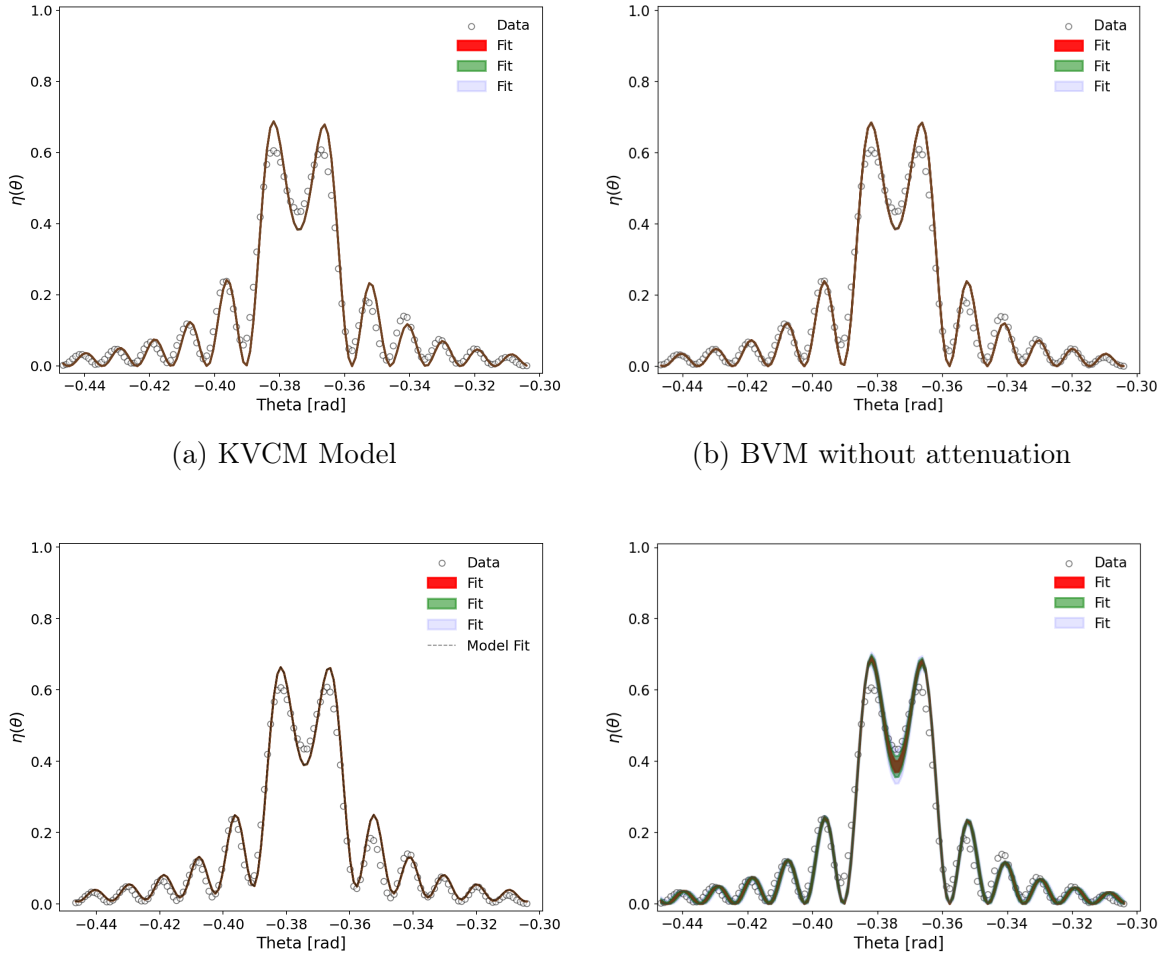

(a) KVCM Model

(b) BVM without attenuation

(c) BVM with attenuation

(d) KVCM with higher $\Delta\eta$ error (5%)

Figure 5.9: Posterior distributions of the three models 1σ (in red), 2σ (in green) and 3σ (in blue) credible intervals.

associated with MCMC and BMS. For example, the analysis of neutron diffraction data, which involves a larger number of fitting parameters, can significantly extend the computation time compared to standard fitting procedures. For context, a standard fit using the BVM based 2-CW model with only two free parameters (using a numerical solver) takes only few seconds or a couple of minutes at most. However, the MCMC sampling took approximately 6 hours and the nested sampling took a bit more than a day for the same data. For neutron data, where more free parameters are included and the complexity is increased, this is not practical. Therefore, in the sections that follow, only standard fitting procedures will be applied.

In the next subsection, the BVM based multi-wave coupling model will be compared to the rigorous coupled waves theory through simulations. A discussion of the legitimacy of the held approximations will be provided.

5.1.2 Evaluation of simplified models for neutron diffraction

In this subsection, the rigorous coupled waves analysis (RCWA) theory is compared to its approximate variant derived in Chapter 2, the multi-coupled waves analysis (MCWA) model. The aim is to evaluate the validity of the approximations employed, particularly for neutron diffraction.

In the RCWA theory, Maxwell's equations (see Section 2.1) are solved by expressing the electromagnetic fields and material properties as Fourier series, and applying boundary conditions at the interfaces of each layer [52, 56]. This process requires constructing a system of second-order coupled wave equations for an infinite number of harmonics. For uniform gratings, matrix transformations are always employed to solve the resulting eigenvalue problem (see Subsection 2.6.2). However, when a modulation profile is involved, the transformation is not feasible, leading to significant numerical complexity. In such cases, the grating is approximated as a series of stacked layers with constant but gradually varying modulation amplitudes [96]. While this approach reduces the computational burden, the numerical cost remains substantial for the RCWA theory. The same approach can be applied to MCWA, as noted in Subsection 2.6.2. Therefore, instead of discussing the numerical resolution, which varies depending on the specific method and algorithm used, attention will be directed to the approximations that simplify the system to be solved.

In simplified models, the exact matching of boundary conditions in rigorous theories is typically replaced by KVCM or BVM boundaries. Both external and internal reflections from the grating are considered negligible, or in other words, the refractive index of the grating is assumed to be more or less equal to the external refractive indices. For neutrons, the condition is valid, requiring no further discussion. However, the approximation is less tenable for light, particularly when high angles are involved. In such cases, Fresnel corrections are applied to the wave amplitudes, and Snell's law is used to predict the direction of the diffracted waves. The internally reflected waves are considered too weak in amplitude to have any significant effect [79]. Good agreement is often achieved in amplitude prediction between rigorous and approximate theories at the Bragg angle [169]. However, as demonstrated in the previous subsection (see Figure 5.1) and in other studies, the BVM method results in a better match to the data in far-off-Bragg replay [90, 91, 162].

The main simplification in the coupled-waves equations, which is interconnected to the one above, consists in disregarding second-order derivatives. It mainly stems from the slowly varying envelope approximation (SVEA). In the derived MCWA model (see Equation 2.38), it consists in assuming that the wave amplitudes (the envelope) vary slowly when compared to the exponential terms. In Ref. [79], the amplitude change has been explained by two contributing mechanisms related to the grating strength and the Bragg-mismatch parameters, respectively. The latter determines the number of diffracted waves involved, as it has been demonstrated that a significant energy interchange can only be achieved for small dephasing values. However, the claim that the SVEA may not apply to strongly modulated gratings must be reconsidered. For example, the first-order BVM model in Figure 5.9 shows excellent matching to light diffraction data collected from a strongly modulated grating. The highest light modulation amplitudes reported to date are at least two orders of magnitude smaller than the average refractive index. For neutrons, the highest modulation achieved for the VCN wavelengths available at PF2 instrument are at least five orders of magnitude smaller

than unity. Though, simulations with non-realistically high modulation amplitudes, may force the MCWA to fail.

A possible validity check is proposed based on a parameter that combines both the grating strength and the energy interchange per wavelength, the extinction length Δ_K (see Equation 2.25). It represents a characteristic length over which significant energy transfer between the forward and diffracted waves occurs. It has to be compared to the probe wavelength. When $\Delta_K \sim \lambda$, which simplifies to $\cos^2(\theta_B) \sim n_1$, it is no longer possible to disregard second order derivatives. It is clear that for neutrons $n_1 \ll \cos^2(\theta_B)$, and hence $\lambda \ll \Delta_K$ provided that $\cos(\theta_B) \approx 1$ and $n_1 \sim 10^{-7} - 10^{-5}$.

Neutron diffraction simulations have been performed to support the above considerations. The Figures Appendix M provide examples of simulations using typical values for the gratings considered in this research, involving a strongly modulated refractive index. Figure M.1 compares 5-RCWA to 5-MCWA simulations, showing excellent congruence between the predictions. While the differences pattern scales with the magnitude of the efficiency, it is always smaller than 10^{-6}. This supports the legitimacy of the first two approximations discussed above. Moreover, since the simulations involve the first and second-order Fourier components of the modulation amplitudes, the third approximation has been evaluated through a comparison of 5-RCWA and 7-RCWA simulations (see Figure M.2). The congruence between the predicted curves is maintained. The observed difference patterns arise from coupling effects with third orders. Their magnitude is small (less than a fraction of a percent), but not negligible. Including additional orders in the simulation does not result in any significant effect, indicating convergence.

Henceforth, fitting procedures will consider truncated systems that include only two more wave harmonics than the relevant modulation amplitudes. For instance, if n_1 and n_2 are included, the system will be extended up to the third-order harmonics. The magnitude of the highest-order components will always be examined to ensure that a sufficient number of wave harmonics has been included.

5.1.3 Exploration of the TMM model and adaptation of the multi-wave coupling model for MVHGs

Exploration of the BVM-based TMM formulation

The performance of the slicing approach has been evaluated through simulations for non-attenuated gratings (for simplicity). These simulations involved comparing: 1) SPSP simulations using BVM-based TMM predictions (see Section 2.7) for a sliced photopolymer, consisting of two 8 µm thick slices separated by a zero-thickness buffer layer. 2) Kogelnik's model for a single 16 µm layer, and 3) two-coupled waves (2-CW) analysis based on BVM predictions also for a single 16 µm layer. The used modulation values and corresponding observations are outlined. The supporting figures are provided in Appendix M, except the here-presented figure for $\Delta n_1 = 0.02$.

- $\Delta n_1 = 0.2$ (Figure M.3): Kogelnik's formulation yields non-physical predictions due to the KVCM failure at such non-realistic strong modulation. The SPSP formulation significantly deviates from the 2-CW BVM predictions at Bragg angle. Though, it quickly converges to perfect congruence far-off-Bragg.

- $\Delta n_1 = 0.04$ (Figure M.4): This is close the highest values reported for Bayfol foils and falls within the third quadrant. At Bragg angle, only minimal deviations are noted for the KVCM model, which then diverges more significantly far-off-Bragg.

- $\Delta n_1 = 0.02$ (Figure 5.10): A typically high value for the considered materials which is within the second quadrant. Better congruence is noted, with observations similar to those at $\Delta n_1 = 0.04$.

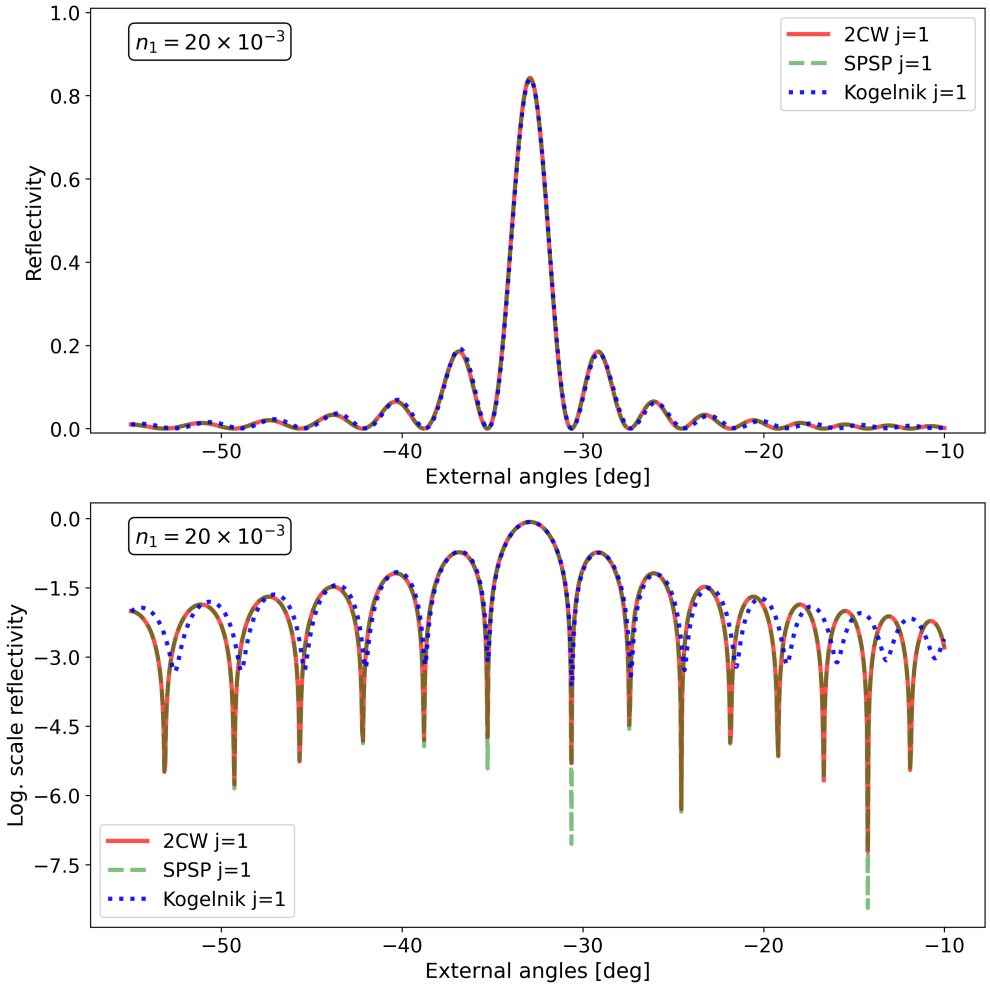

Figure 5.10: Comparison of diffraction efficiency simulations for $\Delta n_1 = 0.02$ using three models: 1) multiwave coupling formulation with BVM boundary (red line) 2) Photopolymer division and amplitude transfer using transfer matrices based on BVM method (dashed green line) 3) Kogelnik formulation (dotted blue line).

The KVCM failure for strongly modulated gratings is once again confirmed. In contrast, the slicing approach in the TMM formulation closely aligns with the BVM based 2-CW model. Minor deviations appear at Bragg angle, increasing with higher modulation amplitudes. These deviations quickly diminish far-off-Bragg, restoring congruence between the two models.

Despite using BVM boundary in the TMM formulation, the transfer matrices are based on Kogelnik's model (see Equation 2.13 and Equation 2.14) [108]. Specifically,

it only differs from KVCM-based TMM matrices (described in Ref. [107]) by a reformulation of the parameter ξ. Its KVCM expression ($\frac{\vartheta d}{2c_{\pm 1}}$) is replaced by a BVM form that involves the Bragg mismatch parameter ($\imath\frac{d}{2}\delta q_{\pm 1}$). This explains the perfect congruence between this method and the 2-CW method far-off-Bragg, and the small deviation towards Kogelnik's predictions at Bragg angle.

To explore the stacked structure of MVHGs compared to single-layer photopolymers, simulations were performed for SP, SPSP, and SPSPSP MVHGs, as shown in Figure 5.11.

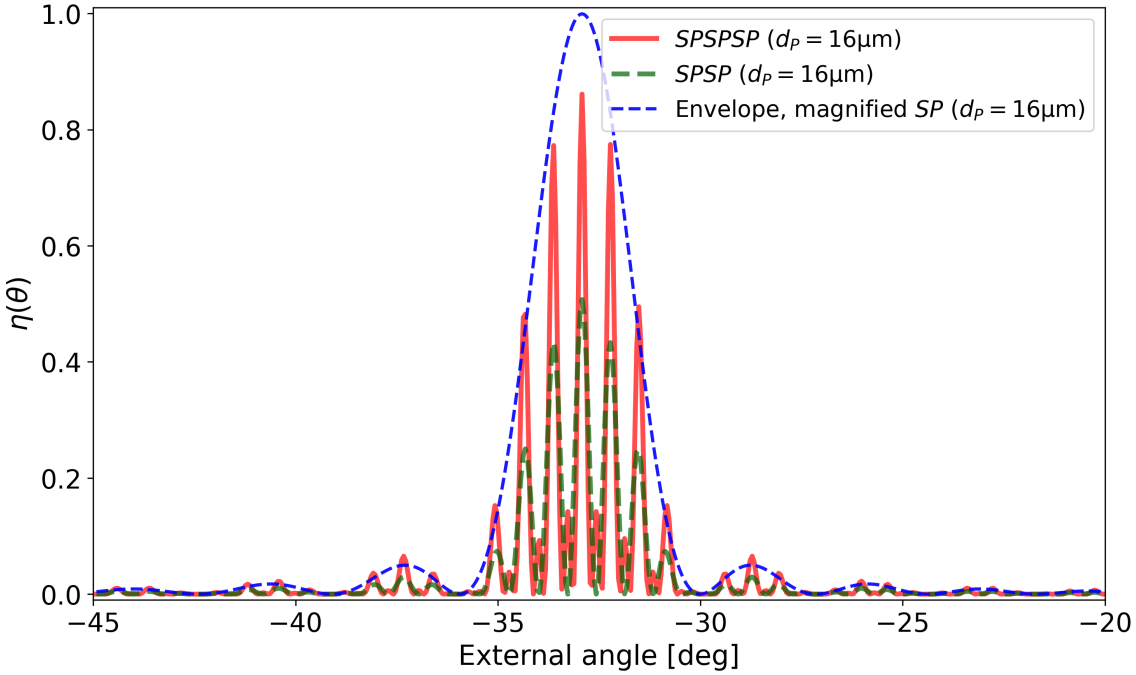

Figure 5.11: Light diffraction simulations using TMM for SP, SPSP and SPSPSP MVHGs using the following realistic parameters: $d_{\mathrm{P1}} = 16\,\mu\mathrm{m}$, $d_{\mathrm{P2}} = 16\,\mu\mathrm{m}$, $d_{\mathrm{P3}} = 16\,\mu\mathrm{m}$, $d_{\mathrm{S1}} = 50\,\mu\mathrm{m}$, $d_{\mathrm{S2}} = 50\,\mu\mathrm{m}$, $n_1 = 4 \times 10^{-3}$, $\lambda_l = 543.5\,\mathrm{nm}$ and $\Lambda = 500\,\mathrm{nm}$.

The simulations show the expected result: rapid oscillations with a period determined by the buffer layer thickness, within an envelope whose frequency depends on the modulated layer thickness (magnification to approximately 7 times the prediction of a single layer for clarity). Adding more SP layers increases diffraction efficiency due to the greater total thickness, while the oscillation frequency (the multiplexing) remains similar.

The main motivation for the consideration of MVHGs in this research, is their potential application as microscale neutron interferometer. TMM simulations have been performed for two distinct values of the substrate SLD, with grating parameters within Bragg diffraction regime. Results are shown in Figure 5.12.
The predicted curves exhibit no visible deviations. However, when calculating the difference between the curves, a beating pattern emerges, matching the modulation period of the envelope. This beating indicates that the two curves oscillate at nearly identical, but slightly different frequencies. The frequency difference is due to the SLD change, causing slight phase shifts at the buffer layers. While this confirms the

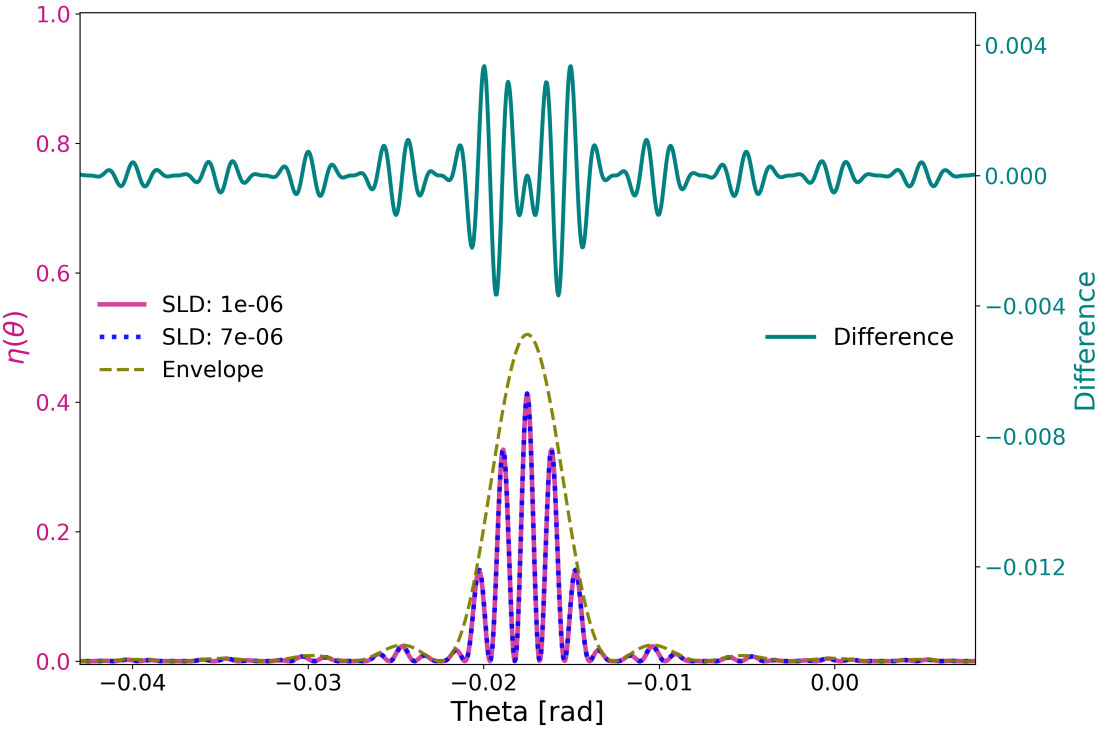

Figure 5.12: TMM simulations for an SPSP structure using two different SLD values of the buffer layer (shown in Å^{-2} unit) and the following arbitrary parameters: $\lambda_{\text{N}} = 7\,\text{nm}$, $\Lambda = 200\,\text{nm}$, $\Delta ß_1 = 2.5\,\mu\text{m}^{-2}$, $d_{\text{P1}} = d_{\text{P2}} = 40\,\mu\text{m}$, $d_{\text{S}} = 100\,\mu\text{m}$.

sensitivity of MVHGs to the SLD, the effect is small—only a fraction of a percent. This implies that using such structures as neutron interferometers may pose challenges, particularly in terms of statistical precision, detector performance, and the need for highly accurate knowledge of grating parameters and substrate thickness.

In summary, the TMM and its slicing approach have been validated. The sensitivity of MVHG structures to the neutron refractive index of the substrate material, thereby, their potential use as microscale interferometer systems have been confirmed. Next, an MCWA adaptation for MVHGs will be presented, and a comparative analysis with TMM simulations will be performed.

Adaptation of the MCWA for MVHGs

In most practical cases for neutron diffraction from transmission holographic gratings, and particularly for the ones considered in this research, multiple diffracted waves are involved. In this case, the previously described TMM models fail. Therefore, an alternative model is suggested and evaluated.

The suggested procedure consists of using the MCWA model described in Chapter 2, with wave amplitudes being transferred and matched between layers. At $z = 0$ for transmission gratings, the wave amplitudes are: $S_0(0) = 1$, and $S_j(0) = 0$ for $j \neq 0$. After propagating in the first modulated layer P1 having a thickness d_{P1}, the output amplitudes are transmitted by the subsequent buffer layer S2 with a certain accumulated phase. This phase is determined by the thickness of the layer d_{S2} and the Bragg mismatch parameter of the considered order which set the path differences for

waves. Hence, the input wave at the second modulated layer P2 takes this form:

$$S_j(z = d_{\mathrm{P1}} + d_{\mathrm{S2}}) = S_j(z = d_{\mathrm{P1}}) \cdot \exp(-i \cdot \delta q_j \cdot d_{\mathrm{S2}})$$

The approach follows the same principles as the TMM described in Section 2.7, particularly in accounting for the refractive index differences between layers. The only distinction is the application of MCWA in modulated layers, where multiple waves are involved. Their evaluation can be performed through simulations using grating parameters that satisfy the Bragg diffraction regime, where both models are applicable. This has been done for an SPSP structure, as shown in Figure 5.13.

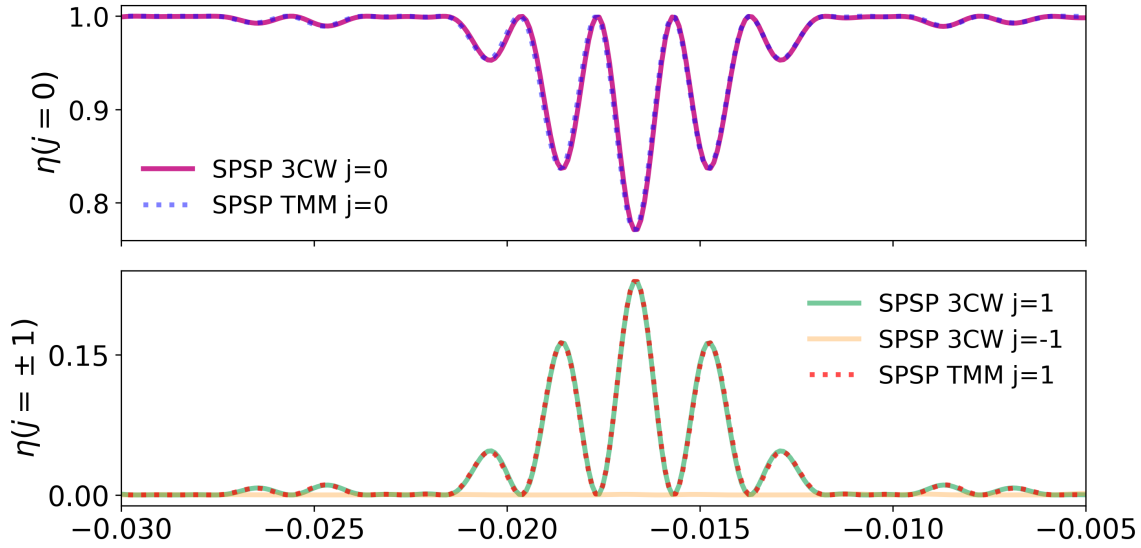

Figure 5.13: Comparison of 3CW and TMM simulations for an SPSP structure at Bragg diffraction regime. The parameters used are: $\Lambda = 300\,\mathrm{nm}$, $\lambda_{\mathrm{N}} = 10\,\mathrm{nm}$, $d_{\mathrm{P1}} = d_{\mathrm{P2}} = 50\,\mu\mathrm{m}$, $d_{\mathrm{S2}} = 100\,\mu\mathrm{m}$, and $\Delta ß_1 = 1\,\mu\mathrm{m}^{-2}$.

The predictions are nearly identical, with only negligible variations, thus both models mutually validate each other. To further exploit the possibilities offered by such stacked structures, simulations for the case of three coupled waves have been performed. In neutron interferometry, having information on the evolution of wave amplitudes and their corresponding phases is important for predicting the behavior of neutron waves in complex structures. Figure M.5, Figure M.6, and Figure M.7 show the evolution of the modulus of the complex wave amplitudes S_1, S_0, and S_{-1}, as well as their corresponding phases across the layers. These phases correspond to the argument of the propagating complex wave amplitudes, and not their relative phases. The S_0 component remains dominant with minimal variation, while S_1 and S_{-1} exhibit stronger modulation. These results underline the potential of MVHGs for neutron interferometry applications, where precision and sensitivity to minute changes are essential.

In brief, an MCWA adaptation for the MVHGs has been introduced. For fitting procedures of light and neutron diffraction data in Bragg regime, both TMM and MCWA adaptation models can be used more or less equivalently. Otherwise, the MCWA adaptation must be applied.

5.2 Optimization of commercial Bayfol® HX200 photopolymers neutron optical response

This research focuses on the optimization of the materials neutron optical response, based on controllable physical recording conditions. This mainly includes single layer unslanted transmission gratings, though, results from proof-of-concept experiments involving multilayer and slanted reflection gratings will also be presented.

To evaluate recording saturation behavior, the reaction-diffusion model based on Photopolymerization Driven Diffusion (PDD) model and its extension to Non-local Photopolymerization Driven Diffusion (NPDD) provides reliable predictions [170]. A basic assumption in this model is that only non-reacted monomers are mobile, as those incorporated into the polymer matrix are immobilized, hence, focusing only on free monomers that contribute to the ongoing polymerization. The model describes three key phases: 1) Induction period: the polymerization rate is initially low due to limited formation of free radicals. 2) Autoacceleration phase: as the polymer network grows, the rate of photopolymerization accelerates. This phase is driven by the "gel effect," where the growing polymer network entraps reactive radicals, increasing their local concentration and reactivity. 3) Diffusion limited phase: the reaction rate declines as the polymer network solidifies and restricts monomer movement.

For the same context and considering Bayfol foils in Refs. [24, 171], it has been demonstrated that the saturation n_1 depends on the local reaction-diffusion parameter R (for $\sigma_P = 0$) and the material resolution described by the non-local variance parameter σ_P i.e. $n_1 = n_1(R, K^2\sigma_P^2)$ [127]. The reaction-diffusion parameter is defined as the ratio of the monomer diffusion rate and the polymerization rate F_0.

$$n_1(R) = n_1\Big(\frac{D_m K^2}{F_0}\Big) = n_1\Big(\frac{D_m K^2}{\kappa_P (I_a')^\gamma}\Big) \tag{5.3}$$

Here, $D_m = 2.5 \times 10^{-10}\,\mathrm{cm}^2/\mathrm{s}$ is the monomer diffusion constant. $F_0 = \kappa_P (I_a')^\gamma$ represents the polymerization rate from the NPDD model, with $\kappa_P = 1.0\,\mathrm{cm}^{2\gamma}/(\mathrm{s}\cdot\mathrm{mW}^\gamma)$—a constant that incorporates various factors from the optically induced photopolymerization—and I_a' being the recording intensity (see Equation 3.4). The power parameter $\gamma = 0.8$ for Bayfol [171], and can take values between 0.5 and 1.5, according to Ref. [170]. For simplicity, a linear variation with $\gamma = 1$ will be assumed. The given values for the monomer diffusion constant and κ_P are those used in Ref. [24] for Bayfol photopolymers. Nevertheless, $K^2\sigma_P^2$ is indicative of the high spatial frequency cut-off, with $\sigma_P^2 < 100\,\mathrm{nm}^2$ for the considered high resolution Bayfol material. The model's reliability has already been demonstrated, but may miss few aspects that may affect the photopolymerization process e.g. Oxygen quenching. Having established a robust framework for predicting the dependence of grating performance on the recording photophysical aspects, it is now possible to discuss the results obtained from this research.

5.2.1 Results from single-layer Bayfol gratings with different photopolymer thicknesses recorded at varying intensities

The holographic gratings recorded on single-layer Bayfol photopolymers described in Table 3.4 are considered. For the readout and preliminary evaluation of the formed

hologram gratings, a light wavelength $\lambda_l = 543.5\,\text{nm}$ was used. Afterwards, selected samples (not all of them due to time constraints at large scale facilities) were measured with neutrons at PF2/VCN instrument using the setup described in Subsection 3.2.3. The selected WLD of the incoming neutrons before collimation is shown in Figure 3.6. As an example, light and neutron diffraction results from the sample SM_32µm_30mW, are shown in Figure 5.14 and Figure 5.15, respectively.

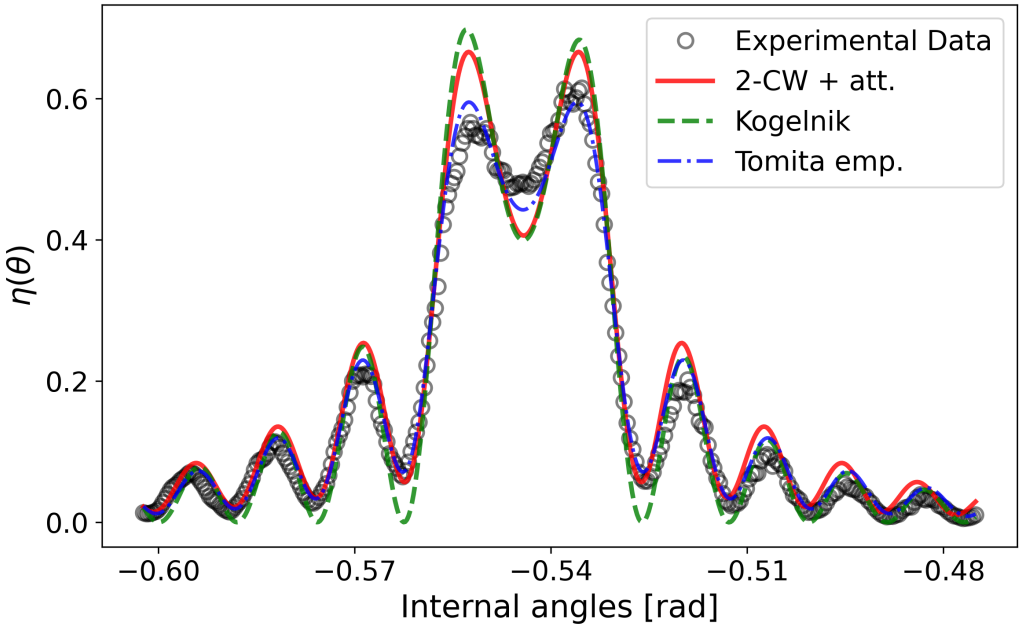

Figure 5.14: Light diffraction efficiency curve of the sample SM_32µm_30mW measured at a wavelength of 543.5 nm. The circular markers correspond to experimental data, while the lines correspond to fits using three models: Kogelnik theory (green dashed line), Tomita's empirical formula (blue dashdotted line) and two-wave coupling with n_1 attenuation (red line).

Some asymmetry is observed in the light diffraction peak, which is likely stemming from inhomogeneities due to holographic scattering. Three models were used for fitting the light data: BVM based 2-CW (see Equation 2.38), Kogelnik's model (see Equation 2.15) and Tomita's empirical formula (see Equation 2.17). All of them align closely. The best match to the data has been obtained using Tomita's empirical formula, despite lacking a theoretical foundation. The obtained fit parameters are summarized in Table 5.5. Comparing results from theoretical models (Kogelnik and BVM based 2-CW), an excellent agreement is achieved with minor differences in the modulation amplitudes ($\sim 10^{-4}$) and in the grating thickness ($\sim 10^{-1}\,\mu\text{m}$). Despite showing the best match to the data, Tomita's empirical formula provides an accurate estimate of the thickness and of the decay length, but it seems that the modulation amplitude determined by this model corresponds directly to the thickness averaged value. This has been further verified by comparing fits to other samples' light data. Given ambiguity and lack of theoretical foundation, this model should only be used as an approximate formula for finding good starting parameters, and not for any reliable analysis.

The calculated Klein-Cook parameter Q and the grating strength ν confirm that the grating operates within the Bragg diffraction regime, with $Q = 565$ and $\nu = 3.83$.

Model	Thickness [µm]	$n_1(z=0) \times 10^{-3}$	L [µm]	$\langle n_1 \rangle \times 10^{-3}$
Kogelnik	30.4 ± 0.1	18.6 ± 0.1	∞	18.6 ± 0.1
Tomita emp.	30.2 ± 0.1	19.0 ± 0.0	30.5 ± 0.7	12.1 ± 0.4
BVM with att.	30.3 ± 0.1	30.1 ± 0.7	29.2 ± 1.5	18.7 ± 1.5

Table 5.5: Results from light diffraction data measured from Bayfol "SM_32µm_30mW" sample using three models for fitting.

The criteria $(Q\nu/\cos(\theta_B)) = 2530 \gg 1$ and $(Q/2\nu\cos(\theta_B)) = 86 > 10$ support this conclusion. This suggests that two-wave coupling theory can be used for fitting. The value of ν corresponds to a phase in the third quadrant and suggests overmodulation or non-ideal coupling. This implies that the grating is operating under conditions that may cause reverse coupling, affecting the angular response by reducing efficiency at the Bragg angle and leading to higher side lobe maxima, as seen in Figure 5.16. Moreover, lifted side lobe minima suggest non-uniformity in the grating strength. Therefore, the BVM based multi-wave coupling model that includes a profile attenuation of the grating strength should be used (for both light and neutrons). The determined decay length $L = (29.2 \pm 1.5)\,\mu\text{m}$ from the (2-CW + att.) model has been fixed for fitting the neutron data shown in Figure 5.15.

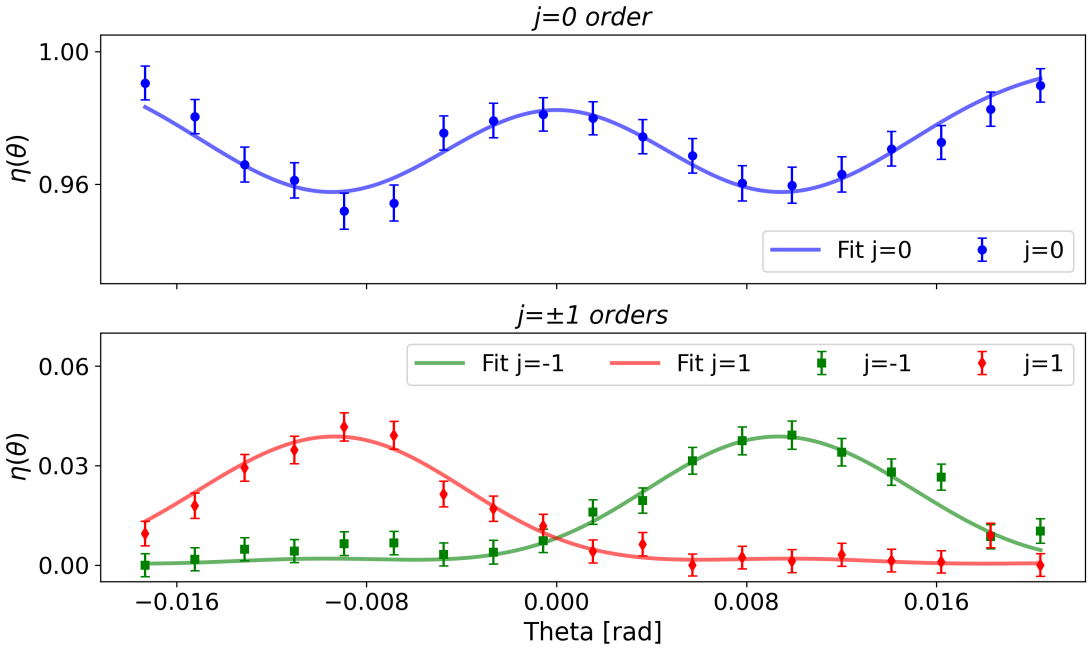

Figure 5.15: Neutron diffraction efficiency curves of the sample SM_32µm_30mW measured at the PF2/VCN instrument. The data points show the experimental measurements, and the lines represent the corresponding theoretical fit for each order.

The determined mean wavelength $\lambda_{N,\text{mean}} = (5.7 \pm 4.5)\,\text{nm}$ aligns with expectations from Figure 3.6, though the uncertainty is extremely large. The same applies to the rest of the sample measurements. The post-collimation wavelength distribution obtained from the fit is shown in Figure M.8. In the fitting procedure, the WLD is accounted for by discretizing the pre-assumed exponentially modified Gaussian (EMG) probability density function [141] into bins. The PDF is evaluated over a range of wavelengths,

and weights are assigned to each bin using Simpson's rule. These weights reflect the relative probability of each wavelength. The coupled wave equations are then solved for each wavelength, weighted by these probabilities, to model the overall diffraction efficiency. This method ensures the influence of WLD is incorporated, with a binning deviation of 7.56×10^{-5} for a bin size of half an Angstrom, indicating minimal error from discretization. This approach has been compared to fitting procedures which include a continuous PDF without discretizing, but rather by integrating over the full spectrum for fitting results from an NPC grating. The results from both approaches were consistent, and the discretization has been opted for in this study for reducing the numerical cost. As previously discussed, the WLD primarily reflects the convolution of the source distribution with collimation. The WLD determined by fitting the diffraction data captures the grating's diffraction characteristics, which are influenced by both wavelength and angular selectivity. For highly selective gratings the bin size should be further reduced to keep the binning errors within acceptable margins.

Results from fitting the light and neutron diffraction data measured from the other samples are summarized in Table 5.6. Figure 5.16 presents these results and illustrates the observed systematic trends.

Nominal thick.	**Intensity**	**Light** $\langle n_1 \rangle \times 10^{-3}$	$\langle \Delta ß_1 \rangle$ [μm^{-2}]
16 µm	10 mW	26.0 ± 1.3	3.8 ± 0.8
	30 mW	22.3 ± 0.1	-
	50 mW	20.0 ± 0.1	-
32 µm	10 mW	26.1 ± 2.4	3.9 ± 0.3
	30 mW	18.7 ± 1.5	2.7 ± 0.4
	50 mW	16.1 ± 2.4	2.6 ± 0.6
50 µm	10 mW	12.0 ± 0.1	-
	30 mW	7.3 ± 0.0	-
	50 mW	6.8 ± 0.1	0.8 ± 1.5

Table 5.6: Thickness-averaged light refractive index modulation amplitude $\langle n_1 \rangle$ and neutron SLD modulation amplitude $\langle \Delta ß_1 \rangle$ as a function of laser power for Bayfol foils of different thicknesses.

From all results, a decrease of the modulation amplitudes is observed for increasing intensities, irrespective of the nominal photopolymer thickness. A potential explanation could be that a higher intensity amplifies the rate of radical generation and accelerates the photopolymerization process. This, in turn, restricts the mobility of monomers and reactive species and results in a rapid gelation [116]. As a result, the diffusion-limited phase sets in earlier, resulting in lower spatial densities of imaging components, which manifest as reduced light modulation amplitude $\langle n_1 \rangle$ and neutron $\langle \Delta ß_1 \rangle$ values. These observations align with recognized principles in photopolymerization kinetics, where balancing polymerization rate and monomer diffusion is crucial for effective grating formation. Specifically, increasing the recording intensity leads to a lower reaction-diffusion parameter R, as the polymerization rate F_0 rises. A known consequence of lower R values is the reduction in light modulation amplitudes observed [24, 128]. Our findings confirm this effect in both light and neutron measurements, reinforcing the reliability of these observations.

On the other hand, thicker samples exhibit a systematic trend of lower light modulation amplitude $\langle n_1 \rangle$ values across all writing intensity values. The neutron SLD modulation for the 16 µm and 32 µm samples is relatively high at 10 mW. For the

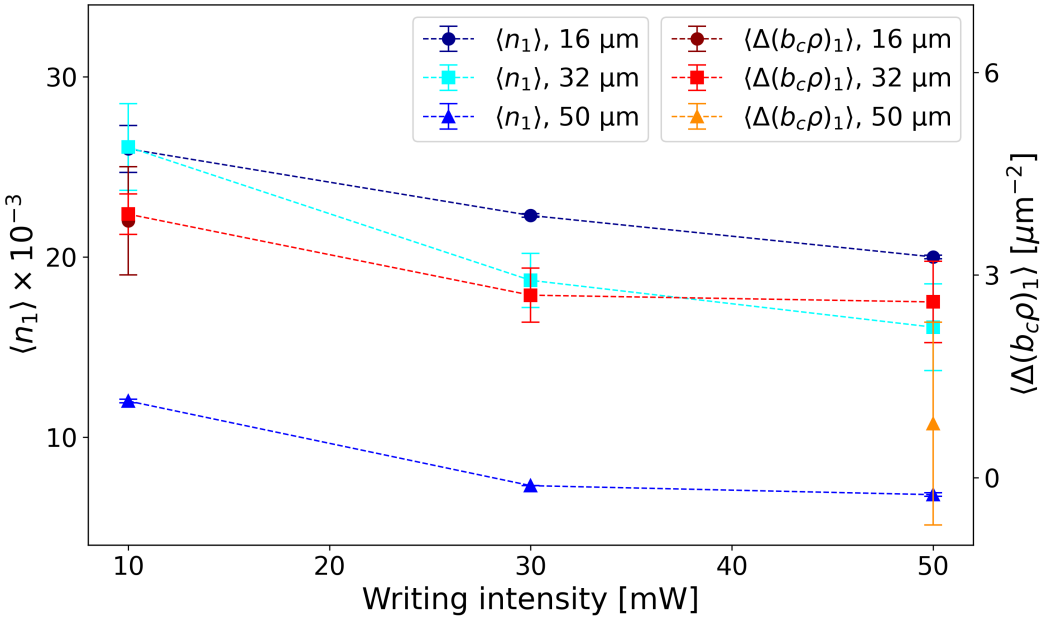

Figure 5.16: Variations of the thickness-averaged light refractive index modulation amplitude $\langle n_1 \rangle$ and neutron SLD modulation amplitude $\langle \Delta ß_1 \rangle$ as a function of laser power for Bayfol foils of different thicknesses.

50 µm sample, the lower SLD modulation exhibits substantial error bars at 50 mW, suggesting non-uniformity in the grating structure at high power. In thicker samples ($\sim$ 50 µm), the formation of secondary gratings, indicated by the observation of holographic scattering rings during readout (conical diffraction), points to non-uniform polymerization and spatial inhomogeneity within the hologram. Holographic scattering in Bayfol foils has also been reported in Ref. [172]. This effect is exacerbated in thicker foils, potentially leading to more uneven polymerization across the sample depth. Such inhomogeneities further reduce the effective modulation amplitudes in both light and neutron measurements by creating local variations. These observations underscore the reliability of these findings as both probes reflect the same underlying photophysical mechanisms, as expected.

5.2.2 Results from single-layer Bayfol gratings recorded at varying dosages

Having explored the optimization of single-layer Bayfol gratings based on writing intensity at a fixed recording dosage, this subsection examines the influence of varying the dosage. The samples described in Table 3.2 and Table 3.3 are considered.

The same setup at the Laser Laboratory of the University of Vienna was used with a readout wavelength $\lambda_l = 543.5$ nm. The observations and conclusions from the previous subsection regarding light diffraction measurements from Bayfol foil gratings are applicable here. Neutron diffraction measurements were conducted in a separate experimental campaign [149], but this does not affect the data analysis, as the reduction procedure remains consistent. To avoid redundancy, the key parameters of interest obtained from fitting the diffraction data, the first-order light refractive index modulation amplitudes $\langle n_1 \rangle$ and neutron SLD modulation amplitudes $\langle \Delta(b_c\rho)_1 \rangle$, are presented in

Table 5.7. The systematic trends observed in these parameters with varying dosages are shown in Figure 5.17 and Figure 5.18.

Dosage [mJ/cm^2]	**Light** $\langle n_1 \rangle \times 10^{-3}$	$\langle \Delta ß_1 \rangle$ [μm^{-2}]
4.3	0	0
6.9	15.9 ± 2.8	0.9 ± 0.6
17.8	17.2 ± 4.0	1.8 ± 0.4
28.7	16.8 ± 10.4	2.5 ± 0.1
32.0	13.9 ± 0.9	1.1 ± 0.4
51.4	12.8 ± 1.3	1.5 ± 0.3
82.5	11.6 ± 5.0	1.2 ± 0.3
133.1	9.8 ± 1.3	1.2 ± 0.2
213.9	8.8 ± 0.5	1.4 ± 0.4

Table 5.7: Thickness-averaged first-order light refractive index modulation amplitude $\langle n_1 \rangle$ and neutron SLD modulation amplitude $\langle \Delta ß_1 \rangle$ for varying recording dosages.

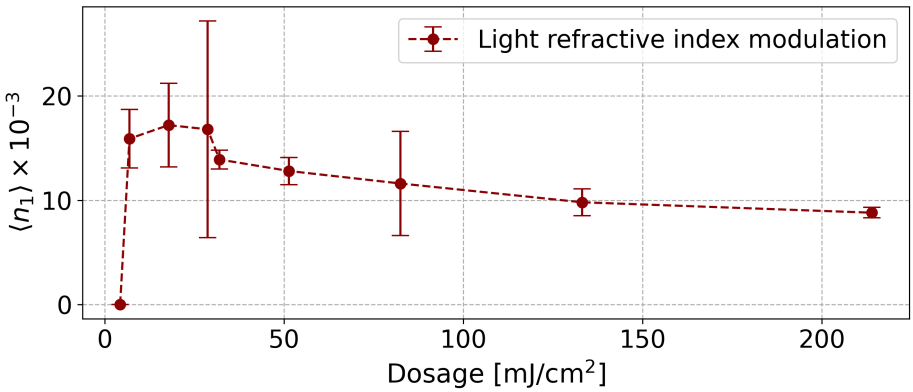

Figure 5.17: Light refractive index modulation $\langle n_1 \rangle$ as a function of dosage for Bayfol HX200 gratings.

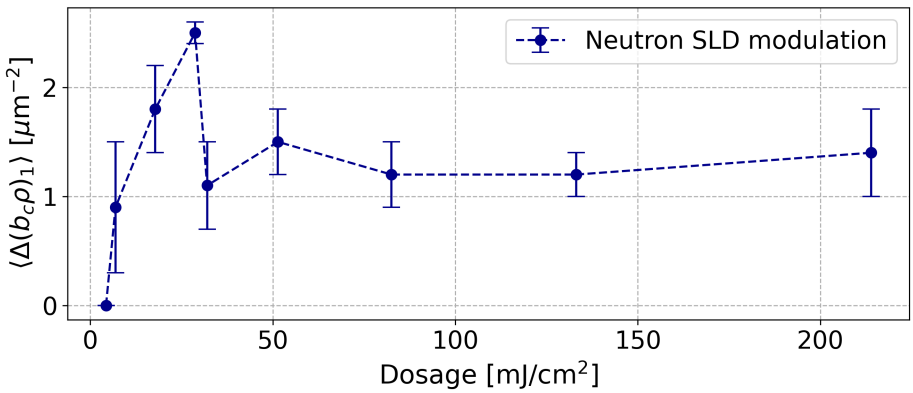

Figure 5.18: Neutron SLD modulation $\langle \Delta ß_1 \rangle$ as a function of recording dosage for Bayfol HX200 gratings.

The results reveal a clear threshold behavior, with no observable polymerization or hologram formation below a critical dosage (around 5 mJ/cm^2). Bayfol foils are known

for their superior stability compared to other photopolymer materials, both during and after recording, due to the use of orthogonal two-chemistry. In this approach, a pre-formed cross-linked matrix provides structural integrity, while the imaging components are free to diffuse within the matrix [171]. Beyond this threshold, effective photopolymerization occurs, balancing monomer diffusion with the advancing polymerization front. This balance leads to optimal modulation amplitudes at intermediate dosages.

If the dosage is further increased, which also corresponds to higher writing intensities in the considered case, a gradual decline or stabilization in both the light refractive index and neutron SLD modulation manifests. This behavior aligns with previously discussed predictions based on the reaction-diffusion parameter R. Though, the tendency for reduced modulation amplitudes at lower R values, due to increased intensities, is compensated or stabilized by more important quantum yield of excited state dyes and free radical generation resulting from the higher dosage. In fact, similar variations have been reported in Figure 2 and Figure 4 in Ref. [126] for an increasing propagation rate constant and for a decreasing termination rate, respectively. Both the latter cases and the considered one result in variations in F_0, which seem to decrease and stabilize upon reaching an optimal photosensitive response, influenced by varying material photophysical and photochemical properties or recording conditions.

These findings are consistent with similar studies reported in the literature on Bayfol foils using light probes (see Figure 3 in Ref. [24]) and, for the first time, reveal similar behavior with neutron diffraction. This deepens our understanding of the neutron optical response of photopolymers and aids in optimizing the use of this material in neutron diffraction applications.

5.2.3 Reproducibility of the neutron diffraction results from Bayfol foils

In this study, the sample "pp70_SP," described in Table 3.5, is considered. Neutron diffraction measurements using this sample were performed during two separate experimental campaigns at the PF2/VCN instrument in 2021, few months apart. Despite the time gap, the experimental setup remained unchanged, with no components being moved in principle. This is evidenced by the closely aligned curves in Figure 5.19, indicating no significant variation in the setup-dependent WLD.

Even a slight displacement of an aperture or a tilt of the supermirror could have altered the WLD, and would result in noticeable deviations in the diffraction efficiency curves. However, no substantial deviations were observed. Minor differences can be attributed to slight variations in the grating's position and alignment, differences in angular positioning during the rocking curve measurements, or potential changes in background levels affecting the data which may not have been evenly addressed during the data reduction process etc. Despite the multiple origins that may cause significant deviations in the curves, the results are nearly identical. This demonstrates the following: 1) the stability of Bayfol foils over time and the reproducibility of the neutron diffraction results under challenging conditions where multiple factors may generate errors. 2) The stability of the VCN source at PF2 instrument and the possibility of conducting a reliably consistent study over two separate cycles, if the setup and surrounding environment conditions are preserved (which is the case here).

This sample is the grating with the highest diffraction efficiency among Bayfol

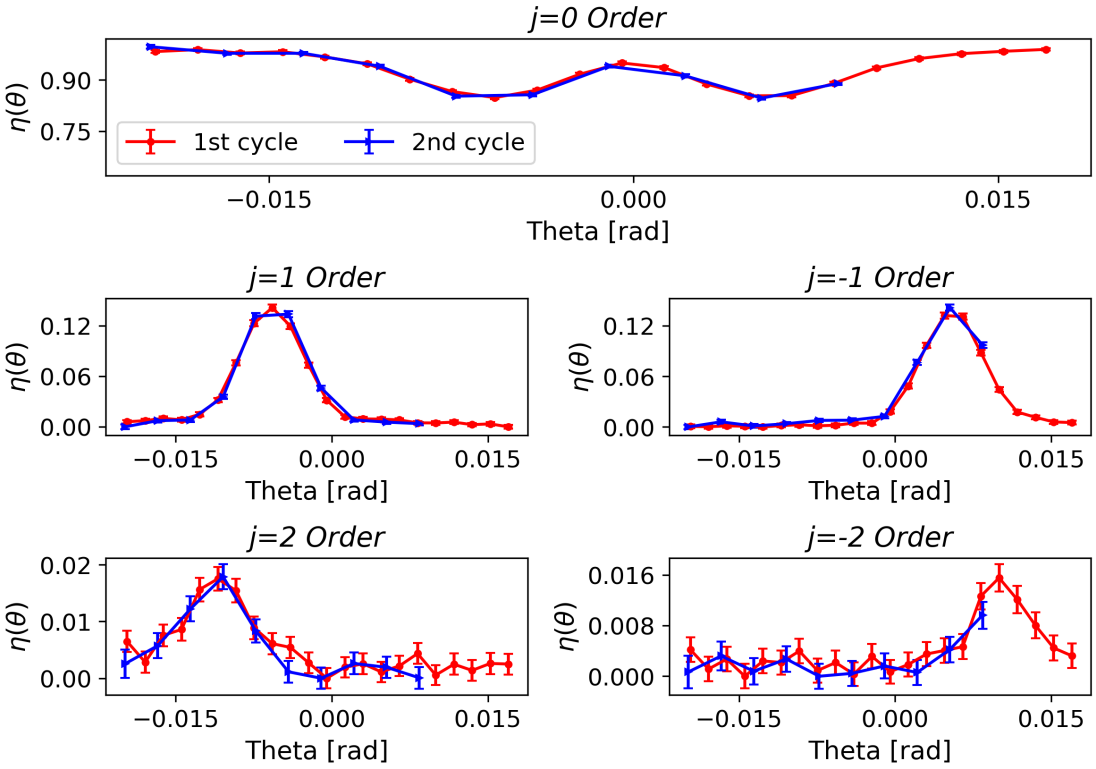

Figure 5.19: Comparison of neutron diffraction efficiency curves from two separate experimental campaigns using the "pp70_SP" sample, demonstrating the reproducibility of the setup and the stability of Bayfol gratings over time.

foil gratings considered in this study ($\eta_{\pm 1} = 14\%$). A 7-CW analysis including profile attenuation was applied, as shown in Figure 5.20. The goodness of the fit was evaluated by the calculation of the reduced chi-square $\chi_{red} = 1.29$, suggesting a good match between the data and model predictions. The best-fit parameters indicate a grating thickness $d_N = (69.3 \pm 1.7)\,\mu\text{m}$, with first and second-order thickness-averaged SLD modulation amplitudes of $\langle \Delta ß_1 \rangle = (2.6 \pm 1.1)\,\mu\text{m}^{-2}$ and $\langle \Delta ß_2 \rangle = -(0.9 \pm 0.4)\,\mu\text{m}^{-2}$, at a mean wavelength $\lambda_N = (4.6 \pm 0.2)\,\text{nm}$. The negative sign in $\langle \Delta ß_2 \rangle$ corresponds to a relative phase equal to π between first and second order FC of the refractive index modulation amplitudes. The estimated thickness is in good agreement with parameters obtained from fitting the measured light data, with two models used for fitting (see Figure M.9). The corresponding results are summarized in Table 5.8, supporting the consistency across different fitting models and using both light and neutrons for probing the material structure.

Model	**Thickness [µm]**	L **[µm]**	$\langle n_1 \rangle \times 10^{-3}$
Kogelnik	72.0 ± 0.3	N.A	15.6 ± 0.0
BVM with att.	71.3 ± 0.3	63.2 ± 4.9	15.8 ± 2.0

Table 5.8: Results from fitting light diffraction data measured from Bayfol "pp70_SP" sample using two models.

While the SLD modulation amplitudes are modest, they are good enough for performing proof-of-concept experiments. The potential use of commercial Bayfol foils

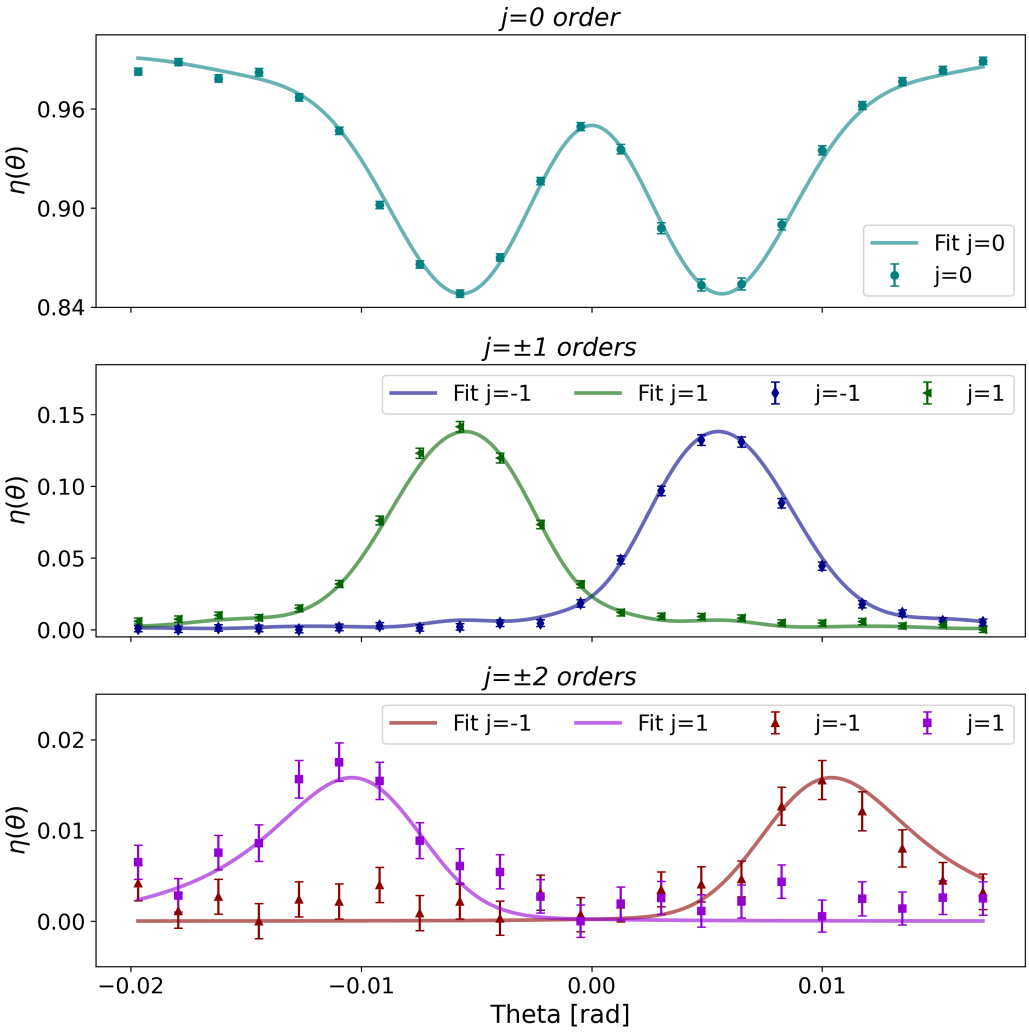

Figure 5.20: Measured diffraction efficiency curves for the "pp70_SP" Bayfol grating, along with 5-CW model fits incorporating refractive index attenuation.

for neutron diffraction applications has been demonstrated as a fine efficiency of 14% could be obtained without further increasing the grating thickness. The possibility of further enhancing efficiency exists through increased thickness by tilting, albeit at the cost of greater wavelength and angular selectivity.

5.2.4 Light and neutron diffraction results from an SPSP structure MVHG

The multilayer volume holographic grating, labeled "pp50_SPSP" in Table 3.5 is considered. As hinted by the label, the MVHG corresponds to an SPSP structure formed by two laminated SP films. Each of these films consists of a 50 µm photopolymer layer on the top of a triacetate cellulose (TAC) substrate that also have the same nominal thickness. The light diffraction measurement have also been performed at the laser lab of the University of Vienna using the same wavelength $\lambda_l = 543.5\,\text{nm}$. The neutron diffraction measurement was conducted at PF2/VCN instrument before the modernization program, using the setup described in Subsection 3.2.3.

The light optical data was evaluated using two different models for comparison: the TMM and the MCWA adaptation for MVHGs model described in Subsection 5.1.3. The purpose from this comparison is to explore the limitations of the Au's formulation [108], which is already superior to its KVCM variant suggested in Ref. [107] when compared to the developed MCWA model. The summary of all results from both models is provided in Table 5.9. For each of these models, two fitting procedures were used. For the latter, which is the model of choice in this study, a first fit has been performed with a fixed refractive index value for the substrate material $n_S = 1.485$. This value was measured using a prism coupler according to the Material description provided by the manufacturer [173]. Figure 5.21 shows a good match between the model predictions and the rapidly oscillating data, an expected feature of the structure for the used photopolymer and substrate thicknesses.

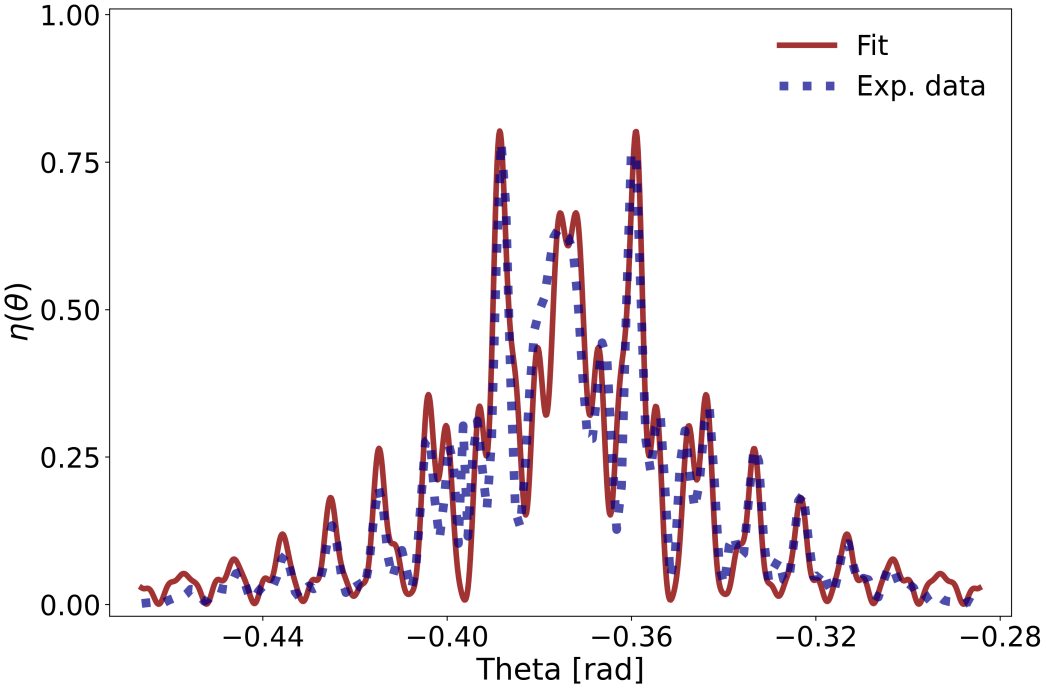

Figure 5.21: Light diffraction data (dotted line) from an SPSP structure and corresponding best match fit (darkred line) according to the BVM based multi-wave coupling theory adaptation for MVHGs.

Parameters	**MCWA fixed n_S**	**TMM-5**	**TMM-10**
d_{P1} [μm]	49.5 ± 0.2	48.6 ± 0.2	48.7 ± 0.2
d_S [μm]	55.0 ± 0.4	53.0 ± 0.2	52.9 ± 0.2
d_{P2} [μm]	42.1 ± 0.8	47.2 ± 0.5	47.3 ± 0.5
n_S	1.485	1.485	1.485
L [μm]	88.7 ± 1.7	44.2 ± 0.8	44.3 ± 0.8
$\langle n_1 \rangle \times 10^{-3}$	16.4 ± 0.5	14.0 ± 0.4	14.0 ± 0.4

Table 5.9: Comparison of fitting parameters from light diffraction data measured using an SPSP structure MVHG across different models.

The performed TMM fits-both with a fixed value for n_S-include a first model that di-

vides each modulated layer into 5 sublayers, and a second one that considers 10 sublayers. This was done in order to evaluate the effect of smoothing the attenuation. No notable deviations were observed between the smoothed and the less smoothed models predictions. Therefore, only the latter has been shown in Figure 5.22 for conciseness and clarity. Though, the TMM curves clearly show a lower quality fit to the data when compared to the MCWA model predictions, irrespective of the number of sublayers included. This means that the lower quality of the fits is not the result of a poor smoothing of the attenuation profile due to an insufficient number of sublayers, but rather inherent to Au's TMM formulation itself. This demonstrates the superiority of the MCWA model adaptation for MVHGs over the TMM model, which we described in the previous section as a BVM projection on a KVCM based formulation.

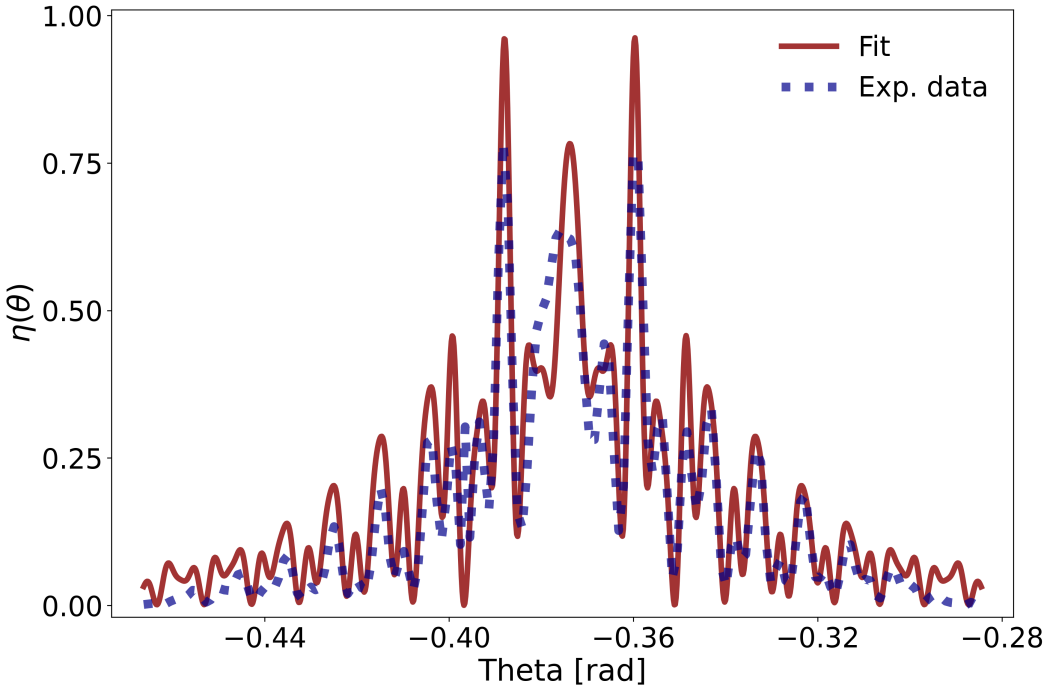

Figure 5.22: Light diffraction data (dotted line) from an SPSP structure and corresponding best match fit (darkred line) according to the TMM model with 10 sublayers per modulated layer.

Using neutrons to probe the considered sample structure, diffraction data has been collected and the diffraction efficiency curves have been derived using the approach presented in Chapter 4. The calculated efficiencies and their corresponding fits are displayed in Figure 5.23.
Unlike the light data, the neutron efficiency curves barely show any characteristic oscillations of MVHGs. This is not surprising, as they are averaged by the wide WLD of the VCN beam. The determined WLD from the fit is shown in Figure M.10, and includes a significant neutron flux from 2 nm-8 nm. Simulations using both TMM and MCWA models demonstrate the absence of any resolved characteristic oscillations for MVHGs when exposed to such a broad spectrum. The rapidly oscillating angular response from each wavelength component overlaps, creating an envelope-averaged profile. This profile is modulated by a frequency typical of a single-layer grating. The averaging across wavelengths and angles causes the oscillations to blend into a smooth, hand-drawn-like

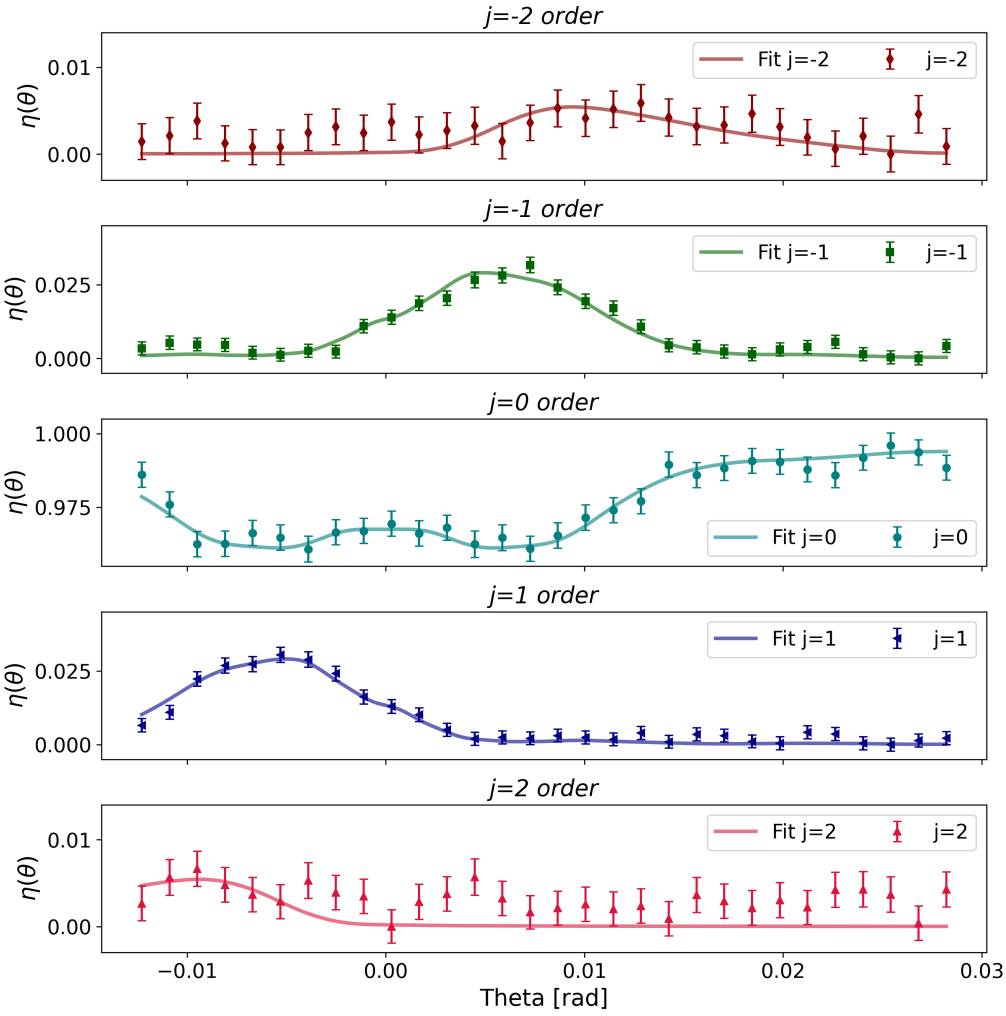

Figure 5.23: Neutron diffraction efficiency curves and corresponding fits for an SPSP structure MVHG.

curve. As a result, the fine structure of individual oscillations is obscured, and the angular response resembles that of a single-layer grating. For fitting the curves corresponding to the five diffracted orders, a 7-CW analysis has been performed. This involves first and second FC of the SLD modulation amplitudes and an attenuation profile according using a fixed decay length. The value determined from fitting the light data has been used. This choice has been made to reduce the already high number of fitting parameters: three parameters for the EMG WLD, three layer thicknesses for the SPSP structure and two FC of the modulation amplitudes. To further reduce the number of free parameters, two fitting procedures were performed, each using a fixed phase between the modulation amplitudes: one with a phase of 0 and the other with a phase of π. The latter better matches the data as demonstrated by the calculation of the reduced chi-square $\chi_{red} = 1.07$, and hence, it has been retained.

The determined thickness parameters are $(46.0 \pm 2.40)\,\mu m$, $(60.0 \pm 19.3)\,\mu m$ and $(25.0 \pm 33.3)\,\mu m$ for d_{P1}, d_S and d_{P2}, respectively. The results are fairly reasonable and non-contradictory of what has been obtained from light diffraction results. For the determination of the buffer layer SLD, an initial value was calculated us-

ing the chemical formula of TAC ($C_6H_7O_2(OOCCH_3)_3)_n$). It was determined using its density (1.29 g/cm^3) and molar mass (288 g/mol), yielding a number density of 2.697×10^{-3} Å^{-3}. Coherent neutron scattering lengths of 6.646 fm for carbon, -3.739 fm for hydrogen, and 5.803 fm for oxygen were used, with stoichiometries of 12, 16, and 8 respectively. The total coherent scattering length b_c was calculated as 66.352 fm. This, combined with the number density, resulted in an SLD of 1.790×10^{-6} Å^{-2}, equivalent to 179 μm^{-2}. However, the obtained value from the fit (≈ 399) has an extremely high uncertainty, several orders of magnitude larger than the value itself. This suggests that for precision measurements using such structures, it is essential to have a well-defined and fixed WLD, or ideally, to use a monochromatic VCN beam. Without these conditions, the high number of fitting parameters leads to greater ambiguity, making precise measurements unfeasible. The modulation amplitudes of the first and second order SLD modulation amplitudes are $\langle \Delta ß_1 \rangle = (1.6 \pm 0.9)\,\mu\text{m}^{-2}$ and $\langle \Delta ß_2 \rangle = -(0.8 \pm 0.5)\,\mu\text{m}^{-2}$, at an mean wavelength $\lambda_N = (4.3 \pm 0.8)$ nm.

To further validate the model for neutron diffraction analysis, a p-value of 27% has been calculated. This statistical parameter is used to evaluate a null hypothesis, which in this case states that the model accurately represents the data and that any observed discrepancies are due to random variation. The p-value, calculated using the chi-squared distribution, represents the probability of obtaining a result as extreme as the observed chi-squared value under the null hypothesis. In simpler terms, a p-value of 27% indicates that the result falls within typical percentiles, rather than in the most extreme (e.g., lowest 5%). Typically, a p-value below a threshold of 5% would indicate significant evidence against the null hypothesis, suggesting that the model does not fit well. Here, the calculated p-value is well above this threshold, providing no significant evidence against the null hypothesis. This result implies that the model aligns well with the data, with observed differences falling within expected random variations.

5.2.5 Neutron diffraction from a slanted light reflection grating

The spatial frequency of holographic gratings prepared using two beam mixing in transmission geometry cannot exceed a certain limit. This limit is set by the used wavelength (lowest is 488 nm for visible range laser) and the external recording angle which cannot be higher than approximately 70°. Consequently, the smallest period that can be obtained with this geometry is approximately $\Lambda_{\text{min}} = 260$ nm. While numerous industrial techniques now allow for recording gratings with much smaller periods, the objective here is to surpass this limit solely by adjusting the configuration, without the need to acquire or construct additional equipment beyond what is already available in the lab.

With the same recording wavelength employed for the recording of the previously presented Bayfol samples (λ_{rec}= 514 nm), slanted reflection gratings for light with a grating period $\Lambda \simeq (\lambda_{rec}/2n_0) = 172$ nm have been prepared by M. Fally [174]. Some of these samples were recorded using Denisyuk geometry [175]. A couple of these samples were tested with neutrons during the commissioning of the PF2 instrument after the installed upgrades, but no diffraction signal was measured. The reasons are not yet well-understood and could be due to the samples or due to other issues that were related to the commissioning at the time. Additionally, another setup was used for recording similar slanted reflection gratings for light, as depicted in Figure **??**. The

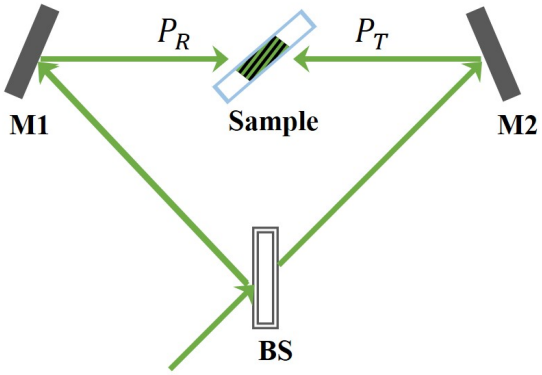

Figure 5.24: Sketch of the recording geometry for slanted light reflection gratings.

setup consists of using two (nearly) counter propagating p-polarized light beams and a rotated sample to an angle $\theta_{\text{br}} = 57.1^\circ$ with respect to the normal of its surface. The latter corresponds to the Brewster angle. The slant angle of the formed grating is 56.1°.
Neutron diffraction measurements have been performed at PF2/VCN platform during the 2023 experimental campaign (setup described in Subsection 3.2.3). At VCN wavelengths, the sample operates as a slanted transmission grating, not in reflection mode as for light. Neutron diffraction signal was successfully measured. The sum of all detector images from the rocking curve as well as the derived efficiency are displayed in Figure 5.25 and Figure 5.26, respectively.

The total sum of detector images clearly shows a diffracted spot corresponding to the first order. The spot is well-resolved and considerably separated from the forward diffracted beam thanks its small grating period. Unfortunately, as seen in the Figure 5.26, this was the last measurement during the 2023 experimental campaign, and it was interrupted by the reactor shutdown. Consequently, the angular range could not be further extended to measure a full rocking curve in order to analyze the structure. Though, the measured signal is already an unprecedented achievement that confirms the possibility of using such structures when larger spatial frequencies are desired. This opens the path for the use of small-period slanted reflection gratings for light as transmission gratings for diffracting neutrons.

5.3 Results from nanodiamond based NPC gratings

In this study, the considered nanodiamond dispersed polymer composites (NDPC) gratings were produced and delivered by our Japanese collaborators led by Prof. Yasuo Tomita. They also conducted the light diffraction measurements at a readout wavelength of 633 nm. Details about the composition and preparation of the samples have been presented in Section 3.1.2. The neutron diffraction measurements were performed at PF2/VCN platform using the 2021 experimental setup described in Section 3.2.3. Sample measurements were conducted consecutively within the same cycle to ensure consistency and comparability. The data reduction procedure elaborated in Chapter 4 was used for the the diffraction efficiency calculations. In this section, we will explore results from one representative sample of this material class. Next, results from all

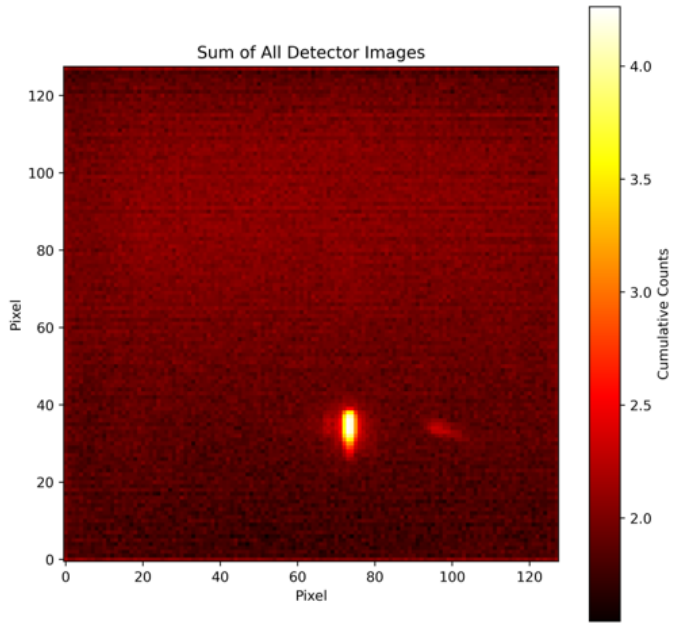

Figure 5.25: Sum of all detector images from the rocking curve, obtained from neutron diffraction measurement on a slanted grating in transmission mode.

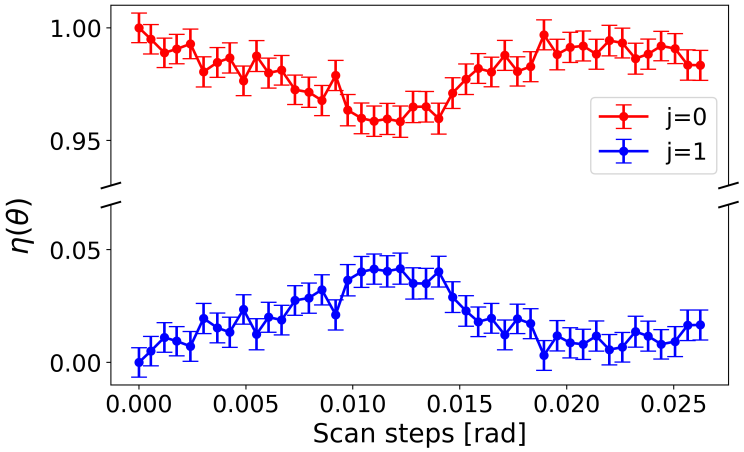

Figure 5.26: Restricted range neutron diffraction efficiency as a function of scan angle for the slanted grating.

measurements will be presented and discussed.

5.3.1 Results from representative samples of the studied NDPC gratings

In this Subsection, light and neutron optical performance of a couple of representative samples of the similarly prepared NDPC gratings under consideration will be explored.

Preliminary results from grating-6 have been shared in Ref. [176]. Additionally, a full exploration of the results from grating-1 has been communicated in Ref. [148], with an announcement of record breaking SLD modulation amplitudes for NPC gratings. The choice of grating-1 for this communication was based on the following criteria: undeniable reliability of the results which are obtained from a *full* rocking curve analysis, and the goodness of the fit reflected by the calculation of the reduced chi-square parameter $\chi_{red} = 1.20$. In fact, the analysis of the data collected from grating-7 revealed even greater modulation amplitudes and higher first order diffraction efficiency, however, the corresponding neutron diffraction measurement does not satisfy the previously stated criteria which are met by grating-1. Therefore, the latter has been selected for a thorough exploration.

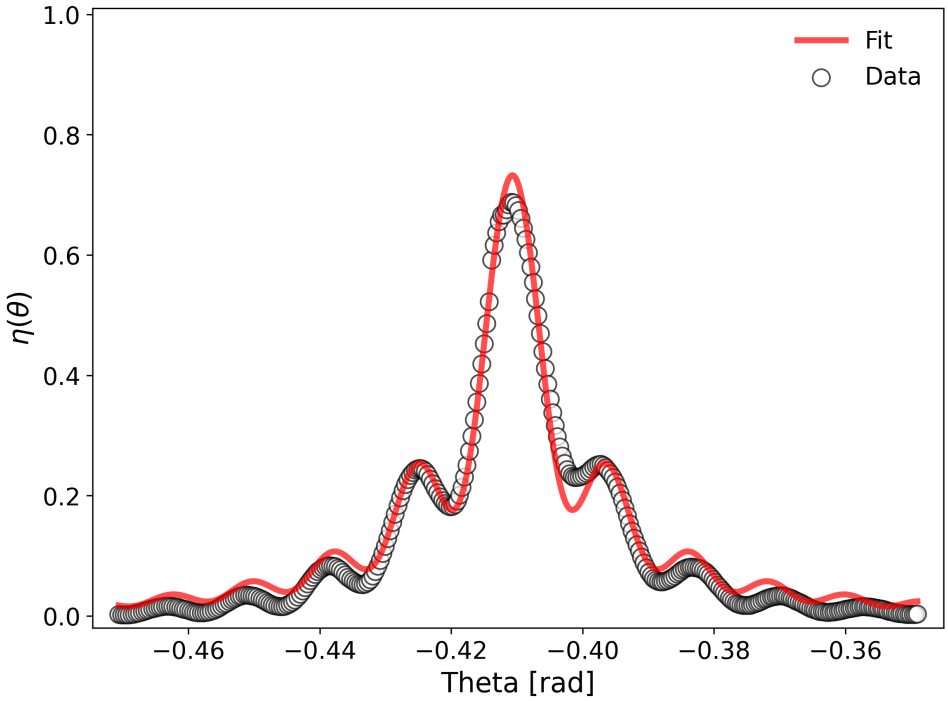

Figure 5.27: Light diffraction data (circular markers) from an NDPC grating and corresponding best match fit (red line) according to the 2-CW model with an Uchida-type attenuation. The readout wavelength is $\lambda_l = 633\,\text{nm}$

The grating recording and light diffraction measurement were carried out using a setup similar to the one shown in Figure 2 in Ref. [116]. Build-up dynamics (not-shown here) were followed using a readout wavelength of 633 nm until reaching saturation, as depicted in Figure 10 and Figure 11 in Ref. [22]. The saturated diffraction efficiency derived from the calculated light diffraction data and its corresponding best match fit are shown in Figure 5.27. The analysis was performed using a two-wave coupling that includes an exponential decay of the modulation. This revealed a grating thickness of $d = (42.9 \pm 0.2)\,\mu\text{m}$ and a strong attenuation reflected by a decay length $L \approx (d/2)$. The non-uniformity is apparent from the highly lifted side lobe minima, which is fairly captured by the fit. The observed asymmetry is the result of strong holographic effects in the recording of NPC gratings e.g. for the case of silica NPC films reported in Refs. [177, 178]. This secondary (often unwanted) scattering manifests by the observation of conical diffraction during the recording. It causes the deterioration of the

visibility of the interference pattern as it propagates through the sample, and may result in the formation of parasites gratings. The calculated thickness-averaged modulation amplitude according to Equation 2.34 is $\langle n_1 \rangle = (9.1 \pm 0.2) \times 10^{-3}$. This value demonstrates an improved optical performance of the three components photoinitiator system holograms compared to the calculated value for the sample reported in Ref. [148]. This corresponds to an increase by a factor of 4 to the highest reported value $\langle n_1 \rangle = (2.2 \pm 0.2) \times 10^{-3}$ in previous studies of NDPC gratings [22]. Moreover, the calculation of the volume fraction spatial modulation amplitude $\langle a_1 \Delta f \rangle = 0.021$ (See Equation 3.1) shows an increase of approximately four times when compared to previous results, instead of only three times as reported in Ref. [148]. The supremacy of this new generation of NDPC gratings is evident.

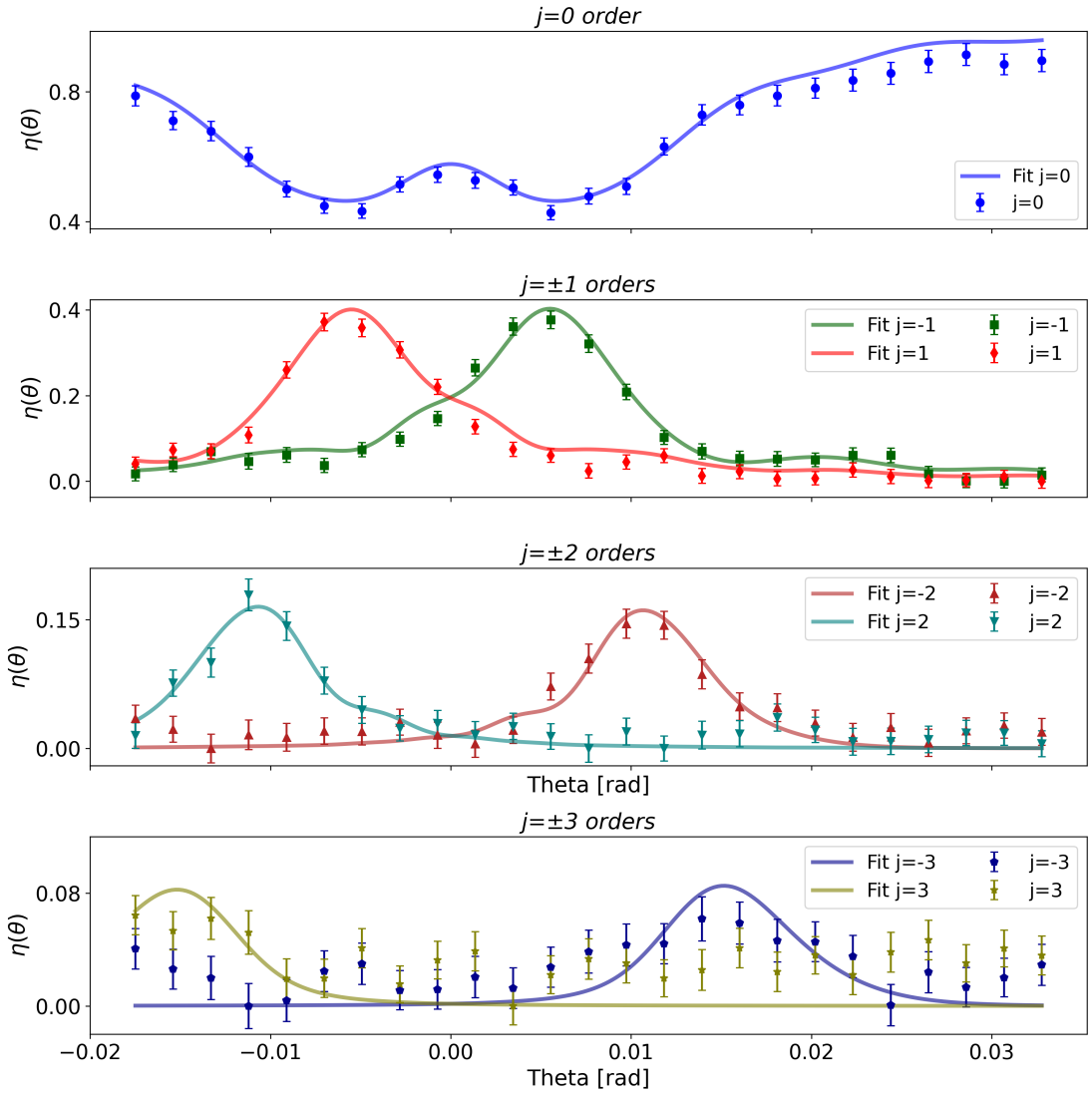

Figure 5.28: Neutron diffraction efficiency curves of the NDPC grating-7 (markers) and corresponding fits (lines) at a mean wavelength of 4.6 nm.

Neutron diffraction from these gratings also occurs in transmission mode. The derived diffraction efficiencies are based on the transmitted fraction of neutrons. Hence, it is essential to evaluate the transparency of the gratings. An empty measurement has

been performed for 600 seconds, and a frequency of approximately 24.23 counts/s has been measured. With an NDPC sample in place, frequencies around 21.4-22.3 counts/s is measured. This corresponds to an excellent transparency of approximately 90%. The derived neutron diffraction efficiency curves and their corresponding best match fits are shown in Figure 5.28. A very high diffraction efficiency of 40% has been reached for the first orders at zero-tilt at a mean wavelength $\lambda_N = (4.6 \pm 0.5)$ nm. This value is well-above any measured diffraction efficiency from the considered samples at zero-tilt, and also from any reported study of NDPC gratings. Moreover, the peaks are broad and do not show any angular or wavelength selectivity issues like those encountered in silica NPC gratings with mirror-like diffraction [19]. The determined WLD for this sample is depicted in Figure M.11. The diffraction regime has been inferred by the calculation of the Klein-Cook parameter $Q_{\mathrm{N}} = 5.4$ and the grating strength $\nu_{\mathrm{N}} = 0.5$, described in Subsection 2.6.1. The subsequent calculation of the following parameters $Q\nu = 5.1 > 1$ and $Q/(2\nu) = 2.9 < 10$ demonstrates that diffraction occurs in the intermediate regime. Consequently, the RCWA model has to be applied. However, its simplified multi-wave coupling is also applicable based on the legitimate approximations discussed previously.

For the considered sample, seven diffraction orders were measured. Therefore, a 9-CW analysis including three FC of the refractive index modulation and an EMG WLD has been applied. Non-optimal, but rather acceptable, goodness of the fit $\chi_{red} = 1.93$ has been achieved. The analysis revealed a grating thickness $d_{\mathrm{N}} = (46.6 \pm 1.8)$ µm and an attenuation length $L = (21.8 \pm 1.4)$ µm. The comparability between the estimates derived from light diffraction measurements and neutron diffraction measurements demonstrate that the effective longitudinal coherence length $\ell'_{//,c}$ of the incoming neutrons is sufficient for the study of the grating structure. The deduced thickness-averaged modulation amplitudes are $\Delta ß_1 = (8.8 \pm 0.9)\,\mu\mathrm{m}^{-2}$, $\Delta ß_2 = (-3.4 \pm 0.4)\,\mu\mathrm{m}^{-2}$ and $\Delta ß_3 = (2.7 \pm 0.4)\,\mu\mathrm{m}^{-2}$. These values correspond to extremely high refractive index modulation amplitudes $\langle n_1 \rangle \approx 2.9 \times 10^{-5}$, $\langle n_2 \rangle \approx -1.2 \times 10^{-5}$ and $\langle n_3 \rangle \approx 0.9 \times 10^{-5}$ for neutrons. They are comparable to the recently reported modulation results (see Ref. [148]), with the first-order Fourier coefficient of the refractive index modulation surpassing the previous record. Moreover, they are significantly higher than any previously reported values for NPC gratings.

The first-order diffraction efficiency at Bragg angle is about 20-40%, at zero-tilt, for this set of gratings evaluated under the same conditions and during the same experimental campaign. In order to explore Pendellösung effect, the effective thickness of some gratings have been increased. As depicted in Figure M.12, grating-5 has been tilted to 60° at a first time, which doubled the diffraction efficiency, and then to 70°, which resulted in a small decrease of the diffraction efficiency. This shows how the diffracted intensity is modulated by the thickness. Additionally, as shown in the previous Chapter, a diffraction efficiency of approximately 50% has been reached at zero-tilt for grating-5 using the longer wavelengths selected in the 2023 experimental campaign setup. In this case, the variation of the grating strength has been achieved by a change of the mean wavelength. On the other hand, during the 2021 campaign experiments, grating-4 has been tilted to 68°. This resulted in a clear rise of both first and second order efficiencies, reaching a maximum of approximately 60% for the former (See Figure M.13). Using the same 2021 setup, grating-1 allowed for reaching the highest measured first-order efficiency as depicted in Figure 5.29. This was achieved by tilt-

ing the grating to 69°, which corresponds to an effective thickness of approximately 90 µm. A common observation across all tilted grating measurements is that the peaks remained broad. No significant losses from angular/wavelength selectivity effects accompanied the increase of the effective thickness. Only negligible shifts in the mean wavelength towards shorter estimates were noted, as indicated by the small shifts in the Bragg angle positions. In brief, the excellent optical properties of these gratings can be explored by tuning adjustable parameters to respond to the requirements of VCN experiments.

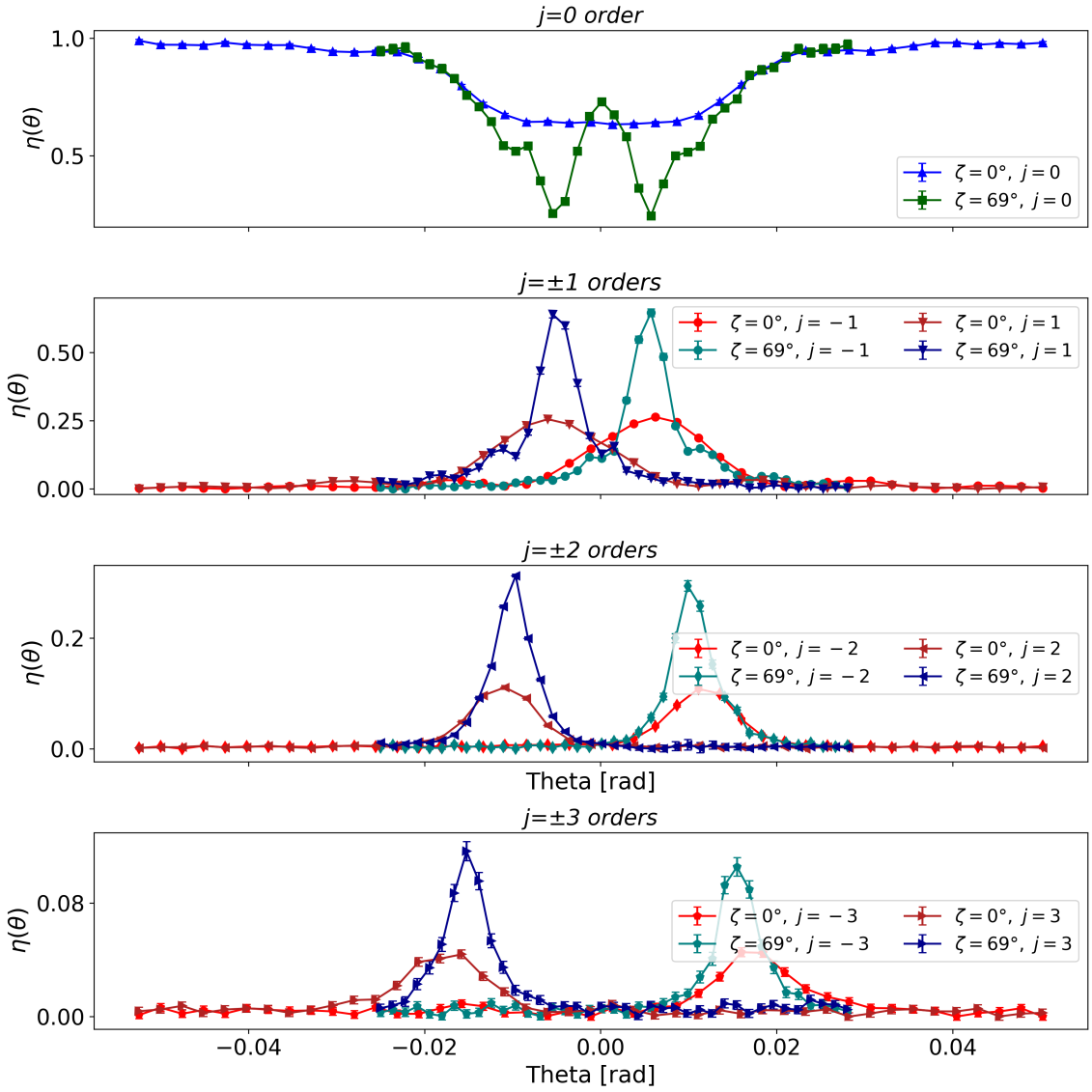

Figure 5.29: Diffraction efficiency curves of the NDPC grating-1 at 0° and 69° tilt angles measured at PF2/VCN instrument.

5.3.2 Summary of the NDPC gratings results

Table 5.10 and Table 5.11 summarize the results obtained from fitting the collected light and neutron diffraction data. In both cases, a multi-wave coupling model with

an attenuation profile has been used for the analysis.

Sample \ Results	Thick. [µm]	L [µm]	$n_1(z=0)\times10^{-3}$	$\langle n_1\rangle\times10^{-3}$	$\langle a_1\Delta f\rangle$
grating-1	33.0 ± 1.3	22.2 ± 0.3	12.3 ± 0.1	6.4 ± 0.1	0.015
grating-2	38.6 ± 0.2	21.1 ± 0.3	8.9 ± 0.1	4.1 ± 0.1	0.009
grating-3	32.7 ± 0.1	20.4 ± 0.25	10.7 ± 0.1	5.3 ± 0.1	0.012
grating-4	46.3 ± 0.4	26.6 ± 0.6	18.1 ± 0.3	8.5 ± 0.3	0.019
grating-5	46.6 ± 0.4	26.6 ± 0.6	18.0 ± 0.3	8.5 ± 0.3	0.019
grating-6	44.8 ± 0.3	21.4 ± 0.2	20.7 ± 0.2	8.7 ± 0.2	0.020
grating-7	42.9 ± 0.2	22.4 ± 0.3	20.5 ± 0.2	9.1 ± 0.2	0.021

Table 5.10: Summary of light diffraction results from NDPC gratings, obtained using a multi-wave coupling model with an attenuation profile for fitting. A readout wavelength of 633 nm was used in these measurements.

Sample	d_{N} [µm]	L [µm]	$\langle\Delta ß_1\rangle$	$\langle\Delta ß_2\rangle$	$\langle\Delta ß_3\rangle$	φ_2/π	φ_3/π
grating-1	32.0 ± 0.1	42.6 ± 2.0	8.2 ± 0.7	3.7 ± 0.3	1.6 ± 0.1	1.0 ± 0.0	0.0 ± 0.0
grating-2	39.1 ± 11.6	10.5 ± 1.2	3.9 ± 1.4	N.A	N.A	N.A	N.A
grating-3	30.1 ± 0.3	28.0 ± 1.9	7.2 ± 0.8	3.0 ± 0.3	1.8 ± 0.2	1.0 ± 0.0	0.0 ± 0.1
grating-4	47.8 ± 1.4	16.5 ± 0.4	4.3 ± 0.2	1.5 ± 0.1	0.8 ± 0.2	1	0
grating-5	43.2 ± 0.6	20.6 ± 0.5	6.0 ± 0.2	2.0 ± 0.1	1.1 ± 0.1	1	0
grating-6	47.6 ± 4.4	18.9 ± 2.0	6.5 ± 1.2	2.8 ± 0.5	1.8 ± 0.8	1	0
grating-7	46.6 ± 1.8	21.8 ± 1.4	8.8 ± 0.9	3.4 ± 0.4	2.7 ± 0.4	1.0 ± 0.0	0.0 ± 0.1

Table 5.11: Summary of neutron diffraction results from NDPC gratings, obtained using a BVM based two-wave coupling model with an attenuation profile for fitting. The neutron SLD modulation amplitudes are shown in $\mu\mathrm{m}^{-2}$ units.

The calculated parameters are fairly consistent among samples with similar compositions. In particular, gratings 1-3 and gratings 4-7 show comparable results within their respective groups. This emphasizes the stability of the production process for the nanodiamond-based NPC gratings and the reproducibility of light and neutron optical characteristics. Though, grating-2 shows a significant variability, suggesting non-optimal preparation compared to other samples. This is mainly attributed to variances related to manual manipulations in the preparation process of NDPC films, not to the composition of the sample. Moreover, despite overall consistency, minor variations are observed in the estimates of the decay length L, particularly in the neutron diffraction data. This variability is due to the broad WLD used in the measurements, which has similar effects to the attenuation L. This introduces some ambiguity in accurately determining L, leading to slight discrepancies in the decay length estimates. These effects highlight the limitations inherent in sample preparation and fitting of the neutron data under wide WLD conditions.

A notable enhancement in the thickness-averaged modulation estimates, $\langle n_1\rangle$, and the volume fraction spatial modulation amplitude $\langle a_1\Delta f\rangle$ has been achieved for gratings 4-7 compared to gratings 1-3. This demonstrates that the three-component photoinitiation system, which incorporates TCT, enhances the mutual diffusion mechanism and the formed hologram structure. On the other hand, the higher estimates of both light modulation amplitudes $\langle n_1\rangle$ and neutron SLD modulation amplitudes $\langle\Delta ß_1\rangle$ between gratings 4-5 (thicker substrate) and gratings 6-7 (thinner substrate) suggest that substrate thickness has an effect on the recording quality.

In brief, the compositional enhancements play a crucial role in achieving higher diffraction efficiencies, underscoring the importance of optimized formulations in developing high-performance HOEs. This advancement establishes new standards in VCN optics, highlighted by the unprecedented SLD modulation amplitudes achieved using NDPC materials.

5.4 Results from HBP dispersed NPC gratings

In order to investigate the neutron diffractive capabilities of a new class of material, hyperbranched polymer (HBP) dispersed nanocomposites have been considered. The HBP based NPC grating described in Subsection 3.1.4 was provided by our Japanese collaborators led by Prof. Yasuo Tomita along with its corresponding light data for the saturated diffraction efficiency [111]. The light data was collected using the setup shown in Figure 2 in Ref. [116]. The readout was performed using a readout wavelength of 532 nm provided that the prepared NPC film was red-sensitive. The saturated diffraction efficiency data along with its best match fit are shown in Figure 5.30.

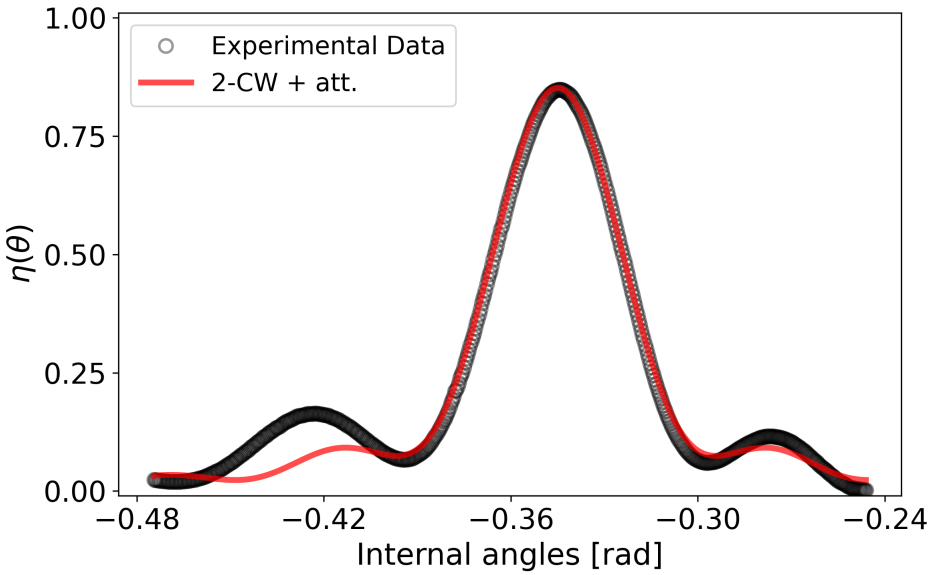

Figure 5.30: Light diffraction data (circular markers) from a HBP dispersed NPC grating and corresponding best match fit (red line). The readout wavelength is $\lambda_l = 532\,\text{nm}$

The evaluation was performed using a two-wave coupling model with an attenuation profile. The fit matches the data closely around Bragg angle, resulting in a modulation amplitude estimate $\langle n_1 \rangle = (19.1 \pm 0.6) \times 10^{-3}$. The diffraction efficiency is notably high despite the small sample thickness $d = (9.8 \pm 0.1)\,\mu\text{m}$. Far-off Bragg, the fit does not seem to fully capture the angular response of the grating, which shows highly asymmetric side lobes. The asymmetry's origin is known to be due to holographic scattering, which has been reported in Ref. [116]. This feature results in a non-accurate and unreasonable estimate of the attenuation length ($L \approx 6$) µm. This value is considered unreasonable because the reported value for the inverse of the absorption constant α in Ref. [116], at a recording wavelength λ_{rec}=640 nm, is 72 µm before the recording

and 725 µm after. this should allow, in principle, for the recording of uniform gratings that are two and three times thicker than this sample. Though, the evaluation using Kogelnik model and Tomita's empirical formula suggest similar values for the modulation amplitudes, the thickness and for the decay length (using Tomita's formula). The calculation of the volume fraction spatial modulation amplitude reveals an extremely high estimate $\langle a_1 \Delta f \rangle = 0.060$ (three times larger than the highest value for NDPC gratings).

Neutron diffraction from the HBP dispersed nanocomposite grating has been carried out at SANS-I instrument using the setup described in Subsection 3.2.4. The grating structure has been reconstructed using a neutron wavelength of 2 nm. The derived diffraction efficiency curves and their corresponding best match fits are shown in Figure 5.31.

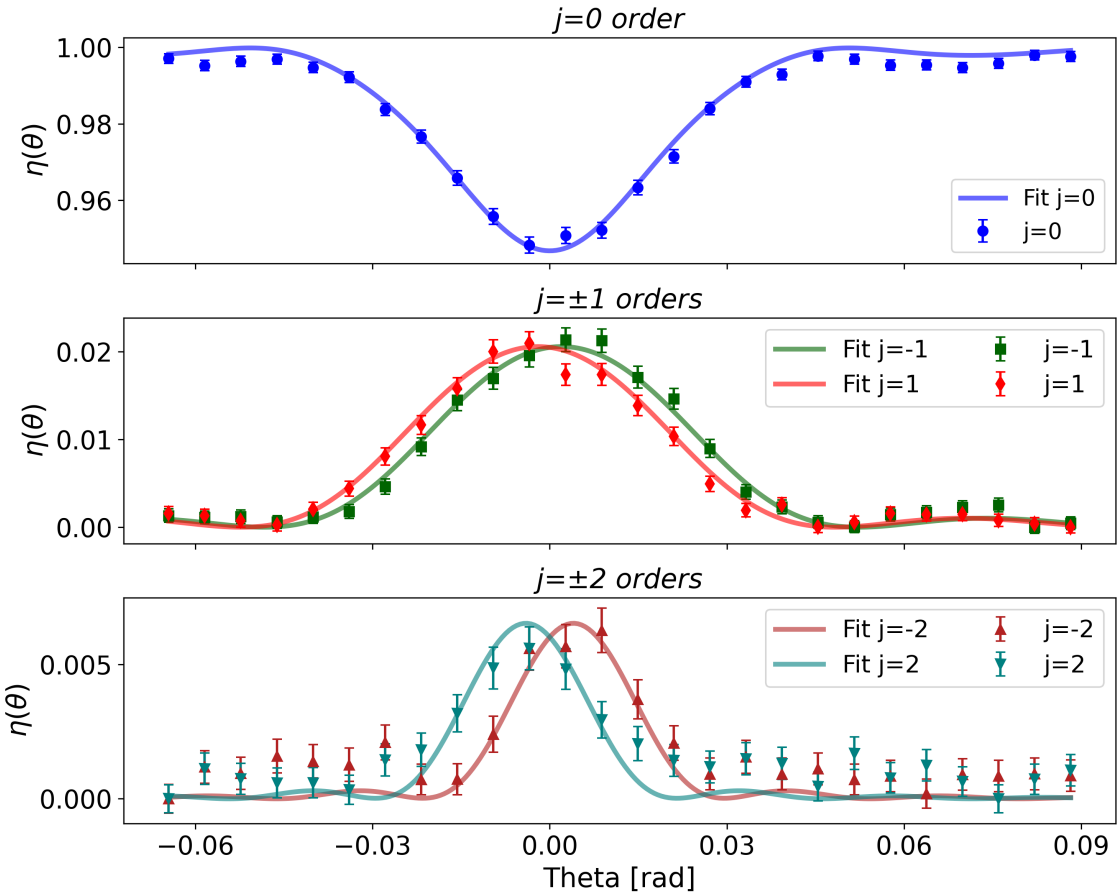

Figure 5.31: Neutron diffraction efficiency curves of the HBP dispersed NPC grating (markers) and corresponding fits (lines) at a wavelength of 2 nm. The sample was tilted to an angle $\zeta = 45$.

The analysis has been performed using a 7-CW model which involves two FC of the SLD modulation amplitudes. The goodness of the fit is not optimal, but acceptable with a reduced chi-square $\chi_{red} = 1.83$. The analysis revealed a grating thickness $d_N = (9.9 \pm 0.2)$ µm. The comparable estimates from light and neutron data analysis indicate that the effective longitudinal coherence length $\ell'_{//,c}$ of the monochromatic neutron beam is fairly sufficient. The deduced thickness-averaged modulation amplitudes are

$\Delta ß_1 = (14.9 \pm 0.2)\,\mu\mathrm{m}^{-2}$ and $\Delta ß_2 = (-8.2 \pm 0.3)\,\mu\mathrm{m}^{-2}$. The best match has been achieved using a fixed relative phase $\varphi_2 = \pi$ between these amplitudes, which is clear from the negative sign in the second order FC. These estimates are by far higher than any previously reported values for neutrons, even the recently published record values in Ref. [148] achieved with NDPC gratings.

In summary, this new class of material has been investigated for the first time for neutron diffraction applications. Surprisingly from the very first test, new record values of the SLD modulation have been achieved.

Chapter 6

Conclusions and perspectives

6.1 Summary of key findings

This study has advanced the understanding and application of light and neutron diffraction in holographic gratings by exploring and validating several theoretical models, investigating a range of novel materials, and developing techniques for optimal experimental and data reduction methods.

Theoretical model development and validation

A-1) Bayesian inference techniques in model comparison For the first time, Bayesian inference techniques, specifically Markov Chain Monte Carlo (MCMC) sampling and Bayesian Model Selection (BMS), were applied to evaluate theoretical models for diffraction in holographic gratings. A comparative analysis between the K-vector Closure Method (KVCM) and Beta-Value Method (BVM) boundary conditions demonstrated the efficacy of the BVM model for the considered data, particularly when enhanced with an Uchida-type attenuation profile. Bayesian inference facilitated a more comprehensive evaluation by enabling the exploration of a wide parameter space and by providing posterior distributions rather than simple point estimates. This approach proves especially valuable in cases of samples with multiple sources of nonuniformity, offering insights that support more informed model selection. While Bayesian techniques offer notable advantages, their application to neutron diffraction, where multiple diffracted orders and refractive index modulation amplitudes further complicate models, faces challenges from computational demands, especially under broad WLD. This work demonstrates the benefits and highlights the potential limitations of these methods, establishing a foundation for model evaluation and future implementation in neutron optics.

A-2) Validation of the simplified multi-wave coupling model The simplified multi-wave coupling model, derived in Chapter 2, was compared to the Rigorous Coupled-Wave Analysis (RCWA) model and yielded congruent results under typical experimental and grating parameters. This validation underscores the legitimacy of the approximations employed. The conditions in which these simplifications remain valid have been discussed. This finding supports the use of this streamlined model as

a reliable and computationally efficient alternative to the RCWA approach, reducing the numerical burden in diffraction modeling for both light and neutron data analysis.

A-3) Exploration of the transfer matrix method (TMM) theoretical model and the adaptation of the multi-wave coupling model for MVHGs An exploration of the Transfer Matrix Method (TMM) model, initially presented in Chapter 2, was conducted to assess its sensitivity to the scattering length density (SLD) of buffer layers in multilayer volume holographic gratings (MVHGs). This sensitivity suggests the applicability of these structures as microscale interferometers for neutrons. Though, the magnitude of the differences induced by a change of the substrate SLD poses some challenges at the detection and data reduction sides. Additionally, a multi-wave coupling model inspired by the TMM has been developed specifically for neutron diffraction in MVHGs. Unlike the latter, which is limited to applications involving only two coupled waves under the Bragg diffraction regime, the multi-wave coupling model accommodates the presence of multiple waves—typically more than three—which are intrinsic to neutron diffraction. By comparing this new model to the TMM under Bragg conditions, further insights into model applicability and boundary conditions were gained, highlighting the necessity of a tailored approach for neutron diffraction modeling.

Material-specific findings

- **Bayfol photopolymer gratings:** Single-layer Bayfol foils demonstrated strong performance for both light and neutron diffraction. A significant finding was the alignment of optimal conditions for light and neutron applications, with specific writing intensities and dosages enhancing performance based on the NPDD reaction-diffusion model. Furthermore, Bayfol's stability over time was validated by consistent results across different measurement cycles, highlighting its reliability for neutron diffraction applications. The versatility of the material has been explored for a couple of proof-of-concept experiments. The possibility of stacking the material layers allowed for the creation of an MVHG structure. It has been used to experimentally demonstrate the sensitivity of the MCWA adaptation for modeling MVHGs to changes in the scattering length density (SLD) of buffer layers. The angular response of these structures under a wide neutron WLD has been studied and averaging effects have been noted. The potential use of multilayer gratings as microscale interferometers has been experimentally demonstrated and corresponding challenges have been identified. In particular, the increased number of fitting parameters presented challenges when a broad wavelength distribution was employed, indicating a need for precise parameter control and for the use of a monochromatic beam (or a fixed and well-known WLD) in future investigations.

- **NDPC gratings:** Nanodiamond-based nanoparticle composite gratings achieved record-breaking SLD modulation amplitudes, a central accomplishment of this study. These gratings offer a unique combination of high diffraction efficiency and minimal loss from angular and wavelength selectivity. Their robust structural properties and large cross-sectional area simplify high-tilt experimental configurations, making them versatile and accessible for a wide range of applications.

The introduction of the third photoinitiator component, TCT, has further optimized the grating structure, improving the spatial uniformity and performance of the hologram. Future compositional refinements, particularly in the RB dye concentration, are underway at the University of Vienna to mitigate the inherent nonuniformities introduced by RB while maintaining its free radical generation efficiency.

- **HBP dispersed NPC gratings:** A new frontier in neutron diffraction applications was opened with hyperbranched polymer dispersed NPC gratings, provided by Japanese collaborators [111], which have shown potential to set new benchmarks in SLD modulation amplitude. The first ever experiment using neutrons demonstrated outstanding SLD modulation, surpassing previously achieved values with NDPC gratings. However, due to the short grating length and limited neutron wavelength used, the diffraction efficiency was relatively low. Future studies should focus on producing thicker holograms and employing longer neutron wavelengths to harness the full potential of these materials. Additionally, light diffraction experiments revealed a high modulation amplitude of $\langle n_1 \rangle \approx 19.1 \times 10^{-3}$, indicating strong performance. While this result is impressive, even higher modulation amplitudes—up to 40×10^{-3}—have been reported in the literature. These findings suggest that this new class of materials holds significant potential to set new standards in neutron diffraction applications, given its demonstrated capabilities.

6.2 Implications, future perspectives, and concluding remarks

This study has provided substantial advancements in theoretical model selection, material development, and experimental methodologies for light and neutron diffraction in holographic gratings. Building on these findings, several directions are proposed to further enhance the application and development of these materials and models in light and neutron optics.

- **Theoretical model adaptation and comparative analysis:** With the successful validation of the BVM model incorporating an attenuation profile for the analysis of diffraction data from strongly modulated holographic gratings, future work could further expand the use of Bayesian inference methods to compare other models. For example, a comparative analysis between rigorous methods, such as the RCWA theory and Rigorous Modal Theory, could yield deeper insights into the effectiveness and limitations of each theory across different diffraction regimes. Refining these approaches will help define criteria for selecting the most suitable model for varying experimental setups and conditions.

- **Insights from Bayfol photopolymers and implications for advanced neutron optics:** The observation that both neutron and light diffraction results from Bayfol gratings exhibited the same tendencies and variations of the optical performance under varying writing intensities, nominal photopolymer thicknesses, and recording dosages underscores the alignment with the non-local

photopolymerization-driven diffusion (NPDD) model. This consistency highlights the potential for more targeted modeling and simulations to refine our understanding of holographic grating formation. Furthermore, the demonstrated sensitivity of multilayer gratings to the refractive index (or neutron SLD) of buffer layers using both simulations and modeling of experimental data opens new opportunities for exploring neutron microscale interferometry. The notable impact of a broad neutron WLD has emphasized the importance of using a monochromatic beam to achieve the precision required for such applications, and to reduce ambiguities in parameter determination. This is particularly significant given the challenges associated with preparing MVHGs and the increased number of parameters to consider compared to single gratings. These insights lay a solid foundation for optimizing future designs and experimental setups, enabling more precise and effective applications in neutron optics. Nevertheless, the explored capability of Bayfol material to record small-period slanted gratings, even at the limits imposed by available laser sources, introduces new pathways for optimizing neutron diffraction in space-constrained setups. Future studies focusing on more efficient, slanted and small-period neutron transmission gratings could address part of the challenges in platforms like PF2/VCN, where higher diffraction angles are essential for effective beam manipulation in limited spaces.

- **Material composition and structural optimization:** The high-performance results of NDPC and HBP-based NPC gratings point to the need for continued material composition studies, particularly to improve uniformity and optimize diffraction efficiency. Adjustments in the concentration of RB dye and the composition of photoinitiator systems could enhance SLD modulation amplitudes and structural stability, supporting even more robust applications in neutron optics.

- **Development of a new VCN interferometer with NDPC holographic gratings:** Planned tests for 2025 at the PF2/VCN instrument aim to evaluate a new very cold neutron interferometer employing the highly efficient NDPC gratings presented in this research. This initiative holds promise for expanding the utility of NDPC materials in neutron interferometry, potentially opening new applications and advancing the field of cold and very cold neutron optics.

This research bridges a critical gap in neutron diffraction by advancing the practical utility of nanodiamond dispersed nanoparticle polymer composites, hyperbranched polymer composites, and Bayfol photopolymers, providing experimental insights that highlight their potential for neutron optical applications. The study demonstrated the adaptability of these materials, including record-breaking SLD modulation amplitudes and optimized grating performance, establishing a strong foundation for future developments. Building on these experimental achievements, this thesis also explored and adapted theoretical models, leading to the development of a simplified and efficient framework for analyzing neutron diffraction data from holographic gratings. These advancements not only refined our understanding of light and neutron optical performance but also unveiled the underlying physics of the holographic recording process that drives material functionality. Moreover, the established models and methodologies offer broader applicability to single-layer and multilayer systems, expanding their utility beyond the specific materials studied here. Collectively, these contributions

establish a versatile platform for interdisciplinary research, fostering innovations in neutron diffraction, materials science, and experimental physics.

Appendix A: Equation of wave propagation

In rigorous methods, it is proposed to solve the following Maxwell equations for the particular case of non magnetic, isotropic and lossless dielectric media in the absence of free charge.

$$\nabla \cdot \vec{\mathrm{E}} = 0 \quad ; \qquad \nabla \times \vec{\mathrm{E}} = -\mu_0 \frac{\partial \vec{\mathrm{H}}}{\partial t} \tag{A.1}$$

$$\nabla \cdot \vec{\mathrm{H}} = 0 \quad ; \qquad \nabla \times \vec{\mathrm{H}} = \epsilon_v \epsilon_r \frac{\partial \vec{\mathrm{E}}}{\partial t} \tag{A.2}$$

Here, $\vec{\mathrm{E}}$ and $\vec{\mathrm{H}}$ denote the electric and the magnetic fields, respectively. These equations are solved in order to describe wave propagation in planar phase gratings **1)** Analytically, in the case of two coupled waves **2)** Numerically for multiple coupled waves. For this purpose, a list of assumptions is defined to simplify the tasks. Whether an assumption is legitimate or not will be discussed later. For the case of multiple coupled waves, a more rigorous numerical approach will be adopted, in a pragmatic sense regarding compile time [52, 56].

For a given vector $\vec{\mathrm{A}}$, one can write $\nabla \times (\nabla \times \vec{\mathrm{A}}) = -\nabla^2 \vec{\mathrm{A}} + \nabla(\nabla \cdot \vec{\mathrm{A}})$. It is then possible to establish this equality using Equation A.1 and Equation A.2:

$$\nabla \times (\nabla \times \vec{\mathrm{E}}) = -\nabla^2 \vec{\mathrm{E}} = -\mu_0 \frac{\partial \nabla \times \vec{\mathrm{H}}}{\partial t} = -\mu_0 \epsilon_v \epsilon_r \frac{\partial^2 \vec{\mathrm{E}}}{\partial t^2}$$

Consequently:

$$\nabla^2 \vec{\mathrm{E}}(\vec{\mathrm{r}}, t) - \mu_0 \epsilon_v \epsilon_r \frac{\partial^2 \vec{\mathrm{E}}(\vec{\mathrm{r}}, t)}{\partial t^2} = 0 \tag{A.3}$$

For a more general form that involves losses (only lossless gratings are considered here), Equation A1-10 in Syms Practical book of holography [79] is referred to. Otherwise, one gets this expression from the calculation of $\nabla \times (\nabla \times \vec{\mathrm{H}})$:

$$\nabla^2 \vec{\mathrm{H}}(\vec{\mathrm{r}}, t) - \mu_0 \epsilon_v \epsilon_r \frac{\partial^2 \vec{\mathrm{H}}(\vec{\mathrm{r}}, t)}{\partial t^2} = 0 \tag{A.4}$$

Both the electric and the magnetic fields propagate as a periodic electromagnetic wave in space and time. A plane wave solution to Equation A.3 takes this form:

$$\vec{\mathrm{E}}(\vec{\mathrm{r}}, t) = \vec{\mathrm{E}}(\vec{\mathrm{r}} + \vec{\lambda}, t) = \vec{\mathrm{E}}(\vec{\mathrm{r}}, t + T) = \vec{\mathrm{E}}_0 \exp\left[\imath(\vec{\mathrm{k}} \cdot \vec{\mathrm{r}}\sqrt{\epsilon_r} - \omega t)\right] \tag{A.5}$$

The modulus of $\vec{\mathrm{E}}_0$ is the amplitude of the wave, and its orientation defines the instantaneous polarization of the field. As $\exp\left(\imath\sqrt{\epsilon_r}\vec{\mathrm{k}}(\vec{\lambda}/\sqrt{\epsilon_r}\right) = \exp\left(\imath\omega T\right) = 1$, the

propagation vector $\vec{\mathrm{k}}$ and the temporal period T are defined as follows, given that C is the speed of the wave in free space.

$$|\vec{\mathrm{k}}| = k = \frac{2\pi}{\lambda} \quad ; \quad T = \frac{2\pi}{\omega} \tag{A.6}$$
$$k\lambda = \omega T \implies k = \omega\frac{T}{\lambda} = \frac{\omega}{C}$$

The nature of the propagating wave can be determined as follows:

$$\nabla \times \vec{\mathrm{E}} = (\imath\epsilon_r^{1/2}\vec{\mathrm{k}}) \times \vec{\mathrm{E}} = \imath\omega\mu_0\vec{\mathrm{H}}$$
$$\implies \epsilon_r^{1/2}\vec{\mathrm{k}} \times \vec{\mathrm{E}} = \frac{\omega}{C}\sqrt{\frac{\mu_0}{\epsilon_v}}\vec{\mathrm{H}} \tag{A.7}$$
$$\nabla \times \vec{\mathrm{H}} = (\imath\epsilon_r^{1/2}\vec{\mathrm{k}}) \times \vec{\mathrm{H}} = -\imath\omega\epsilon_v\epsilon_r\vec{\mathrm{E}}$$
$$\implies \epsilon_r^{1/2}\vec{\mathrm{k}} \times \vec{\mathrm{H}} = -\frac{\omega}{C}\epsilon_r\sqrt{\frac{\epsilon_v}{\mu_0}}\vec{\mathrm{E}} \tag{A.8}$$

The wave is transverse as both fields oscillate in an orthogonal plane with respect to the propagation vector. Therefore, based on Assumption 2.1, Equation A.5 can be rewritten as a plane wave with a complex amplitude that only depends on the x and z parameters. his assumption allows the electric field to be represented by a single scalar component, simplifying the vector wave equation to a scalar form that captures the field behavior in the $x - z$ plane.

$$\mathrm{E}(\vec{\mathrm{r}}, t) = \tilde{\mathrm{E}}(x, z)\exp(-\imath\omega t) \Rightarrow \frac{\partial^2\mathrm{E}}{\partial t^2} = -\omega^2\mathrm{E}$$

Consequently:

$$\nabla^2\tilde{\mathrm{E}}(x, z) + \frac{\omega^2\epsilon_r}{C^2}\tilde{\mathrm{E}}(x, z) = 0$$

Appendix B: Solving the first order coupled waves equations from Kogelnik's theory

The following KVCM 1-st order differential equations system is obtained after disregarding second derivatives:

$$\begin{aligned}
\frac{\partial^2}{\partial x^2}\tilde{\mathrm{E}}(x,z) &= -\rho_x^2\tilde{R}(z)\exp\left[-\imath(\rho_x x+\rho_z z)\right]-\delta_x^2\tilde{S}(z)\exp\left[-\imath(\delta_x x+\delta_z z)\right]\\
\frac{\partial^2}{\partial y^2}\tilde{\mathrm{E}}(x,z) &= 0\\
\frac{\partial^2}{\partial z^2}\tilde{\mathrm{E}}(x,z) &= -2\imath\rho_z\left[\tilde{R}'(z)\exp\left[-\imath(\rho_x x+\rho_z z)\right]+\tilde{S}'(z)\exp\left[-\imath(\delta_x x+\delta_z z)\right]\right]\\
&\quad-\rho_z^2\left[\tilde{R}(z)\exp\left[-\imath(\rho_x x+\rho_z z)\right]+\tilde{S}(z)\exp\left[-\imath(\delta_x x+\delta_z z)\right]\right]
\end{aligned}$$

Now, summing:

$$\begin{aligned}
\nabla^2\tilde{\mathrm{E}}(x,z) &= -\beta^2\tilde{R}(z)\exp\left[-\imath(\rho_x x+\rho_z z)\right]- \delta^2\tilde{S}(z)\exp\left[-\imath(\delta_x x+\delta_z z)\right]\\
&\quad-2\imath\rho_z\left[\tilde{R}'(z)\exp\left[-\imath(\rho_x x+\rho_z z)\right]+\tilde{S}'(z)\exp\left[-\imath(\delta_x x+\delta_z z)\right]\right]
\end{aligned}\tag{B.1}$$

And using Equation 2.6 and Equation 2.7, the second part of the system is calculated:

$$\begin{aligned}
&k^2n^2(x)\tilde{\mathrm{E}}(x,z) = \left[\beta^2+2\beta\kappa\left(\exp\left(\imath Kx\right)+\exp\left(-\imath Kx\right)\right)\right]\tilde{\mathrm{E}}(x,z)\\
&=\left[\beta^2+2\beta\kappa\left(\exp\left(\imath Kx\right)+\exp\left(-\imath Kx\right)\right)\right]\left[\tilde{R}(z)\exp\left[-\imath(\rho_x x+\rho_z z)\right]+\tilde{S}(z)\exp\left[-\imath(\delta_x x+\delta_z z)\right]\right]\\
&=\beta^2\tilde{\mathrm{E}}(x,z)+2\beta\kappa\tilde{R}(z)\left[\exp\left(-\imath\vec{\delta}\cdot\vec{r}\right)+\exp\left(-\imath(\vec{\rho}+\vec{K})\cdot\vec{r}\right]\right.\\
&+2\beta\kappa\tilde{S}(z)\left[\exp\left(-\imath\vec{\rho}\cdot\vec{r}\right)+\exp\left(-\imath(\vec{\delta}-\vec{K})\cdot\vec{r}\right)\right]
\end{aligned}$$

One can clearly observe how κ couples the reference wave $\tilde{R}$ with the signal wave $\tilde{S}$. Moreover, the terms with $\vec{\rho}+\vec{K}$ and $\vec{\delta}-\vec{K}$ are neglected.

$$\begin{aligned}
k^2n^2\tilde{\mathrm{E}}(x,z) &= \beta^2\left[\tilde{R}(z)\exp\left(-\imath\vec{\rho}\cdot\vec{r}\right)+\tilde{S}(z)\exp\left(-\imath\vec{\delta}\cdot\vec{r}\right)\right]\\
&+ 2\beta\kappa\tilde{R}(z)\exp\left(-\imath\vec{\delta}\cdot\vec{r}\right)+2\beta\kappa\tilde{S}(z)\exp\left(-\imath\vec{\rho}\cdot\vec{r}\right)
\end{aligned}\tag{B.2}$$

Summing Equation B.2 and Equation B.1:

$$\begin{aligned}
(\beta^2-\delta^2)\tilde{S}\exp\left(-\imath\vec{\delta}\cdot\vec{r}\right)-2\imath\rho_z\left[\tilde{R}'\exp\left(-\imath\vec{\rho}\cdot\vec{r}\right)+\tilde{S}'\exp\left(-\imath\vec{\delta}\cdot\vec{r}\right)\right]\\
+2\kappa\beta\tilde{R}\exp\left(-\imath\vec{\delta}\cdot\vec{r}\right)+2\beta\kappa\tilde{S}\exp\left(-\imath\vec{\rho}\cdot\vec{r}\right) = 0
\end{aligned}\tag{B.3}$$

It is now possible to derive first order differential equations of two coupled waves by arranging the terms according to their propagation directions:

$$c_z \quad \tilde{R}' = -\imath\kappa\tilde{S} \tag{B.4}$$

$$c_z \quad \tilde{S}' + \imath\vartheta\tilde{S} = -\imath\kappa\tilde{R} \tag{B.5}$$

With $c_z = \frac{\rho_z}{\beta} = \cos\theta$ being the unique obliquity factor in the case of unslanted gratings where $\rho_z = \sigma_z$. For transmission gratings, the following boundary conditions are considered:

$$\tilde{R}(z=0) = 1 \quad ; \quad \tilde{S}(z=0) = 0 \tag{B.6}$$

Consequently, one can derive these two extra boundary conditions:

$$\tilde{R}'(z=0) \;= -\frac{\imath\kappa}{c_z}\tilde{S}(0) \implies \tilde{R}'(0) = 0 \tag{B.7}$$

$$\tilde{S}'(z=0) \;= -\frac{\imath\kappa}{c_z}\tilde{R}(0) - \frac{\imath\vartheta}{c_z}\tilde{S}(0) \implies \tilde{S}'(0) = \frac{-\imath\kappa}{c_z} \tag{B.8}$$

These equations reflect Kogelnik's physical model: the signal and the reference waves are coupled through κ, while the dephasing constant destroys the synchronism between the two waves as one moves far from Bragg. Multiplying Equation B.4 by $\tilde{R}^*$ (the complex conjugate of $\tilde{R}$) and Equation B.5 by $\tilde{S}^*$, and summing the results together with results from the complex conjugates of theses equations, one gets the energy balance relation of Kogelnik's model, which also indicates the conservation of the power flux in the z-direction for this particular case of a lossless dielectric grating.

$$\left(\tilde{R}\tilde{R}^* + \tilde{S}\tilde{S}^*\right)' = 0 \tag{B.9}$$

From Equation B.4, one gets $\tilde{S}' = \frac{\imath c_z}{\kappa}\tilde{R}''$. Inserting this into Equation B.5 this second order differential equation to solve for $\tilde{R}$ is obtained.

$$\tilde{R}'' + \frac{\imath\vartheta}{c_z}\tilde{R}' + \frac{\kappa^2}{c_z^2}\tilde{R} = 0 \tag{B.10}$$

The square root of the discriminant $\sqrt{\Delta} = \pm\frac{\imath}{c_z}\sqrt{\vartheta^2 + (2\kappa)^2}$ and the roots of this equation are:

$$\gamma_{1,2} = \frac{-\imath}{2c_z}\left(\vartheta \pm \sqrt{\vartheta^2 + (2\kappa)^2}\right) \tag{B.11}$$

And the solution to Equation B.10 is:

$$\tilde{R}(z) = A\exp(\gamma_1 z) + B\exp(\gamma_2 z) \tag{B.12}$$

A and B are determined using the boundary conditions for a transmission grating:

$$\begin{aligned}
&\tilde{R}(0) = 1 \implies A + B = 1 \\
&\tilde{R}'(0) = 0 \implies A\gamma_1 + B\gamma_2 = 0 \\
\implies &A = \frac{\gamma_2}{\gamma_2 - \gamma_1} \quad ; \quad B = \frac{-\gamma_1}{\gamma_2 - \gamma_1} \\
\implies &\tilde{R}(z) = \frac{\gamma_2}{\gamma_2 - \gamma_1}\exp(\gamma_1 z) - \frac{\gamma_1}{\gamma_2 - \gamma_1}\exp(\gamma_2 z)
\end{aligned}$$

Given that $\gamma_1\gamma_2 = (\frac{\kappa}{c_z})^2$ and $\tilde{S}(z) = \frac{\imath c_z}{\kappa}\tilde{R}'$, the solutions can be written as follows:

$$\tilde{R}(z) = \frac{1}{\gamma_2 - \gamma_1}\left[\gamma_2 \exp(\gamma_1 z) - \gamma_1 \exp(\gamma_2 z)\right] \tag{B.13}$$

$$\tilde{S}(z) = \frac{\imath\kappa}{c_z(\gamma_2 - \gamma 1)}\left[\exp(\gamma_1 z) - \exp(\gamma_2 z)\right] \tag{B.14}$$

Next, it is possible to check the validity of the approximation $\tilde{R}'' \ll \rho_z\ \tilde{R}'$ and $\tilde{S}'' \ll \delta_z\ \tilde{S}'$ by calculating the derivatives of $\tilde{R}$ and $\tilde{S}$.

$$\begin{aligned}
\tilde{R}'(z) &= \frac{\gamma_1\gamma_2}{\gamma_2 - \gamma_1}\left[\exp(\gamma_1 z) - \exp(\gamma_2 z)\right] \\
\tilde{S}'(z) &= \frac{\imath\kappa}{c_z(\gamma_2 - \gamma 1)}\left[\gamma_1 \exp(\gamma_1 z) - \gamma_2 \exp(\gamma_2 z)\right] \\
\tilde{R}''(z) &= \frac{\gamma_1\gamma_2}{\gamma_2 - \gamma_1}\left[\gamma_1 \exp(\gamma_1 z) - \gamma_2 \exp(\gamma_2 z)\right] \\
\tilde{S}''(z) &= \frac{\imath\kappa}{c_z(\gamma_2 - \gamma 1)}\left[\gamma_1^2 \exp(\gamma_1 z) - \gamma_2^2 \exp(\gamma_2 z)\right]
\end{aligned}$$

Therefore, the condition translates to $|\gamma_{1,2}| \ll \beta$, and by considering the above expression of the dephasing measure ϑ this implies small variations $\Delta\theta$ and/or $\Delta\lambda$ from Bragg's condition. As a result, the first order approximation fails at least in far-off-Bragg replay for Kogelnik's model. The parameter of prime interest for diffractive components is the diffraction efficiency η defined as the fraction of power transferred from the incident beam to the signal wave, which takes this form for unslanted gratings within Kogelnik's formulation:

$$\eta = \tilde{S}\tilde{S}^* = \frac{\kappa^2}{\vartheta^2 + (2\kappa)^2}\left[(\exp(\gamma_1 d) - \exp\gamma_2 d)(\exp(\gamma_1^* d) - \exp\gamma_2^* d)\right] \tag{B.15}$$

If one writes $\gamma_1 = \imath(a + b)$ and $\gamma_2 = \imath(a - b)$ with $a = \frac{-\vartheta}{2c_z}$ and $b = \frac{\sqrt{\vartheta^2 + (2\kappa)^2}}{2c_z}$, the calculation becomes:

$$\begin{aligned}
\eta &= \frac{2\kappa^2}{\vartheta^2 + (2\kappa)^2}\left[1 - \cos(2bd)\right] \\
&= \frac{(2\kappa)^2}{\vartheta^2 + (2\kappa)^2}\sin^2\left(\frac{d\sqrt{\vartheta^2 + (2\kappa)^2}}{2c_z}\right)
\end{aligned}$$

Appendix C: Simplification of the coupled waves equation

The calculation of the second part of the wave equation may start by simplifying the expression of $k^2n^2(x,z)$:

$$\begin{aligned} k^2n^2(x,z) &= k^2\Big[n_0 + n_1(z)\cos(Kx) + n_2(z)\cos(2Kx) + n_3(z)\cos(3Kx) + \cdots\Big]^2 \\ &\simeq k^2\Big[n_0^2 + 2n_0n_1(z)\cos(Kx) + 2n_0n_2(z)\cos(2Kx) + 2n_0n_3(z)\cos(3Kx)\Big] \\ &= \beta^2\Big[1 + 2\frac{n_1(z)}{n_0}\cos(Kx) + 2\frac{n_2(z)}{n_0}\cos(2Kx) + 2\frac{n_3(z)}{n_0}\cos(3Kx)\Big] \end{aligned} \tag{C.1}$$

The above expression was obtained by disregarding the terms involving a multiplication of $n_jn_{j'}$ as the approximation $n_j(z) << n_0$ is always a valid assumption, particularly for neutrons. Given that $\cos(aKx) = \left[\exp(\imath aKx) + \exp(-\imath aKx)\right]/2$, the second part of the wave equation becomes:

$$\begin{aligned} k^2n^2(x,z)\cdot\psi(x,z) &= \sum_j \beta^2 S_j(z)\exp(-\imath\vec{k_j}\cdot\vec{r})\Big[1 + 2\frac{n_1(z)}{n_0}\cos(Kx) \\ &+ 2\frac{n_2(z)}{n_0}\cos(2Kx) + 2\frac{n_3(z)}{n_0}\cos(3Kx)\Big] \\ &= \sum_j \beta^2\Big[S_j(z)\exp(-\imath\vec{k_j}\cdot\vec{r}) + \frac{n_1(z)}{n_0}S_j(z)\exp(-\imath\vec{k_j}\cdot\vec{r})\left[\exp(\imath Kx) + \exp(-\imath Kx)\right] \\ &+ \frac{n_2(z)}{n_0}S_j(z)\exp(-\imath\vec{k_j}\cdot\vec{r})\left[\exp(\imath 2Kx) + \exp(-\imath 2Kx)\right] \\ &+ \frac{n_3(z)}{n_0}S_j(z)\exp(-\imath\vec{k_j}\cdot\vec{r})\left[\exp(\imath 3Kx) + \exp(-\imath 3Kx)\right]\Big] \\ &= \sum_j \beta^2\Big[S_j(z)\exp(-\imath\vec{k_j}\cdot\vec{r}) + \frac{n_1(z)}{n_0}S_j(z)\Big[\exp(-\imath(\vec{k_j}-\vec{K})\cdot\vec{r}) + \exp(-\imath(\vec{k_j}+\vec{K})\cdot\vec{r})\Big] \\ &+ \frac{n_2(z)}{n_0}S_j(z)\Big[\exp(-\imath(\vec{k_j}-2\vec{K})\cdot\vec{r}) + \exp(-\imath(\vec{k_j}+2\vec{K})\cdot\vec{r})\Big] \\ &+ \frac{n_3(z)}{n_0}S_j(z)\Big[\exp(-\imath(\vec{k_j}-3\vec{K})\cdot\vec{r}) + \exp(-\imath(\vec{k_j}+3\vec{K})\cdot\vec{r})\Big]\Big] \end{aligned} \tag{C.2}$$

It is possible to simplify further by inserting the following **Floquet conditions** in Equation C.2:

$$\vec{k_j} + m\vec{K} = \vec{k}_{j+m} + (\delta q_{j+m} - \delta q_j)\cdot\vec{z}\ , \qquad m\in\mathbb{Z} \tag{C.3}$$

$$\vec{k_j} - m\vec{K} = \vec{k}_{j-m} + (\delta q_{j-m} - \delta q_j)\cdot\vec{z}\ , \qquad m\in\mathbb{Z} \tag{C.4}$$

with $\vec{z}$ corresponding to the unit vector perpendicular to the surface of the grating. Consequently, one gets:

$$
\begin{aligned}
k^2 n^2(x,z)\cdot\psi(x,z) = \beta^2\Bigg\{ & \sum_j S_j(z)\exp\big(-\imath\vec{k_j}\cdot\vec{r}\big) \\
+ \frac{n_1(z)}{n_0}\sum_j S_j(z)\Big[& \exp\big(-\imath[\vec{k}_{j-1}\cdot\vec{r}+(\delta q_{j-1}-\delta q_j)\cdot\vec{z}]\big)+\exp\big(-\imath[\vec{k}_{j+1}\cdot\vec{r}+(\delta q_{j+1}-\delta q_j)\cdot\vec{z}]\big)\Big] \\
+ \frac{n_2(z)}{n_0}\sum_j S_j(z)\Big[& \exp\big(-\imath[\vec{k}_{j-2}\cdot\vec{r}+(\delta q_{j-2}-\delta q_j)\cdot\vec{z}]\big)+\exp\big(-\imath[\vec{k}_{j+2}\cdot\vec{r}+(\delta q_{j+2}-\delta q_j)\cdot\vec{z}]\big)\Big] \\
+ \frac{n_3(z)}{n_0}\sum_j S_j(z)\Big[& \exp\big(-\imath[\vec{k}_{j-3}\cdot\vec{r}+(\delta q_{j-3}-\delta q_j)\cdot\vec{z}]\big)+\exp\big(-\imath[\vec{k}_{j+3}\cdot\vec{r}+(\delta q_{j+3}-\delta q_j)\cdot\vec{z}]\big)\Big]\Bigg\}
\end{aligned}
\tag{C.5}
$$

This allows us to re-write Equation C.5 as:

$$
\begin{aligned}
k^2 n^2(x,z)\cdot\psi(x,z) = \beta^2\sum_j \exp\big(-\imath\vec{k_j}\cdot\vec{r}\big)\Bigg\{ & S_j(z)+\frac{n_1(z)}{n_0}\Big[S_{j-1}(z)\exp\big(\imath(\delta q_{j-1}-\delta q_j)z\big) \\
+ S_{j+1}(z)\exp\big(\imath(\delta q_{j+1}-\delta q_j)z\big)\Big] & + \frac{n_2(z)}{n_0}\Big[S_{j-2}(z)\exp\big(\imath(\delta q_{j-2}-\delta q_j)z\big) \\
+ S_{j+2}(z)\exp\big(\imath(\delta q_{j+2}-\delta q_j)z\big)\Big] & + \frac{n_3(z)}{n_0}\Big[S_{j-3}(z)\exp\big(\imath(\delta q_{j-3}-\delta q_j)z\big) \\
+ S_{j+3}(z)\exp\big(\imath(\delta q_{j+3}-\delta q_j)z\big)\Big]\Bigg\} &
\end{aligned}
\tag{C.6}
$$

Appendix D: Experimental area at PF2/VCN before and after the 2021-2023 long shutdown.

The Figure shows the shielding of the experimental area before and after the upgrade program. Upstream, the absorbing concrete blocks, visible in Fig.D.1b, and the entire wall were covered using plastic composite sheet incorporating Boron Carbide (the black material) instead of the few pieces that were initially used. The same material was to cover the upstream side of all the new apertures and the wall separating the VCN platform from the EDM platform. This lowers the detected background and ensures the safety of the users in both sides of the PF2 instrument.

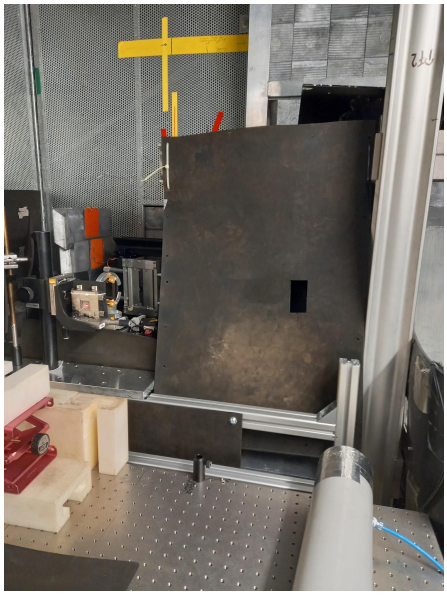

(a) Shielding of the VCN cabin in 2021

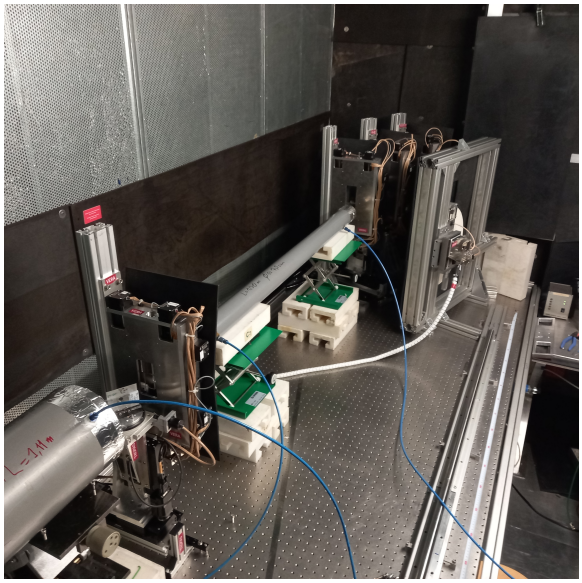

(b) Shielding of the VCN cabin in 2023

Figure D.1: Experimental area in (a) 2021 before the long-shutdown; (b) 2023 after the modernization program.

Appendix E: Comparison of possible strategies for defining the zero-th order background: observations and discussion

The graphs in Figure E.1 illustrate three different methods with a focus on the unclear definition of the zero-th order background. For the other orders, background is determined using off-Bragg values, determined as the minimum number of counts found in the scan. These approaches, applied to an NDPC sample, reveal how different methods can lead to varying and clearly inconsistent net count results.

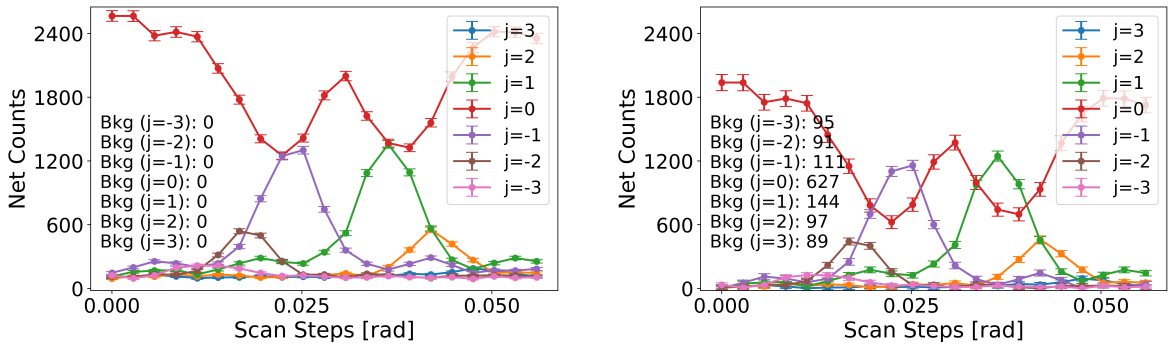

(a) Raw counts

(b) Net counts (*Method 1*)

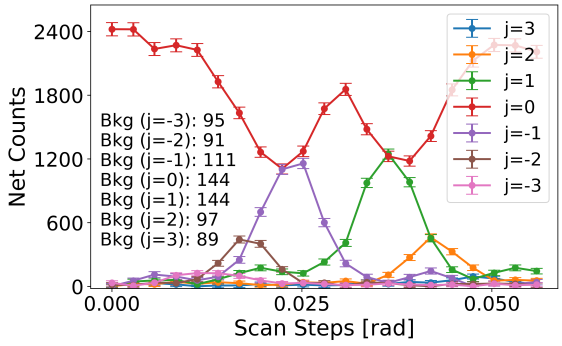

(c) Net counts (*Method 2*)

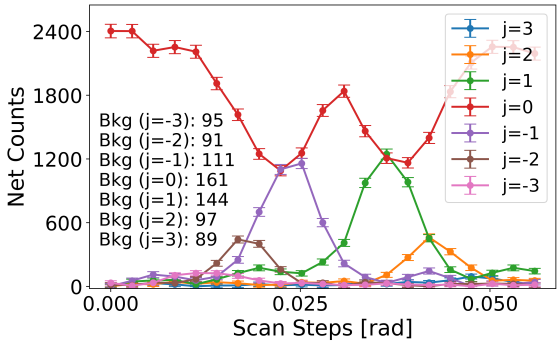

(d) Net counts (*Method 3*)

Figure E.1: (a) Raw counts from the ROIs, without background treatment. (b) Background-subtracted intensities using *Method 1*. (c) Background-subtracted intensities using *Method 2*. (d) Background-subtracted intensities using *Method 3*.

At the outset, an offset in the extracted raw counts from zero is noted. This offset is due to the overall background level in the other diffracted orders. With a wide angular range in the rocking curve, off-Bragg measurement for all orders was possible,

allowing us to set the background as the minimum counts across this range. The zero-th order background remains unclear. Hence, few possible and intuitive methods for removing background noise will be described, as a good basis for a start. These are called *Method 1*, *Method 2*, and *Method 3*. Later, other here-developed approaches will be introduced for a detailed study of the data. These will be referred to as *Approach 1*, *Approach 2*, *Approach 3*, and so on.

Outlined Methods:

1. *Method 1* (Figure E.1b): The background for $j = 0$ is assumed to be the sum of the other orders' backgrounds. This assumption is based on the fact that a decrement (or an increment) in the zero-th order intensity when passing from neighbouring angular positions in the scan, is equal to the sum of increments (and/or decrements) of all other diffracted orders. Consequently, one would also assume that its background is equivalent to the sum of all backgrounds from other orders.

2. *Method 2* (also referred to as "Off-Bragg Max") (Figure E.1c): The background for $j = 0$ is assumed equivalent to the maximal background among other orders. Given the experimental evidence (by considering horizontal profiles of the neutron counts) that the background is generally the highest for the zero-th order, it is assumed that it has the same value as the highest measured background of the other orders derived from the off-Bragg subtraction.

3. *Method 3* (Figure E.1d): The background for $j = 0$ is deduced as the average of the $\pm$1-st order backgrounds plus a mean increment for the transition from a higher to a lower order background.
   In fact, when employing raw counts instead of net counts for computation (and the analysis) of the diffraction efficiency, while retaining the background as a fit parameter, the resultant background values from the fit typically exhibit lower values for higher orders (this has to be also checked for the particular case when a higher diffraction order exhibits higher diffraction efficiency than lower orders, which never occurred in the performed experiments). This could be attributed to residual intensity fluctuations or increased diffuse scattering as a shift further off-Bragg might be necessary for solely measuring background for lower orders [151]. This could be a result of higher counts leading to an escalated background. Consequently, in this approach, a mean background increment is calculated from passing the 3-rd to the 2-nd orders, and from the 2-nd to the 1-st orders, which is then added to an averaged 1st order background value.

Post background subtraction, a marked difference emerges in the zero-th order net counts among the three methods, clearly observable by inspecting its position in relation to the first order peaks at the Bragg position. This distinction highlights the second and the third approach as most aligned with the raw data (experimentally measured counts without any treatment), while the first method seems to widely overestimate the zero-th order's background (the values depicted within the plots). However, this initial observation necessitates a more comprehensive analysis of background distribution and variation. A miscalculated background may significantly skew the diffraction efficiency curves, as seen in Figure E.2, further amplifying errors post background subtraction.

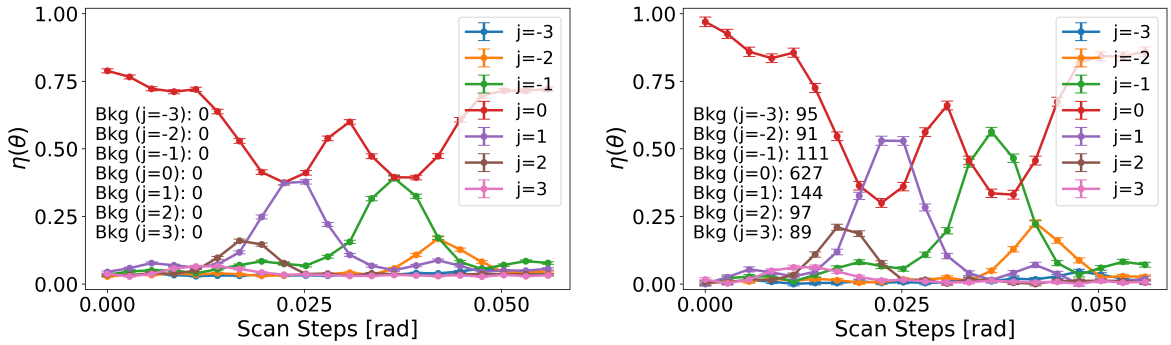

(a) Diff. eff. using raw counts

(b) Diff. eff. (*Method 1*)

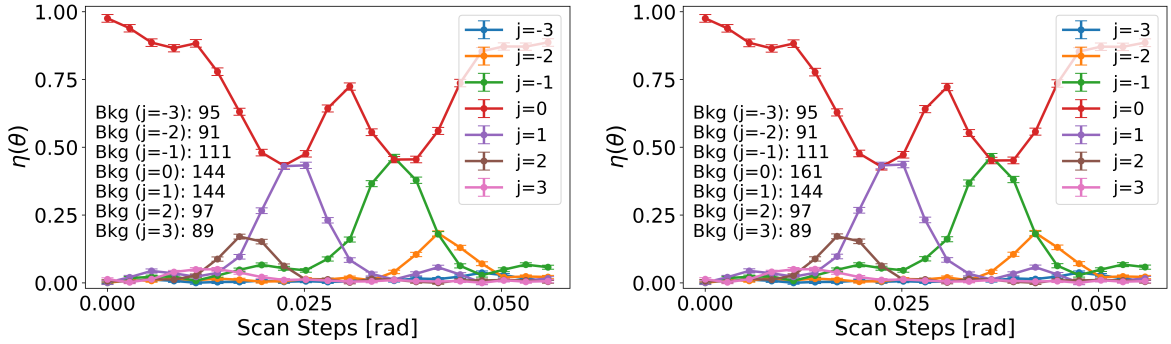

(c) Diff. eff. (*Method 2*)

(d) Diff. eff. (*Method 3*)

Figure E.2: Calculated diffraction efficiency using (a) raw counts as extracted from the ROIs (b) background-subtracted intensities using *Method 1*. (c) background-subtracted intensities using *Method 2*. and (d) background-subtracted intensities using *Method 3*.

This demonstrates that it is not merely a procedural detail but a critical factor influencing the robustness and credibility of the study, especially with regard to error propagation. Following that, a full statistical study of the background spread will be conducted to support informed decisions on the method to be employed.

Appendix F: Impact of the instrument modernization

The upgrades at PF2, detailed in subsection 3.2.3, complicate direct comparisons of measurements taken before and after the modernization due to changes in the neutron guide and non-reproducibility of the previous positions of the old collimation apertures. Other methods, such as neutron capture calculations and full primary beam characterization—though not covered in the study—may offer insights into the improvements in neutron flux. Despite the inherent difficulties in direct comparison due to the setup changes, initial evaluations of global instrument performance are feasible through the examination of aggregate detector images from NDPC grating-5 measurements. The 2021 dataset comprises 40 images at 4000s each, whereas the 2023 dataset includes 21 images at 2500s each, indicating procedural variations (Figure F.1).

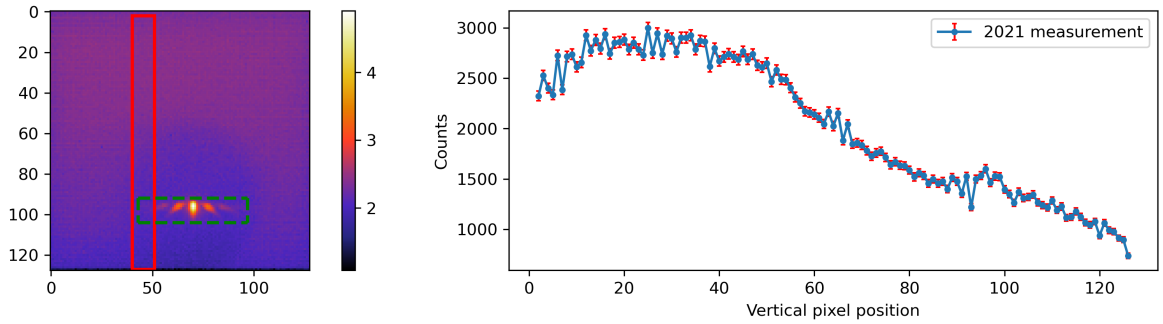

(a) 2021 measurement, inverted y-axis

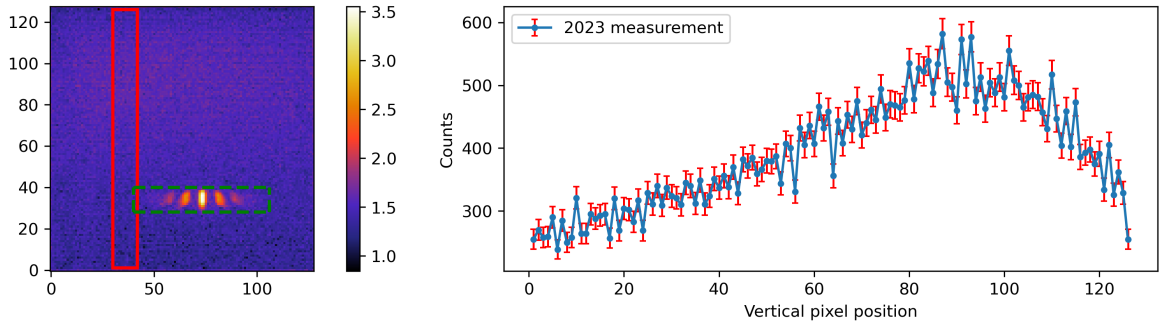

(b) 2023 measurement

Figure F.1: Comparative visualization of the aggregated detector images from NDPC grating-5 measurements before and after the PF2 modernization. The dashed green lines indicate the ROIs encompassing the diffraction spots that form the transmitted signal, and solid red lines demarcating the ROIs used for vertical profile analysis depicted on the right.

Vertical profiles (in red) from both sets of measurements indicate a consistent tendency of an increased background from the bottom to the top of the detector. The background gets multiplied by three from the bottom to the top, underscoring the need for further shielding the detector (particularly its top) with Boron Carbide to further hazardous environmental background. Signal-to-noise ratios, calculated based on a defined ROI around diffraction peaks forming the signal (in green), reveal nuanced performance distinctions. Initial S/N ratio estimations-calculated as the ratio of total counts within the signal ROI to its pixel count versus total counts outside the signal ROI to its pixel count-were 3.92 and 2.96 for 2021 and 2023, respectively. Adjusted calculations, using the same ROI width but positioned atop the signal ROI within the lower background region, yielded ratios of 5.7 and 3.94, respectively. The almost identical S/N ratios of the 2021 setup according to the first definition and the 2023 setup according to the second definition further support suspicions about He leakage. While these findings might suggest a degradation in performance post-modernization, it's critical to consider the differing total exposure times for the 2021 and 2023 images. Normalizing for total counting duration reveals an improvement, with normalized S/N ratios increasing from 35e-5 to 75e-5, indicating a better clarity of the signal despite potential helium flux instabilities.

Appendix G: Raw counts extraction from the ROIs

This section outlines the method employed for extracting data from defined regions of interest (ROIs) of non-conventional shapes within the detector data. The approach utilizes the `matplotlib.path.Path.contains_points()` function to determine if a detector pixel is inside (or outside of) the ROI.

G.1 ROI Path Definition

A `Path` object is created by specifying the vertices, representing the boundary of a ROI.

```
roi_path = Path(roi_vertices)
```

G.2 Coordinate Grid Creation

A grid of x and y coordinates is generated, representing each pixel in the detector data.

```
x_coords, y_coords = np.indices(detector_data[0,:,:].shape)
```

G.3 Pixel Inclusion Check

For each scan step, the `contains_points()` function checks whether each point (pixel center) in the grid is inside the defined ROI path. This results in a Boolean array (mask), with `True` indicating the pixel is inside the ROI and `False` indicating it is outside.

```
roi_mask = roi_path.contains_points(
    np.column_stack((x_coords.flatten(), y_coords.flatten()))
).reshape(full_data.shape)
```

G.4 Data Extraction and Summation

The mask is used to extract data from corresponding pixels in the detector data. Pixels marked as `True` in the mask are included in the summation to compute the total counts within the ROI.

```
roi_data = full_data[roi_mask]
total_counts = roi_data.sum()
```

Appendix H: Uncertainty from the diffraction efficiency expression employing the Net counts

The diffraction efficiency of the j-th order at a position θ, denoted as $\eta_j(\theta)$, using the net counts N is defined by:

$$\eta_j(\theta) = \frac{N_j(\theta)}{\sum_{i=-m}^{+m} N_i(\theta)},$$

where $N_j(\theta)$ is the net counts of the particular order and the denominator is the sum of net counts of all diffracted orders at this position, including the j-th order. Let $D = \sum_{i=-m}^{+m} N_i(\theta)$ for simplification.

The uncertainty in diffraction efficiency, $\Delta\eta_j(\theta)$, can be derived using standard error propagation methods. The error in N_j is denoted as ΔN_j, and the error in each count N_i as ΔN_i.
To derive the uncertainty $\Delta\eta_j(\theta)$, we first calculate the partial derivatives of $\eta_j(\theta)$. They are given by:

$$\frac{\partial \eta_j}{\partial N_i} = -\frac{N_j}{D^2} \quad \text{for } i \neq j,$$
$$\frac{\partial \eta_j}{\partial N_j} = \frac{D - N_j}{D^2}.$$

The uncertainty $\Delta\eta_j(\theta)$ can then be calculated using the error propagation formula:

$$\Delta\eta_j = \sqrt{\left(\frac{\partial \eta_j}{\partial N_j}\Delta N_j\right)^2 + \sum_{i=-m, i\neq j}^{+m} \left(\frac{\partial \eta_j}{\partial N_i}\Delta N_i\right)^2},$$

which simplifies to:

$$\Delta\eta_j = \frac{1}{D^2}\sqrt{\left[(D - N_j)\,\Delta N_j\right]^2 + \sum_{i=-m, i\neq j}^{+m} \left[N_j \Delta N_i\right]^2}. \tag{H.1}$$

This expression represents the uncertainty in diffraction efficiency $\Delta\eta_j(\theta)$, derived by standard error propagation from the diffraction efficiency expression that employs the Net counts instead of the raw counts and their corresponding background estimates.

Appendix I: Statistical study of the vertical background spread using data from a post-upgrade setup measurement at PF2/VCN

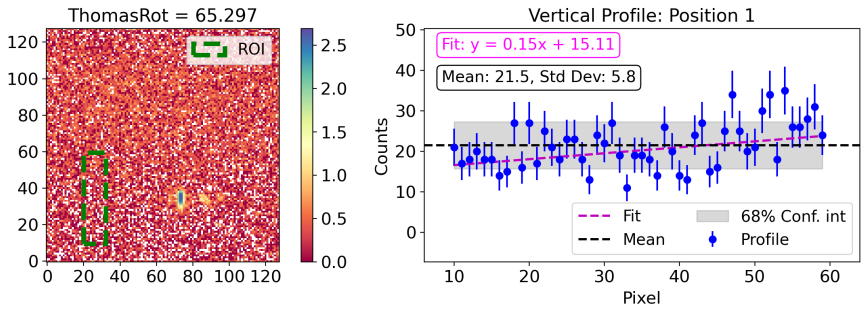

Figure I.1: Vertical variations of the background at Scan Position 1.

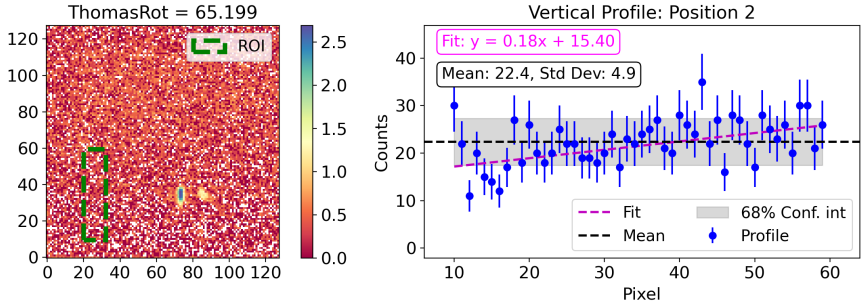

Figure I.2: Vertical variations of the background at Scan Position 2.

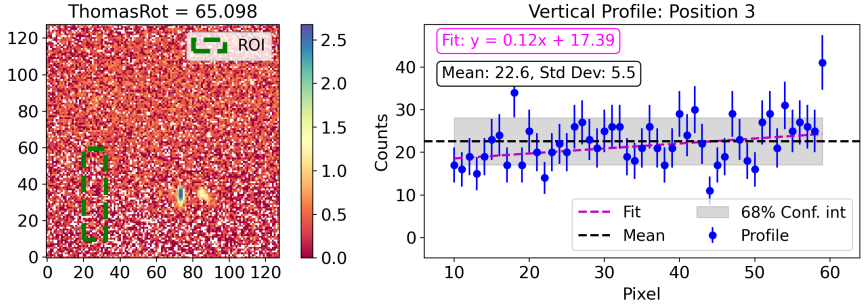

Figure I.3: Vertical variations of the background at Scan Position 3.

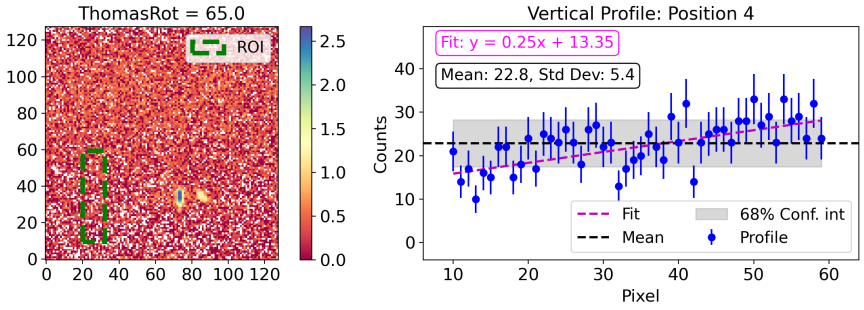

Figure I.4: Vertical variations of the background at Scan Position 4.

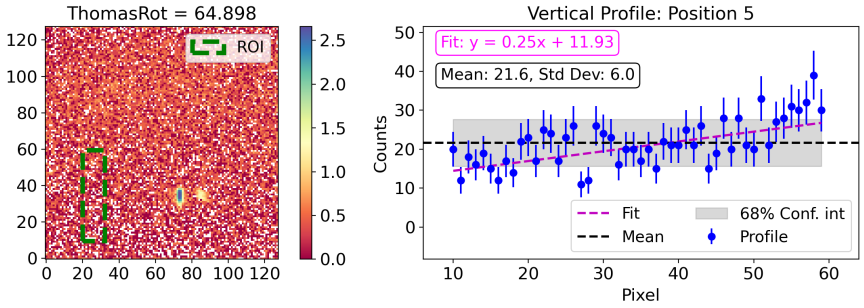

Figure I.5: Vertical variations of the background at Scan Position 5.

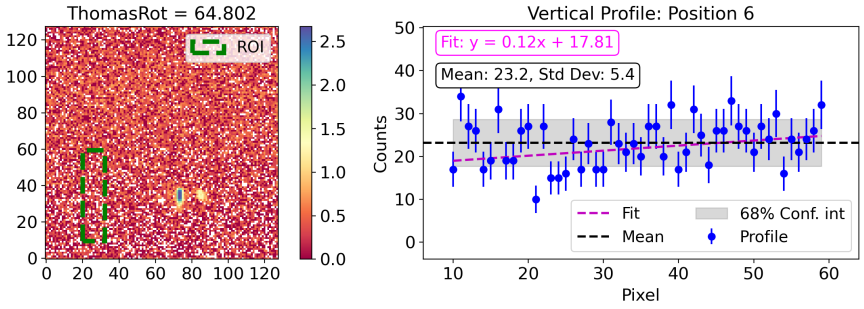

Figure I.6: Vertical variations of the background at Scan Position 6.

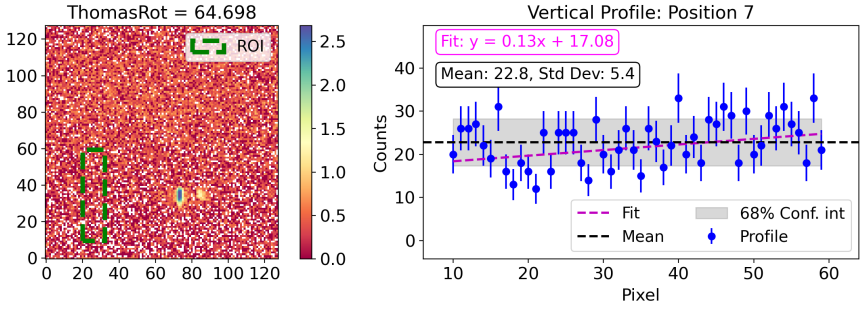

Figure I.7: Vertical variations of the background at Scan Position 7.

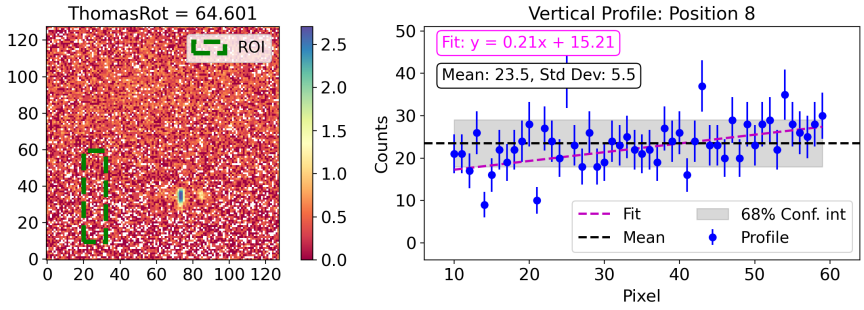

Figure I.8: Vertical variations of the background at Scan Position 8.

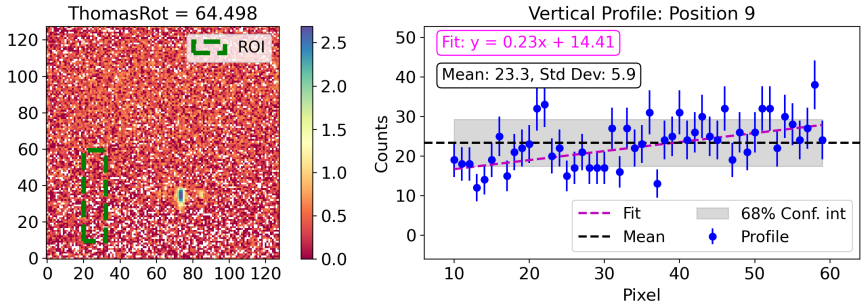

Figure I.9: Vertical variations of the background at Scan Position 9.

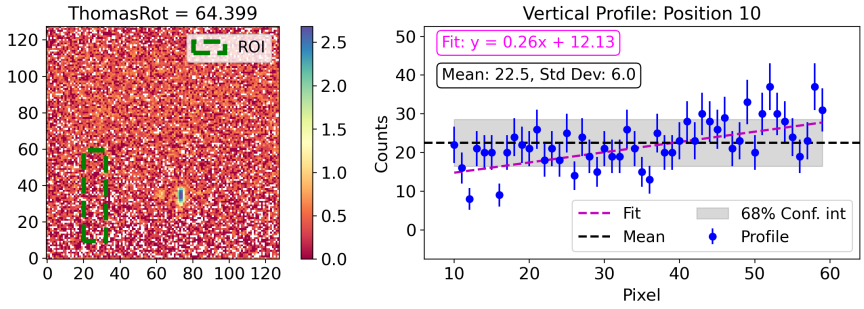

Figure I.10: Vertical variations of the background at Scan Position 10.

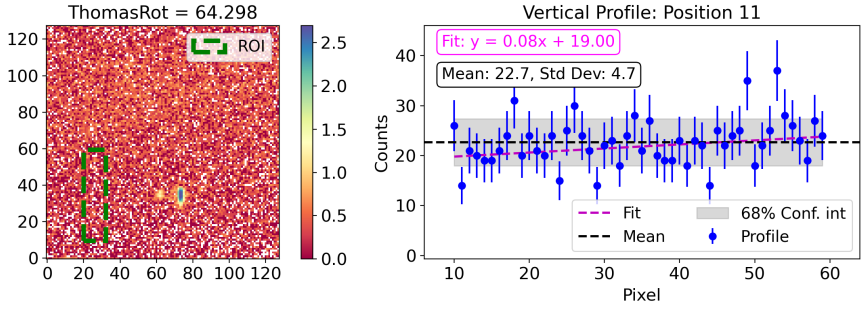

Figure I.11: Vertical variations of the background at Scan Position 11.

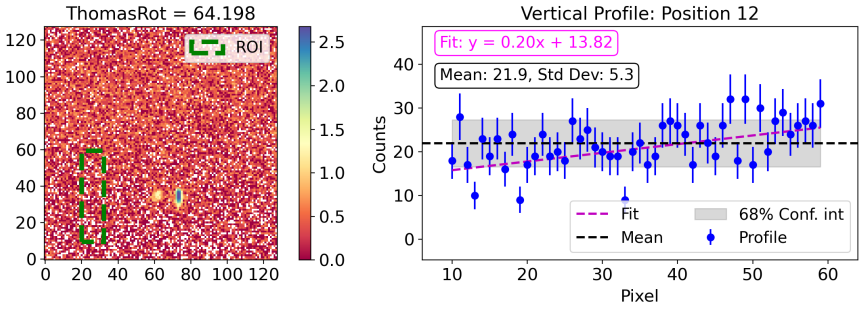

Figure I.12: Vertical variations of the background at Scan Position 12.

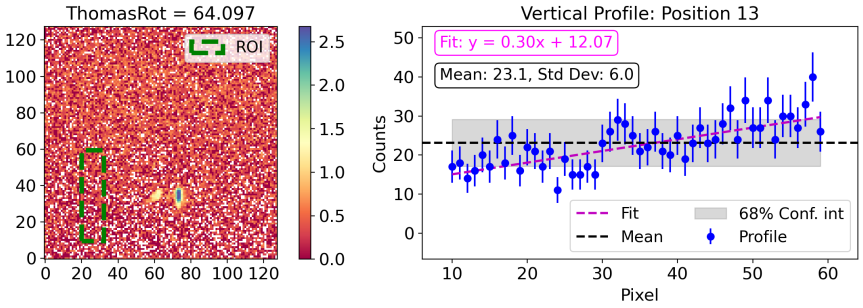

Figure I.13: Vertical variations of the background at Scan Position 13.

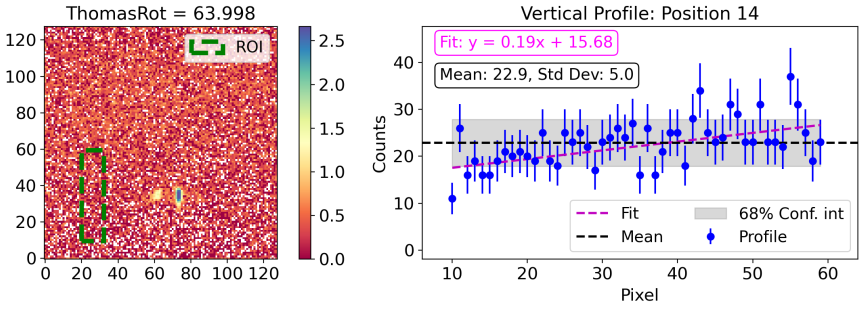

Figure I.14: Vertical variations of the background at Scan Position 14.

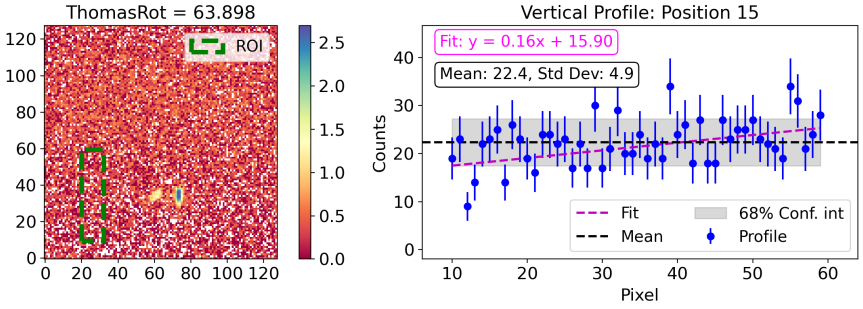

Figure I.15: Vertical variations of the background at Scan Position 15.

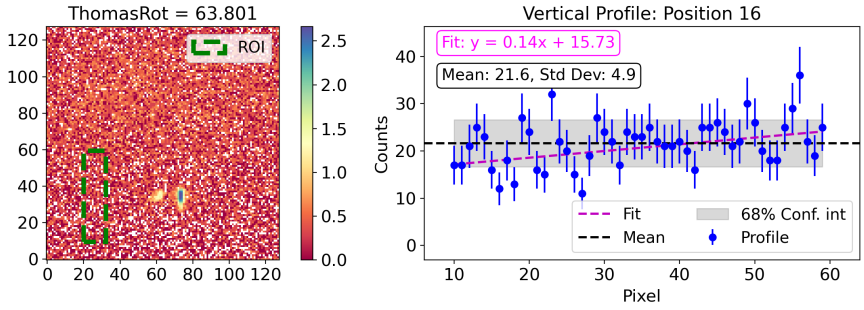

Figure I.16: Vertical variations of the background at Scan Position 16.

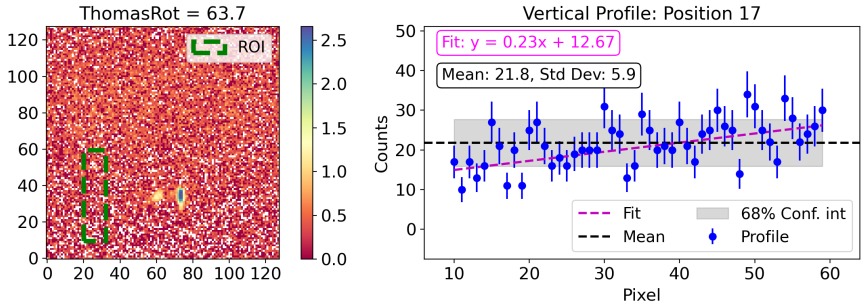

Figure I.17: Vertical variations of the background at Scan Position 17.

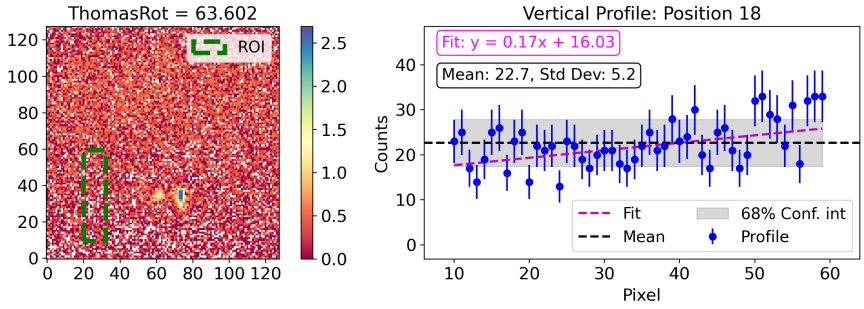

Figure I.18: Vertical variations of the background at Scan Position 18.

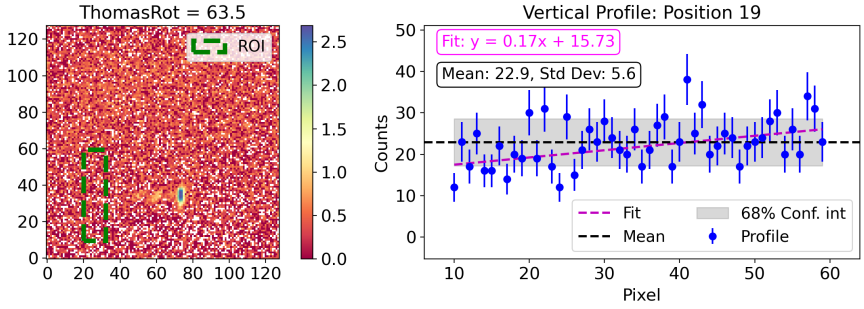

Figure I.19: Vertical variations of the background at Scan Position 19.

Appendix J: Statistical study of the horizontal background spread

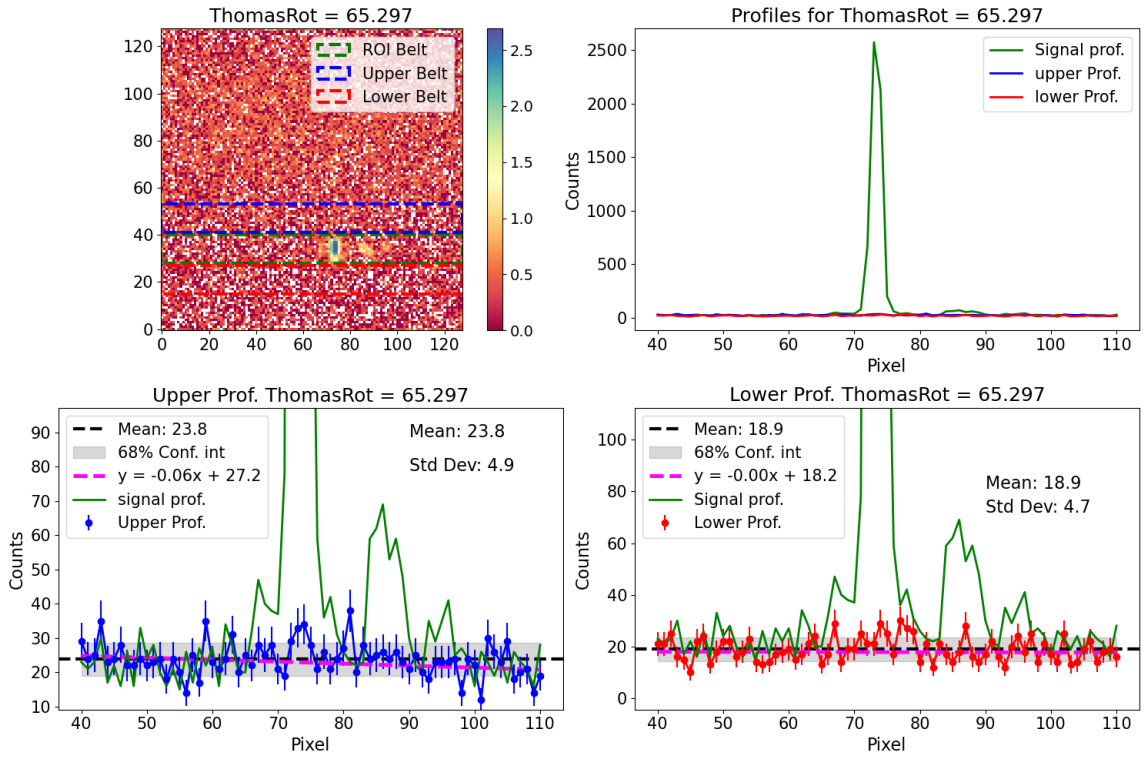

Figure J.1: Background analysis at Scan Position 1.

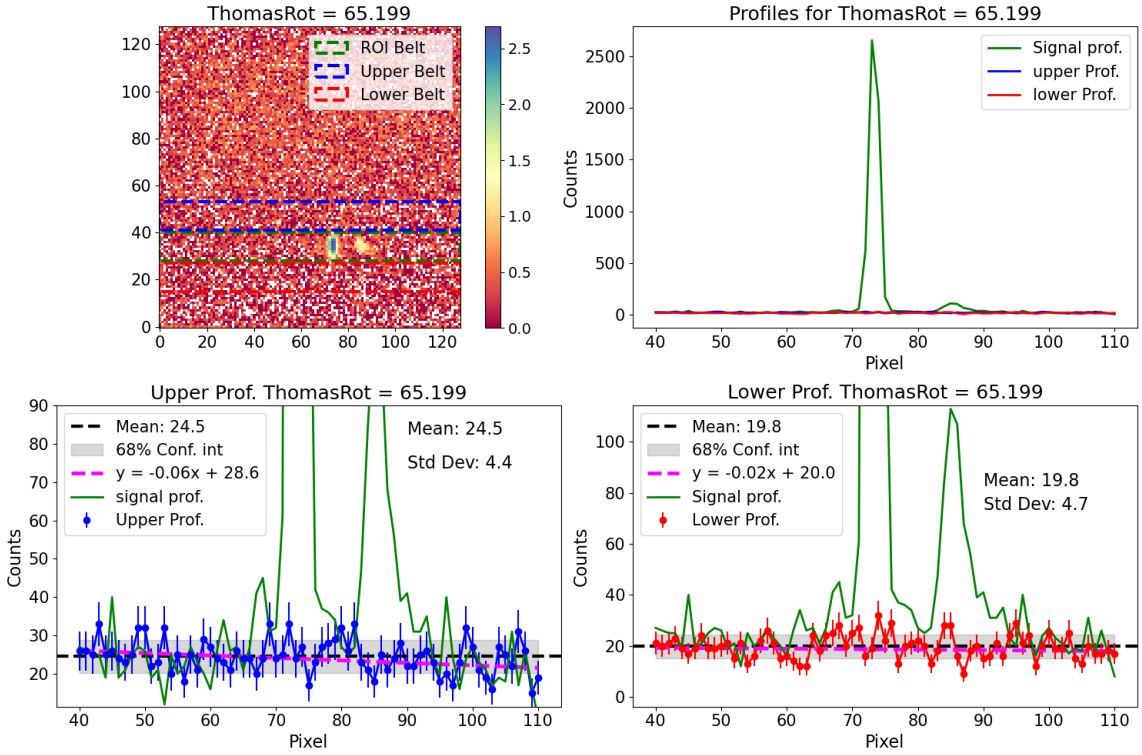

Figure J.2: Background analysis at Scan Position 2.

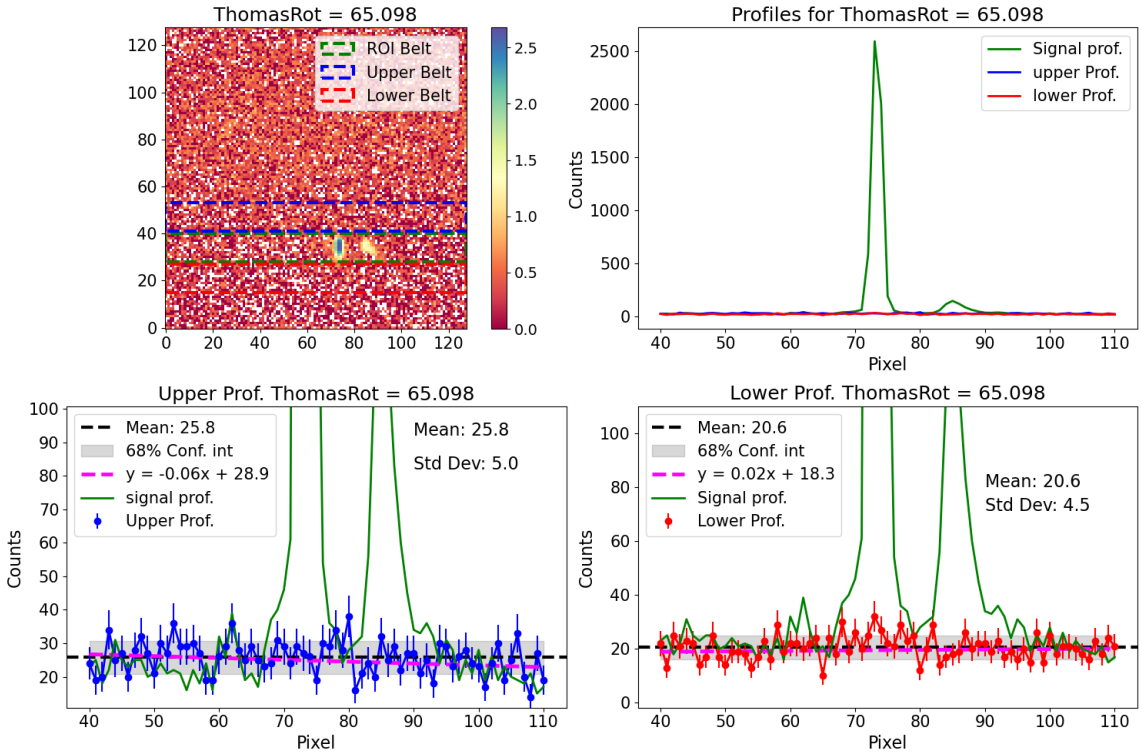

Figure J.3: Background analysis at Scan Position 3.

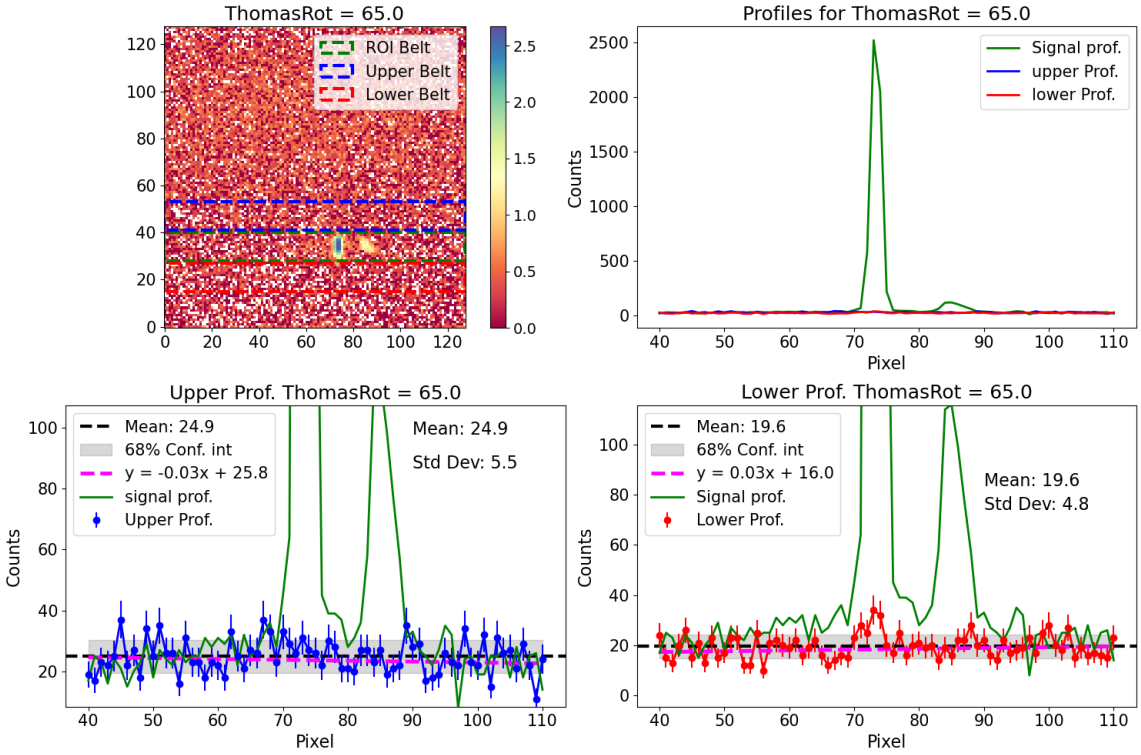

Figure J.4: Background analysis at Scan Position 4.

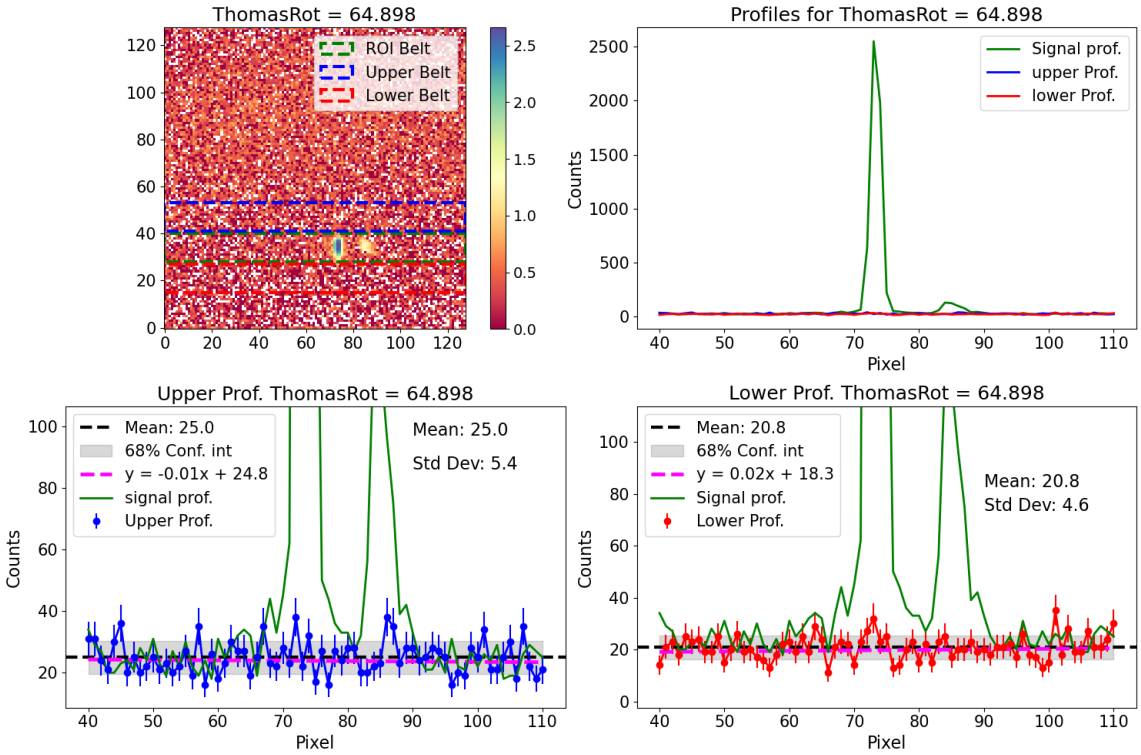

Figure J.5: Background analysis at Scan Position 5.

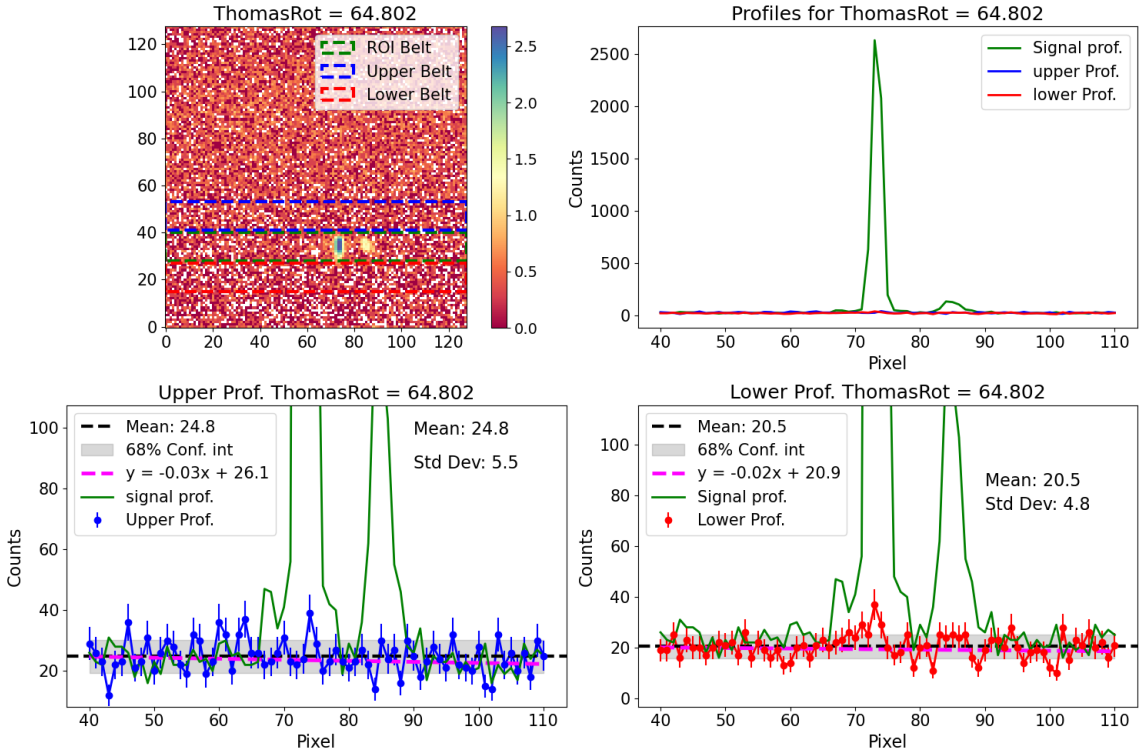

Figure J.6: Background analysis at Scan Position 6.

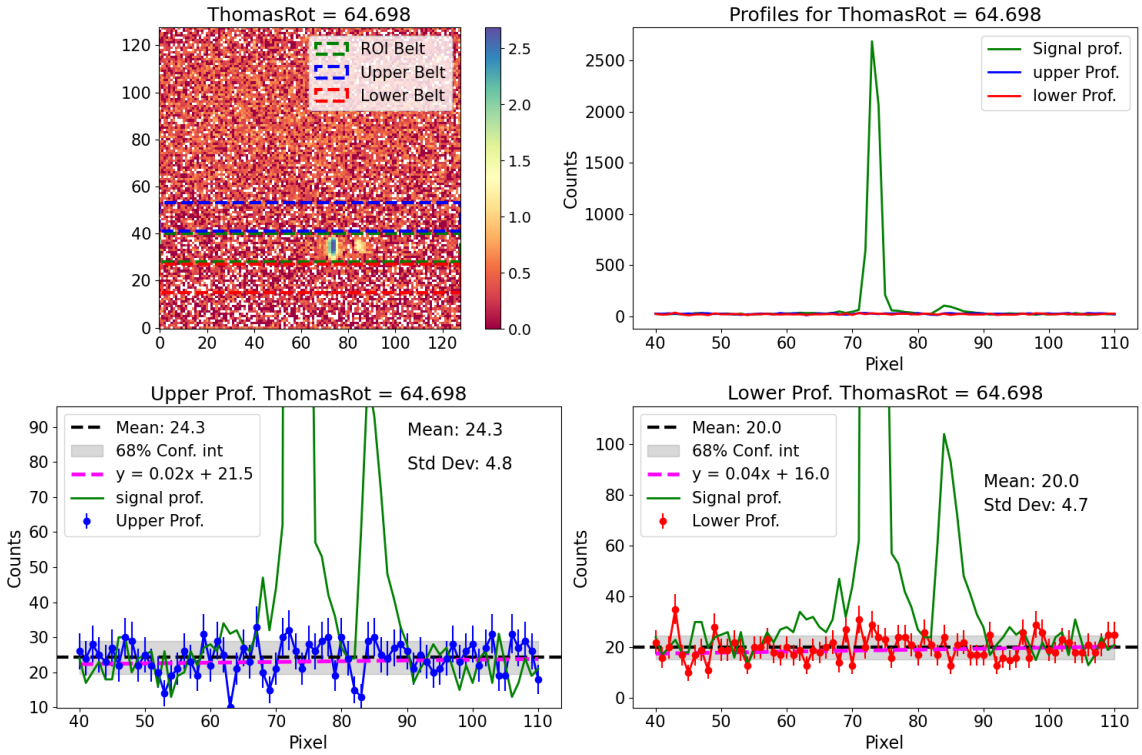

Figure J.7: Background analysis at Scan Position 7.

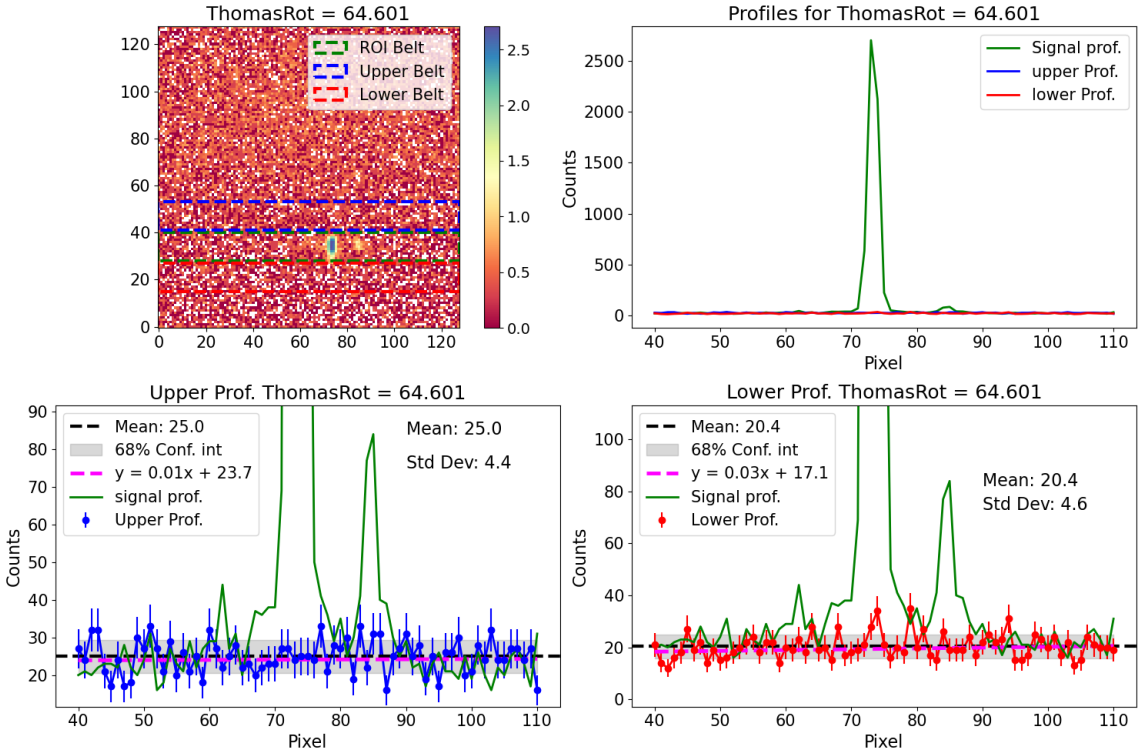

Figure J.8: Background analysis at Scan Position 8.

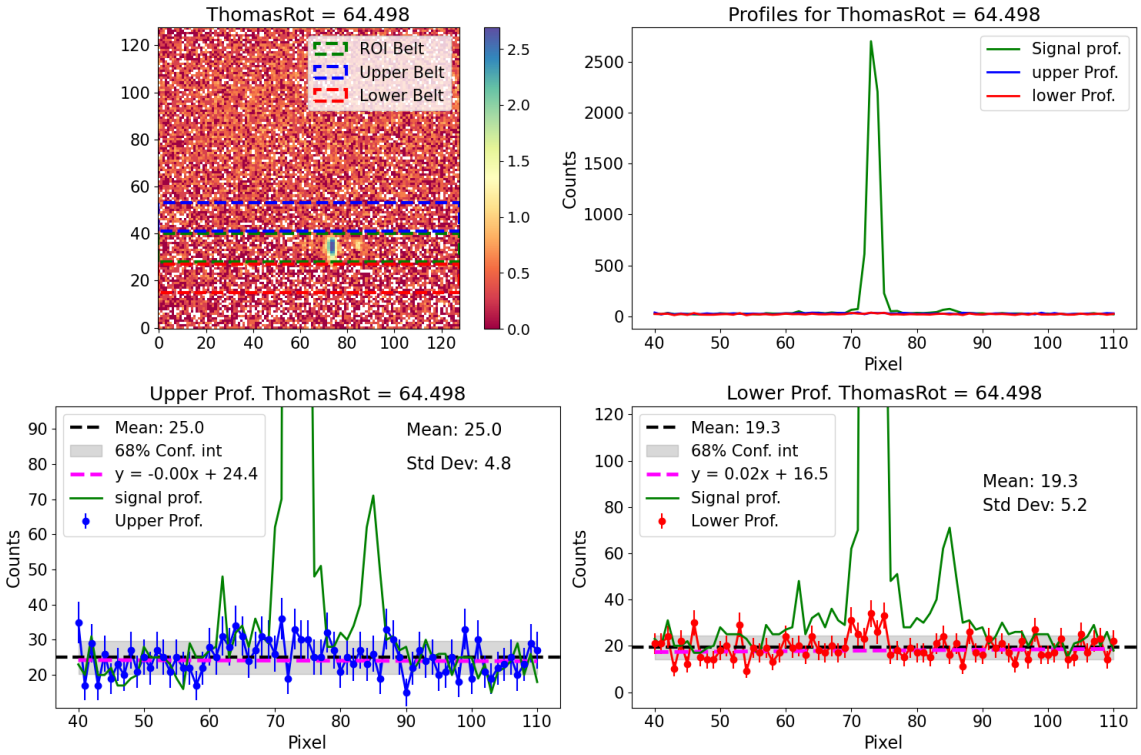

Figure J.9: Background analysis at Scan Position 9.

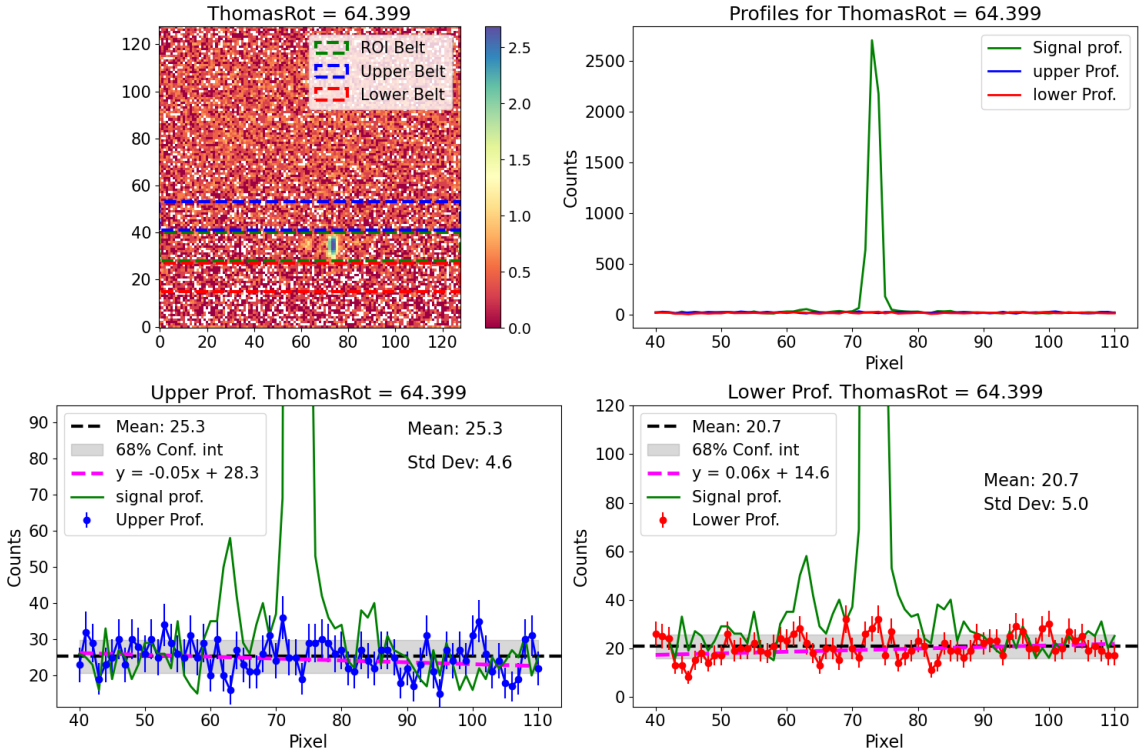

Figure J.10: Background analysis at Scan Position 10.

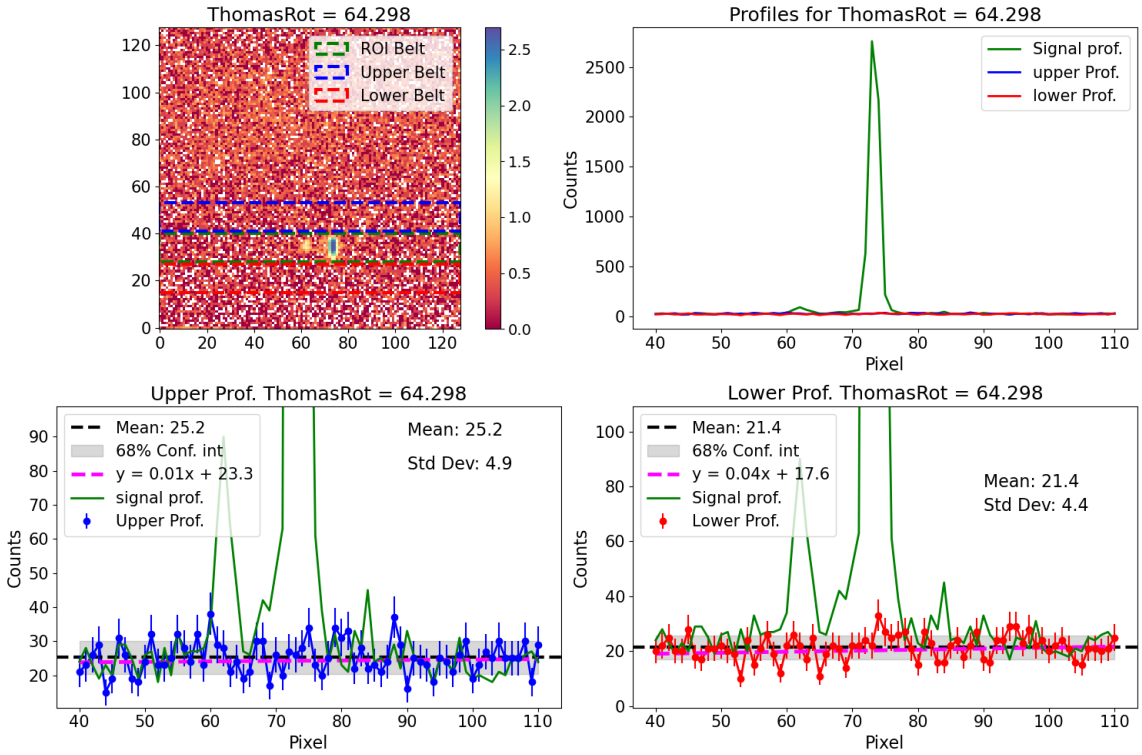

Figure J.11: Background analysis at Scan Position 11.

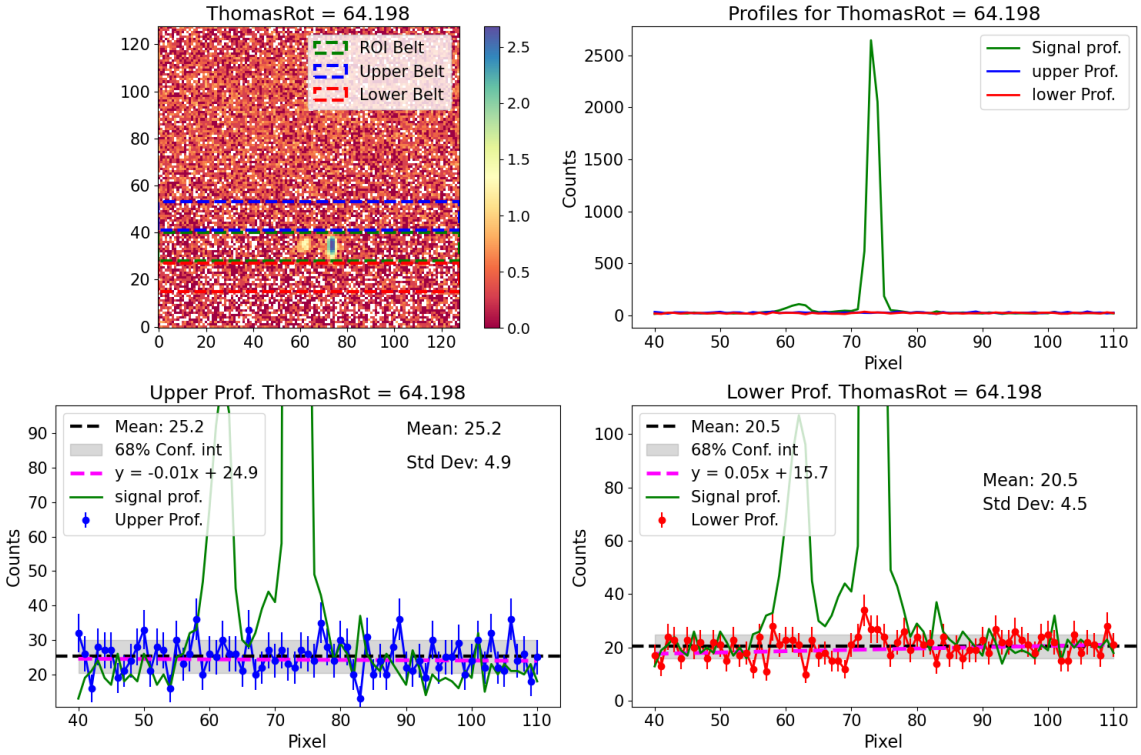

Figure J.12: Background analysis at Scan Position 12.

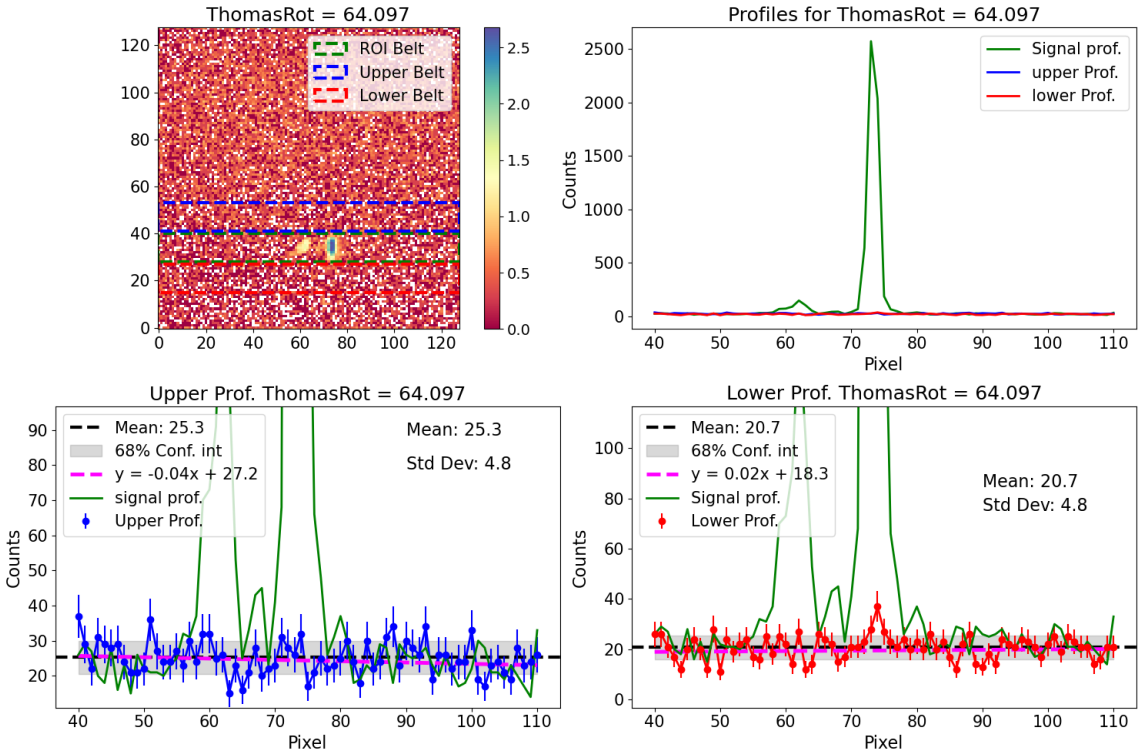

Figure J.13: Background analysis at Scan Position 13.

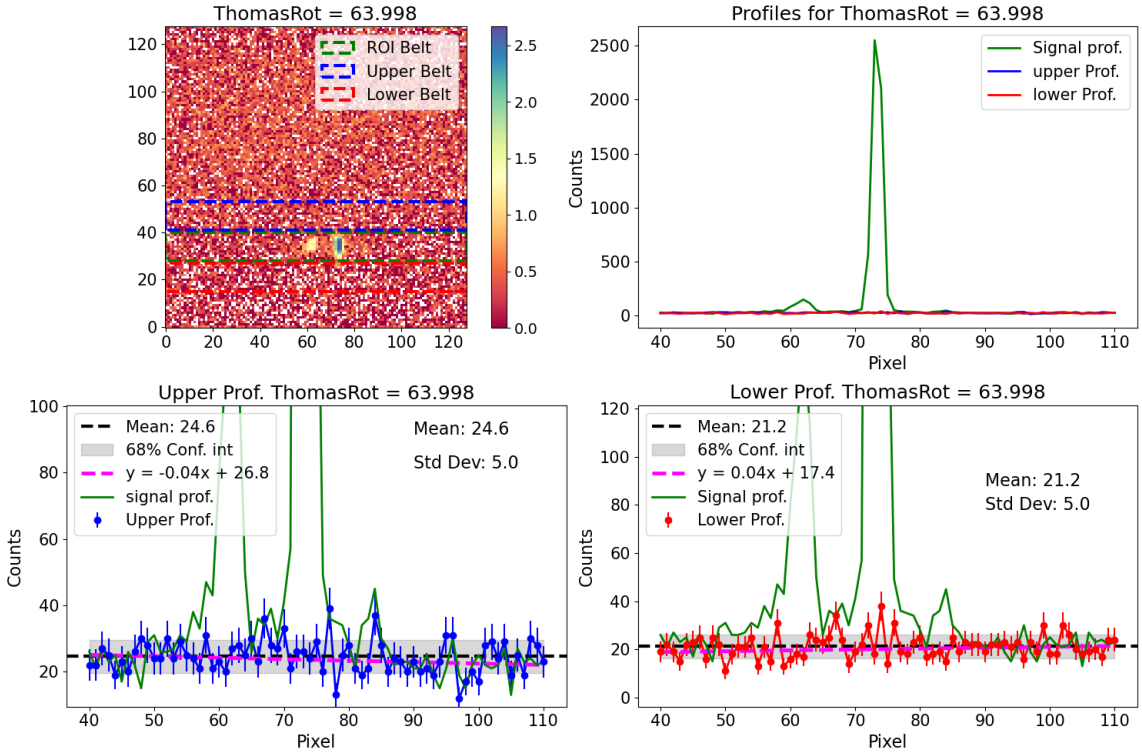

Figure J.14: Background analysis at Scan Position 14.

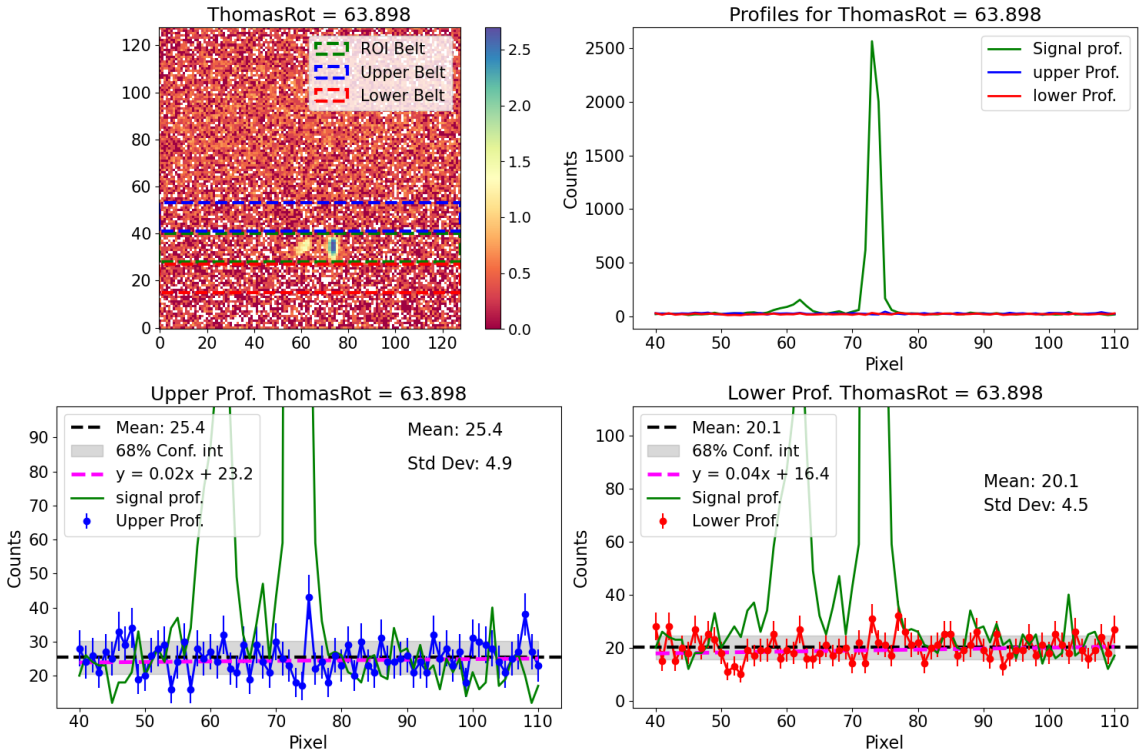

Figure J.15: Background analysis at Scan Position 15.

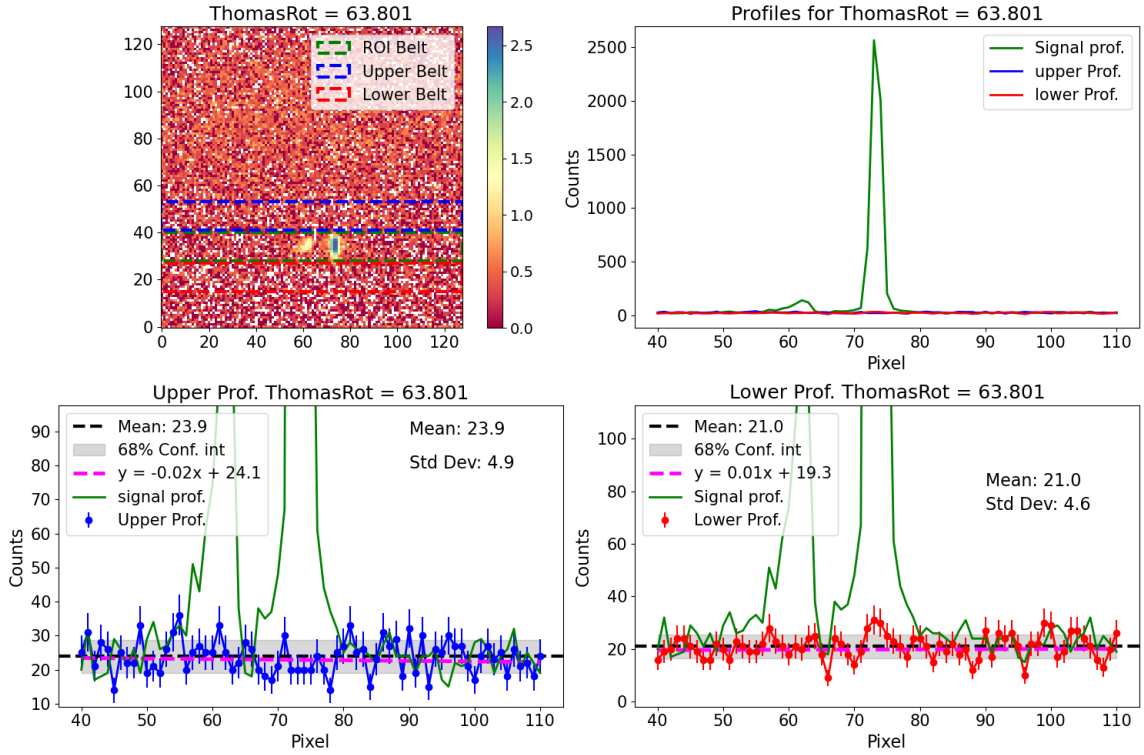

Figure J.16: Background analysis at Scan Position 16.

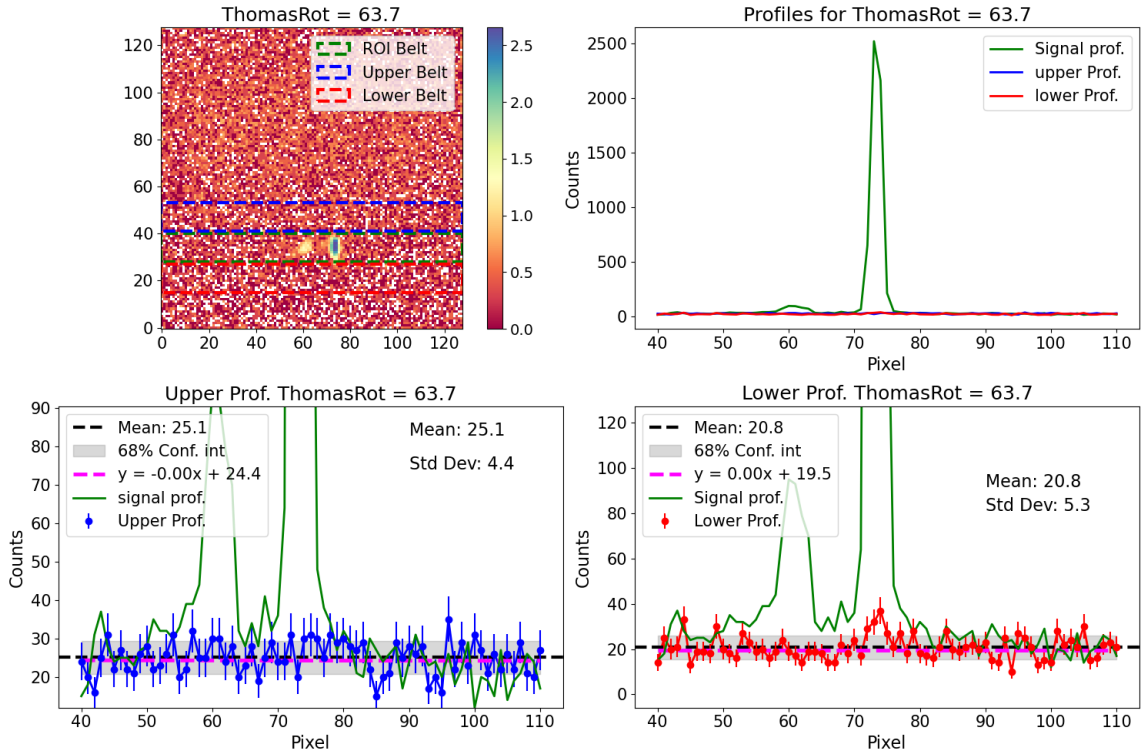

Figure J.17: Background analysis at Scan Position 17.

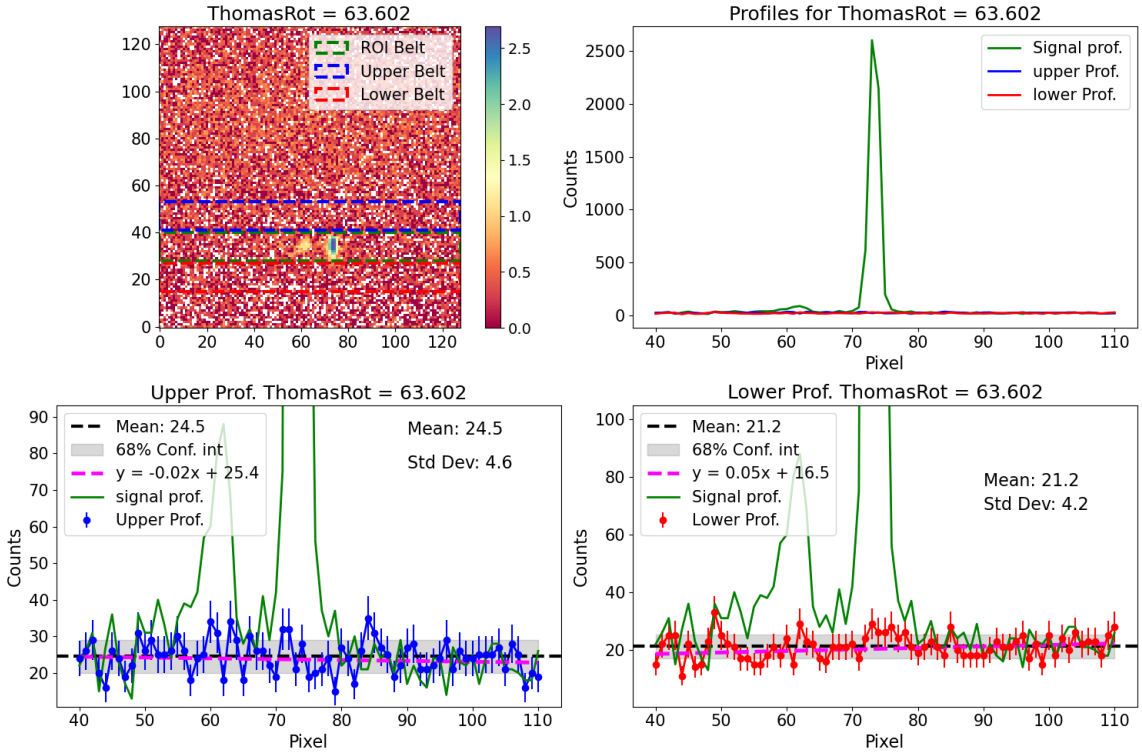

Figure J.18: Background analysis at Scan Position 18.

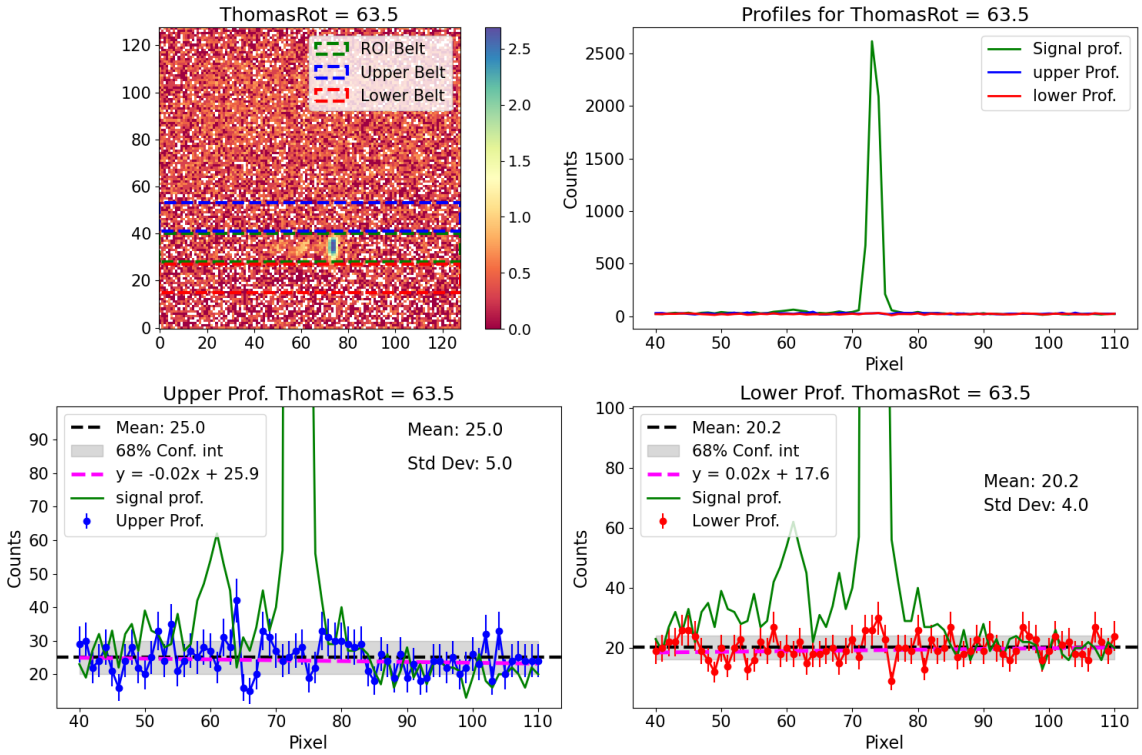

Figure J.19: Background analysis at Scan Position 19.

Appendix K: Direct extraction of the net counts and background estimation by fitting the horizontal profile of the signal (middle) ROI

This section elaborates on the fourth approach described in the main text. It involves fitting the horizontal profile of the ROI with a combination of Gaussian and Lorentzian functions. The approach is rooted in the understanding that the convolution of the incoming beam profile with the collimation creates a Gaussian-shaped beam, while diffuse scattering is aptly represented by a Lorentzian distribution.

Methodological details

The methodology involves several streamlined steps (The detailed code is not included due to its length.):

1. **Peak Identification**: Peaks are initially detected using the 'find_peaks' function from the scipy module, with a threshold height of 'th_counts'. These peaks undergo a filtering process, ensuring a minimum distance between successive peaks to avoid misidentification of Yoneda fringes or high-intensity oscillations as diffraction peaks. Filtered peaks must exceed 'th_counts' in at least two successive positions or surpass a higher threshold 'th2_counts' at least once.

2. **Profile Fitting**: The full ROI profile is fitted using a combination of Gaussian and Lorentzian functions, centered at each identified peak position.

3. **Net Count Calculation**: The net counts for each diffraction order are calculated directly from the area under the Gaussian component of the fitted curve. This area is indicative of the intensity of the peak, corresponding to the specific diffraction order.

4. **Background Estimation**: The total background estimation involves integrating the Lorentzian component of the fit, combined with a global background estimate. This global background is derived from the profile's minimum at each position. The integration is performed within a smaller ROI around each peak (the span of the ROI used for data extraction), rather than over the full span of the Lorentzian component. This focused approach allows for a more accurate estimation of the background contribution specific to each peak.

This approach facilitates a comprehensive analysis of the diffraction patterns, enabling accurate determination of net counts and approximate quantification of background contributions. The methodology yields consistent and reliable outcomes for

high-efficiency diffraction peaks. However, for peaks of lower intensity, the results exhibit notable inconsistencies. These are primarily influenced by the initial parameters and their bounds in the fitting process. Additionally, manual interventions, such as the insertion of expected second-order peaks in this specific measurement, can lead to unanticipated outcomes and numerical discrepancies. The figures below offer a detailed view of the performed fits at each angular position.

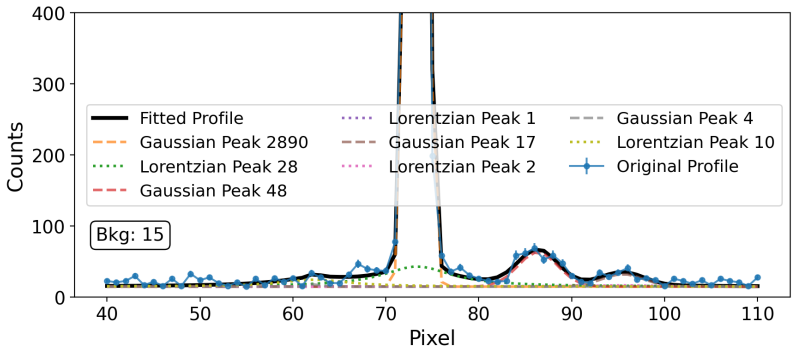

Figure K.1: Analysis for Scan step index 1.

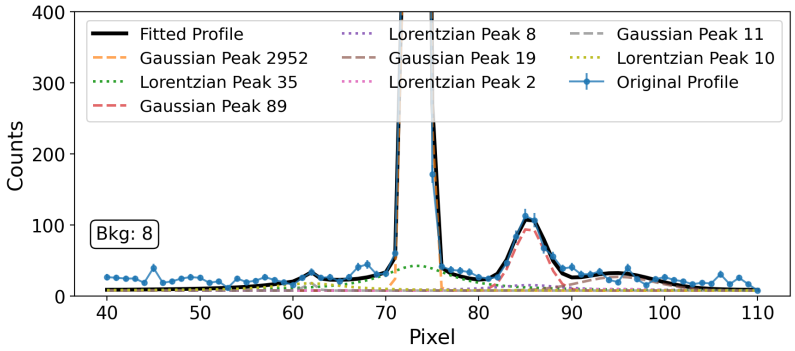

Figure K.2: Analysis for Scan step index 2.

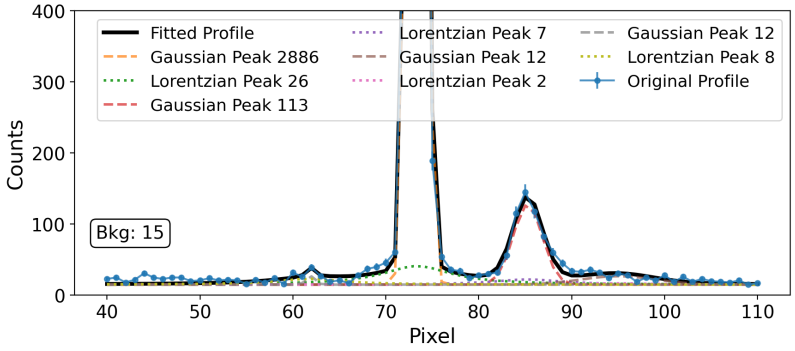

Figure K.3: Analysis for Scan step index 3.

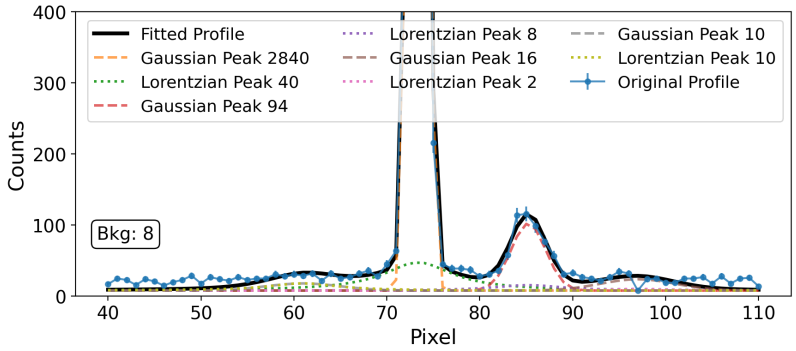

Figure K.4: Analysis for Scan step index 4.

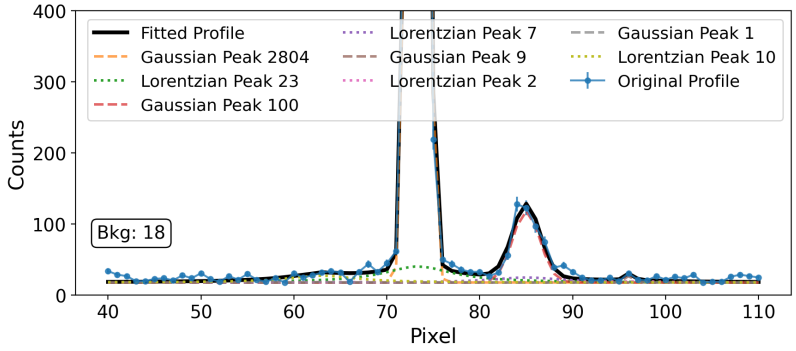

Figure K.5: Analysis for Scan step index 5.

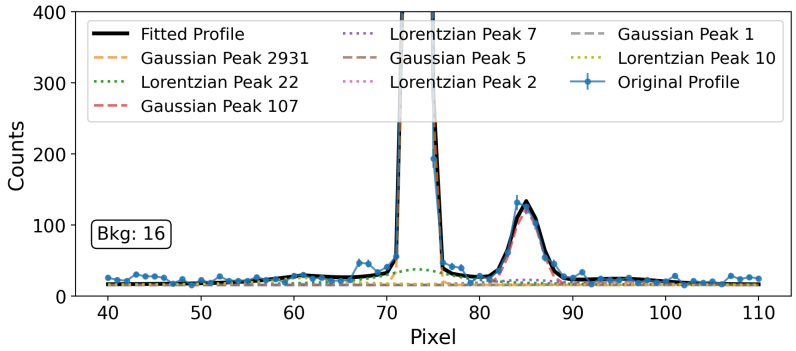

Figure K.6: Analysis for Scan step index 6.

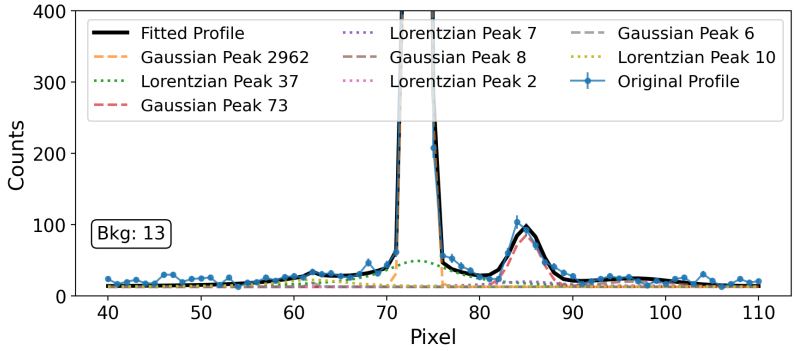

Figure K.7: Analysis for Scan step index 7.

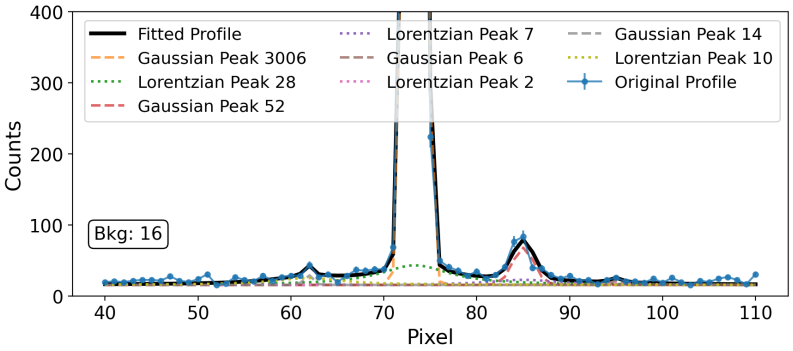

Figure K.8: Analysis for Scan step index 8.

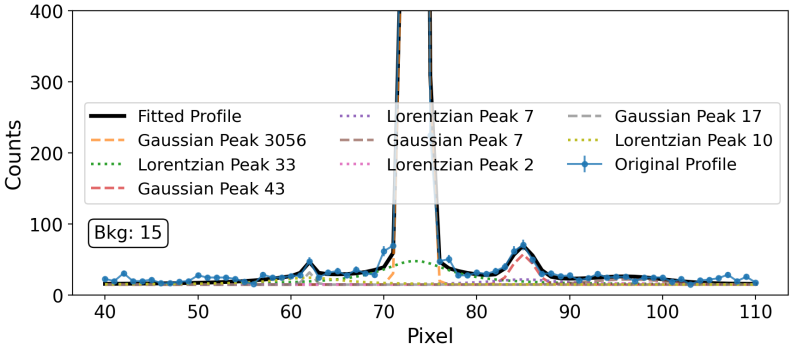

Figure K.9: Analysis for Scan step index 9.

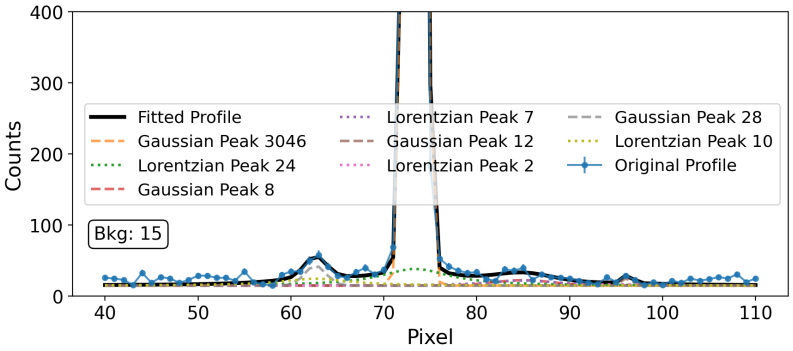

Figure K.10: Analysis for Scan step index 10.

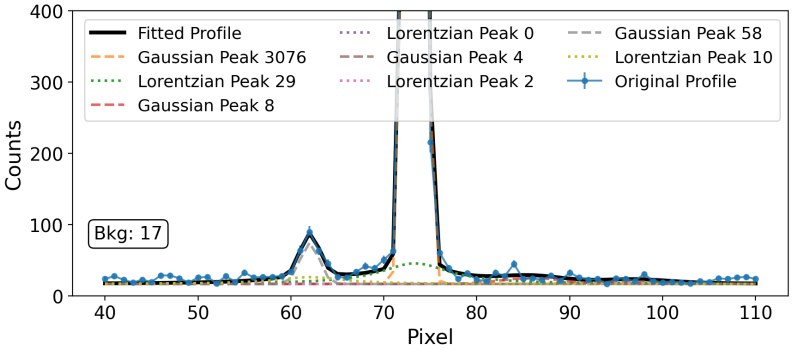

Figure K.11: Analysis for Scan step index 11.

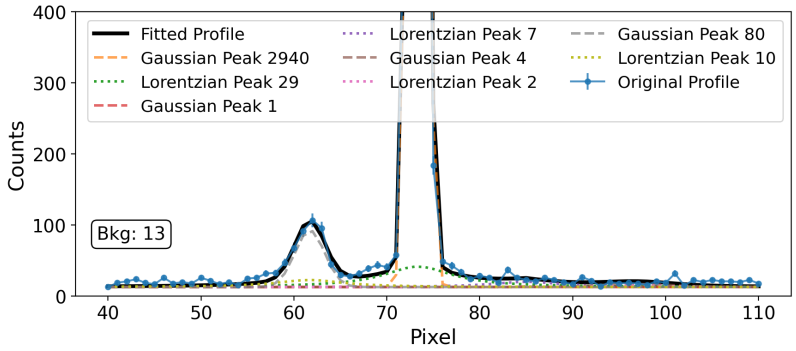

Figure K.12: Analysis for Scan step index 12.

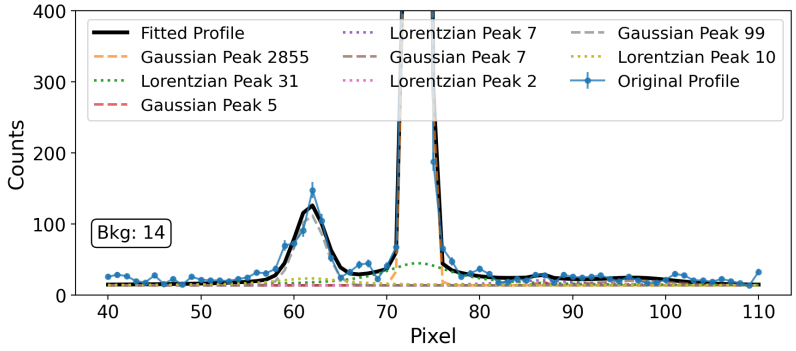

Figure K.13: Analysis for Scan step index 13.

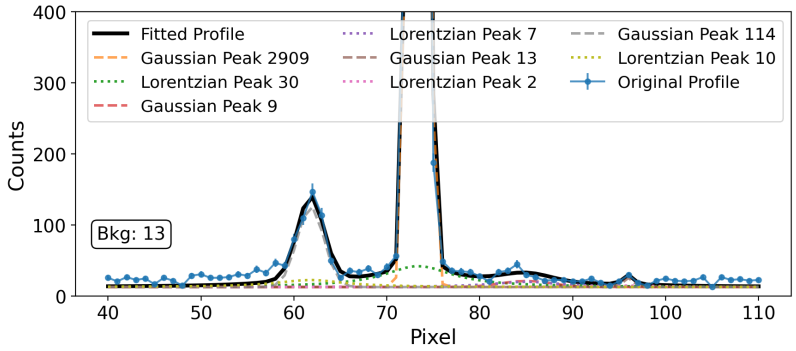

Figure K.14: Analysis for Scan step index 14.

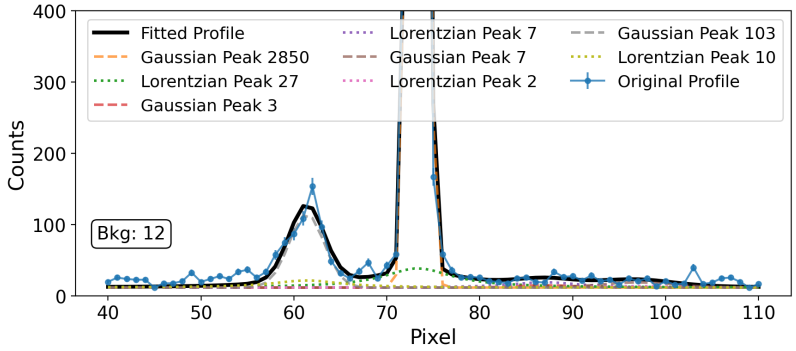

Figure K.15: Analysis for Scan step index 15.

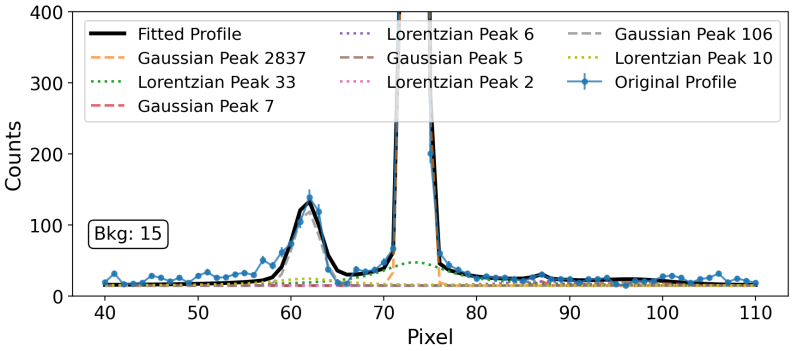

Figure K.16: Analysis for Scan step index 16.

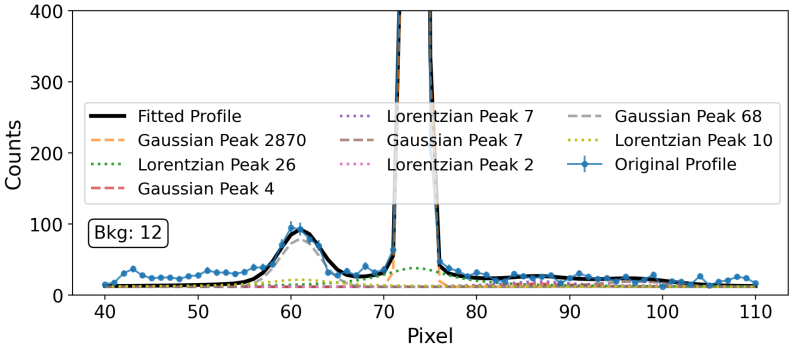

Figure K.17: Analysis for Scan step index 17.

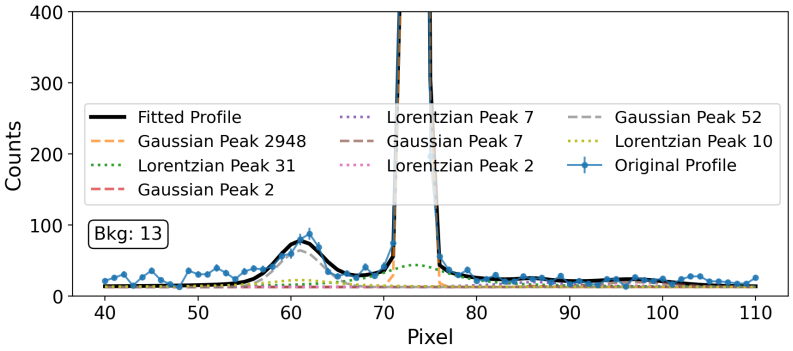

Figure K.18: Analysis for Scan step index 18.

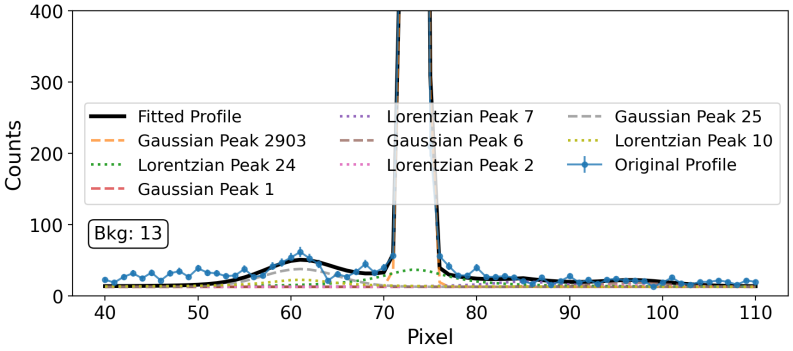

Figure K.19: Analysis for Scan step index 19.

Appendix L: Intersection area calculation for a rectangular beam and a circular aperture

The codes detailed in this section primarily aim to fit the variations of the total neutron counts hitting the detector. This is achieved by combining the Beer-Lambert attenuation with the computation of an area of intersection between an infinite-height rectangle and a circle. The rectangular beam is capable of displacing along the x-axis. Specifically, we consider the particular case where the width of the rectangular beam is smaller than the radius of the circular aperture.

Intensity ratio based on displacement

The `intensity_ratio` function computes the ratio of the intersection area at a given displacement (dx) to the intersection area when there's no displacement (i.e., $dx = 0$).
The python code (example code):

```
R = 0.5    # Radius of the circular aperture in cm
W_rec = 0.2    # Width of the rectagular beam in cm

def circle_segment_area(h, R):
    """
    Calculate the area of a segment of a circle given the radius R
    and the sagitta h.
    """
    if 0 < np.abs(h) <= R and R>0:
        h= np.abs(h)
        d_apothem = R - h
        theta_circ = 2* np.arccos(d_apothem / R)
        chord = 2 * np.sqrt(R**2 - d_apothem**2)
        circular_sector = (theta_circ/2) * R**2
        triangular_area = (d_apothem * chord) / 2
        circle_segment = circular_sector - triangular_area
        return circle_segment
    else:
        print("h>R or h=0 or R=0")
        circle_segment = 0
        return circle_segment

def rectangle_circle_intersection_area(dx, W_rec, R):
    """
```

```
    Compute the intersection area between an infinite-height rectangle
    and a circle as per the given scenarios.
    """
    x_0 = 0
    x= x_0 + dx
    half_width = W_rec / 2
    x1_0 = x_0 + half_width
    x2_0 = x_0 - half_width

    x1 = x1_0 + dx
    x2 = x2_0 + dx

    circle_area = np.pi * R**2

    # Case (a)
    if x2_0 <= x <= x1_0:
        h1 = R - x1
        h2 = R - np.abs(x2)
        segment_area_1 = circle_segment_area(h1, R)
        segment_area_2 = circle_segment_area(h2, R)
        return circle_area - segment_area_1 - segment_area_2

    # Case (b)
    elif x1_0 < x < (R - half_width):
        h1 = R - x1
        h2 = R - x2
        segment_area_1 = circle_segment_area(h1, R)
        segment_area_2 = circle_segment_area(h2, R)
        return segment_area_2 - segment_area_1

    # Case (c)
    elif x >= (R - half_width) and x2 < R:
        h = R - x2
        segment_area = circle_segment_area(h, R)
        return segment_area

    # Case (d)
    elif  (half_width - R) < x < x2_0:
        h1 = R + x1
        h2 = R + x2
        segment_area_2 = circle_segment_area(h2, R)
        area_1 = circle_area - circle_segment_area(h1, R)
        return circle_area - segment_area_2 - area_1

    # Case (e)
    elif x <= (half_width - R) and x1 > (0-R):
        h = R + x1
```

```
        segment_area = circle_segment_area(h, R)
        return segment_area

    else:
        return 0  # No intersection

# Define a function that calculates the intensity ratio after
displacement dx
def intensity_ratio(dx, W_rec, R):
    """
    Calculate the intensity ratio based on the displacement ratio.
    """
    int_ratio = rectangle_circle_intersection_area(dx, W_rec, R) /
    rectangle_circle_intersection_area(0, W_rec, R)
    return int_ratio
```

Fitting procedure accounting for horizontal displacement

To account for the impact of horizontal displacement in modulating the beam's intersection with the circular aperture, a modification to the traditional Beer-Lambert attenuation function is introduced.

First, the effective thickness, d_{eff}, is adjusted for various angles θ, using the equation:

$$d_{\text{eff}} = \frac{d_0}{\cos(\theta)}$$

The variations are minuscule though, because we only rotate for a couple of degrees in SANS experiments. Here, d_0 is the physical thickness of the sample.
The modified fit function integrates both attenuation properties and the intensity ratio resulting from horizontal displacement:

$$\text{flux\_fit}(\theta) = I_0 \times \exp(-\mu \times d_{\text{eff}}) \times \text{intensity\_ratio}(K\theta, W_{\text{rec}}, R)$$

In this equation, I_0 denotes the incident flux intensity, K represents the factor relating horizontal displacement to θ (assuming a linear dependance $dx = K\theta$), μ is the linear attenuation coefficient, W_{rec} stands for the width of the rectangle, and R refers to the radius of the circle.
It is important to make a reasonable choice for the starting parameters K and μ.
A least-squares minimization approach is employed for the fitting, enabling the determination of optimal parameters that best encapsulate the relationship between theoretical and experimental intensity values, while factoring in the horizontal displacement of the rectangular beam.

The python code (an example):

```
# Calculate d_eff for all theta values
d_0_fixed = 32e-4 #sample thickness at theta = 0
```

```
d_eff = d_0_fixed / np.cos(theta)

def modified_fit_function(theta, K, mu, d_eff_values, W_rec, R):
    """
    Beer-Lambert attenuation function modified by the intensity ratio
    due to horizontal displacement.
    """
    dx = K*theta
    flux_modification = [intensity_ratio(displacement, W_rec, R)
    for displacement in dx]
    flux_fit = max_value * np.exp(-mu * d_eff_values) *
    flux_modification
    return flux_fit

# Initial parameters
initial_params = [57.3, 1]  # K in [cm/rad], mu in [cm-1]

# Curve fitting
popt, pcov = curve_fit(lambda t, K,
mu: modified_fit_function(t, K, mu, d_eff, W_rec, R),
                       theta, total_detector_counts,
                       p0=initial_params,
                       sigma=errors, absolute_sigma=True)

fit_errors = np.sqrt(np.diag(pcov))

fitted_data = modified_fit_function(theta, *popt, d_eff, W_rec, R)
```

Appendix M: Supplement to the Results and Discussion Chapter

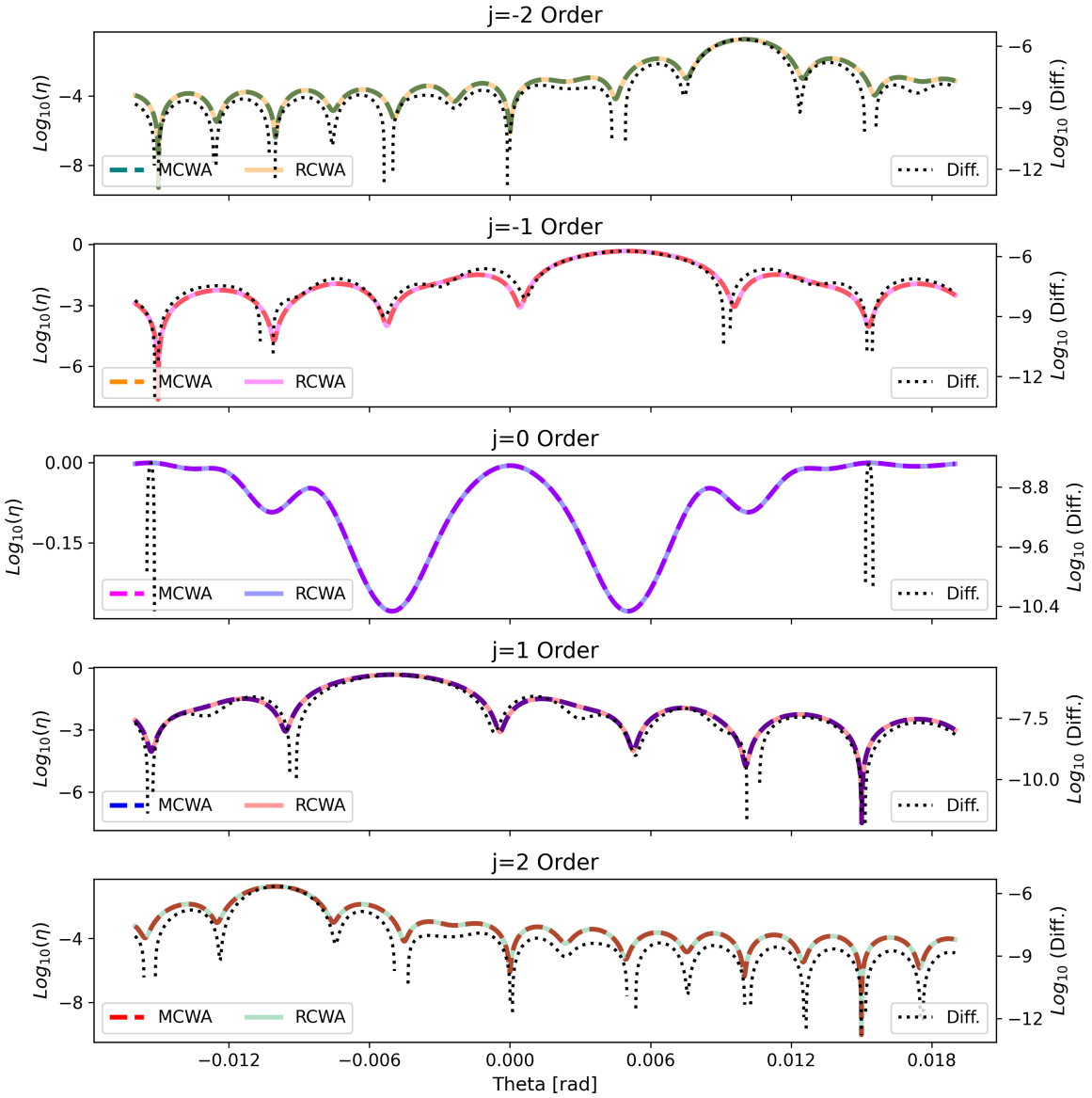

Figure M.1: Comparison of 5-RCWA and 5-MCWA simulations. The parameters used are $\Delta ß_1 = 9\,\mu\mathrm{m}^{-2}$, $\Delta ß_2 = 4\,\mu\mathrm{m}^{-2}$, $\lambda = 3\,\mathrm{nm}$, $\Lambda = 300\,\mathrm{nm}$, and $d_\mathrm{N} = 60\,\mu\mathrm{m}$.

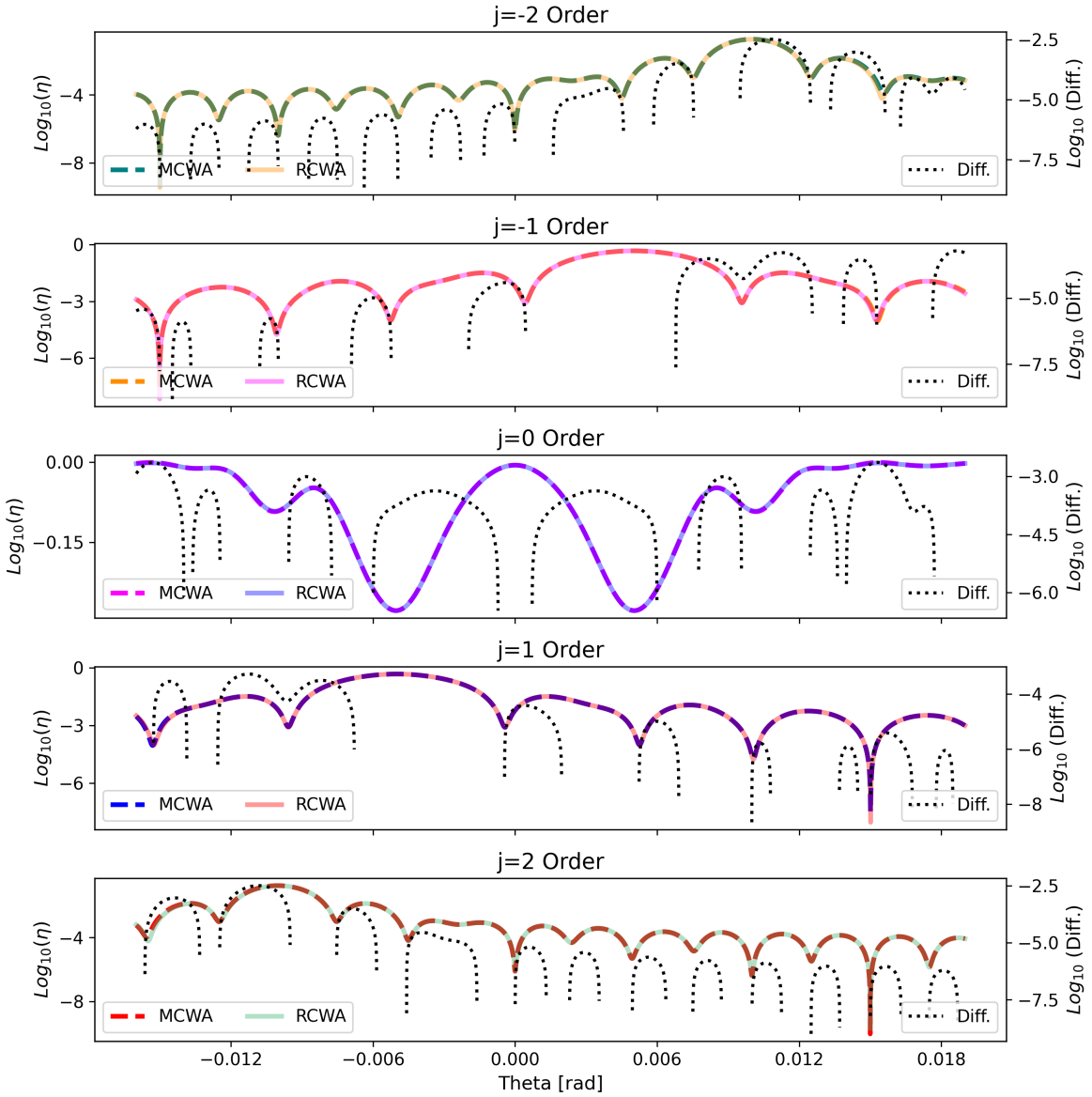

Figure M.2: Comparison of 5-RCWA and 7-RCWA simulations. The parameters used are $\Delta ß_1 = 9\,\mu\text{m}^{-2}$, $\Delta ß_2 = 4\,\mu\text{m}^{-2}$, $\lambda = 3\,\text{nm}$, $\Lambda = 300\,\text{nm}$, and $d_\text{N} = 60\,\mu\text{m}$.

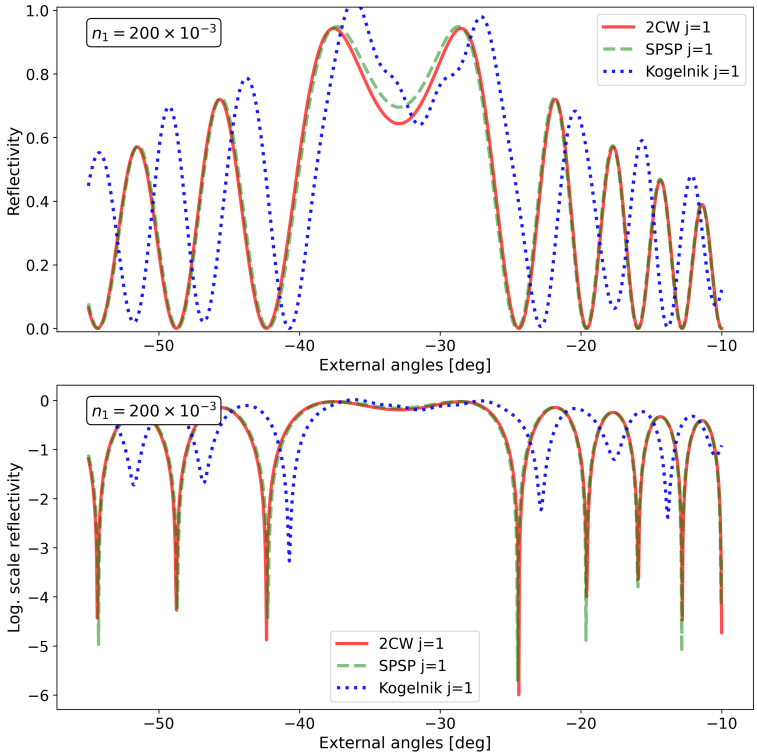

Figure M.3: Comparison of simulations for $\Delta n_1 = 0.2$

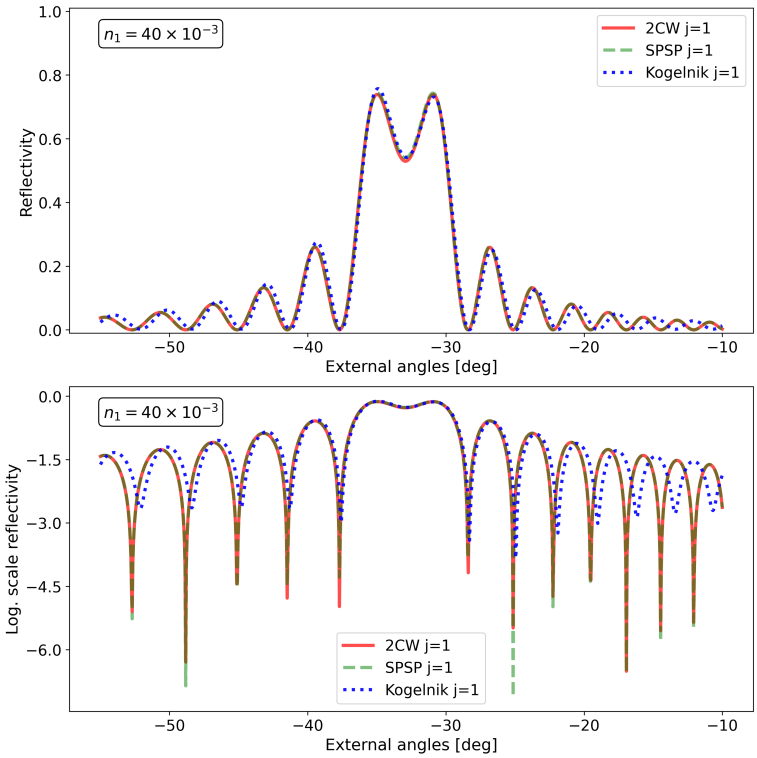

Figure M.4: Comparison of simulations for $\Delta n_1 = 0.04$

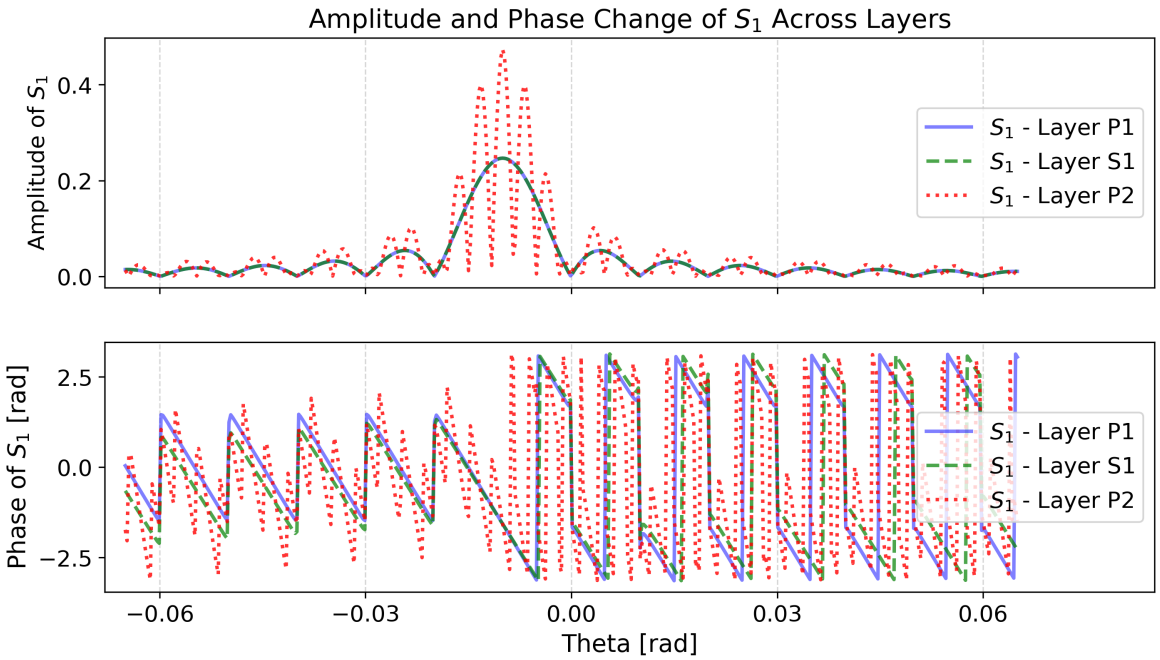

Figure M.5: Modulus and phase changes of the complex wave amplitude S_1 across the layers.

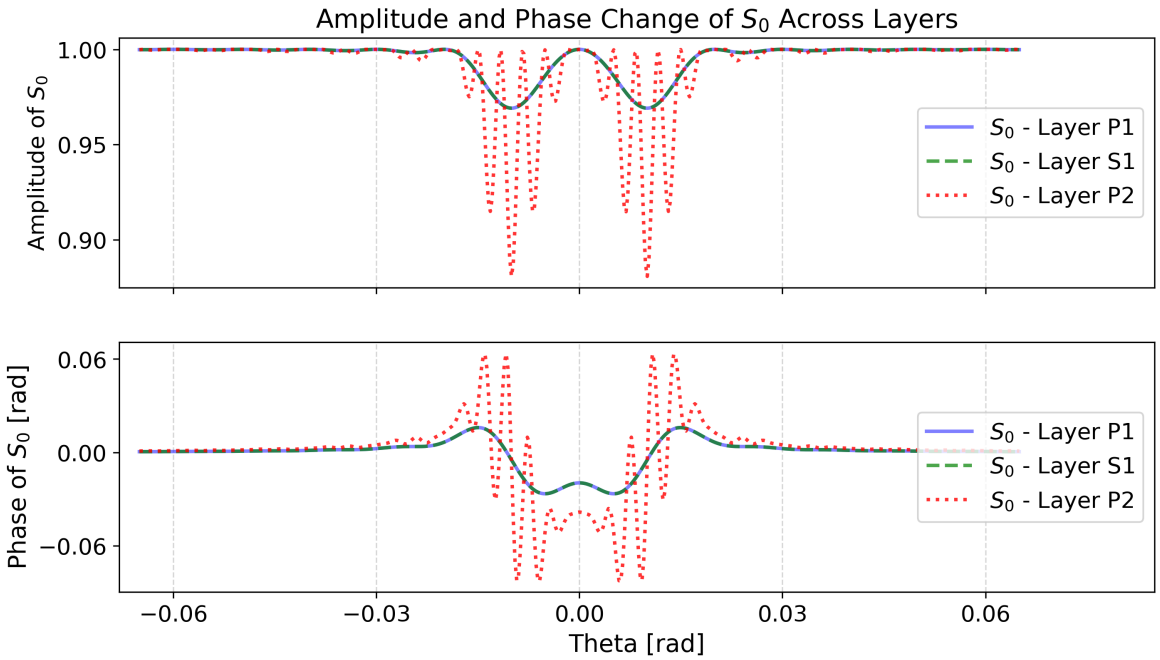

Figure M.6: Modulus and phase changes of the complex wave amplitude S_0 across the layers.

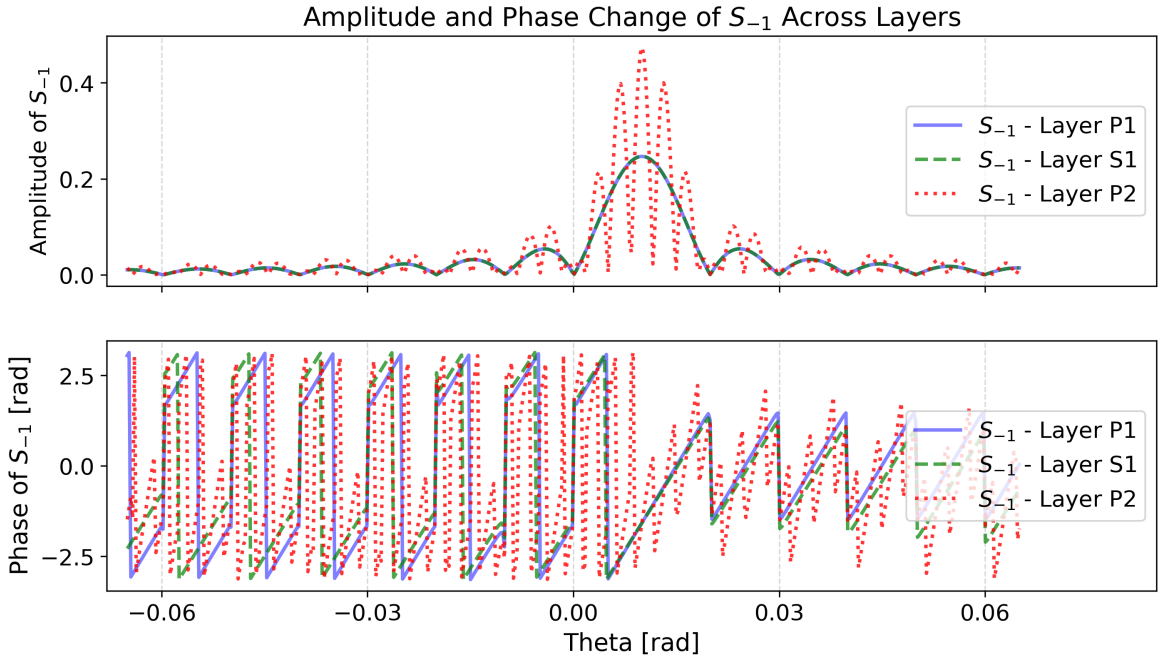

Figure M.7: Modulus and phase changes of the complex wave amplitude S_{-1} across the layers.

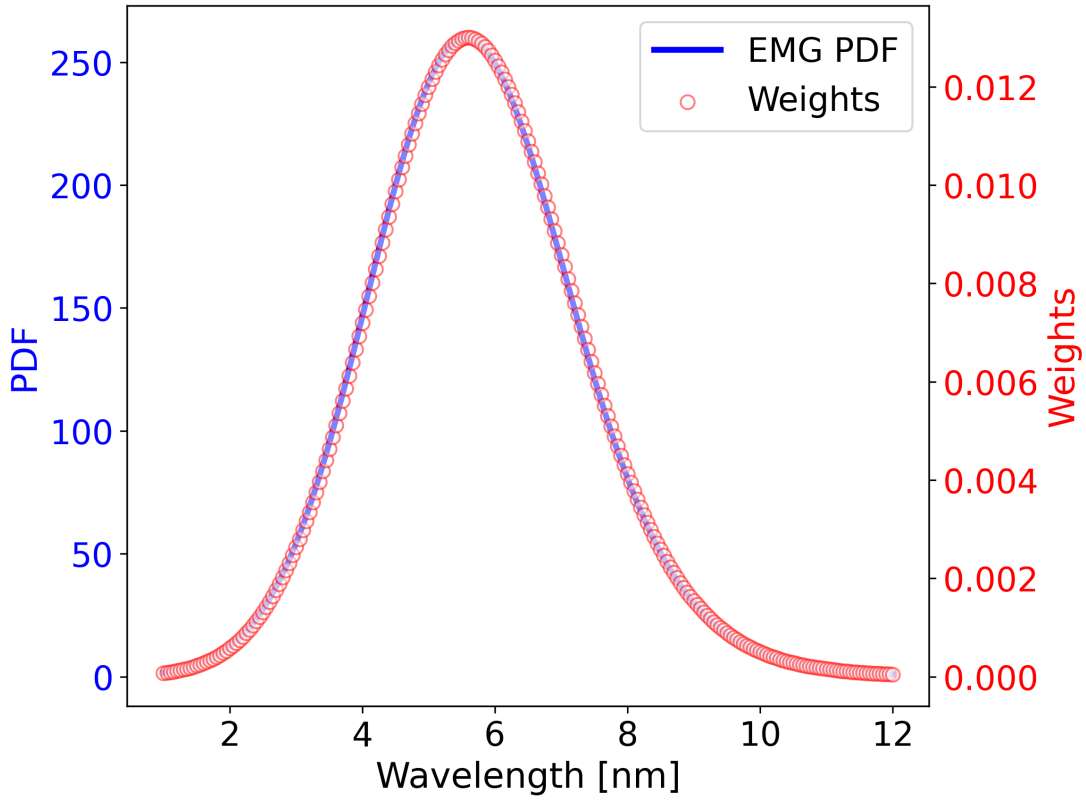

Figure M.8: Post-collimation WLD obtained by fitting neutron diffraction data of the sample SM_32µm_30mW.

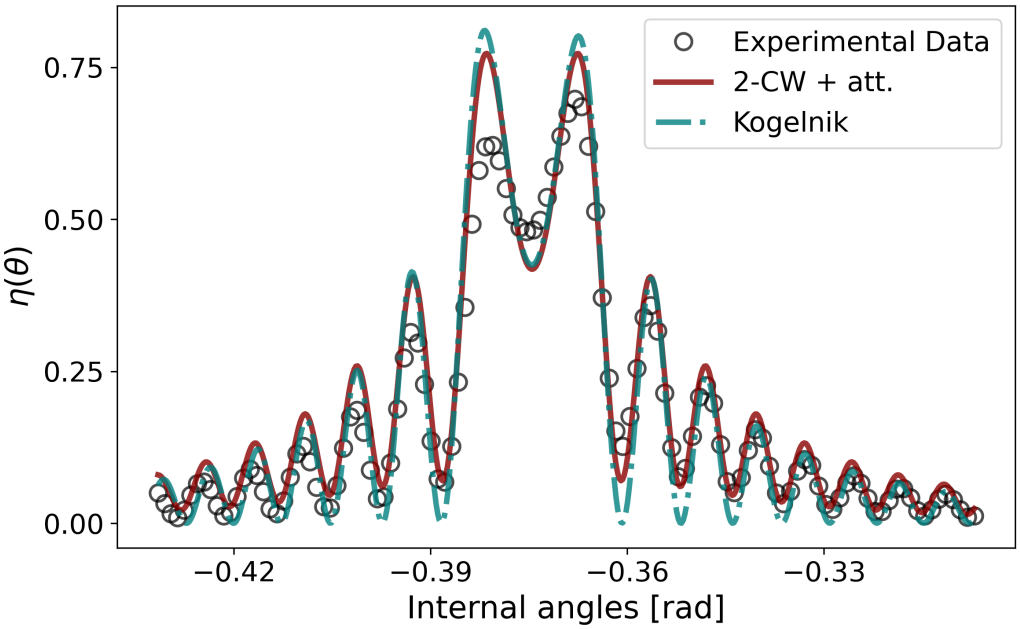

Figure M.9: Light diffraction efficiency curve of the sample "pp70_SP" measured at a wavelength $\lambda_l = 543.5\,\text{nm}$. Circular markers correspond to the data, while the lines correspond to fits using two models: Kogelnik theory (dashdotted line) and two-wave coupling with n_1 attenuation (dark-red line).

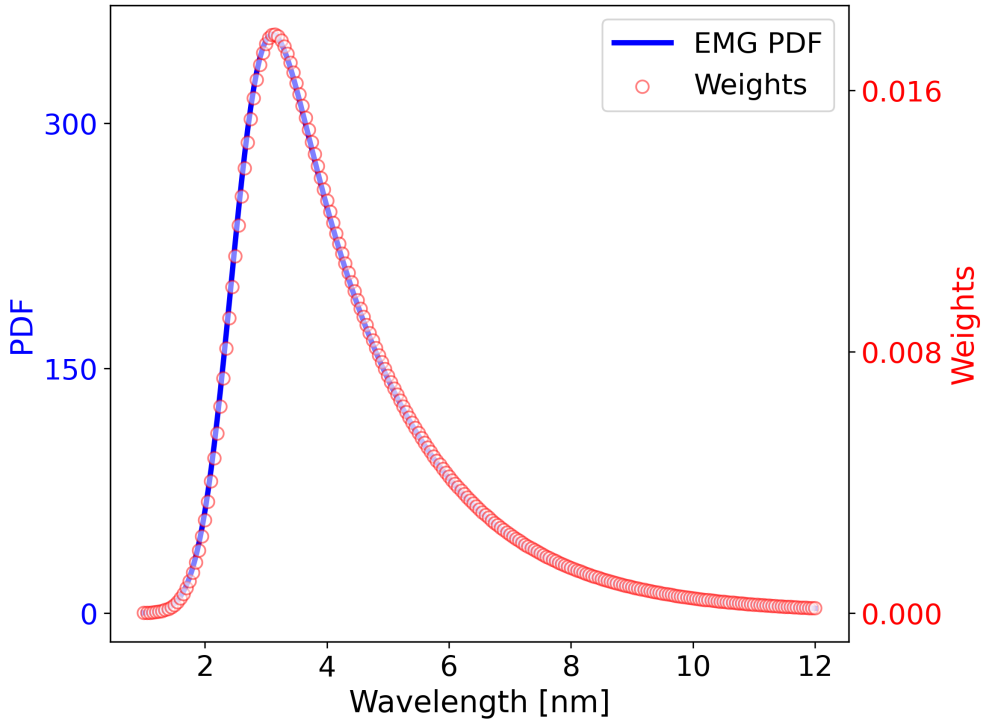

Figure M.10: Neutron WLD determined from a 7-CW fit to the efficiency curves measured from the Bayfol SPSP structure MVHG.

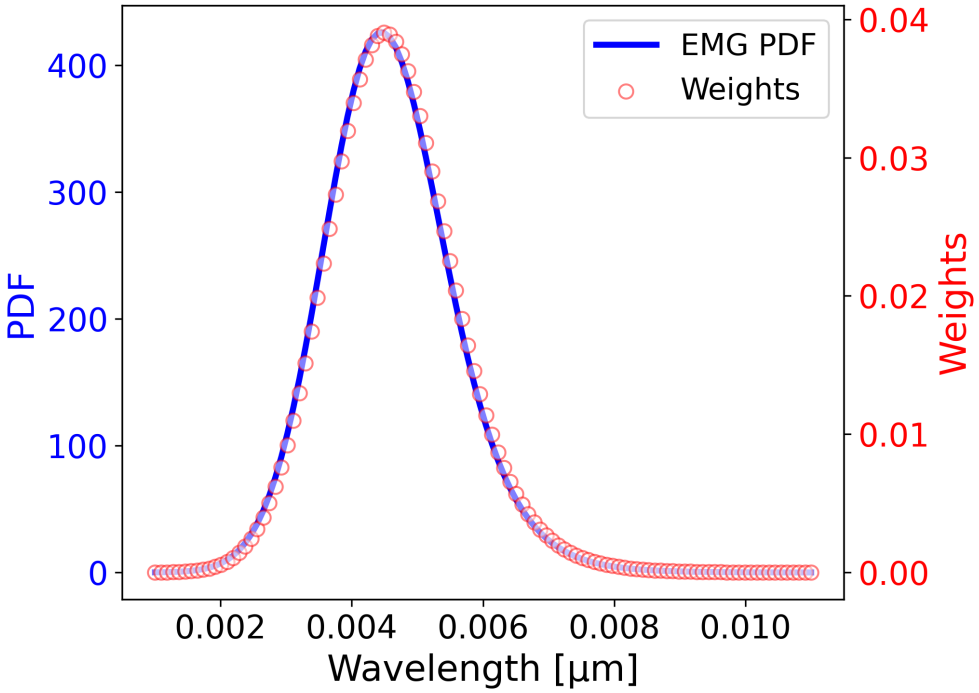

Figure M.11: Neutron WLD determined from a 9-CW fit to the efficiency curves measured from the NDPC grating-7.

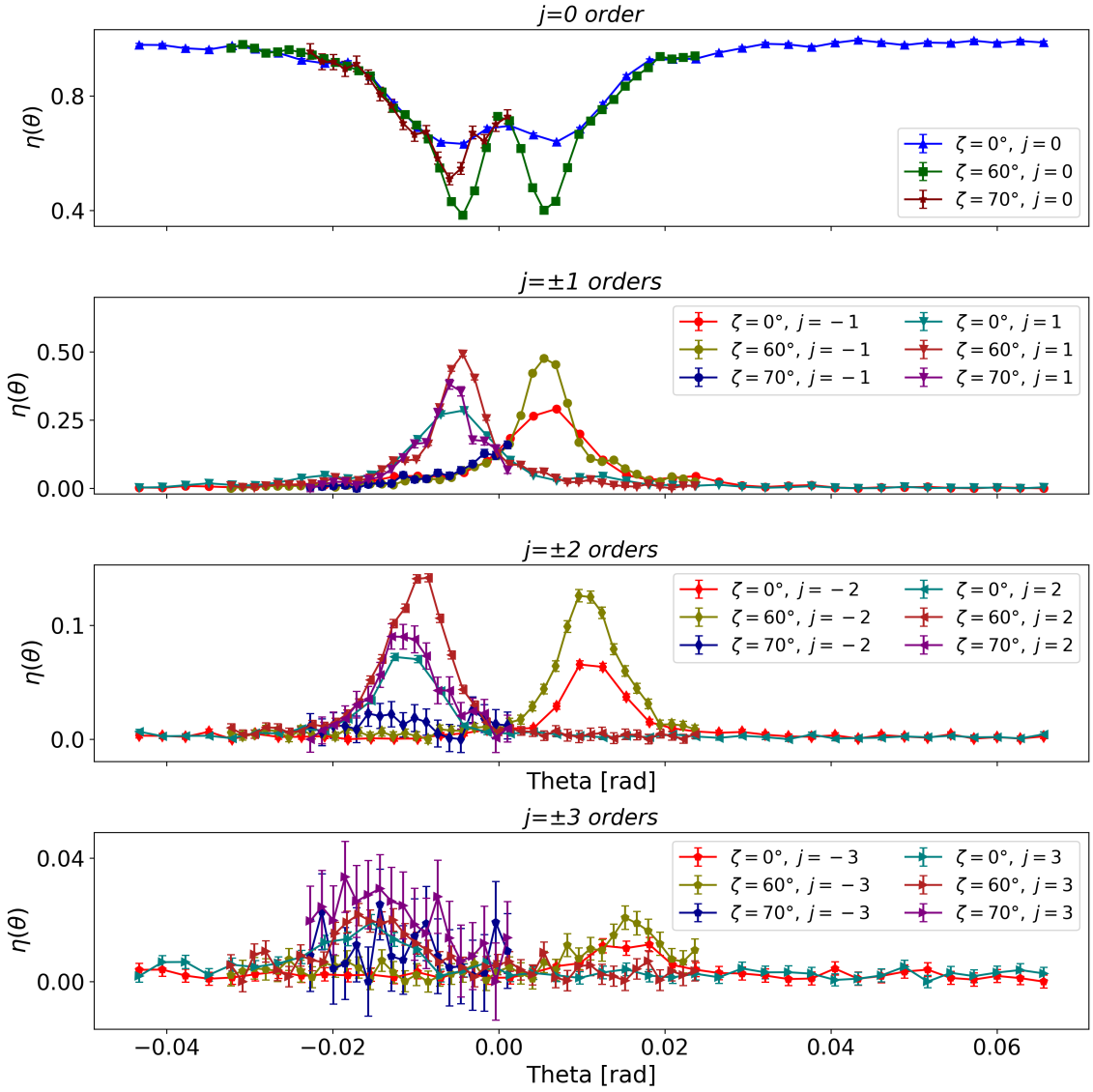

Figure M.12: Diffraction efficiency curves of the NDPC grating-5 at 0°, 60° and 70° tilt angles measured at PF2/VCN instrument..

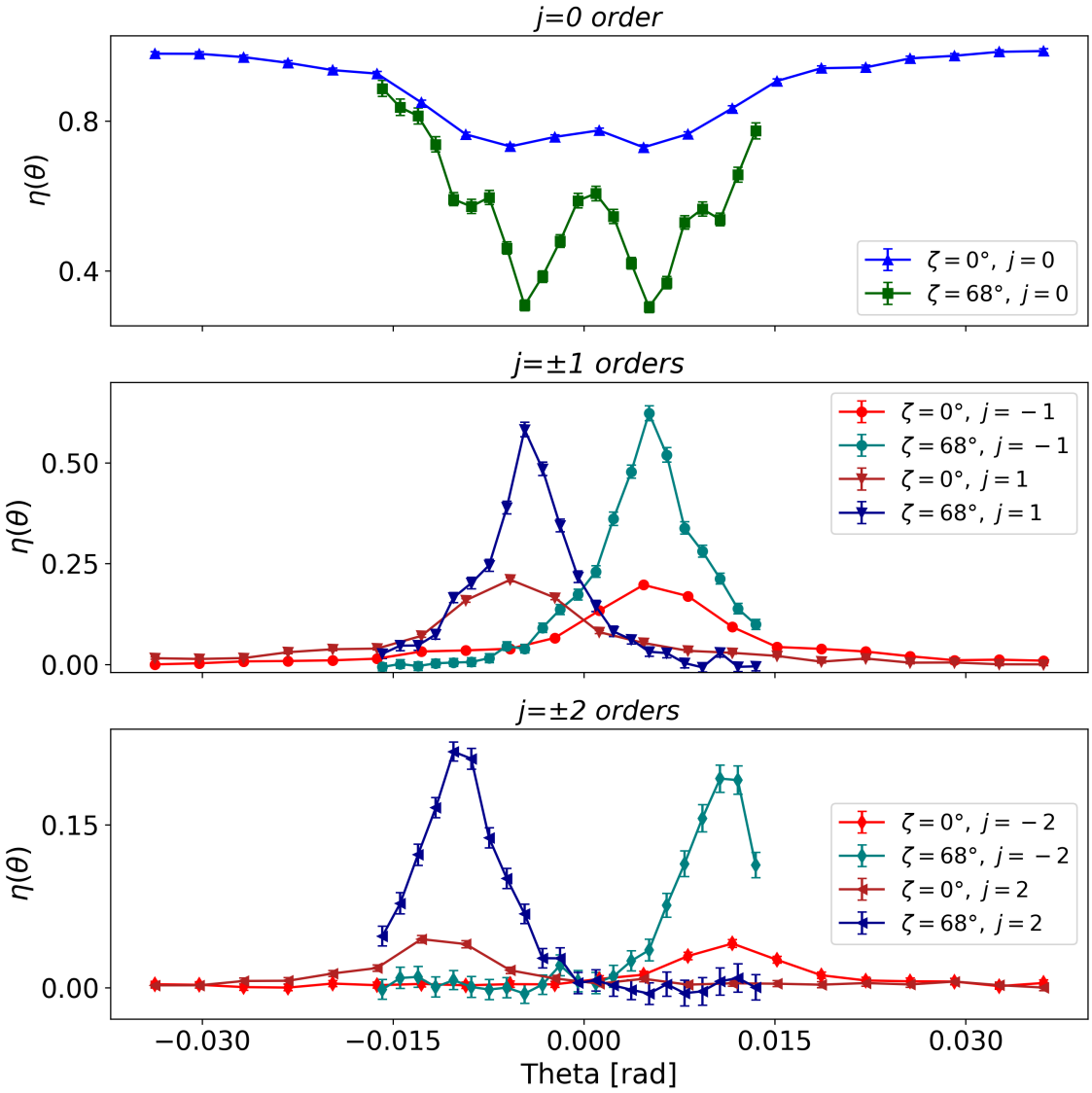

Figure M.13: Diffraction efficiency curves of the NDPC grating-4 at 0° and 68° tilt angles measured at PF2/VCN instrument..

Bibliography

[1] H. Abele et al. "Particle physics at the European Spallation Source". In: *Physics Reports* 1023 (2023). Particle Physics at the European Spallation Source, pp. 1–84. DOI: 10.1016/j.physrep.2023.06.001.

[2] F. Mezei. "Very cold neutrons in condensed matter research". In: *Journal of Neutron Research* Preprint (2022), pp. 1–6. DOI: 10.3233/JNR-220012.

[3] A. Zeilinger. "Long wavelength neutron interferometry". In: *The Investigation of Fundamental Interactions with Cold Neutrons* (1986), p. 112. URL: https://nvlpubs.nist.gov/nistpubs/Legacy/SP/nbsspecialpublication711.pdf#page=120.

[4] V. Santoro, K. H. Andersen, D. DiJulio, E. B. Klinkby, T. Miller, D. Milstead, G. Muhrer, M. Strobl, A. Takibayev, L. Zanini, et al. "Development of high intensity neutron source at the European Spallation Source". In: *Journal of Neutron Research* 22.2-3 (2020), pp. 209–219. DOI: 10.3233/JNR-200159.

[5] L. Zanini, E. Dian, D. Dijulio, B. Folsom, E. Klinkby, Z. Kókai, J. I. Marquez Damian, B. Rataj, N. Rizzi, V. Santoro, M. Strothmann, A. Takibayev, R. Wagner, and O. Zimmer. "Very cold and ultra cold neutron sources for ESS". In: *Journal of Neutron Research* 24.2 (2022), pp. 77–93. DOI: 10.3233/JNR-220040.

[6] V. Santoro, K. Andersen, P. Bentley, M. Bernasconi, M. Bertelsen, Y. Beßler, A. Bianchi, T. Brys, D. Campi, A. Chambon, et al. "The HighNESS project at the European Spallation Source: Current status and future perspectives". In: *Nuclear Science and Engineering* 198.1 (2024), pp. 31–63. DOI: 10.1080/00295639.2023.2204184.

[7] A. Steyerl, H. Nagel, F.-X. Schreiber, K.-A. Steinhauser, R. Gähler, W. Gläser, P. Ageron, J. Astruc, W. Drexel, G. Gervais, and W. Mampe. "A new source of cold and ultracold neutrons". In: *Physics Letters A* 116.7 (1986), pp. 347–352. DOI: 10.1016/0375-9601(86)90587-6.

[8] T. Ederth. "Neutrons for scattering: What they are, where to get them, and how to deal with them". In: *EPJ Web of conferences*. Vol. 188. EDP Sciences. 2018, p. 01002. DOI: 10.1051/epjconf/201818801002.

[9] A. Graf, H. Rauch, and T. Stern. "Diffraction of cold neutrons by ruled gratings". In: *Atomkernenergie Kerntechnik* 33.4 (1979), pp. 298–301. URL: https://inis.iaea.org/search/search.aspx?orig_q=RN:10472101.

[10] A. Ioffe, V. Zabiyakin, and G. Drabkin. "Test of a diffraction grating neutron interferometer". In: *Physics Letters A* 111.7 (1985), pp. 373–375. DOI: 10.1016/0375-9601(85)90373-1.

[11] G. van der Zouw, M. Weber, J. Felber, R. Gähler, P. Geltenbort, and A. Zeilinger. "Aharonov–Bohm and gravity experiments with the very-cold-neutron interferometer". In: *Nuclear Instruments and Methods in Physics Research Section A: Accelerators, Spectrometers, Detectors and Associated Equipment* 440.3 (2000), pp. 568–574. DOI: 10.1016/S0168-9002(99)01038-4.

[12] M. Qian, W. Zhang, D. Trefilov, M. Ji, Y. Cui, C. Yuan, W. Li, H. Ge, and Y. Chen. "Tuning the period of nanogratings using mechanical stretching and nanoimprint lithography". In: *Applied Physics A* 122 (2016), pp. 1–7. DOI: 10.1007/s00339-016-0106-8.

[13] C. Guo, L. Chen, K. Zhang, X. Ding, Y. Xiong, Y. Guan, Z. Wu, Y. Tian, and G. Liu. "Fabrication of small-period neutron absorption grating by pressurized particle filling method". In: *AIP Advances* 14.1 (Jan. 2024), p. 015026. DOI: 10.1063/5.0189984.

[14] M. Fally, I. Drevensek-Olenik, M. Ellabban, K. Pranzas, and J. Vollbrandt. "Colossal Light-Induced Refractive-Index Modulation for Neutrons in Holographic Polymer-Dispersed Liquid Crystals". In: *Physical review letters* 97 (Nov. 2006), p. 167803. DOI: 10.1103/PHYSREVLETT.97.167803.

[15] J. Klepp, C. Pruner, Y. Tomita, P. Geltenbort, I. Drevenšek-Olenik, S. Gyergyek, J. Kohlbrecher, and M. Fally. "Holographic gratings for slow-neutron optics". In: *Materials* 5.12 (2012), pp. 2788–2815. DOI: 10.3390/ma5122788.

[16] M. A. Ellabban, G. Glavan, J. Klepp, and M. Fally. "A comprehensive study of photorefractive properties in poly (ethylene glycol) dimethacrylate—Ionic liquid composites". In: *Materials* 10.1 (2016), p. 9. DOI: 10.3390/ma10010009.

[17] P. Flauger, M. A. Ellabban, G. Glavan, J. Klepp, C. Pruner, T. Jenke, P. Geltenbort, and M. Fally. "Light-and neutron-optical properties of holographic transmission gratings from polymer-ionic liquid composites with submicron grating spacing". In: *Polymers* 11.9 (2019), p. 1459. DOI: 10.3390/polym11091459.

[18] J. Klepp, C. Pruner, Y. Tomita, C. Plonka-Spehr, P Geltenbort, S Ivanov, G. Manzin, K. Andersen, J Kohlbrecher, M. Ellabban, and M. Fally. "Diffraction of slow neutrons by holographic SiO_2 nanoparticle-polymer composite gratings". In: *Physical Review A - PHYS REV A* 84 (June 2011). DOI: 10.1103/PhysRevA.84.013621.

[19] J. Klepp, C. Pruner, Y. Tomita, K. Mitsube, P. Geltenbort, and M. Fally. "Mirrors for slow neutrons from holographic nanoparticle-polymer free-standing film-gratings". In: *Applied Physics Letters* 100.21 (2012). DOI: 10.1063/1.4720511.

[20] J. Klepp, Y. Tomita, C. Pruner, J. Kohlbrecher, and M. Fally. "Three-port beam splitter for slow neutrons using holographic nanoparticle-polymer composite diffraction gratings". In: *Applied Physics Letters* 101.15 (2012). DOI: 10.1063/1.4758686.

[21] J. Klepp, I. Drevenšek-Olenik, S. Gyergyek, C. Pruner, R. A. Rupp, and M. Fally. "Towards polarizing beam splitters for cold neutrons using superparamagnetic diffraction gratings". In: *Journal of Physics: Conference Series* 340.1 (2012), p. 012031. DOI: 10.1088/1742-6596/340/1/012031.

[22] Y. Tomita, A. Kageyama, Y. Iso, K. Umemoto, A. Kume, M. Liu, C. Pruner, T. Jenke, S. Roccia, P. Geltenbort, M. Fally, and J. Klepp. "Fabrication of nanodiamond-dispersed composite holographic gratings and their light and slow-neutron diffraction properties". In: *Phys. Rev. Applied* 14 (4 2020), p. 044056. DOI: 10.1103/PhysRevApplied.14.044056.

[23] M. Fally, J. Klepp, C. Pruner, T. Jenke, P. Geltenbort, A. Kageyama, Y. Iso, K. Umemoto, M. Liu, and Y. Tomita. "Nanodiamond-polymer composite gratings as diffractive optical elements for light and neutrons II: neutron optical diffraction properties". In: *Photosensitive Materials and their Applications*. Vol. 11367. SPIE. 2020, pp. 46–53. DOI: 10.1117/12.2555474.

[24] F.-K. Bruder, T. Fäcke, and T. Rölle. "The chemistry and physics of Bayfol® HX film holographic photopolymer". In: *Polymers* 9.10 (2017), p. 472. DOI: 10.3390/polym9100472.

[25] Y. Tomita, T. Aoi, J. Oshima, and K. Odoi. "Hyperbranched-polymer nanocomposite gratings with ultrahigh refractive index modulation amplitudes for volume holographic optical elements". In: *Holography: Advances and Modern Trends VI*. Vol. 11030. SPIE. 2019, pp. 31–38. DOI: 10.1117/12.2520512.

[26] H. Rauch and S. A. Werner. *Neutron Interferometry: Lessons in Experimental Quantum Mechanics, Wave-Particle Duality, and Entanglement*. Oxford, UK: Oxford University Press, 2015. DOI: 10.1093/acprof:oso/9780198712510.001.0001.

[27] R. Gähler, A. Klein, and A. Zeilinger. "Neutron optical tests of nonlinear wave mechanics". In: *Physical Review A* 23.4 (1981), p. 1611. DOI: 10.1103/PhysRevA.23.1611.

[28] R. Gähler and A. Zeilinger. "Wave-optical experiments with very cold neutrons". In: *American Journal of Physics* 59.4 (1991), pp. 316–324. DOI: 10.1119/1.16540.

[29] J. Chadwick. "The neutron and its properties". In: *The British Journal of Radiology* 6.61 (1933), pp. 24–32. DOI: 10.1259/0007-1285-6-61-24.

[30] E. Amaldi, O. D'Agostino, E. Fermi, B. Pontecorvo, F. Rasetti, and E. Segrè. "Artificial radioactivity produced by neutron bombardment—II". In: *Proceedings of the Royal Society of London. Series A-Mathematical and Physical Sciences* 149.868 (1935), pp. 522–558. DOI: 10.1098/rspa.1935.0080.

[31] E. Fermi et al. "Motion of neutrons in hydrogenous substances". In: *Ricerca Scientifica* 7.2 (1936), pp. 13–52.

[32] H. Von Halban and Preiswerk. "Experimental evidence of neutron diffraction". In: *CR Hebd. Séances Acad* 203 (1936), p. 73. URL: https://www.scirp.org/reference/referencespapers?referenceid=2799208.

[33] D. P. Mitchell and P. N. Powers. "Bragg reflection of slow neutrons". In: *Physical Review* 50.5 (1936), p. 486. DOI: 10.1103/PhysRev.50.486.2.

[34] O. Halpern and M. Johnson Jr. "Magnetic scattering of slow neutrons". In: *Physical Review* 52.2 (1937), p. 52. DOI: 10.1103/PhysRev.52.52.

[35] Oak Ridge National Laboratory. *Celebrating 75 Years: A History of Oak Ridge National Laboratory*. Accessed: 2024. n.d. URL: https://neutrons.ornl.gov/content/celebrating-75-years-history-oak-ridge-national-laboratory.

[36] W. Davidson, G. Morton, G. Shull, and E. Wollan. *Neutron diffraction analysis of NaH and NaD*. Vol. 842. Atomic Energy Commission, 1947. URL: https://catalog.hathitrust.org/Record/005979678.

[37] M. Goldberger and F. Seitz. "Theory of the refraction and the diffraction of neutrons by crystals". In: *Physical Review* 71.5 (1947), p. 294. DOI: 10.1103/PhysRev.71.294.

[38] D. Kleinman and G. Snow. "The Index of Refraction for Neutrons". In: *Physical Review* 82.6 (1951), p. 952. DOI: 10.1103/PhysRev.82.952.

[39] O. Halpern. "Remarks on Some Questions of Neutron Optics". In: *Physical Review* 88.5 (1952), p. 1003. DOI: 10.1103/PhysRev.88.1003.

[40] D. Hughes. "Neutron Optics". In: *Annual Review of Nuclear Science* 3.1 (1953), pp. 93–118. DOI: 10.1146/annurev.ns.03.120153.000521.

[41] H. Maier-Leibnitz and T. Springer. "The use of neutron optical devices on beam-hole experiments on beam-hole experiments". In: *Journal of Nuclear Energy. Parts A/B. Reactor Science and Technology* 17.4-5 (1963), pp. 217–225. DOI: 10.1016/0368-3230(63)90022-3.

[42] H. Maier-Leibnitz and T. Springer. "Ein interferometer für langsame neutronen". In: *Zeitschrift für Physik* 167.4 (1962), pp. 386–402. DOI: 10.1007/BF01378119.

[43] R. Gähler, J. Kalus, and W. Mampe. "Experimental limit for the charge of the free neutron". In: *Physical Review D* 25.11 (1982), p. 2887. DOI: 10.1103/PhysRevD.25.2887.

[44] A. Zeilinger, R. Gähler, C. Shull, W. Treimer, and W. Mampe. "Single-and double-slit diffraction of neutrons". In: *Reviews of modern physics* 60.4 (1988), p. 1067. DOI: 10.1103/RevModPhys.60.1067.

[45] H. Kurz and H. Rauch. *Diffraction of thermal neutrons by a ruled grating*. Tech. rep. Oesterreichische Hochschule, Vienna, 1969. DOI: 10.1007/BF01394786.

[46] W. Just, C. Schneider, R. Ciszewski, and C. Shull. "Refraction of thermal neutrons by shaped magnetic fields". In: *Physical Review B* 7.9 (1973), p. 4142. DOI: 10.1103/PhysRevB.7.4142.

[47] H. Rauch, W. Treimer, and U. Bonse. "Test of a single crystal neutron interferometer". In: *Physics Letters A* 47.5 (1974), pp. 369–371. DOI: 10.1016/0375-9601(74)90132-7.

[48] A. G. Klein and G. Opat. "Observation of 2 π rotations by Fresnel diffraction of neutrons". In: *Physical Review Letters* 37.5 (1976), p. 238. DOI: 10.1103/PhysRevLett.37.238.

[49] A. Klein and G. Opat. *Applications of the fresnel diffraction of neutrons*. Tech. rep. Melbourne Univ., 1978. URL: https://www.researchgate.net/publication/313712403_Applications_of_the_Fresnel_Diffraction_of_Neutrons.

[50] P. Kearney, A. Klein, G. Opat, and R. Gähler. "Imaging and focusing of neutrons by a zone plate". In: *Nature* 287.5780 (1980), pp. 313–314. DOI: 10.1038/287313a0.

[51] A. G. Klein, P. D. Kearney, G. I. Opat, A. Cimmino, and R. Gähler. "Neutron Interference by Division of Wavefront". In: *Phys. Rev. Lett.* 46 (15 1981), pp. 959–962. DOI: 10.1103/PhysRevLett.46.959.

[52] T. Gaylord and M. Moharam. "Planar dielectric grating diffraction theories". In: *Applied Physics B* 28 (1982), pp. 1–14. DOI: 10.1007/BF00693885.

[53] T. K. Gaylord and M. Moharam. "Thin and thick gratings: terminology clarification". In: *Applied optics* 20.19 (1981), pp. 3271–3273. DOI: 10.1364/AO.20.003271.

[54] M. Moharam, T. Gaylord, and R. Magnusson. "Criteria for Bragg regime diffraction by phase gratings". In: *Optics Communications* 32.1 (1980), pp. 14–18. DOI: 10.1016/0030-4018(80)90304-1.

[55] M. Moharam, T. Gaylord, and R. Magnusson. "Criteria for Raman-Nath regime diffraction by phase gratings". In: *Optics Communications* 32.1 (1980), pp. 19–23. DOI: 10.1016/0030-4018(80)90305-3.

[56] M. Moharam, E. B. Grann, D. A. Pommet, and T. Gaylord. "Formulation for stable and efficient implementation of the rigorous coupled-wave analysis of binary gratings". In: *JOSA a* 12.5 (1995), pp. 1068–1076. DOI: 10.1364/JOSAA.12.001068.

[57] A. Klein and S. Werner. "Neutron optics". In: *Reports on Progress in Physics* 46.3 (1983), p. 259. DOI: 10.1088/0034-4885/46/3/001.

[58] V. F. Sears. *Neutron Optics*. Vol. 3. Neutron Scattering in Condensed Matter. New York: Oxford University Press, 1989. URL: https://books.google.fr/books?id=iNXvAAAAMAAJ.

[59] G. Greene. "The investigation of fundamental interactions with cold neutrons". In: *NBS Special Publication* 711 (1986). URL: https://inis.iaea.org/search/search.aspx?orig_q=RN:18000879.

[60] IAEA, ed. *Proceedings of the International Workshop on Matter Wave Interferometry in the Light of Schrödinger Wave Mechanics*. Preface. Vienna, Austria, 1987. URL: https://inis.iaea.org/collection/NCLCollectionStore/_Public/20/000/20000018.pdf.

[61] M. Gruber, K. Eder, A. Zeilinger, R. Gähler, and W. Mampe. "A phase-grating interferometer for very cold neutrons". In: *Physics Letters A* 140.7-8 (1989), pp. 363–367. DOI: 10.1016/0375-9601(89)90068-6.

[62] Institut Laue-Langevin. *PF2 Instrument*. Accessed: 2024. 2024. URL: https://www.ill.eu/users/instruments/instruments-list/pf2/description/instrument-layout.

[63] J. Valsecchi, R. P. Harti, M. Raventós, M. D. Siegwart, M. Morgano, P. Boillat, M. Strobl, P. Hautle, L. Holitzner, U. Filges, et al. "Visualization and quantification of inhomogeneous and anisotropic magnetic fields by polarized neutron grating interferometry". In: *Nature communications* 10.1 (2019), p. 3788. DOI: 10.1038/s41467-019-11590-2.

[64] F. M. Piegsa. "Novel concept for a neutron electric charge measurement using a Talbot-Lau interferometer at a pulsed source". In: *Physical Review C* 98.4 (2018), p. 045503. DOI: 10.1103/PhysRevC.98.045503.

[65] U. Schellhorn, R. A. Rupp, S. Breer, and R. P. May. "The first neutron interferometer built of holographic gratings". In: *Physica B: Condensed Matter* 234 (1997), pp. 1068–1070. DOI: 10.1016/S0921-4526(97)00015-X.

[66] K. Eder, M. Gruber, A. Zeilinger, R. Gähler, and W. Mampe. "Diffraction of very cold neutrons at phase gratings". In: *Physica B: Condensed Matter* 172.3 (1991), pp. 329–338. DOI: 10.1016/0921-4526(91)90451-J.

[67] D. Sarenac, D. A. Pushin, M. G. Huber, D. S. Hussey, H. Miao, M. Arif, D. G. Cory, A. D. Cronin, B. Heacock, D. L. Jacobson, et al. "Three phase-grating moiré neutron interferometer for large interferometer area applications". In: *Physical review letters* 120.11 (2018), p. 113201. DOI: 10.1103/PhysRevLett.120.113201.

[68] Y. Kim, J. Kim, D. Kim, D. Hussey, S. W. Lee, et al. "Characterization of the phase sensitivity, visibility, and resolution in a symmetric neutron grating interferometer". In: *Review of Scientific Instruments* 90.7 (2019). DOI: 10.1063/1.5089588.

[69] T. Reimann, S. Mühlbauer, M. Horisberger, B. Betz, P. Böni, and M. Schulz. "The new neutron grating interferometer at the ANTARES beamline: design, principles and applications". In: *Journal of Applied Crystallography* 49.5 (2016), pp. 1488–1500. DOI: 10.1107/S1600576716011080.

[70] A. Gustschin, T. Neuwirth, A. Backs, M. Schulz, and F. Pfeiffer. "Fabrication of gadolinium particle-based absorption gratings for neutron grating interferometry". In: *Review of Scientific Instruments* 89.10 (2018). DOI: 10.1063/1.5047055.

[71] M. Hino, S. Tasaki, Y. Kawabata, T. Ebisawa, P. Geltenbort, T. Brenner, J. Butterworth, R. Gähler, N. Achiwa, and M. Utsuro. "Development of a very cold neutron spin interferometer at the ILL". In: *Physica B: Condensed Matter* 335.1 (2003). Proceedings of the Fourth International Workshop on Polarised Neutrons for Condensed Matter Investigations, pp. 230–233. DOI: 10.1016/S0921-4526(03)00244-8.

[72] V. Gudkov, H. M. Shimizu, and G. L. Greene. "Parametric resonance enhancement in neutron interferometry and application for the search for non-Newtonian gravity". In: *Phys. Rev. C* 83 (2 2011), p. 025501. DOI: 10.1103/PhysRevC.83.025501.

[73] J. Klepp, S. Sponar, and Y. Hasegawa. "Fundamental phenomena of quantum mechanics explored with neutron interferometers". In: *Progress of Theoretical and Experimental Physics* 2014.8 (2014), 082A01. DOI: 10.1093/ptep/ptu085.

[74] M. Utsuro, M. Hino, P. Geltenbort, and J. Butterworth. "Observation on the visibility decrease in a VCN spin resonator interferometry". In: *Journal of Research of the National Institute of Standards and Technology* 110.3 (2005), p. 245. DOI: 10.6028/jres.110.033.

[75] H. Kogelnik. "Coupled wave theory for thick hologram gratings". In: *Bell System Technical Journal* 48.9 (1969), pp. 2909–2947. DOI: 10.1002/j.1538-7305.1969.tb01198.x.

[76] M. Fally, Y. Tomita, A. Fimia, R. F. Madrigal, J. Guo, J. Kohlbrecher, and J. Klepp. "Experimental determination of nanocomposite grating structures by light- and neutron-diffraction in the multi-wave-coupling regime". In: *Opt. Express* 29.11 (2021), pp. 16153–16163. DOI: 10.1364/OE.424233.

[77] D. R. Corson and P. Lorrain. *Introduction to electromagnetic fields and waves*. A series of books in physics. W. H. Freeman, 1962. URL: https://cir.nii.ac.jp/crid/1130000793940781696.

[78] P. V. Rysselberghe. "Remarks concerning the Clausius-Mossotti law". In: *The Journal of Physical Chemistry* 36.4 (2002), pp. 1152–1155. DOI: 10.1021/j150334a007.

[79] R. R. A. Syms. "Practical volume holography". In: *Oxford University Press* (1990). URL: https://books.google.fr/books?id=bS58AAAAIAAJ.

[80] N. Uchida. "Calculation of diffraction efficiency in hologram gratings attenuated along the direction perpendicular to the grating vector". In: *JOSA* 63.3 (1973), pp. 280–287. DOI: 10.1364/JOSA.63.000280.

[81] Y. Tomita, T. Aoi, S. Hasegawa, F. Xia, Y. Wang, and J. Oshima. "Very high contrast volume holographic gratings recorded in photopolymerizable nanocomposite materials". In: *Opt. Express* 28.19 (2020), pp. 28366–28382. DOI: 10.1364/OE.400092.

[82] M. Fally. "The photo-neutronrefractive effect". In: *Applied Physics B* 75 (Oct. 2002), pp. 405–426. DOI: 10.1007/s00340-002-1035-0.

[83] V. Sears. "Schrödinger equation for neutron optics". In: *Physica B+ C* 151.1-2 (1988), pp. 156–159. DOI: 10.1016/0378-4363(88)90160-X.

[84] R. Cubitt and G. Fragneto. "Chapter 2.8.3 - Neutron Reflection:: Principles and Examples of Applications". In: *Scattering*. Ed. by R. Pike and P. Sabatier. London: Academic Press, 2002, pp. 1198–1208. DOI: 10.1016/B978-012613760-6/50065-6.

[85] J. Klepp, C. Pruner, M. Ellabban, Y. Tomita, H. Lemmel, and M. Rauch H .and Fally. "Neutron-optical gratings from nanoparticle-polymer composites". In: *Nuclear Instruments and Methods in Physics Research Section A: Accelerators, Spectrometers, Detectors and Associated Equipment* 634.1 (2011), S59–S62. DOI: 10.1016/j.nima.2010.06.360.

[86] C. G. Shull. "Observation of Pendellösung Fringe Structure in Neutron Diffraction". In: *Phys. Rev. Lett.* 21 (23 1968), pp. 1585–1589. DOI: 10.1103/PhysRevLett.21.1585.

[87] V. I. Punegov. "X-ray Laue diffraction by sectioned multilayers. I. Pendellösung effect and rocking curves". In: *Journal of Synchrotron Radiation* 28.5 (2021), pp. 1466–1475. DOI: 10.1107/S1600577521006408.

[88] V. Somenkov, S. Shilstein, N. Belova, and K. Utemisov. "Observation of dynamical oscillations for neutron scattering by Ge crystals using the inclination method". In: *Solid State Communications* 25.8 (1978), pp. 593–595. DOI: 10.1016/0038-1098(78)91497-7.

[89] M. Fally, J. Klepp, Y. Tomita, T. Nakamura, C. Pruner, M. A. Ellabban, R. A. Rupp, M. Bichler, I. D. c. v. Olenik, J. Kohlbrecher, H. Eckerlebe, H. Lemmel, and H. Rauch. "Neutron Optical Beam Splitter from Holographically Structured Nanoparticle-Polymer Composites". In: *Phys. Rev. Lett.* 105 (12 2010), p. 123904. DOI: 10.1103/PhysRevLett.105.123904.

[90] J. Sheridan. "A comparison of diffraction theories for off-Bragg replay". In: *Journal of Modern Optics* 39.8 (1992), pp. 1709–1718. DOI: 10.1080/713823578.

[91] M. Fally, J. Klepp, and Y. Tomita. "An experimental study on the validity of diffraction theories for off-Bragg replay of volume holographic gratings". In: *Applied Physics B* 108 (2012), pp. 89–96. DOI: 10.1007/s00340-012-5090-x.

[92] J. A. Kong. "Second-order coupled-mode equations for spatially periodic media∗". In: *J. Opt. Soc. Am.* 67.6 (1977), pp. 825–829. DOI: 10.1364/JOSA.67.000825.

[93] J. Klepp, C. Pruner, Y. Tomita, P. Geltenbort, J. Kohlbrecher, and M. Fally. "Advancing data analysis for reflectivity measurements of holographic nanocomposite gratings". In: *Journal of Physics: Conference Series* 746.1 (2016), p. 012022. DOI: 10.1088/1742-6596/746/1/012022.

[94] W. Moerner and S. M. Silence. "Polymeric photorefractive materials". In: *Chemical reviews* 94.1 (1994), pp. 127–155. DOI: 10.1021/cr00025a005.

[95] W. Klein and B. D. Cook. "Unified approach to ultrasonic light diffraction". In: *IEEE Transactions on sonics and ultrasonics* 14.3 (1967), pp. 123–134. DOI: 10.1109/T-SU.1967.29423.

[96] C. Neipp, J. T. Sheridan, S. Gallego, M. Ortuño, A. Márquez, I. Pascual, and A. Beléndez. "Effect of a depth attenuated refractive index profile in the angular responses of the efficiency of higher orders in volume gratings recorded in a PVA/Acrylamide photopolymer". In: *Optics communications* 233.4-6 (2004), pp. 311–322. DOI: 10.1016/j.optcom.2004.01.064.

[97] I. V. Masiello. "Master thesis, Univ. of Aarhus". 2022.

[98] X. Yan, L. Gao, X. Yang, Y. Dai, Y. Chen, and G. Ma. "Generation of individually modulated femtosecond pulse string by multilayer volume holographic gratings". In: *Opt. Express* 22.21 (2014), pp. 26128–26140. DOI: 10.1364/OE.22.026128.

[99] X. Yan, X. Wang, Y. Chen, Y. Wang, Y. Dai, X. Yang, and G. Ma. "Influence of buffer layer and grating layer on diffraction of multilayer volume holographic grating". In: *Applied Physics B* 125 (2019), pp. 1–8. DOI: 10.1007/s00340-019-7173-4.

[100] X. Yan, M. Qian, L. Gao, X. Yang, Y. Dai, X. Yan, and G. Ma. "Pulse splitting by modulating the thickness of buffer layer of two-layer volume holographic grating". In: *Optics Express* 21.26 (2013), pp. 31852–31861. DOI: 10.1364/OE.21.031852.

[101] S. Wang and R. Magnusson. "Multilayer waveguide-grating filters". In: *Applied optics* 34.14 (1995), pp. 2414–2420. DOI: 10.1364/AO.34.002414.

[102] G. P. Nordin, R. V. Johnson, and A. R. Tanguay. "Diffraction properties of stratified volume holographic optical elements". In: *J. Opt. Soc. Am. A* 9.12 (1992), pp. 2206–2217. DOI: 10.1364/JOSAA.9.002206.

[103] B. Wang, J. Jiang, D. M. Chambers, J. Cai, and G. P. Nordin. "Stratified waveguide grating coupler for normal fiber incidence". In: *Optics letters* 30.8 (2005), pp. 845–847. DOI: 10.1364/OL.30.000845.

[104] Y. Shi, C. Wan, D. Chenjie, Z. Wang, S. Wan, G. Zheng, S. Zhang, and Z. Li. "Augmented Reality Enabled by On-Chip Meta-Holography Multiplexing". In: *Laser & Photonics Reviews* 16 (May 2022). DOI: 10.1002/lpor.202100638.

[105] P. Stoeva, T. Mikulchyk, I. Naydenova, and K. Murphy. "Holographic multiplexing in a photopolymerisable hybrid sol-gel". In: *Optics Continuum* 3 (May 2024). DOI: 10.1364/OPTCON.516825.

[106] S. S. Lahijani, T. Jenke, C. Pruner, J. Klepp, and M. Fally. "Multilayer volume holographic gratings from BayFol HX: light and neutron optical characteristics". In: *Holography: Advances and Modern Trends VIII*. Vol. 12574. SPIE. 2023, p. 1257403. DOI: 10.1117/12.2665169.

[107] M. Y. Rodionov and E. Pen. "Simulation of the multilayer volume holographic gratings". In: *Proceedings of the IASTED International Conference*. Vol. 693. 004. 2010, p. 270. DOI: 10.2316/P.2010.693-004.

[108] L. Au, J. Newell, and L. Solymar. "Non-uniformities in thick dichromated gelatin transmission gratings". In: *Journal of Modern Optics* 34.9 (1987), pp. 1211–1225. DOI: 10.1080/09500348714551101.

[109] V. A. Markel. "Introduction to the Maxwell Garnett approximation: tutorial". In: *J. Opt. Soc. Am. A* 33.7 (2016), pp. 1244–1256. DOI: 10.1364/JOSAA.33.001244.

[110] P. Chen, Y. Li, Y. Nishiyama, S. V. Pingali, H. M. O'neill, Q. Zhang, and L. A. Berglund. "Small angle neutron scattering shows nanoscale PMMA distribution in transparent wood biocomposites". In: *Nano Letters* 21.7 (2021), pp. 2883–2890. DOI: 10.1021/acs.nanolett.0c05038.

[111] Y. Tomita and collaborators. *Acknowledgment of NPC Sample Production*. Private communication. All NPC samples used in this PhD research were produced in Japan by our collaborators led by Prof. Yasuo Tomita. 2024.

[112] Daicel Corporation. *High-purity nanodiamonds*. Accessed: 2024. URL: https://www.daicel.com/en/nanodiamond/.

[113] V. Y. Dolmatov. "Detonation-synthesis nanodiamonds: synthesis, structure, properties and applications". In: *Russian Chemical Reviews* 76.4 (2007), p. 339. DOI: 10.1070/RC2007v076n04ABEH003643.

[114] Y. Tomita, E. Hata, K. Momose, S. Takayama, X. Liu, K. Chikama, J. Klepp, C. Pruner, and M. Fally. "Photopolymerizable nanocomposite photonic materials and their holographic applications in light and neutron optics". In: *J. Mod. Opt.* 63.sup3 (2016), S1–S31. DOI: 10.1080/09500340.2016.1143534.

[115] Z. Grigale-Sorocina, M. Kalnins, and K. Gross. "Influence of monomer on structure, processing and application characteristics of UV curable urethane acrylate composite coatings". In: *IOP Conference Series: Materials Science and Engineering*. Vol. 111. 1. IOP Publishing. 2016, p. 012008. DOI: 10.1088/1757-899X/111/1/012008.

[116] A. Narita, J. Oshima, Y. Iso, S. Hasegawa, and Y. Tomita. "Red-sensitive organic nanoparticle-polymer composite materials for volume holographic gratings with large refractive index modulation amplitudes". In: *Optical Materials Express* 11.3 (2021), pp. 614–628. DOI: 10.1364/OME.415422.

[117] K. Tezuka, M. Umezawa, T.-I. Liu, K. Nomura, K. Okubo, H.-C. Chiu, M. Kamimura, and K. Soga. "Upconversion luminescent nanostructure with ultrasmall ceramic nanoparticles coupled with rose bengal for NIR-induced photodynamic therapy". In: *ACS Applied Bio Materials* 4.5 (2021), pp. 4462–4469. DOI: 10.1021/acsabm.1c00213.

[118] Y.-C. Chen, Y.-T. Kuo, and T.-H. Ho. "Photo-polymerization properties of type-II photoinitiator systems based on 2-chlorohexaaryl biimidazole (o-Cl-HABI) and various N-phenylglycine (NPG) derivatives!" In: *Photochemical & Photobiological Sciences* 18 (2019), pp. 190–197. DOI: 10.1039/c8pp00300a.

[119] R. Podsiadły, R. Michalski, A. Marcinek, and J. Sokołowska. "Benzothiazine Dyes/2,4,6-Tris(trichloromethyl)-1,3,5-triazine as a New Visible Two-Component Photoinitiator System". In: *International Journal of Photoenergy* 2012.1 (2012), p. 497620. DOI: https://doi.org/10.1155/2012/497620.

[120] E. Düker. "Master thesis, Univ. of Aarhus". 2021.

[121] S. Moser. "Master thesis, Univ. of Vienna". 2023.

[122] A. Narita, J. Oshima, S. Hasegawa, Y. Iso, and Y. Tomita. "Supplementary document for Red-sensitive organic nanoparticle-polymer composite materials for volume holographic gratings with large refractive index modulation amplitudes - 5040792.pdf". In: (Feb. 2021). DOI: 10.6084/m9.figshare.13634240.v2.

[123] K. Ishizu, K. Tsubaki, A. Mori, and S. Uchida. "Architecture of nanostructured polymers". In: *Progress in polymer science* 28.1 (2003), pp. 27–54. DOI: 10.1016/S0079-6700(02)00025-4.

[124] Y. Tomita, H. Urano, T. aki Fukamizu, Y. Kametani, N. Nishimura, and K. Odoi. "Nanoparticle-polymer composite volume holographic gratings dispersed with ultrahigh-refractive-index hyperbranched polymer as organic nanoparticles". In: *Opt. Lett.* 41.6 (2016), pp. 1281–1284. DOI: 10.1364/OL.41.001281.

[125] E. K. Macdonald, J. C. Lacey, I. Ogura, and M. P. Shaver. "Aromatic polyphosphonates as high refractive index polymers". In: *European Polymer Journal* 87 (2017), pp. 14–23. DOI: 10.1016/j.eurpolymj.2016.12.003.

[126] M. R. Gleeson, J. Guo, and J. T. Sheridan. "Optimisation of photopolymers for holographic applications using the Non-local Photo-polymerization Driven Diffusion model". In: *Opt. Express* 19.23 (2011), pp. 22423–22436. DOI: 10.1364/OE.19.022423.

[127] J. T. Sheridan and J. R. Lawrence. "Nonlocal-response diffusion model of holographic recording in photopolymer". In: *J. Opt. Soc. Am. A* 17.6 (2000), pp. 1108–1114. DOI: 10.1364/JOSAA.17.001108.

[128] J. Guo, M. R. Gleeson, and J. T. Sheridan. "Analysis of the effects of viscosity, volume, and temperature in photopolymer material for holographic applications". In: *Holography: Advances and Modern Trends III*. Ed. by M. Hrabovský, J. T. Sheridan, and A. Fimia-Gil. Vol. 8776. International Society for Optics and Photonics. SPIE, 2013, 87760J. DOI: 10.1117/12.2018330.

[129] G. Zhao and P. Mouroulis. "Diffusion Model of Hologram Formation in Dry Photopolymer Materials". In: *Journal of Modern Optics* 41.10 (1994), pp. 1929–1939. DOI: 10.1080/09500349414551831.

[130] N. Noiret, C. Meyer, and D. J. Lougnot. "Photopolymers for holographic recording. V. Self-processing systems with near infrared sensitivity". In: *Pure and Applied Optics: Journal of the European Optical Society Part A* 3.1 (1994), p. 55. DOI: 10.1088/0963-9659/3/1/007.

[131] E. HADDEN, M. FALLY, H. FILTER, T. JENKE, J. KLEPP, and C. PRUNER. "Investigation of the diffraction properties of holographic optical elements for cold neutrons". In: *Institut Laue-Langevin (ILL): Grenoble,* (2023). DOI: 10.5291/ILL-DATA.3-14-433.

[132] U. Bons and W. Graeff. "X-ray and neutron interferometry". In: *X-Ray Optics: Applications to Solids*. Ed. by H.-J. Queisser. Berlin, Heidelberg: Springer Berlin Heidelberg, 1977, pp. 93–143. DOI: 10.1007/3-540-08462-2_10.

[133] A. Zeilinger, C. Shull, M. Horne, and G. Squires. *Two-crystal neutron interferometry*. 1978. URL: https://inis.iaea.org/search/search.aspx?orig_q=RN:10474132.

[134] J. Arthur, C. G. Shull, and A. Zeilinger. "Dynamical neutron diffraction in a thick-crystal interferometer". In: *Phys. Rev. B* 32 (9 1985), pp. 5753–5763. DOI: 10.1103/PhysRevB.32.5753.

[135] H. Lemmel. "Dynamical diffraction of neutrons and transition from beam splitter to phase shifter case". In: *Phys. Rev. B* 76 (14 2007), p. 144305. DOI: 10.1103/PhysRevB.76.144305.

[136] P. Ageron and W. Mampe. *Cold and ultra cold neutron beams for fundamental physics research at the Institute Laue-Langevin*. Tech. rep. 1986. URL: https://inis.iaea.org/search/searchsinglerecord.aspx?recordsFor=SingleRecord&RN=18002754.

[137] A. Steyerl and S. Malik. "New developments in cold and ultracold neutron research". In: *Physica B+ C* 137.1-3 (1986), pp. 270–281. DOI: 10.1016/0378-4363(86)90333-5.

[138] R. Cubitt, R. Schweins, and P. Lindner. "Countering the effects of gravity on a small angle neutron scattering instrument". In: *Nuclear Instruments and Methods in Physics Research Section A: Accelerators, Spectrometers, Detectors and Associated Equipment* 665 (2011), pp. 7–10. DOI: 10.1016/j.nima.2011.11.034.

[139] C. Desalme. "Evaluation of thermal and vibrational stability and simulation of the beam transport at PF2/VCN". Supervised by Elhoucine Hadden, Tobias Jenke, and Michael Jentschel. BSc thesis. Grenoble, France: INP Grenoble - Phelma, 2022.

[140] T. Oda, M. Hino, M. Kitaguchi, H. Filter, P. Geltenbort, and Y. Kawabata. "Towards a high-resolution TOF-MIEZE spectrometer with very cold neutrons". In: *Nuclear Instruments and Methods in Physics Research Section A: Accelerators, Spectrometers, Detectors and Associated Equipment* 860 (2017), pp. 35–41. DOI: https://doi.org/10.1016/j.nima.2017.03.014.

[141] M. Blaickner, B. Demirel, I. Drevenšek-Olenik, M. Fally, P. Flauger, P. Geltenbort, Y. Hasegawa, R. Kurinjimala, M. Ličen, C. Pruner, et al. "Monte-Carlo simulation of neutron transmission through nanocomposite materials for neutron-optics applications". In: *Nuclear Instruments and Methods in Physics Research Section A: Accelerators, Spectrometers, Detectors and Associated Equipment* 916 (2019), pp. 154–157. DOI: 10.1016/j.nima.2018.11.074.

[142] T. Crane and M. Baker. "Neutron detectors". In: *Passive Nondestructive Assay of Nuclear Materials* 13 (1991), pp. 1–28. URL: https://inis.iaea.org/search/search.aspx?orig_q=RN:23009217.

[143] I. P. Tobias Jenke. *Acknowledgment about the time-of-flight measurements*. Private communication. This experiment was done in internal commissioning time of the PF2 instrument. Results provided by Dr. Tobias Jenke. 2024.

[144] K. Eder, M. Gruber, A. Zeilinger, R. Gähler, W. Mampe, and W. Drexel. "The new very-cold-neutron optics facility at ILL". In: *Nuclear Instruments and Methods in Physics Research Section A: Accelerators, Spectrometers, Detectors and Associated Equipment* 284.1 (1989), pp. 171–175. DOI: 10.1016/0168-9002(89)90273-8.

[145] Paul Scherrer Institute. *Swiss Spallation Neutron Source (SINQ)*. Accessed: 2024. 2024. URL: https://www.psi.ch/en/sinq.

[146] Paul Scherrer Institut. *SANS-I: Small Angle Neutron Scattering Instrument*. Accessed: 2024. 2024. URL: https://www.psi.ch/en/sinq/sansi.

[147] Institute Laue-Langevin (ILL). *GRASP*. Accessed: 2023. 2022. URL: https://www.ill.eu/users/support-labs-infrastructure/software-scientific-tools/grasp.

[148] E. Hadden, M. Fally, Y. Iso, T. Jenke, J. Klepp, A. Kume, K. Umemoto, and Y. Tomita. "Holographic nanodiamond–polymer composite grating with unprecedented slow-neutron refractive index modulation amplitude". In: *Applied Physics Letters* 124.7 (Feb. 2024), p. 071901. DOI: 10.1063/5.0186753.

[149] J. Klepp, M. Fally, E. Hadden, T. Jenke, and C. Pruner. "Neutron diffraction from commercially available Bayfol photopolymer film gratings." In: *Institut Laue-Langevin (ILL): Grenoble,* (2021). DOI: 10.5291/ILL-DATA.3-14-409.

[150] D. R. Maddison, D. L. Swofford, and W. P. Maddison. "Nexus: An Extensible File Format for Systematic Information". In: *Systematic Biology* 46.4 (Dec. 1997), pp. 590–621. DOI: 10.1093/sysbio/46.4.590.

[151] R. Pynn, S. M. Baker, G. Smith, and M. Fitzsimmons. "Off-specular scattering in neutron reflectometry". In: *Journal of Neutron Research* 7.3, 4 (1999), pp. 139–158. DOI: 10.1080/10238169908200113.

[152] A. Maconnachie. "On the assessment of incoherent neutron scattering intensities from polymer systems". In: *Polymer* 25.8 (1984), pp. 1068–1072. DOI: 10.1016/0032-3861(84)90340-9.

[153] C. J. Glinka. "Incoherent neutron scattering from multi-element materials". In: *Journal of Applied Crystallography* 44.3 (2011), pp. 618–624. DOI: 10.1107/S0021889811008223.

[154] W. Dubner, J. Schultz, and G. Wignall. "Estimation of incoherent backgrounds in SANS studies of polymers". In: *Journal of applied crystallography* 23.6 (1990), pp. 469–475. DOI: 10.1107/S0021889890006215.

[155] F.-K. Bruder, T. Fäcke, R. Hagen, D. Hönel, E. Orselli, C. Rewitz, T. Rölle, G. Walze, and B. Wewer. "Second harmonics HOE recording in Bayfol HX". In: *Holography: Advances and Modern Trends IV*. Vol. 9508. SPIE. 2015, pp. 122–134. DOI: 10.1117/12.2178269.

[156] F.-K. Bruder, T. Fäcke, R. Hagen, D. Hönel, D. Jurbergs, E. Orselli, C. Rewitz, T. Rölle, G. Walze, and B. Wewer. "Edge-lit volume holograms recorded by free space exposure: diffraction by 2nd harmonics in Bayfol(R) HX film". In: *Practical Holography XXIX: Materials and Applications*. Ed. by H. I. Bjelkhagen and V. M. B. Jr. Vol. 9386. International Society for Optics and Photonics. SPIE, 2015, p. 938601. DOI: 10.1117/12.2077868.

[157] D. I. Derevyanko, E. F. Pen, and V. V. Shelkovnikov. "Reflection holographic photopolymer gratings with an anharmonic modulation of the refractive index". In: *J. Opt. Technol.* 90.5 (2023), pp. 278–281. DOI: 10.1364/JOT.90.000278.

[158] G. F. Knoll. *Radiation detection and measurement*. John Wiley & Sons, 2010. URL: https://www.wiley.com/en-nz/Radiation+Detection+and+Measurement%2C+4th+Edition-p-9780470131480.

[159] V. Sears. "Optimum counting times in experiments governed by poisson statistics". In: *Nuclear Instruments and Methods in Physics Research Section B: Beam Interactions with Materials and Atoms* 12.3 (1985), pp. 430–433. DOI: https://doi.org/10.1016/0168-583X(85)90044-8.

[160] N. I. of Standards and Technology. *Activation Calculations*. Accessed: 2023-10-31. 2023. URL: https://www.ncnr.nist.gov/resources/activation/.

[161] O. Blaschko, W. Schranz, M. Fally, G. Krexner, and Z. Łodziana. "Strain-stabilized precursor clusters in potassium thiocyanate". In: *Physical Review B* 58.13 (1998), p. 8362. DOI: 10.1103/PhysRevB.58.8362.

[162] M. Prijatelj, J. Klepp, Y. Tomita, and M. Fally. "Far-off-Bragg reconstruction of volume holographic gratings: A comparison of experiment and theories". In: *Phys. Rev. A* 87 (6 2013), p. 063810. DOI: 10.1103/PhysRevA.87.063810.

[163] Wikipedia contributors. *Markov chain Monte Carlo – Wikipedia, The Free Encyclopedia*. [Online; accessed 28-September-2024]. 2023. URL: https://en.wikipedia.org/wiki/Markov_chain_Monte_Carlo.

[164] D. W. Hogg and D. Foreman-Mackey. "Data analysis recipes: Using markov chain monte carlo". In: *The Astrophysical Journal Supplement Series* 236.1 (2018), p. 11. DOI: 10.3847/1538-4365/aab76e.

[165] European Spallation Source (ESS) Data Management and Software Centre (DMSC). *ESS DMSC Summer School*. https://ess-dmsc-dram.github.io/dmsc-school/intro.html. Accessed: 2024-09-12.

[166] A. Vehtari, A. Gelman, D. Simpson, B. Carpenter, and P.-C. Bürkner. "Rank-normalization, folding, and localization: An improved $\hat{R}$ for assessing convergence of MCMC (with discussion)". In: *Bayesian Analysis* 16.2 (2021), pp. 667–718. DOI: 10.1214/20-BA1221.

[167] A. D. Team. *ArviZ Documentation: R-hat Diagnostic*. Accessed: 16 September 2024. 2024. URL: https://python.arviz.org/en/latest/api/generated/arviz.rhat.html.

[168] F. Feroz and M. P. Hobson. "Multimodal nested sampling: an efficient and robust alternative to Markov Chain Monte Carlo methods for astronomical data analyses". In: *Monthly Notices of the Royal Astronomical Society* 384.2 (Jan. 2008), pp. 449–463. DOI: 10.1111/j.1365-2966.2007.12353.x.

[169] R. R. A. Syms and L. Solymar. "Planar volume phase holograms formed in bleached photographic emulsions". In: *Appl. Opt.* 22.10 (1983), pp. 1479–1496. DOI: 10.1364/AO.22.001479.

[170] J. V. Kelly, F. T. O'Neill, J. T. Sheridan, C. Neipp, S. Gallego, and M. Ortuno. "Holographic photopolymer materials: nonlocal polymerization-driven diffusion under nonideal kinetic conditions". In: *J. Opt. Soc. Am. B* 22.2 (2005), pp. 407–416. DOI: 10.1364/JOSAB.22.000407.

[171] F.-K. Bruder, F. Deuber, T. Fäcke, R. Hagen, D. Hönel, D. Jurbergs, T. Rölle, and M.-S. Weiser. "Reaction-diffusion model applied to high resolution Bayfol HX photopolymer". In: *Practical Holography XXIV: Materials and Applications*. Ed. by H. I. Bjelkhagen and R. K. Kostuk. Vol. 7619. International Society for Optics and Photonics. SPIE, 2010, p. 76190I. DOI: 10.1117/12.841956.

[172] G. Riva, A. Zanutta, F.-K. Bruder, and A. Bianco. "Tuning the Δn and scattering in Bayfol® HX based holograms". In: *Optical Materials* 109 (2020), p. 110362. DOI: https://doi.org/10.1016/j.optmat.2020.110362.

[173] C. AG. *Covestro - High-tech Polymer Materials*. https://www.covestro.com/. Accessed: 2024-11-05.

[174] M. Fally, J. Klepp, C. Pruner, E. Hadden, A. Bianco, J. Kohlbrecher, H. Filter, T. Jenke, and Y. Tomita. "Photosensitive materials for neutron optics". In: *Photosensitive Materials and their Applications III*. Vol. 13015. SPIE. 2024, pp. 75–86. DOI: 10.1117/12.3022432.

[175] V. Bavigadda, R. Jallapuram, E. Mihaylova, and V. Toal. "Design and fabrication of holographic optical elements for applications in electronic speckle pattern interferometry and laser Doppler vibrometry". In: *Eighth International Conference on Vibration Measurements by Laser Techniques: Advances and Applications*. Ed. by E. P. Tomasini. Vol. 7098. International Society for Optics and Photonics. SPIE, 2008, 70980O. DOI: 10.1117/12.803006.

[176] E. Hadden, Y. Iso, A. Kume, K. Umemoto, T. Jenke, M. Fally, J. Klepp, and Y. Tomita. "Nanodiamond-based nanoparticle-polymer composite gratings with extremely large neutron refractive index modulation". In: *Photosensitive Materials and Their Applications II*. Vol. 12151. SPIE. 2022, pp. 70–76. DOI: 10.1117/12.2623661.

[177] Y. Tomita and H. Nishibiraki. "Improvement of holographic recording sensitivities in the green in SiO2 nanoparticle-dispersed methacrylate photopolymers doped with pyrromethene dyes". In: *Applied Physics Letters* 83.3 (July 2003), pp. 410–412. DOI: 10.1063/1.1593816.

[178] N. Suzuki and Y. Tomita. "Holographic scattering in SiO2 nanoparticle-dispersed photopolymer films". In: *Appl. Opt.* 46.27 (2007), pp. 6809–6814. DOI: 10.1364/AO.46.006809.

Acknowledgments

I would like to begin by expressing my deepest gratitude to my academic supervisors, Prof. Martin Fally and Dr. Jürgen Klepp, for their unwavering support, guidance, and expertise throughout my PhD journey. I am equally grateful to my ILL supervisor, Dr. Tobias Jenke, whose contributions were indispensable. While the first page of this thesis does not include the local supervisor's name for administrative reasons only, I would like to take this opportunity to highlight the significant role Dr. Tobias Jenke has played in my progress and to express my heartfelt gratitude for his support and guidance.

I extend my sincere thanks to Prof. Yasuo Tomita and his research group in Japan for their exceptional collaboration and for generously sharing their knowledge and expertise. I would like to acknowledge the contributions of Y. Iso, A. Kume, and K. Umemoto to the work involving NDPC gratings, as well as T. Shimada, A. Narita, and J. Oshima to the work involving HBP-dispersed nanocomposite grating. This collaboration has been a cornerstone of this research, and I am profoundly grateful for their efforts.

Part of this work is based on experiments performed at the Swiss spallation neutron source SINQ, Paul Scherrer Institute, Villigen, Switzerland. Special thanks are due to Dr. Joachim Kohlbrecher, the SANS-I instrument responsible, for his critical support during the neutron experiments. I am particularly grateful for his assistance in performing a measurement remotely due to travel restrictions, as well as his overall willingness to accommodate and support our work.

I also wish to acknowledge that some of the Bayfol gratings studied in this thesis were prepared by Simon Moser during his Master's thesis and others by Elias Dücker during his Bachelor's thesis. I am grateful to Dr. Friedrich Karl Bruder and Covestro Deutschland AG for providing Bayfol photopolymer films in non-commercialized thicknesses, which were essential for this study.

I also acknowledge that parts of the work presented in this thesis have been published in a peer-reviewed journal article and two peer-reviewed conference papers, contributing to the wider scientific discourse in the field. References to these publications are provided in the "List of publications" section of this thesis.

I wish to express my gratitude to the University of Vienna and Vienna Doctoral School in Physics (VDSP) for the financial support provided through a mobility fellowship (6000€), as well as for the access to university infrastructures, guidance through administrative procedures, and opportunities to build connections with fellow researchers during prestigious conferences and workshops. The experiences and support provided by VDSP have significantly contributed to the success of my PhD journey.

I extend my gratitude to Dr. Michael Jentschel, my mentor and the head of the

NPP group at the ILL, for his constant support, open-door policy, and encouragement. His guidance and readiness to assist have made a significant difference during my PhD. I also wish to thank M. Thomas Brenner for his support during experiments and Prof. Stephanie Roccia and Dr. Hanno Filter for their presence and assistance during key experimental sessions. I am thankful to the ILL data management group, particularly M. Stuart Caunt, for providing additional virtual infrastructure for scientific analysis (VISA) instances during the final phase of my PhD. This support was instrumental in completing the analysis presented in this thesis.

I would like to extend my heartfelt thanks to all the BSc and MSc students I had the pleasure to work with or whose contributions I directly or indirectly benefited from during this PhD journey, in particular to I. V. Masiello, C. Desalme, S. Moser, and E. Dücker. I am also deeply grateful to Dr. Manon Letiche, my MSc supervisor, to whom I owe the discovery of neutron science. Her continued support, even during my PhD, was invaluable, especially through her co-supervision of M. Okhrymenko's internship.

I would like to express my sincere gratitude to the members of the ILL's Nuclear and Particle Physics (NPP) group, the Physics of Functional Materials (PFM) group at the University of Vienna, and the ILL Graduate School (IGS). Being part of these esteemed groups has been a privilege that greatly enriched my academic and personal journey. The stimulating discussions during seminars, meetings, and scientific gatherings, as well as the camaraderie shared during social events, have profoundly shaped my understanding and perspective. This acknowledgment also extends to anyone from these groups or beyond whose insights, support, or contributions, whether direct or indirect, have enriched this work in ways that may not be explicitly detailed but are nonetheless valued.

Finally, I am deeply indebted to my family for their unwavering support and encouragement. To my parents, Rafik and Raoudha, who have tirelessly invested in my education and supported me at every step of this journey, I owe my deepest gratitude. To my wife, Maha, and my son, Yacine, thank you for your love, patience, and sacrifices, which have been my source of strength and motivation throughout this journey. To my brother, Riadh, and his wife, Lina, your constant encouragement and kindness have meant so much to me. To my extended family and friends, your encouragement and presence have been a source of joy and reassurance during challenging times. Without their belief in me and their relentless sacrifices, this work would not have been possible.

List of publications and conferences

This section lists the peer-reviewed publications and conference contributions resulting from the research conducted during this thesis.

Peer-reviewed publications

1. E. Hadden, M. Fally, Y. Iso, T. Jenke, J. Klepp, A. Kume, K. Umemoto, and Y. Tomita, "Holographic nanodiamond–polymer composite grating with unprecedented slow-neutron refractive index modulation amplitude," *Applied Physics Letters*, vol. 124, no. 7, p. 071901, Feb. 2024. doi:10.1063/5.0186753.

2. E. Hadden, Y. Iso, A. Kume, K. Umemoto, T. Jenke, M. Fally, J. Klepp, and Y. Tomita, "Nanodiamond-based nanoparticle-polymer composite gratings with extremely large neutron refractive index modulation," in *Photosensitive Materials and Their Applications II*, SPIE Proceedings, vol. 12151, pp. 70–76, 2022. doi:10.1117/12.2623661.

3. M. Fally, J. Klepp, C. Pruner, E. Hadden, A. Bianco, J. Kohlbrecher, H. Filter, T. Jenke, and Y. Tomita, "Photosensitive materials for neutron optics," in *Photosensitive Materials and Their Applications III*, SPIE Proceedings, vol. 13015, pp. 75–86, 2024. doi:10.1117/12.3022432.

Contributions to conferences and workshops

The following conference participations have been fully or partly funded by the Institut Laue Langevin (ILL) and a mobility fellowship provided by the Vienna Doctoral School in Physics (VDSP).

- **2024**: JDN 2024 Conference, organized by Société française de neutronique (SFN), Iles Porquerolles, France. *Participation with an oral presentation.*
- **2024**: The German Conference on Neutron Scattering 2024, Aachen, Germany. *Participation with an oral presentation.*
- **2024**: ESS Data Management and Software Centre (DMSC), Copenhagen & Lund, Denmark & Sweden. *Participation with a Poster.*
- **2023**: European Conference on Neutron Scattering (ECNS), Garching, Germany. *Participation with an oral presentation.*

- **2022**: VCQ and AppQInfo 2022 Summer School: Concepts and Applications of Quantum Information, Vienna, Austria. *Participation with a Poster.*
- **2022**: SPIE Photonics Europe 2022, Strasbourg, France. *Invited speaker.*
- **2022**: HERCULES European School and Conference, Grenoble, France. *Participation with a Poster.*